
Growth and fuelling of galactic nuclei

Nicolas Guillard



München 2018

Growth and fuelling of galactic nuclei

Nicolas Guillard

Dissertation
an der Fakultät für Physik
der Ludwig–Maximilians–Universität
München

vorgelegt von
Nicolas Guillard
aus Bordeaux (Frankreich)

München, den 5. April 2018

Erstgutachter: Prof. Dr. Andreas Burkert

Zweitgutachter: Prof. Dr. Markus Kissler-Patig

Tag der mündlichen Prüfung: 24 Mai 2018

To my family

This project has been carried at the European Southern Observatory (ESO, Garching) under the supervision of Eric Emsellem and within the Excellence Cluster *Universe* student fellowship programme. Members of the Thesis Committee were Andreas Burkert, Markus Kissler-Patig, Stefan Hofmann and Jeannine Wagner-Kuhr.

Contents

Zusammenfassung	xv
Abstract	xvii
1 Introduction	1
1.1 Galaxies: a complex history	1
Open clusters	3
Globular clusters	4
Young massive clusters	5
Nuclear clusters	5
1.2 Nuclear Clusters: a link between galaxies	6
1.3 The RAMSES code: covering several spatial scales simultaneously	9
1.3.1 The AMR technique	9
1.3.2 Sub-grid models	12
Heating and cooling processes	12
Star formation	13
Stellar feedback	13
Unconsidered processes	15
1.3.3 Setup for simulations	16
1.4 The purpose of this work	17
2 Observations of galactic nucleus: the example of NGC 300	21
2.1 Overview of NGC 300	21
2.2 Integral-field spectroscopy: the SINFONI instrument	23
2.3 Reduction of the data	26
2.3.1 Telluric correction	27
2.3.2 Other corrections	31
2.4 Stellar kinematic extraction	31
2.4.1 The penalized pixel fitting method	31
2.4.2 Stellar kinematics	34
2.5 Improvements and steps forward	36
2.5.1 Errors and h3 and h4 moments	36
2.5.2 The Line Spread Function	36

2.5.3	Stellar dynamics: Jeans Axisymmetric model	36
2.6	Conclusion	37
3	Importance of gas reservoirs in the formation of NCs	39
3.1	Numerical tools and convergence	41
3.1.1	Initial conditions and final state	42
3.1.2	Numerical convergence	42
3.1.3	Clusters detection	44
3.2	Formation of NC	44
3.2.1	Formation by migration	47
3.2.2	NC-cluster merger	51
3.2.3	Merger: a mandatory process?	54
3.3	Cluster populations	56
3.3.1	Cluster disruption	56
3.3.2	Surviving clusters	56
3.4	Discussion & Conclusion	60
4	Gas-stars cycle: impact of stellar feedback and application to NCs	65
4.1	Introduction	65
4.2	Numerical methods	67
4.3	Stellar feedback and the star clusters population	69
4.3.1	The star clusters populations	69
4.3.2	The effect on dense gas	71
4.3.3	Radiative versus Supernova feedback	73
4.3.4	The ability of clusters to grow	75
4.4	Discussion & Conclusion	79
5	Outlook: nuclear clusters and cosmological gas accretion	85
5.1	Galaxy formation from halos	86
5.1.1	Modeling the halo collapse	86
5.1.2	Early star formation	88
5.2	Radiation feedback: the challenge of forming star clusters populations	91
5.3	SNe feedback and star clusters	93
5.3.1	Properties of the ISM	95
5.3.2	Consequences on star clusters	98
5.4	Summary and discussion	99
6	Summary and conclusions	103
A	Example of namelist in RAMSES	107
B	Clustered feedback	111
C	Article from broader collaboration	115

List of Figures

1.1	Kinematic classification of galaxies	3
1.2	Classes of clusters	4
1.3	Scaling relations of NCs	7
1.4	Formation of nuclear clusters: paradigm	8
1.5	The AMR grid of RAMSES	10
1.6	The AMR hierarchy	11
1.7	Rho-T diagram	14
2.1	Picture of NGC 300	22
2.2	The SINFONI instrument	24
2.3	The treatment of SINFONI data	25
2.4	SINFONI association map	28
2.5	Telluric correction	30
2.6	Voronoi cube	33
2.7	S/N voronoi cube	34
2.8	Fitted CO absorption line spectra	35
2.9	Velocity/velocity dispersion maps of CO lines of NGC 300 nucleus	35
3.1	Formation of nuclear clusters	40
3.2	Rotation curves	44
3.3	Stellar maps of dwarf galaxies at the beginning and end of the simulation	45
3.4	Star formation rate and numerical convergence	46
3.5	History of the formation of nuclear cluster	48
3.6	Seeds of nuclear clusters	49
3.7	Growth of the nuclear cluster progenitors	50
3.8	Star formation rate within nuclear cluster progenitors	50
3.9	Orbit of the nuclear clusters progenitors	51
3.10	Disturbance on the way of becoming a nuclear cluster	52
3.11	PDFs of the gas density during merger	53
3.12	Star formation history with and without merger	55
3.13	Disruption of clusters	56
3.14	Comparison of the growth of smaller clusters	57
3.15	Size-mass evolution of clusters	58

3.16	PDFs of the gas density during gas ejection	59
3.17	NC-galaxy mass and radius diagram	61
4.1	Feedback vs no-feedback: stellar maps	69
4.2	Feedback vs no-feedback: Cluster Mass Function	70
4.3	Feedback vs no-feedback: PDFs	72
4.4	Individual feedback processes in action: stellar maps	73
4.5	Clusers growth: energetic budget	76
4.6	Impact of the mass loading factor	78
4.7	Another configuration for H _{II} regions	81
5.1	Disc vs halo	87
5.2	Halo early star formation rate	89
5.3	Halo early evolution	90
5.4	Star clusters in forming galaxies	93
5.5	Star clusters disruption in forming galaxies	94
5.6	Halo kinetic feedback	95
5.7	Halo thermal feedback	96
5.8	Gas PDF: kinetic vs thermal feedback	96
5.9	Star formation rate: kinetic vs thermal feedback	97
5.10	Cluster mass function: kinetic vs thermal feedback	98
B.1	Feedback short-term effects on gas clouds density	112
B.2	Feedback short-term effects on the temperature of gas clouds	113

List of Tables

2.1	SINFONI specifications	24
2.2	Characteristics of the telluric stars used for NGC 300	31
3.1	Initial conditions for simulations of discs	43
5.1	Initial conditions for halos simulations	92

Zusammenfassung

In den letzten Jahrzehnten wurde durch Beobachtungen gezeigt dass die meisten Galaxien eine zentral gebundene Struktur aufweisen: einen zentralen Sternhaufen. Diese stellaren Systeme gehen zu den dichtesten Objekten des Universums und es wird angenommen, dass ihre Entwicklung mit der Entwicklung der Galaxie zusammenhängt. Aufgrund ihres häufigen Vorkommens, eignen sich zentrale Sternhaufen zur Untersuchung von Galaxien. Obwohl die Entstehung der zentralen Sternhaufen noch nicht wirklich verstanden ist, werden momentan zwei mögliche Szenarien angenommen: in-situ Entstehung, bei der sich Gas im galaktischen Zentrum anheftet und verdichtet bis Sterne darin entstehen, und das dry merger Szenario, bei dem die Sternhaufen aus der Scheibe durch dynamische Reibung ins Zentrum wandern und sich miteinander vereinen.

Das Ziel dieses Projektes ist es, die Prozesse einzugrenzen, die für die Entstehung und das Wachstum der zentralen Sternhaufen verantwortlich sind. Zu Beginn dieser Arbeit wird ein Beobachtungsbeispiel vorgestellt, in dem Nahinfrarot-Beobachtungen mit dem Instrument SINFONI von der zentralen Region der unter kleiner Inklination erscheinenden Galaxie NGC 300 gemacht wurden. Ich erkläre, wie ich diese Daten mit der SINFONI Pipeline reduziert habe und beschreibe detailliert, wie die Daten analysiert wurden, um eine kinematische Karte des galaktischen Zentrums zu erstellen. Erste Ergebnisse zeigen, dass das galaktische Zentrum nicht rotiert und nur sehr geringe Geschwindigkeitsdispersionen aufweist.

Aus einer theoretischen Perspektive heraus, untersuche ich die Entstehung und das Wachstum zentraler Sternhaufen-Vorgänger mit state-of-the-art hydrodynamischen Simulationen gasreicher Zwerggalaxien mit vorbestimmten Eigenschaften und einer räumlichen Auflösung von einigen Parsec. Ein Schlüsselergebnis dieser Studie ist, dass das galaktische Zentrum durch sogenannte wet-merger entstehen kann, welche die Prozesse der beiden genannten Szenarien verbindet: Ein massiver Sternhaufen entsteht in der gasreichen Scheibe, behält seinen Gasvorrat und wächst weiter während er ins galaktische Zentrum wandert.

In solchen gasreichen Umgebungen formt das induzierte stellare Feedback die Eigenschaften des Sternhaufens und kann möglicherweise die Entstehung der zentralen Sternhaufen abändern. Vor allem der Strahlungsdruck scheint die wichtigste Rolle zu spielen, bei der Zerstrahlung der dichten Gasstrukturen und beim Abändern und Abschwächen der Haufenentstehung.

Zuletzt untersuche ich die Entwicklung von Sternhaufen wenn ein Gas halo kollabiert,

um eine neue Galaxie zu bilden und zu formen. In dieser Situation ist es eine Herausforderung, eine Population stabiler Sternhaufen in den ersten paar hundert Millionen Jahren zu bilden, da alle Haufen durch den Effekt des Strahlungsdrucks wieder zerstört werden. Letzterer tendiert dazu, das Gas von den Haufen weg zu treiben und verursacht Lücken in der Gasdichte und führt zur Expansion der Scheibe.

Die dominanten und zerstörerischen Effekte, die Strahlungs-Feedback auf Sternhaufen haben kann, stellt das Überleben letzterer in Frage. Da Sternhaufen sowohl bei kleinen als auch bei grossen Rotverschiebungen beobachtet werden, rufen unsere vorläufigen Ergebnisse dazu auf, dass diese Art von Feedback und ihre Wirkung auf kleinen und grossen Skalen besser verstanden werden muss.

Abstract

Over the last decades, observations have shown that a majority of galaxies host a bound structure at their centre: a nuclear cluster. These stellar systems are among the densest objects in the universe and it has been suggested that their evolutionary path is closely linked to that of their host. Due to their ubiquity, nuclear clusters are objects of choice to study galaxies. Although the formation of nuclear cluster is still poorly understood, the current paradigm offers two possible scenarios: “*in-situ*” formation where gas piles up at the galactic centre and collapses into stars, and “*dry-merger*” scenario where star clusters in the disc migrate towards the galactic centre through dynamical friction and merge.

The aim of this project is to constrain the fuelling and growth mechanisms at play in the formation of nuclear clusters. The thesis first presents an example of observations in the near-infrared of the nuclear region of the low-inclined galaxy NGC 300 with the SINFONI instrument. I explain how I reduced these data using the SINFONI pipeline and detail the first steps in their analysis, leading to the kinematic maps of the nucleus. Preliminary results show the apparent absence of rotation of the nucleus with low velocity dispersion.

From a theoretical perspective, I study the formation and growth of nuclear cluster progenitors using state-of-the-art hydrodynamical simulations of gas-rich dwarf galaxies with predetermined properties, at parsec resolution. A key result is that a nucleus can form through a “wet-merger” which combines the processes involved in the two paradigm scenarios: a massive star cluster forms in the gas-rich disc, keeps a gas reservoir, and grows further while migrating to the centre.

In such gas-rich environments, the induced stellar feedback shapes the properties of star clusters and can potentially alter the formation channel of nuclear clusters. In particular, the radiation feedback seems to play the most important role in destroying dense gas structures, and altering or quenching the subsequent cluster formation.

I finally study the evolution of star clusters when a gaseous halo collapses to form and shape the galaxy from scratch. In this situation, it is challenging to form a stable star cluster population during the first few hundreds of Myr, with all clusters being destroyed by the effect of radiative feedback. The latter tends to expel the gas away from the clusters, creates gaps in the gas density and leads to the expansion of the disc.

The dominant and damaging effects that radiation feedback can have on star clusters question their survivability. Since clusters are observed both at low and high redshift, our preliminary results call for a better understanding of the inner workings of this mode of feedback at small and large scales.

Chapter 1

Introduction

1.1 Galaxies: a complex history

What is our place in the universe? Are we just accidents of history or were we meant to exist? These questions have been in the minds of humans for as long as they looked up to the sky and considered the existence of something bigger than Earth. From the planets of our solar system to the discovery of galaxies, we have come to realize how vast and seemingly limitless the universe is. Our Galaxy, the Milky-Way is just one galaxy among many others. Indeed, the number of observed galaxies is enormous and keeps increasing as telescopes and analysis tools improve: we nowadays estimate that the observable universe contains over two trillion galaxies. On smaller scales, we have thus far discovered over 3,500¹ (at the time of writing) exoplanets, i.e. planets outside our solar system. With scales so different yet linked into a single history, understanding the inner working of the universe and its various components (stars, gas clouds, galaxies, galaxy clusters, etc.) is extremely challenging but very exciting.

In that regard, galaxies represent a link between “small” objects (planets, stars) and “large” structures (galaxy clusters, cosmological filaments) and are thus crucial keys for our comprehension of the universe. Observations and theories have worked together trying to get the full life story of any galaxy, observations by getting its properties at a time t and theories by explaining the physics at play and its dynamics. A single observational image of a galaxy already teaches us a lot about it (e.g. its current morphology, size, its potential past and future; see the following paragraphs) and can be compared with other galaxies to get hints of its history. Over the last decades, theorists, using simulations of galaxies, have attempted to reproduce and predict the observed galactic properties, while also understanding the physical origins that led to such properties. As computer performances increase, scientists have used larger numerical simulations (called cosmological simulations) to study the history of galaxies within large-scale structures and have given us a paradigm on their evolution. They suggest that galaxies form from the collapse of hot gas which

¹See <https://exoplanetarchive.ipac.caltech.edu/> for a regularly updated number of the confirmed planets and candidates

cooled and fell into potential wells drawn by invisible matter (the Dark Matter) gravity. This scheme lies within the Λ Cold Dark Matter (CDM) model (see e.g. White and Rees 1978; Blumenthal et al. 1984)². The formation of the large structures in the universe begins with the collapse of small linear perturbations which originate from quantum fluctuations (Linde 1982). These density perturbations produce dark matter halos in which galaxies will form. As these halos collapse through gravity, external non-linear gravitational pulls create torques on them, thus causing these halos to have angular momentum (Barnes and Efstathiou 1987). Hot gas is then dragged into these hot halos by gravity, carrying the same specific angular momentum as the halo it falls into. Having an angular momentum, the baryon distribution cools, dissipates, flattens and forms exponential discs (Fall and Efstathiou 1980; Mo et al. 1998). Through combinations of cooling and heating processes, the gas enters into a multiphase state, i.e. having a hot ($> 10^4\text{K}$) and a cold (several 10 K) component, from which stars can form. Galaxies are born. They then experience external and internal processes, such as galaxy mergers, gas stripping, star formation, stellar feedback, which shape them into what we observe today.

Galaxies are gravitationally bound systems that are composed of stars, interstellar gas, dust and (hypothetically) dark matter, if the CDM model is correct. They can take different morphologies as some show prominent structures such as discs, bulges, spirals, bars or double bars, star clusters or nuclear clusters (i.e. star clusters in or near the galactic center). Their spatial size varies from galaxy to galaxy, spanning up to 3 orders of magnitude (few hundreds of parsecs³ for dwarf galaxies to several 10,000 parsecs for giant galaxies). Since their discovery, astronomers have attempted to sort galaxies based on certain criteria.

Several works from Hubble (1936) to the Galaxy Zoo project (Raddick et al. 2007) have aimed at classifying galaxies based on their apparent morphology. This led to the Hubble Tuning Fork classification, which separates galaxies in three main categories: the Ellipticals (with an ellipsoidal shape), the Lenticulars (i.e. discs without spirals; referred to as S0 in the literature) and the Spirals (barred or unbarred). Ellipticals and Lenticulars are also often called early-type galaxies, while Spirals are mentioned as late-type galaxies.

The kinematic classification is a more recent method that sorts galaxies looking at their angular momentum (see Figure 1.1 and for example the review by Cappellari 2016). This classification alleviates some issues with the Hubble approach which can misclassify galaxies (Emsellem et al. 2007). This new scheme has been made possible by the use of Integral Field Spectroscopy (IFS) surveys such as SAURON (Bacon et al. 2001) or ATLAS^{3D} (Cappellari et al. 2011a). Galaxies (in the limit of one effective radius⁴) are now divided into slow and fast rotating galaxies, based on a proxy for the spin parameter λ_R

²Other models like the MODified Newtonian Dynamics (MOND) theory or the Warm Dark Matter model exist as alternative frameworks for understanding the formation and evolution of the universe. These theories are beyond the scope of this Thesis and will not be described here. The interested reader can refer to Milgrom (2015) or Bode et al. (2001) for further details.

³1 parsec = 3.26 light-years = 3.09×10^{16} meters $\sim 2,400,000,000$ Earth's diameter

⁴i.e. the region within which half of the total light is emitted. In simulations, the half-mass radius is equivalently used.

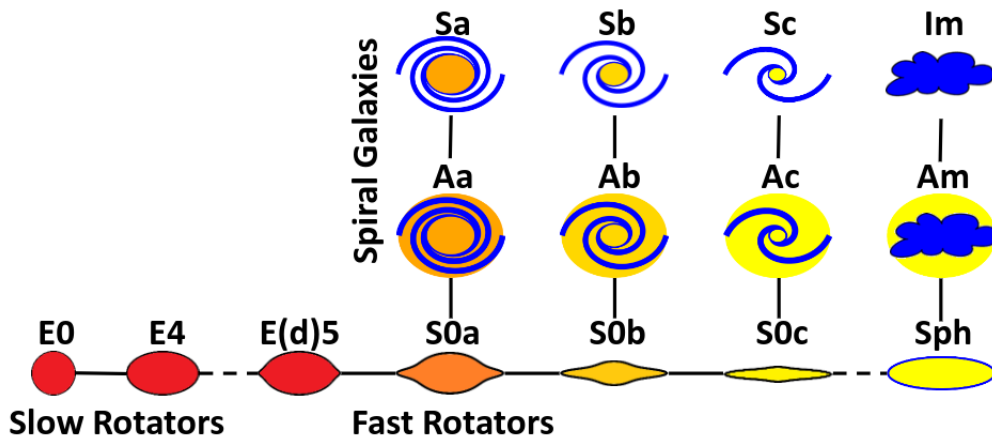


Figure 1.1: The “comb” diagram: a classification of galaxies based on their kinematics. Ellipticals (E), Lenticulars (S0) and Spirals (S) are displayed as a function of their rotation. The number associated with the Ellipticals notation denotes their axis ratio, while the letter associated with the Spirals stands for the opening angle of their spiral arms. Credit: Cappellari et al. (2011b).

(Emsellem et al. 2007, 2011). It is based on a dynamical property which roughly separates galaxies with (fast rotators) and without (slow rotators) discs.

Both the Hubble and the kinematic classifications are the first steps that characterize galaxies based on their apparent and dynamical properties. However, they fail at addressing several questions related to the history of galaxies. In particular, they do not explain (by design) the origin and evolution of structures observed in most galaxies: star clusters. These ubiquitous systems form from the collapse of dense gas clouds and are often considered to be the building blocks of galaxies (e.g. Fellhauer and Kroupa 2002; Kroupa 2005; Portegies Zwart et al. 2010) and the forming location of most (if not all) stars (Lada and Lada 2003). They are thus used as benchmarks for galaxy evolution. Star clusters have been traditionally divided into two main classes, open clusters (in galactic discs) and globular clusters (in galactic halos). Observations in the 1990s of massive clusters widened this cluster classification to two more types: young massive clusters and nuclear clusters. In the following paragraphs, we briefly describe each class (shown in Figure 1.2) and their (proposed) formation scenarios (for a more in-depth review, see Renaud 2018).

Open clusters

Open clusters (also referred to as galactic clusters) are assemblies of several thousand stars, corresponding to densities of the order of 1 star.pc^{-3} . We estimate that our Galaxy contains over 1,100 open clusters, which are observed primarily in the Galactic plane, more specifically in the spiral arms. This pattern is also observed in other spiral galaxies. Open clusters are relatively young objects, with a typical lifetime of around 100 Myr (a few Gyr



Figure 1.2: From *left to right*: The Pleiades open cluster, the globular cluster Omega Centauri, the Young Massive Cluster 30 Doradus in the Large Magellanic Clouds and zoom-in on the nuclear cluster of NGC 2997. Credit: NASA, ESO, NASA, ESO

for the densest ones). After their formation from the collapse of molecular gas clouds, they start to lose stars steadily, and are then disrupted by the galactic tidal field. Due to their young age (compared to the age of their galaxy), galactic clusters are mainly used as test objects for stellar evolution models. Their properties can also be used to probe galactic structures and understand their formation, like the timescale of metal enrichment within the galactic disc (Salaris et al. 2004).

Globular clusters

Globular clusters (GCs) have higher densities (more than hundred star.pc^{-3}) and are much older (several billion years) than open clusters. To this date, 157 globular clusters have been observed in the halo of the Milky Way (Harris 2010). More globally, globular clusters are detected in the majority of galaxies halos which makes them omnipresent in the universe. Due to their average old age and their ubiquity in stellar halos, globular clusters are relics of past galactic evolution since they have survived the harassment of their environment for several billion years. The formation process of globular clusters is still an open question due to the lack of observational constraints and a key topic in astronomy. Hence, GCs have been the subject of intense studies and their physical properties have been examined in order to extract clues pertaining to their formation and evolution.

In particular, globular clusters populations associated with massive galaxies sometimes exhibit a bi-modality in color and metallicity (e.g. Zinn 1985; Peng et al. 2006). Blue clusters are metal-poor and typically located in the outer regions of galaxies (they used to be referred as halo clusters). On the other hand, red clusters are more metal-rich, spatially more concentrated and rotate with their galaxy host. In addition to their high stellar density and their color bi-modality, the precise measurement of the age of GCs can be used to constrain their formation scenario. Unfortunately, the age of GCs is still poorly constrained due to the degeneracy between age and metallicity (the GCs in the Milky Way are thought to have formed 11.5-12.5 Gyr ago).

All these observed properties have been used to constrain the formation process(es) of GCs. Peebles and Dicke (1968) first ventured the idea that GCs formed from the collapse

of gravitationally bound gas clouds even before galaxies formed. Studies like Ricotti et al. (2016) suggested that such collapse likely occurred in potential wells enclosing dark matter. However, these models do not account for the observed color bi-modality (as they imply an unique early formation process) and need to explain the observed absence of dark matter. Alternatively, works by Schweizer (1987) and Ashman and Zepf (1992) proposed that two channels of formation for GCs: the blue clusters form in the early and metal-poor universe and the red, metal-rich clusters form in wet mergers of interacting galaxies. Other scenarios by Forbes et al. (1997) hinted at a formation in several phases: a first phase in which metal-poor clusters form at the same time as the first proto-galaxies and a second phase during the formation of galactic discs where the accumulation of dense enriched gas triggers the formation of a second population of clusters. More recently, simulations from Renaud et al. (2017) show that blue, metal-poor globular clusters may form in satellite galaxies that are then accreted onto the Milky Way. The red, metal-rich globular clusters form in-situ or in massive self-enriched galaxies merging with the Milky Way.

Young massive clusters

Young Massive Clusters (YMCs) were first observed as “bright blue clusters” in NGC 1275⁵ in the early 1990s with the advent of the Hubble Space Telescope (HST). Holtzman et al. (1992) suggested that these populations of clusters were young (< 100 Myr) and dense ($> 10^6 M_{\odot}$ and a few parsec of effective radii), or in other words of the same age as open clusters but with densities similar to globular clusters. After this discovery, more YMCs were found with HST in mergers and starbursts of spiral and dwarf galaxies, and later on in the Milky-Way as well. Two scenarios exist to explain the formation of YMCs (see the reviews from Longmore et al. 2014; Bastian 2016): an “in-situ formation” where all the gas accumulates and collapses to form the final star cluster; a “conveyor belt formation” in which small pockets of gas and young stars converge and gravitationally bind to form the star cluster.

Nuclear clusters

Nuclear clusters (NCs) are among the densest star clusters in the universe (up to $10^4 - 10^6 \text{ star.pc}^{-3}$) and are located at the centers of galaxies.

NCs are present in a wide variety of low-to-intermediate mass galaxies, from early (e.g. Carollo et al. 1998; Turner et al. 2012; den Brok et al. 2014) to late-type galaxies (e.g. Böker et al. 2002; Carson et al. 2015). Observational studies with the Hubble Space Telescope show that about 75% of spiral and dwarf elliptical galaxies have a prominent NC (Côté et al. 2006; Seth et al. 2006, 2008a; Neumayer and Walcher 2012). They are however not observed at the high-mass end distribution of galaxies ($\geq 10^{11} M_{\odot}$).

Nuclear clusters have effective radii in the range of 1-10 pc (e.g. Georgiev and Böker 2014), similarly to globular clusters or young massive clusters (see e.g. the review of Longmore et al. 2014). Their mass typically goes from $10^6 M_{\odot}$ to $10^8 M_{\odot}$ (Walcher et al.

⁵NGC 1275 is a Seyfert galaxy, i.e. a lower-luminosity active galactic nuclei.

2005). This range of high-mass and small-radius makes nuclear clusters the densest stellar ensembles in the universe (Böker et al. 2004; Côté et al. 2006). Measuring such small objects thus requires instruments with high spatial resolution such as SINFONI (see Chapter 2) or simulations of galaxies with a parsec-like resolution at least (see Chapter 4).

Nuclear clusters host multiple stellar populations both in late-type (e.g. Walcher et al. 2006; Rossa et al. 2006) and early-type (Seth et al. 2010; Lyubenova et al. 2013) galaxies. This indicates a complex star formation history although a general pattern is observed. Old stars (i.e. $10^8 - 10^{10}$ yr) constitute the dominant fraction of the stellar population. The younger population ($\lesssim 10^6$ yr) is often more centrally concentrated towards the center of the cluster, as it is observed for the Milky-Way nuclear cluster where the young stars are contained within 0.5 pc around the black hole (Feldmeier-Krause et al. 2015). This trend has also been observed in a larger sample survey by Carson et al. (2015) which shows that the light distribution in the blue filters (thus associated with young stars) is more compact than in the red filters. Moreover, the nuclei seem to be more metal-rich and younger than their galactic host (Koleva et al. 2011).

Finally, we observed that properties of nuclear clusters co-evolve with that of their galactic host. This particular point is introduced in the next section as it sheds light on the special place nuclear clusters hold in the history of galaxies.

1.2 Nuclear Clusters: a link between galaxies

Perhaps one of the most interesting behavior of nuclear clusters (aside from their unique location in the galactic disc) is their apparent co-evolution with their host galaxy. Indeed, it has been pointed out that some properties of nuclear clusters correlate with those of their galaxy. Several types of correlations have been discovered over the years (see Figure 1.3): the mass of the nucleus is linked to the luminosity of the galaxy, to the velocity dispersion of its bulge, to its stellar mass (Carollo et al. 1998; Ferrarese et al. 2006; den Brok et al. 2014; Georgiev et al. 2016). These relationships are interestingly similar to those observed between Supermassive black holes (SMBHs) and their hosts (Gültekin et al. 2009; Bennert et al. 2011; Savorgnan 2016) although some differences have been noticed like the mass relation which is shallower for NCs than SMBHs (e.g. Scott and Graham 2013). It is also worth noting that some galaxies such as the Milky-Way host both a nuclear cluster and a supermassive black hole (Seth et al. 2008a; Graham and Spitler 2009), leading to the suspicion that NCs can be the birthplace of black holes. These scaling relations between nucleus and galaxy, combined with the ubiquity of nuclear clusters in the universe suggest that these clusters are closely linked to the history of their host. Nuclear clusters may thus be used as core tools to constrain how a large variety of galaxies form and evolve. However, due to their small size (parsec-like compared to the kilo-parsec size of their galaxy host), their study involves physics that spans a broad range of spatial scales. This makes the understanding of the history of nuclear clusters both fascinating and challenging. A clear example of such complexity is the mystery that surrounds their formation.

The formation of nuclear clusters currently remains an unsolved problem. To date, two

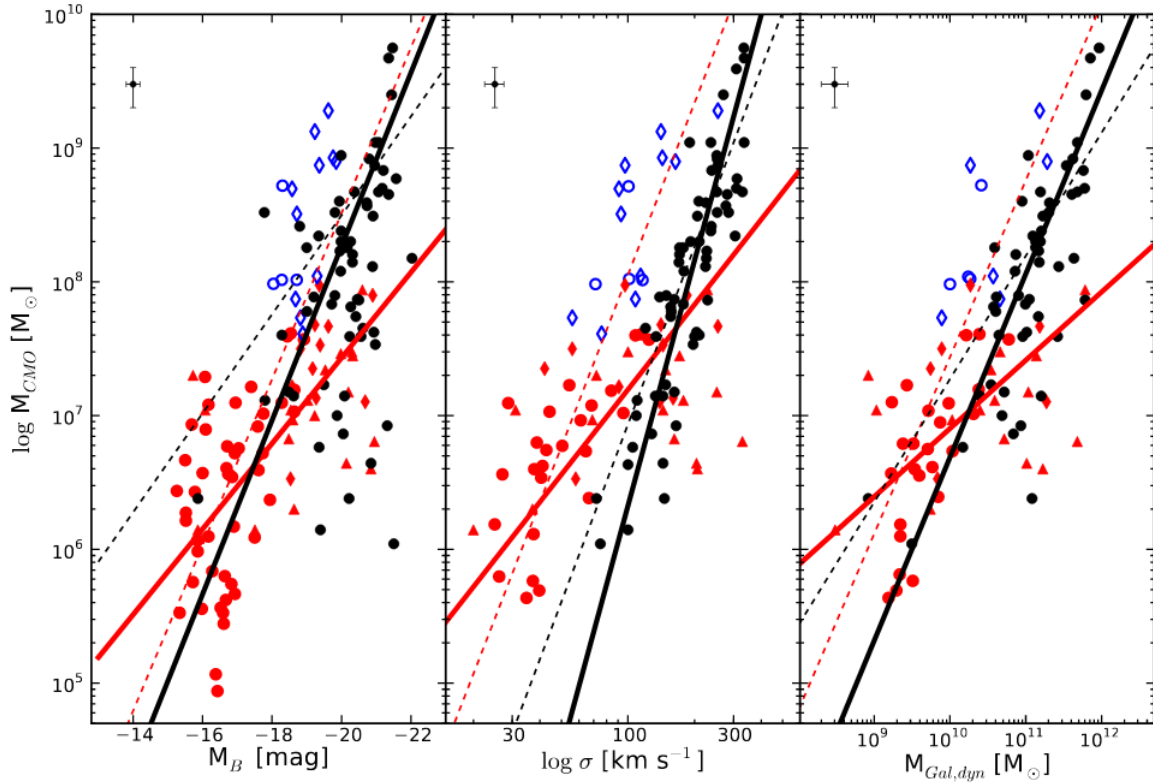


Figure 1.3: Scaling relations between the mass of Central Massive Objects (CMO in the label) with respect to host galaxy properties: galaxy magnitude (left), velocity dispersion (middle) and dynamical mass of the galaxy (right). Supermassive black holes are marked with black dots, NCs with red symbols and Nuclear Discs with open blue symbols. Thick lines display the best fitting linear relations. Credit: Scott and Graham (2013)

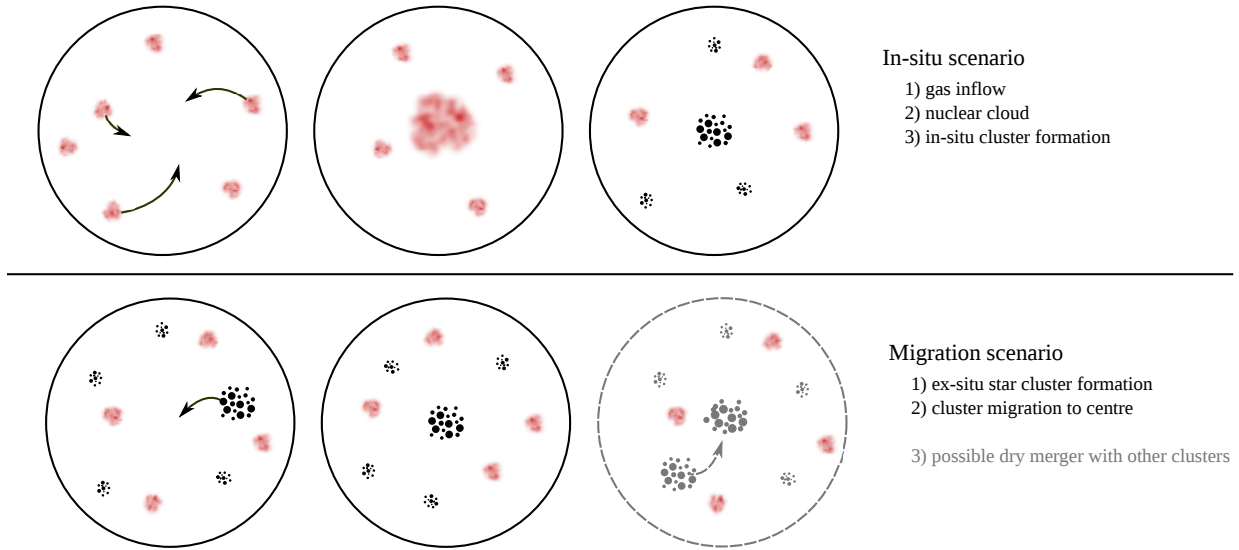


Figure 1.4: Schematics representation of nuclear clusters formation scenarios from the literature. The parts in gray indicate a non-mandatory process.

main formation scenarios have been proposed (see Fig. 1.4):

- in-situ (Milosavljević 2004): gas falls onto the galactic centre which subsequently triggers star formation in the central few parsecs and forms the NC.
- migration (Tremaine et al. 1975): a massive cluster forms, then migrates towards the centre by dynamical friction. This process is potentially followed by dry mergers (i.e., gas free) with other clusters (Andersen et al. 2008; Antonini 2013).

The first scenario has been supported by observations. Molecular gas or similarly evidences of recent star formation have been observed in many nuclear clusters (Schinnerer et al. 2003; Melchior and Combes 2013; Walcher et al. 2006). Moreover, observations of a co-rotating nucleus with the galaxy support the scenario of gas accretion from the disc (Seth et al. 2008b). Detecting feedback activities, such as winds and supernovae are also evidences of recent in-situ star formation activity (Schinnerer et al. 2008). This last topic has been discussed with hydrodynamical simulations which showed that such a cycle of star formation-gas expulsion-gas accretion can occur, given a certain model of feedback (e.g. Bourne and Power 2016). However, this model does not encompass processes such as ionization which could strengthen the role of feedback and prevent the re-accretion of gas.

Evidences of infalling clusters are harder to find with observations and is therefore mainly studied with N-body simulations or semi-analytical models. Their findings indicate that observed properties of nuclear clusters (density, metallicity, etc.) may be recovered by several consecutive infalls of globular clusters (Capuzzo-Dolcetta and Miocchi 2008; Antonini 2013). For the observations of multiple stellar populations, it has been suggested that the accretion of young massive clusters formed in close vicinity of the galactic center

may renew the stellar population of the nucleus (Agarwal and Milosavljević 2011; Arca-Sedda and Capuzzo-Dolcetta 2014). However, Arca-Sedda et al. (2016) warned that some processes such as the interaction of globular clusters and a super-massive black hole may disrupt the infalling cluster, thus stopping the formation of the nucleus.

Numerically, formation of nuclear clusters can be studied with several techniques: analytical or semi-analytical models, or hydrodynamical simulations. Since gas plays a major role in the forming process, regardless of the considered scenario, one would want to include its dynamics and use a hydrodynamical code. We describe in the next section one of these codes, **RAMSES**, which has been previously used by my collaborators to study star clusters (Bournaud et al. 2008; Renaud et al. 2015) and that I utilized during my Thesis.

1.3 The RAMSES code: covering several spatial scales simultaneously

1.3.1 The AMR technique

RAMSES⁶ is a hydrodynamical simulation code designed to solve various problems in astrophysics from the formation of planets to that of galaxies. The code is able to include various components (dark matter, stars, gas, photons) as well as various physical processes (gravity, star formation, stellar feedback, chemical reactions, magnetohydrodynamics). It is written in Fortran 90 and is suited for supercomputers thanks to its parallelization with the MPI library. The main advantage of **RAMSES** is that it uses the Adaptive Mesh Refinement (AMR) scheme which provides high spatial resolution at a reasonable cost.

RAMSES is an Eulerian code, i.e. we study the fluid in a specific location in space as time passes (Leveque 1998). Space is discretized, hence forming a computational grid. The number of cells of the grid gives an idea of the resolution of the simulation. The code solves the Euler equations:

$$\frac{\partial \rho}{\partial t} + \Delta \cdot (\rho \mathbf{v}) = 0 \quad (1.1a)$$

$$\frac{\partial \rho \mathbf{v}}{\partial t} + \Delta \cdot (\rho \mathbf{v} \mathbf{v}) + \Delta p = 0 \quad (1.1b)$$

$$\frac{\partial E}{\partial t} + \Delta \cdot [\mathbf{v}(E + p)] = 0, \quad (1.1c)$$

where ρ is the density of the gas, \mathbf{v} is its velocity and p its pressure. The total energy density E is computed as:

$$E = \frac{1}{2} \rho v^2 + \frac{P}{\gamma - 1}, \quad (1.2)$$

where γ is the adiabatic index. This last equation implies the existence of an equation of state for the pressure P which is given by the user.

⁶<http://www.ics.uzh.ch/~teyssier/ramses/RAMSES.html>

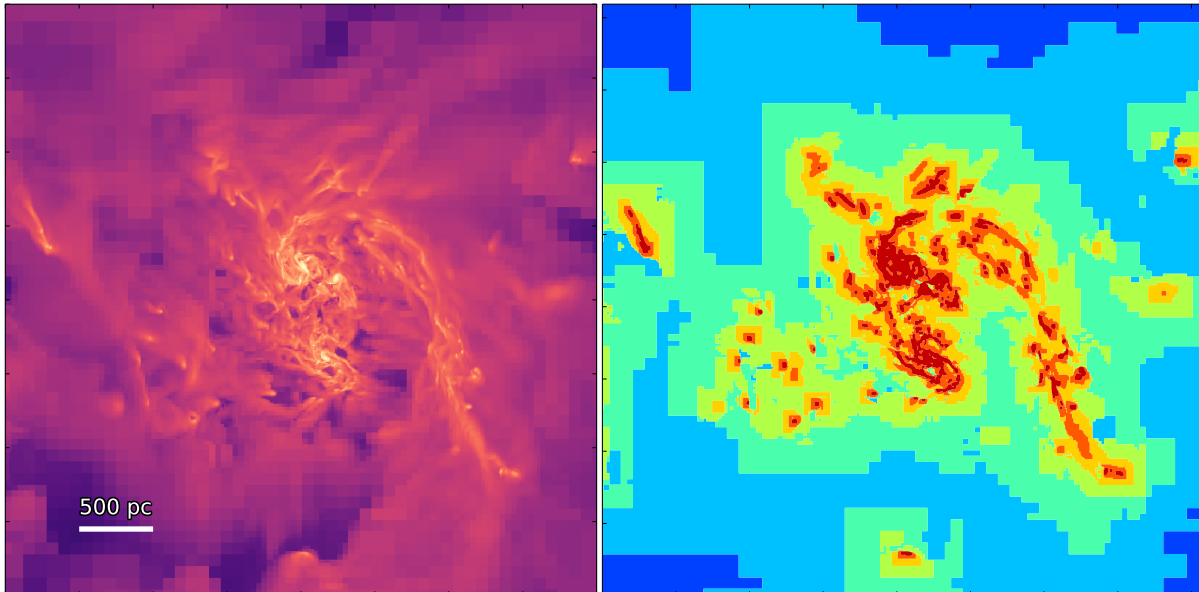


Figure 1.5: Representation of the AMR grid in a **RAMSES** simulation of a forming dwarf galaxy. The map of the gas density is shown in the **left** panel. The corresponding AMR map is shown in the **right** panel, with the lowest level of refinement $l = 9$ in blue and the highest resolution at $l_{max} = 16$ in red. The refinements occur at the location of the dense gas clumps and in the inner regions of the galaxy.

Nowadays, it is possible to create dynamical grids, with an increased resolution locally according to some conditions defined by the user. The overall goal of our simulations is to probe the star forming sites and to accurately resolve the physical properties and conditions of the gas that will give birth to star clusters. Our refinement criterion is thus defined by the density gradients of the gas as shown in Figure 1.5:

In order to refine the relevant cells of the grid, **RAMSES** uses a method elaborated by Kravtsov et al. (1997) which consists of refining *parent* cells into *children* cells in a recursive tree-based structure. Neighbour cells are gathered into octs⁷ that relate within a tree structure (see Figure 1.6). The oct at level l is related both to its father cells and to the $2 \times ndim$ neighboring cells at level $l-1$ ($ndim$ is the number of dimensions). It is also associated with the 2^{ndim} children octs in the upper level. The coarse level is the level with the lowest consistent resolution. Cells that are not refined are called leaf cells, while those which are refined are called split cells. The resolution of the grid is given by the ratio $L_{box}/2^{l_{max}}$ where L_{box} is the total length of the box and l_{max} is the highest level of refinement.

The refinement of cells can be triggered if the thermal Jeans length is resolved by at least four cells. If those cells are already at their finest level, an additional pressure,

⁷An oct is a group of 2^{ndim} sibling cells at a refinement level l . They represent the basic elements of the data structure at a level l .

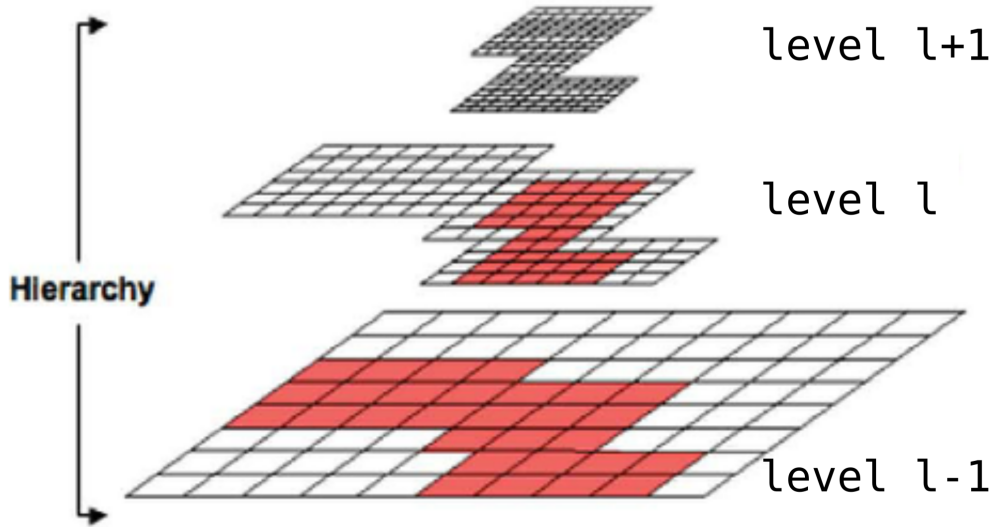


Figure 1.6: Simple illustration of an AMR structure. Basic elements of the structure (called octs) at level l are related to their father cells at level $l-1$ and to their children cells at level $l+1$. The level with the lowest uniform resolution is called the coarse level (in this case, level $l-1$). Credit: J Kamkar et al. (2011).

implemented as a heating function called the Jeans polytrope, is added. This pressure floor avoids an artificial fragmentation of the gas cells and hence artificial star formation. Overall, the AMR scheme allows us to perform parsec-resolution simulations of galaxies by increasing the resolution only in gas regions of high-density.

In **RAMSES**, stars and dark matter are considered as particles. For simulations of galaxies or galaxy clusters, the total number of dark matter and stars particles is usually higher than a few million. Hence, due to its enormous cost in computational resources, solving of the equations of motions for these particles becomes impossible with direct integration methods. Instead, **RAMSES** uses a particle-mesh scheme which groups them in a density field by distributing the mass of particles over the AMR grid. In such collisionless N-body system, particle properties are described by the Vlasov-Poisson equations:

$$\frac{d\mathbf{x}_p}{dt} = \mathbf{v}_p \quad (1.3a)$$

$$\frac{d\mathbf{v}_p}{dt} = -\nabla\phi \quad (1.3b)$$

$$\Delta\phi = 4\pi G\rho \quad (1.3c)$$

where \mathbf{x}_p is the positions of the particles, \mathbf{v}_p their velocities, ϕ is the gravitational potential, G is the gravitational constant and ρ is the density of particles. The computation of the density of stars and dark matter is realized by using the Cloud-In-Cell (CIC) technique (Hockney and Eastwood 1981) which creates a particle density field. The gravitational

potential is then computed by solving the Poisson equation in Fourier Space and the acceleration on the mesh is determined with a standard finite-difference approximation of the gradient of the potential. The acceleration of particles is then retrieved using the inverse CIC interpolation technique. Finally, the velocities and the positions of the particles are recovered based on their acceleration. In order to avoid divergent behaviors for close encounters (since the gravitational forces are inversely proportional to the distance between particles), a softening force is introduced. The gravitational potential is smoothed at the scale of this additional force, whose distance of interaction represents the “spatial resolution” of the particles.

The softening is of major importance as it sets the typical size of the stellar objects in the simulation. We thus have to keep it in mind when we analyse groups of particles like clusters, as such groups may be associated with numerical noise. Typically, a good compromise for a structure to be “physically” resolved is if it is around ten times larger than the value of softening. Star clusters having a size of a few tens of parsecs, we thus need a softening of a few parsec at least⁸. In the code, two kinds of softening are used: one for the particles of the initial conditions (ICs, see next section), namely the original stars and the dark matter particles, and one for the particles we form during the simulation. The latter is defined by the refinement level of the grid while the former is defined by the user during the setup of the simulation (see Section 1.3.2). Since we focus on the clusters that will be formed during the simulation, the softening on the initial particles does not need to be as small as the new stars and we set it around 10-20 parsecs. In both cases, this value for the softening prevents us from probing relaxation, mass segregation within clusters or binaries interactions. Such issues also exist in the gas but can be lessened with sub-grid models.

1.3.2 Sub-grid models

Our limited spatial resolution on the stars and gas implies that not all physical processes will be resolved. The hydrodynamical equations do not take into account for example the cooling/heating of the gas which thus must be implemented aside. To alleviate these issues, we use sub-grid models to include crucial missing physics such as star formation or its associated stellar feedback.

Heating and cooling processes

Gas has the ability to radiate its internal energy and to absorb energy from the radiative field. These are known as radiative cooling and radiative heating respectively. Cooling processes involve the conversion of kinetic energy into radiant energy which escapes from the system. This occurs through collisional excitation which is then followed by radiative decay. It is represented by a cooling function Λ which encompasses the various cooling processes (e.g. recombination, free-free emission, Compton cooling etc.). On the other

⁸We are here talking only about the detection of the object. The sub-structure and internal dynamics of the system (e.g. binary stars) are obviously not resolved at these resolutions.

hand, the heating of the gas mainly occurs through photoionization which is the ejection of an electron from a parent species (atom, ion, molecule). Typically, such process originates from young massive stars emitting UV radiation and is typically observed in clouds primarily composed of ionized hydrogen, the H_{II} regions.

The computation of all those processes would represent a massive slow-down in the computation of the gas dynamics. We instead use tabulated functions for the cooling and the heating of the gas from Courty and Alimi (2004). Also, for the sake of simplicity and computer costs, we do not account for the propagation of metals and set a constant metallicity for the stars of $0.05 Z_{\odot}$. In order to avoid that gas cools to temperature which would increase the computation time by several order of magnitude, we set a temperature floor for gas with densities $10^{-3} < \rho < 300\text{cm}^{-3}$. For low density regions, we model a polytrope with an index 5/3 corresponding to hot virialised gas. As already mentioned, for higher gas densities, a Jeans polytrope is added to prevent artificial fragmentation. An example of temperature-density diagram is given in Figure 1.7

Star formation

The formation of a single solar mass star occurs at spacial scales of the order of the Astronomical Units (AU). This is several orders of magnitude below the resolution we aim for in this Thesis and is thus not considered here. Instead, star formation is modeled on parsec-scale, with a local star formation rate following the Schmidt (1959) law:

$$\rho_{SFR} = \epsilon_{SF} \frac{\rho}{t_{ff}} \quad (1.4)$$

where ϵ_{SF} is the star formation efficiency (SFE), ρ the density of the gas and $t_{ff} = \sqrt{3\pi/(32G\rho)}$ is the free-fall time. The SFE is the percentage of gas that is converted into star and is typically between 1-4% in parsec-scale simulations. At each time-step, gas cells denser than an arbitrary threshold defined by the user can be transformed into stars. A dimensionless number n is then randomly chosen from a Poisson distribution with a mean value of $\rho_{SFR} d_x^3 dt / M_*$ where d_x is the size of the cell, dt the time-step at the local level of refinement and M_* a mass chosen by the user. If $n > 0$, a star of mass nM_* is created with a softening corresponding to the local resolution of the cell. We make sure the mass of our stars is not in a regime where an expensive computation of an Initial Mass Function would be required, typically above a few hundred solar masses.

Stellar feedback

After the star formation event, the young massive stars will emit strong UV emission and will explode in a type-II supernova. For simplicity, only the feedback coming from the OB-type stars is considered and occurs during the first 10 Myr after the formation of the star. In this Thesis, we take into account three types of stellar feedback which we briefly describe below: type-II supernovae, photoionization which creates H_{II} regions and radiative pressure.

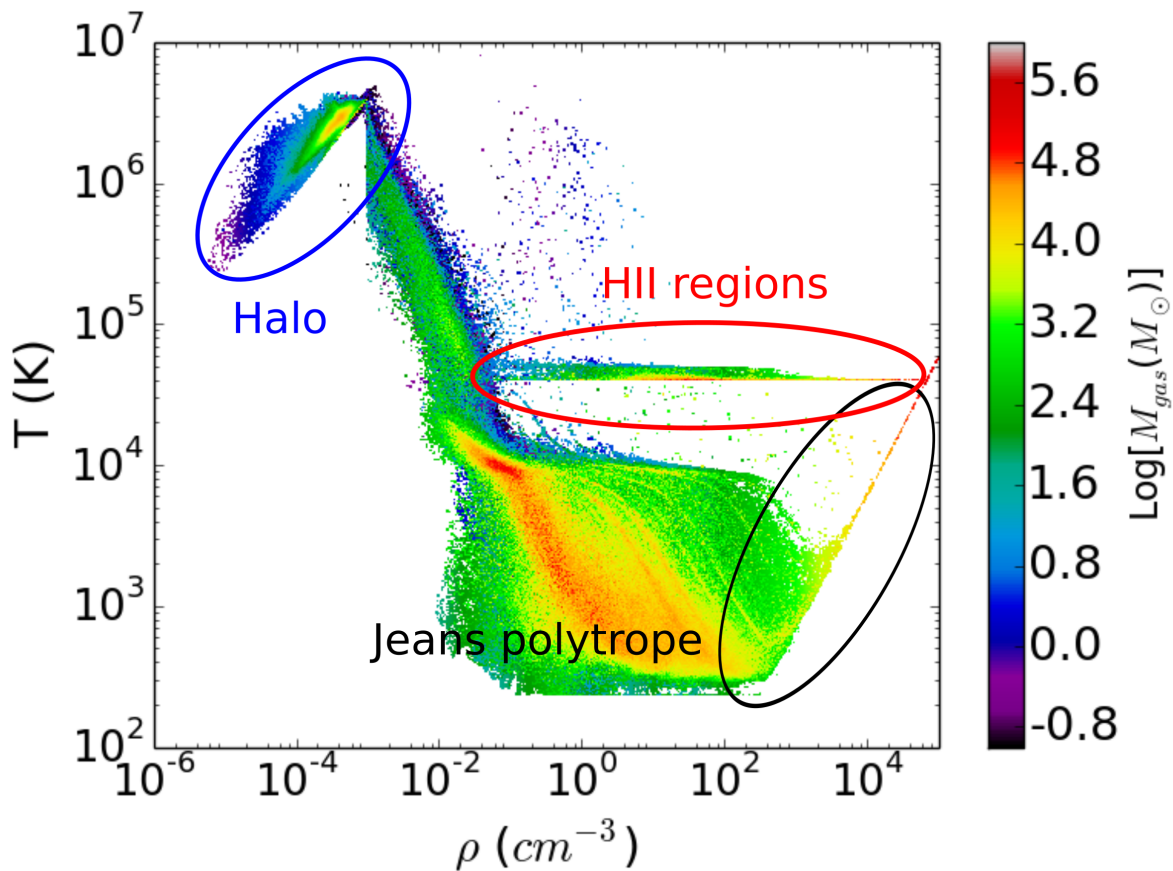


Figure 1.7: Example of a rho-T diagram from a simulation of dwarf galaxy. The gas cooling/heating is based on tabulated functions. The Jeans polytrope avoids artificial fragmentation of the gas by resolving the Jeans length by at least 4 cells. The isothermal curve at 4×10^4 K holds for the temperature within HII regions. In the stellar halo, a polytrope of index 5/3 is implemented to correspond to hot virialised gas.

Type II supernova (SN) feedback is implemented as a Sedov blast wave (see Dubois and Teyssier 2008 for details). These SNe create superbubbles which can be the origin of galactic outflows. In our case, after 10 Myr, the young stellar particle gives 20% of its mass to the neighbouring ISM as well as an energy of 10^{51} erg. This energy can be injected in a kinetic and/or thermal form, depending on the choice of the user.

The ionization of the ISM is done as followed: to speed-up the computation, one out of every ten stars radiates and ionizes the surrounding ISM with an energy ten times higher than a single source. Considering that star formation occurs in dense gas regions in a clustered way, this assures that all of these regions contain at least one bubble. The radius of the H_{II} region is

$$r_{HII} = \left(\frac{3}{4\pi} \frac{L_*}{n_e^2 \alpha_r} \right)^{1/3} \quad (1.5)$$

where L_* is the luminosity of the central stellar source, n_e and α_r the density of electrons and the recombination rate respectively. Within each of these bubbles, we uniformly set the gas at a temperature of 4×10^4 K. The luminosity (corresponding to the ionizing photons) follows:

$$L_* = L_0 M_* \eta_{OB} \begin{cases} 1 & \text{for } t_{ff} < a_* \leq 4 \text{ Myr.} \\ (4\text{Myr})/a_* & \text{for } 4 \text{ Myr} < a_* < 10 \text{ Myr.} \\ 0 & \text{else.} \end{cases} \quad (1.6)$$

where $L_0 = 6.3 \times 10^{46} \text{ s}^{-1} M_{\odot}^{-1}$, M_* is the mass of the star that spawned, $\eta_{OB} = 0.2$ the stellar mass fraction which explodes into SN. If two H_{II} regions overlap each other, the code ensures that the ionized volume is conserved and merges the two bubbles if the separation between the two is smaller than their radii.

Finally, the momentum feedback which here is carried by H_{II} regions, is injected under the form of velocity kicks and is proportional to L_* (see Renaud et al. 2013 for details):

$$\Delta v = s \frac{L_* h \nu}{M_{HII} c} \Delta t \quad (1.7)$$

where h is the Planck constant, M_{HII} the gas mass of the bubble, c the speed of light and ν the frequency of the flux representative of the most energetic part of the spectrum of the source. We consider here the luminosity of the Lyman- α and set $\nu = 2.45 \times 10^{15} \text{ s}^{-1}$. s is a dimensionless parameter accounting for the multiple electron scattering through the bubble and the decay of energy between each collision. This factor has typical values of 2 to 5 (Renaud et al. 2013).

Unconsidered processes

The mechanisms described above account for a limited part of all processes observed in galaxies. Indeed, we choose to ignore some mechanisms for technical and/or physical reasons. As stated above, we do not take into account for example the calculation of the gas cooling and heating functions or the ejection of metal during the stellar feedback

episode for computational reasons. We also exclude the feedback coming from Active Galactic Nuclei (AGN), as its influence on dwarf galaxies is not dominant at high-redshift.

Moreover, the models we use for stellar feedback are simplified recipes. A proper treatment of feedback would require the use of radiative transfer which gives a better modeling of the ISM as it includes more gas dynamics such as gas shielding from UV radiation. Such implementation of radiative transfer is already in place within `RAMSES` (`RAMSES-RT`, see Rosdahl et al. 2013) but requires larger computational resources.

Finally, magnetic fields are thought to play a role in the properties of star clusters. Indeed, studies like Price and Bate (2008) have shown that magnetic fields could increase the star formation rate within the cluster. However, this occurs at sub-parsec scales which we cannot resolve in a simulation of a galaxy over several billion years. Moreover, this was performed for isolated clouds and it is unclear how this additional pressure support brought by magnetic field holds against stellar feedback activity, all in a galactic environment at high-redshift. For these reasons, we choose to neglect the effects of magnetic fields in our simulations.

1.3.3 Setup for simulations

The sub-grid models we described in previous sections rely on a number of free parameters that the user has to choose accordingly to the context of his study. These free parameters are written down in a namelist which the code reads (an example of such namelist is given in Appendix A). In addition to filling the missing gaps of the numerical recipes, the namelist also covers other aspects relevant such as the frequency of the outputs of the simulation, the solver used for the gravity or the level of refinement of the AMR grid. It is also in the namelist that the user sets the parameters for the initial profile of the galaxy, both in particles and gas.

Let us start with the particles. In our case, we want to have our galaxy with pre-determined properties which helps saving computer time. We therefore exclude for now the galaxy formation process from a gaseous halo and adopt a more direct approach. Outside of `RAMSES`, stellar and gaseous discs are generated with a given profile, scaling radius and scaling height. The two discs are embedded within a dark matter halo which we consider spherical for the sake of simplicity. These structures are created with the Multi-Gaussian Expansion method (Monnet et al. 1992; Emsellem et al. 1994) which decomposes the profile and the mass of the different components into Gaussian functions. The velocities of the stars, gas and dark matter particles are then calculated using the Jeans equations. We end up with two ASCII files, one containing the positions, velocities and mass of the stars and dark matter particles and another one containing the total (i.e. stars+gas+DM) velocity curve of the galaxy which will be used to compute the initial velocities of the gas cells. Gaseous particles are not included in the former file as the setup of the AMR grid is done independently (see below). The path to the ICs is specified in the namelist.

The initial setup of the AMR grid is implemented in a routine (named `condinit.f90`⁹).

⁹It is worth noting that the routine `condinit.f90` can be adapted to other initial conditions. In

This routine takes galactic parameters that are written by the user in the namelist, namely the characteristic radius and height of the gaseous disc, the truncation radius and heights which avoids discontinuities at the edges of the disc, the mass of the gaseous disc and its radial and vertical profiles. It then computes the central and intergalactic gas density using these information and write the corresponding densities onto the cells. Finally, the velocity curve data is used to compute the velocity of each cells, then their kinetic energy and their pressure. The AMR grid is then fully set up, with each cells containing the relevant information about their density, momentum, energy and pressure.

1.4 The purpose of this work

The main goal of this Thesis is the study of the processes involved in the formation of nuclear clusters from a theoretical perspective.

As we discussed above, the formation of nuclear clusters is still an unclear process. A paradigm with two different formation scenarios exists and many numerical studies on the formation of nuclear clusters and their correlation with their host galaxies have already been conducted via analytical or semi-analytical models. Recently, many authors have started to suggest that the formation of the nucleus is a combination of both scenarios (Pflamm-Altenburg and Kroupa 2009; Neumayer et al. 2011; Hartmann et al. 2011; den Brok et al. 2014). However, very few studies have been able to quantify the relative importance of each mechanism, even if it seems to correlate with the host galaxy properties (Turner et al. 2012). Moreover, no work has previously taken into account the role of the gas in the formation process, which is often reduced to a star factory that creates the nuclear cluster in a single instant. Yet, gas might have a bigger impact: at the time of the formation of nuclear clusters, gas likely was a more dominant component of the potential; feedback events that follow star formation hence greatly disturb gas dynamics (which in turn can prevent or enhance local star formation); clusters, evolving in gas-dense environment might accrete gas and grow through successive in-situ star formation episodes.

Including gas dynamics with that of stars in a full galactic context requires to run hydrodynamical simulations of galaxies. These simulations have struggled over the years to reconcile large-scales (the galaxy scale, i.e. kilo-parsec) with small-scales (typical size of a cluster or a molecular cloud, i.e. parsec). With the increasing power of super-computers, it is now possible to encompass those scales in one coherent simulation. Using the hydrodynamical code `RAMSES`, we will be able to model galaxy evolution while simultaneously probing the physical conditions of star formation at parsec-scale resolution which is where nuclear clusters originally form. It is however important to remember that we do not capture the internal dynamics of star clusters which occur at sub-parsec scales. Hence, processes like two-body relaxation, mass segregation, stellar collisions are not accessible in these simulations. Also, we have to keep in mind that the potential is smoothed on parsec-scale (recall Section 1.3.1): this implies that the physics observed at this scale (e.g. turbulent motions) must be taken with caution.

Chapter 5, we modify this routine to generate a gas halo which collapses to form a galaxy from scratch.

Therefore, in my PhD, I have focused on hydrodynamical simulations of isolated galaxies with a parsec-like resolution.

In **Chapter 2**, I present some observational data of the nucleus of NGC 300 from SINFONI to get an understanding of how physical properties of nuclear clusters are extracted. I describe the extraction tools (*esorex*) and the methods used to get kinematic maps of the central region. Preliminary results seem to indicate that the nucleus of NGC 300 has little to no rotation with low velocity dispersion. I briefly discuss the next steps that would complete this analysis and expand our understanding of this nuclear cluster.

In **Chapter 3** (based on Guillard et al. 2016), we present the results of a parsec-scale simulation of an isolated gas-rich dwarf galaxy with predetermined properties. We propose an updated formation scenario for NCs. In this “wet migration scenario”, a massive star cluster forms in the gas-rich disc, keeping a gas reservoir, and growing further while it migrates to the centre via a combination of interactions with other substructures and dynamical friction. A wet merger with another dense cluster and its own gas reservoir can occur, although this is not a pre-requisite for the actual formation of the NC. The merging process does significantly alter the properties of the NC (mass, morphology, star formation history), also quenching the on-going local star formation activity, thus leading to interesting observational diagnostics for the physical origin of NCs. A population of lower mass clusters co-exist during the simulation, but these are either destroyed via tidal forces, or have high angular momentum preventing them to interact with the NC and contribute to its growth. The proposed updated scenario emphasises the role of gas reservoirs associated with the densest star clusters formed in a gas-rich low-mass galaxy.

In **Chapter 4** (based on Guillard et al., in press), we discuss the non-linear effects of stellar feedback on the properties of star clusters with a focus on the progenitors of nuclear clusters. We show that radiation feedback (photo-ionization and radiative pressure) plays a more important role than type-II supernovae in destroying dense gas structures, and altering or quenching the subsequent cluster formation. It also disturbs the cluster mass growth, by increasing the internal energy of the gas component to the point when radiation pressure overcomes the cluster gravity. We discuss how these effects may depend on the local properties of the Interstellar Medium (ISM), and also on the details of the subgrid recipes, which can affect the available cluster gas reservoirs, the evolution of potential NC progenitors, and the overall galaxy morphology.

In **Chapter 5**, we present the latest results of simulations which encompass more global mechanisms such as cosmological gas accretion and form the galaxy from the cooling and collapse of a rotating gas halo. We perform several simulations exploring various gas mass values for the halo and different virial masses. We see that in this context, after 100 Myr, the morphology of all our dwarf galaxies has shifted from a disc to an extended spheroidal-ish shape and all star clusters have been disrupted. We show that the expansion of the disc and the disruption of star clusters are caused by stellar feedback. The sole use of supernovae feedback in particular allows us to form a stellar disc with numerous star clusters after 200 Myr, emphasizing the damaging role of radiative feedback for star clusters. We also study more deeply the influence that different injections of energy from supernovae have on the properties of the interstellar medium and star clusters.

Chapter 6 includes a brief summary of the Thesis and provides more perspectives for future studies.

Chapter 2

Observations of galactic nucleus: the example of NGC 300

The major part of my work was dedicated to numerical simulations of isolated dwarf galaxies. However, I also wanted to know more about how astronomers derive the properties of Nuclear Clusters (NCs) from observations. This would also help me getting a better perspective at the relevant parameters observers could use from simulations and vice-versa. To that end, I reduced and briefly analysed observations of the spiral galaxy NGC 300 which hosts in its center a NC and potentially a black hole. This galaxy has the advantage of being close to Earth and observed nearly face-on which make it an excellent case study of the properties of NC. This data set is a part of a larger project led by Nadine Neumayer to study the nuclei of a sample of galaxies (NGC 300 being one of them) in order to identify their formation channel(s).

2.1 Overview of NGC 300

Discovered in 1826 by the Scottish astronomer James Dunlop, the spiral galaxy NGC 300 (Figure 2.1) is one of the closest galaxies in the southern sky with an apparent total B magnitude of 8.95 mag (Böker et al. 2002). It can be observed with a small telescope pointing towards the Sculptor constellation. Observed nearly face-on, it is located around 1.88 Mpc^1 (Gieren et al. 2005) away from Earth which makes this galaxy the nearest low-inclination spiral galaxy in the southern sky. NGC 300 can be considered as a fast rotator with a rotation velocity of 91 km/s . By observing its surface brightness, the galaxy can be decomposed into a disc and a core as done by Kim et al. (2004). The stellar disc has a mass of $1.9 \times 10^9 M_{\odot}$ and an apparent size of 22.5 by 16.5 arcmin (i.e. a diameter of 45.000 ly or $\sim 14 \text{ kpc}$ ²) (Kang et al. 2016 and references therein). The gas fraction of the galaxy lies between 36% and 49% with an amount of HI in the disc of $1.10 - 1.87 \times 10^9 M_{\odot}$. This amount of gas is still collapsing and forming stars within the disc as shown by the

¹or 7 million light years

²At this distance, one arcmin corresponds to 547 pc .



Figure 2.1: Picture of the spiral galaxy NGC 300. *Image credit: ESO*

observations of numerous active H_{II} and supernovae remnants (e.g. Deharveng et al. 1988; Payne et al. 2004; Faesi et al. 2014). The star formation rate in the disc of NGC 300 is thought to be between 0.08 and $0.3 \text{ M}_{\odot} \text{ yr}^{-1}$.

The star formation history of NGC 300 has been investigated in more details using numerical models. Using models of chemical evolution including gas accretion and outflows, Kang et al. (2016) re-constructed its evolution history which is in good agreement with the current galactic radial profile and other observed properties like cold gas or metallicity. They determined that the stellar population of NGC 300 is on average old (i.e. above 5 Gyr within a radius of 4 kpc). They suggested that star formation in NGC 300 started 1 Gyr after its formation (once the high amount of atomic hydrogen converted into molecular hydrogen gas) to reach its maximum of $0.33 \text{ M}_{\odot} \text{ yr}^{-1}$ after 5.5 Gyr. At the same time, the oxygen abundance also increased in the disc with a distribution following a negative radial metallicity gradient. This radial gradient in metallicity was also observed by Faesi et al. (2014) in their study of CO ($J = 2 - 1$) lines of 42 H_{II} regions within the disc or also by Bresolin et al. (2009) who determined the metal abundances within giant H_{II} regions using their temperature. After 7 Gyr, the amount of molecular hydrogen, the star formation and the total rise in metallicity decline as the in-fall rate of gas also keeps dropping. This extensive star formation activity is likely responsible for the formation of star clusters visible on Figure 2.1. Among them is the nuclear star cluster in the galactic center.

The properties of the nucleus of NGC 300 have been studied extensively in the past.

Its stellar mass and stellar velocity dispersion have been estimated to be $10^{6.02} M_{\odot}$ and 13.3 km.s^{-1} respectively (Walcher et al. 2005). Carson et al. (2015) measured that the magnitude in the I-Band (i.e. near infrared, $\lambda = 806 \text{ nm} = 8060 \text{ \AA}$) of the NC is -11.43 mag, compared to -18 mag of the galaxy in the B-band (i.e. visible, $\lambda = 445 \text{ nm} = 4450 \text{ \AA}$). These measurements align with the correlation between the luminosities of NCs in late-type spiral galaxies and the total luminosities of their host made by Böker et al. (2004) and tend to indicate that the mass of the NC is more determined by the mass of the galaxy rather than its star formation rate. The effective radius of the NC changes depending on the filters: it goes from 1.52 pc with a filter centered on $\lambda = 2710 \text{ \AA}$ to 3.12 pc with a filter centered on $\lambda = 15322 \text{ \AA}$. This difference in radius indicates a radial color gradient which can be interpreted as a sign of multiple stellar populations, with the new stars being more concentrated than the old stars. Determination of the axis ratio across all filters indicates that new stars in the NC usually form in a flattened disc.

Carson et al. (2015) findings on the stars populations may be hints for the formation of the nucleus of NGC 300. The presence of young stars concentrated in the center seems to indicate an on-going fuelling of gas onto the nucleus, suggesting the gas infall scenario may not only occur during the formation of the cluster but also during its evolution. Simulations conducted by Hartmann et al. (2011) suggested that the two proposed formation scenarios for galactic nuclei result into two different kinematics for the NC. Hence, resolved measurements of the kinematics of the nucleus may allow us to determine its formation history and the processes involved. To that end, we use data from the integral field spectrograph SINFONI to extract the kinematics of the central regions of NGC 300.

2.2 Integral-field spectroscopy: the SINFONI instrument

The Spectrograph for INtegral Feld Observations in the Near Infrared SINFONI (Eisenhauer et al. 2003, see Figure 2.2) is a near infrared integral field spectrograph mounted on the Very Large Telescope at the Cassegrain focus of UT4. It covers wavelengths from $1.1 \mu\text{m}$ to $2.45 \mu\text{m}$ through 4 bands: J ($1.10 - 1.40 \mu\text{m}$), H ($1.45 - 1.85 \mu\text{m}$), K ($1.95 - 2.45 \mu\text{m}$) and H+K ($1.45 - 2.45 \mu\text{m}$). These bands have a spectral resolution of 2000, 3000, 4000 and 1500 respectively. Three different fields of view can be chosen: $8'' \times 8''$, $3'' \times 3''$ and $0.8'' \times 0.8''$. The spatial sampling for each of these fields of view is 250mas (milli-arcseconds), 100mas and 25mas respectively. A summary of the technical specifications of SINFONI is shown in Table 2.1.

SINFONI is built from 2 component instruments working together: the Sinfoni Adaptive Optics (AO) module which allows corrections for the turbulence of the atmosphere and the SPectrometer for Infrared Faint Field Imaging (SPIFFI). SPIFFI is used as an image slicer: the 2D image coming from the telescope is chopped in 32 slices, each projected onto 64 detector pixels (see Figure 2.3). These spaxels (spectral pixels) are thus rectangular and have a spatial resolution of $125 \text{ mas} \times 250 \text{ mas}$, $50 \text{ mas} \times 100 \text{ mas}$ and $12.5 \text{ mas} \times 25 \text{ mas}$ for

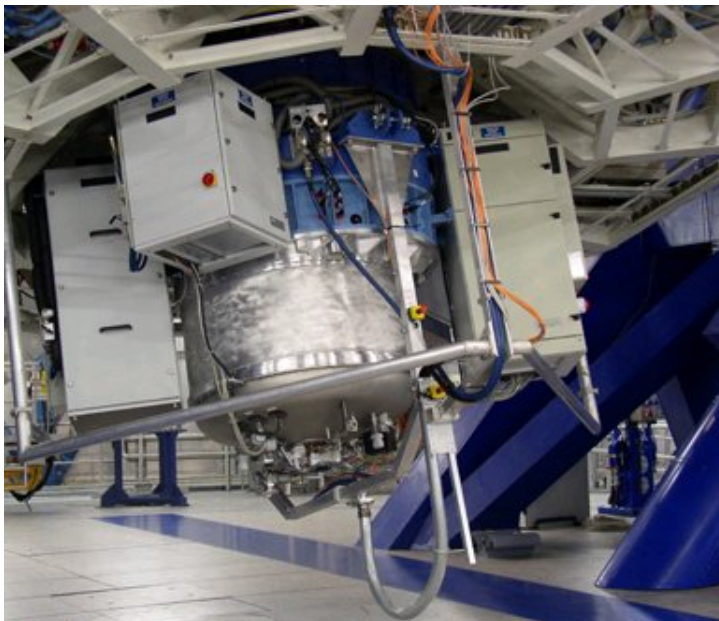


Figure 2.2: Picture of the SINFONI instrument mounted at the cassegrain focus on the VLT telescope. *Image credit: ESO*

Table 2.1: Technical specifications of SINFONI. The table is adapted from the SINFONI user manual.

No. of slices	32		
Wavelengths range	1.1 – 2.45 μ m		
Fields of view	8"×8"	3"×3"	0.8"×0.8"
Spatial resolution	25mas	100mas	250mas

each field of view respectively. SPIFFI then separates the different wavelengths for each slice. The image is then reconstructed at each wavelengths from each individual spaxel. The final product is 3D data-cube with the position, flux and spectrum for each spaxel. SINFONI uses other modes (e.g. the Rapid Response Mode or the Laser Guide Star mode) which are beyond the scope of this Thesis and thus will not be discussed. The interested reader can refer to the SINFONI User Manual available on the ESO website³.

Thanks to its formidable spatial and spectral resolutions, SINFONI is a great instrument to study compact objects such as star-forming regions, galactic nuclei or distant galaxies. Examples of science highlights using SINFONI are the interaction between a gas cloud and the super massive black hole at the center of our Galaxy leading to the disruption of the cloud (Gillessen et al. 2012, 2013), the growth of galaxies which feeds early-on on nearby gas but then interact and “kill” other smaller galaxies (Cresci et al. 2010).

³https://www.eso.org/sci/facilities/paranal/instruments/sinfoni/doc/VLT-MAN-ESO-14700-3517_v101.0.pdf

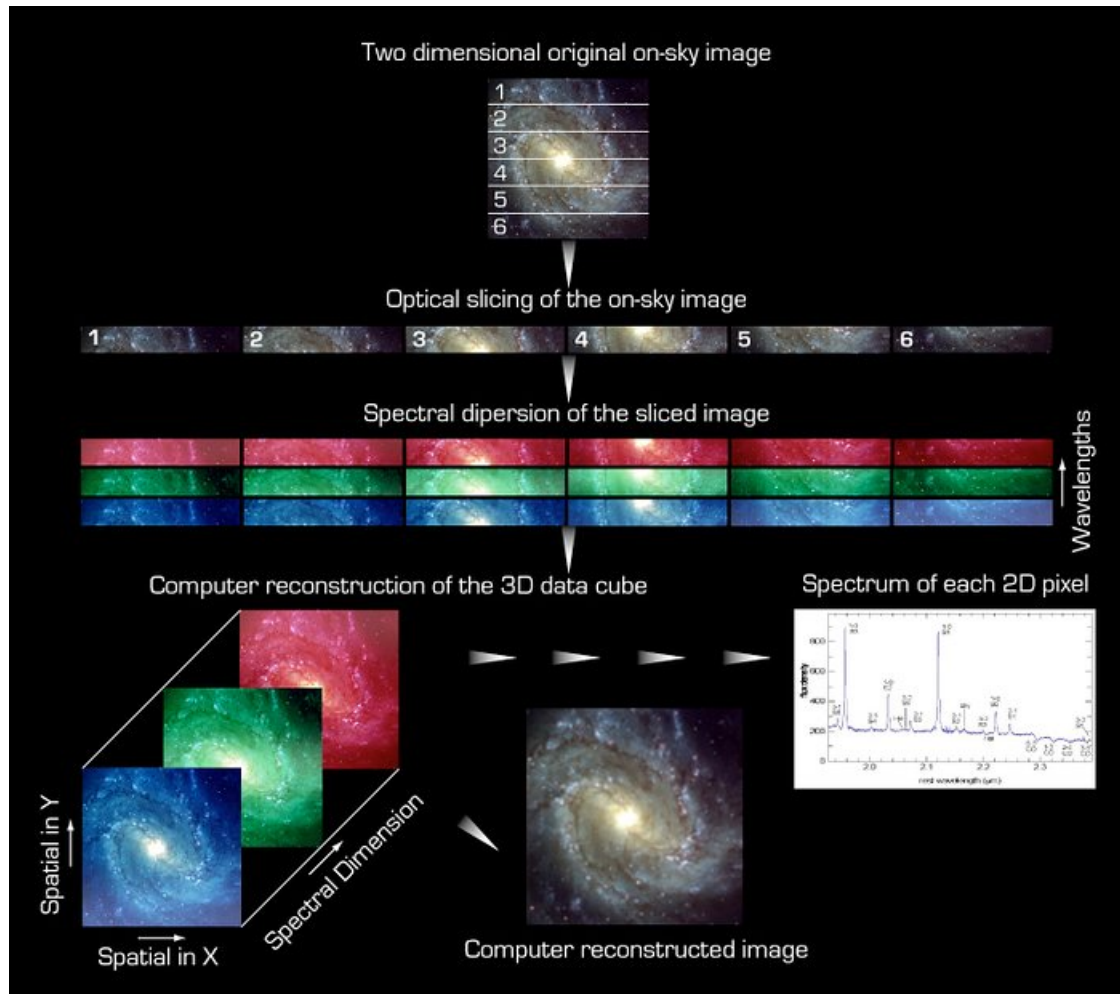


Figure 2.3: Structure of the SINFONI data. A two-dimensional image is divided into 32 slitlets called spaxels and re-arranged by segmented mirrors so that they lie in a line end-to-end, forming an extended slit. The spectrograph splits this slit into its separate wavelengths (illustrated by different colors in the figure). The image is then reconstructed into a 3D data cube. *Image credit: ESO*

Over the past years, SINFONI has also been used to study the fuelling of galactic nuclei: Busch et al. (2017) studied the nuclear regions of NGC 1808 and found signs of gas inflows onto the central super massive black hole; Smajić et al. (2015) suggested that spirals within nuclear gas disk of NGC 1566 might be a mean to channel gas towards the inner parts of the nucleus and thus might trigger in-situ star formation. These observations seem to support the fuelling by gas accretion model of the nucleus. In Section 2.3, we will present the data reduction and first results of the study of the nuclear region of NGC 300 which hosts a bright nuclear cluster using SINFONI.

2.3 Reduction of the data

The data we analyse here come from four nights observations performed in 2013 within the observing program ID 091.B-0685(A) PI:Neumayer.

The data selected over the three nights were reduced using the SINFONI data reduction pipeline provided by ESO in the Eso reflex environment (Freudling et al. 2013). The purpose of this pipeline is to remove from the data the contribution of the sky background, the flat field (i.e. the variation in sensitivity), the distortions and to calibrate the data in wavelengths. The goal is to ultimately get a 3D data cube where the full spatial information is stored in the x and y directions, and the wavelengths along the z axis. The package contains a series of routines (shown in Figure 2.4) that are used in cascade and that we briefly summarize here⁴:

- *sinfo_rec_detlin* computes the response of the detector as a function of the intensity of the pixel and determines which ones are non-linear.
- *sinfo_rec_mdark* determines the master dark and generates a bad pixels map based on flagged hot-current pixels. A dark frame is an exposure taken with a closed shutter of the telescope (namely without illumination). The master dark is created from a set of raw darks.
- *sinfo_rec_mflat* computes a master flat field frame and a bad pixel map which marks pixels with an intensity higher than a given threshold. The flat field is a frame that contains the gain of each pixel that has to be normalized to have an average value of 1. In other words, it compensates for the relative sensitivity of each pixel of the detector.
- *sinfo_rec_distortion* computes the optical distortion and the relative distances of the slitlets from the first one, using a reference line table.
- *sinfo_rec_wavecal* builds a wavelength calibration map and determines the positions of each slitlet edges. Towards that end, the routine uses a set of arc lamp frames, the

⁴The interested reader can refer to the SINFONI pipeline website for further details: <https://www.eso.org/sci/software/pipelines/sinfoni/sinfoni-pipe-recipes.html>

master bad pixel map, the master flat field, the optical distortion and the reference line table. We also include additional parameters that depends on the K-band and the pre-optics of the instrument that were used.

- *sinfo_rec_jitter* accomplishes several tasks:
 - It reduces the point spread function (PSF) standard and get the information on the Strehl's ratio of the instrument ⁵. It uses the PSF standards to the master bad pixel map, the master flat field, the distortion, the slitlets distances, the position table of the slitlet edges and the wavelength calibration map.
 - It reduces the telluric standards (see below for more details on telluric corrections) and get the information of the instrument response. It uses a reference telluric standard, the master bad pixel map, the master flat field, the distortion, the slitlets distances, the position table of the slitlet edges and the wavelength calibration map.
 - It reduces the science data. It runs using the scientific data, the master bad pixel map, the master flat field, the distortion, the slitlets distances, the position table of the slitlet edges and the wavelength calibration map.

As we just saw, the SINFONI pipeline uses several tools to correct the various disturbances that light from stars encounter between the moment of emission and the information we get in the detector. We give more physical details on how these corrections are handled, starting with the telluric correction.

2.3.1 Telluric correction

Before its reaches the detector of a ground-based telescope, light has to go through the Earth atmosphere where it may be scattered or diffused. The purpose of telluric corrections is to recover the most accurately the original properties of the emitted light by correcting these atmospheric perturbations. In order to do that, we need a telluric calibrator which, in our case is a group of stars behaving almost like a blackbody (i.e. with a spectrum which is almost a perfect continuum). Late B, early A and main sequence stars show such behaviour. We exclude Early B stars because they might exhibit emission lines in their spectra due to the accretion of material. It is important to keep in mind that even the spectra of late B, early A and main sequence stars are not perfect as the light can be absorbed by the atmosphere of the star itself. If not taken into account, this feature could result into fake emission lines in the spectrum of the target since we divide it by the normalized telluric standard star. Such emission line, the Brackett-gamma ($\text{Br}\Gamma : 2.166\mu\text{m}, 7 - 4$) is observed in our wavelength range and thus needs to be removed.

⁵The Strehl's ratio is the ratio between the peak intensity of the actual PSF and the peak intensity of the theoretical Airy function for the same source and optical path. It is a measurement for the quality of the adaptive optics correction.

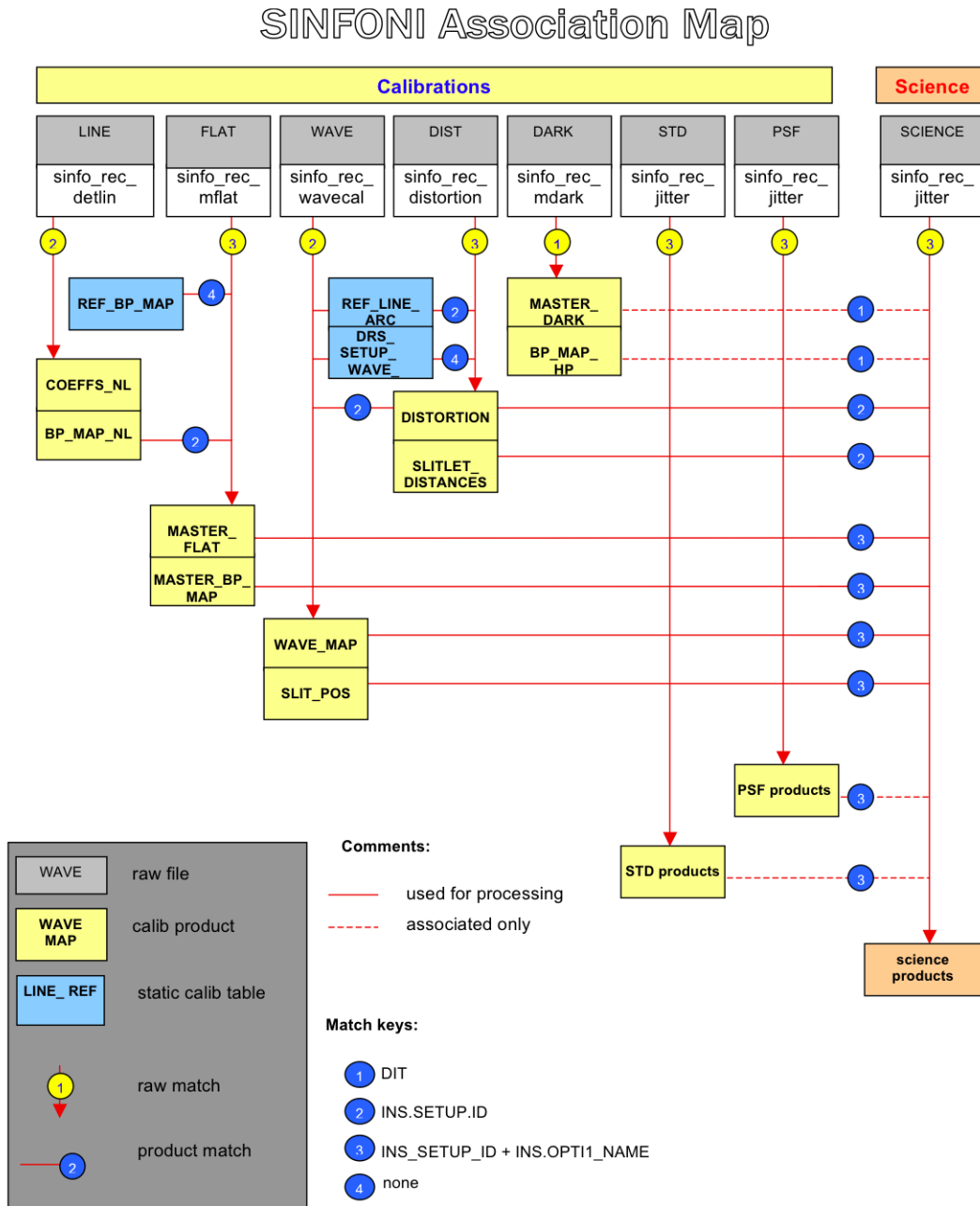


Figure 2.4: SINFONI association map *Image credit: ESO*

In order to properly get the physical properties of the Earth atmosphere, the observation of the telluric star should take place as shortly as possible (max 2 hours) after the science observation. For each science cube, we proceed as follows:

- We identify the telluric star and extract its spectrum from the spaxels around the center of the star using *sinfo_utl_cube2spectrum*. This routine extract a spectrum from a spaxel in a certain aperture.
- We use SIMBAD⁶ to recover the coordinates of the star and then its type and temperature from the literature⁷. We then create a black body spectrum within the wavelength range of the observed spectra and using the recovered temperature.
- We normalize the telluric spectrum using the region where the slope of the spectra is the closest to zero and where minimum features are observed.
- We divide the telluric spectrum with the black body spectrum, after normalizing the latter.
- We remove the contribution of the Brackett-gamma. For that, we fit the absorption line with a Gaussian function and subtract it from the telluric spectrum.
- Each spectrum of the data cube is then divided by the final corresponding telluric spectrum.

Finally, the data cubes are co-added into a single one. Before that operation, each cube must be corrected from the relative offsets between one another, hence setting them in an absolute reference frame. Indeed, each observing blocks has a different reference pointing (usually aligned with the first object frame of the template). We then establish the offsets of each of the cubes from a reference frame. In our case, we choose as a reference the 8th template of the observations of 13-08-2013 since its spectra in the central regions of NGC 300 displayed the least noisy features. It is from this final cube kinematics information will be extracted.

An illustration of such procedure is shown in Figure 2.5. The top panel shows the removal of the Brackett-gamma absorption line, while the bottom panel the initial and the telluric corrected spectrum of the nuclear region of NGC 300 (combined over the four nights). The corrected spectrum is averaged over the 5 central spaxels of the data cube. The information about telluric stars we used for the four nights of observations of NGC 300 are summarized in Table 2.2. One can start to recognize the CO lines at wavelengths longer than 22,900 Å (2.29μm). The corrected spectrum still contains some noise that can be removed. However, because of a lack of time, we did not perform those additional corrections and will instead briefly describe them in the next section.

⁶<http://simbad.u-strasbg.fr>

⁷<http://www.uni.edu/morgans/astro/course/Notes/section2/spectraltemps.html>

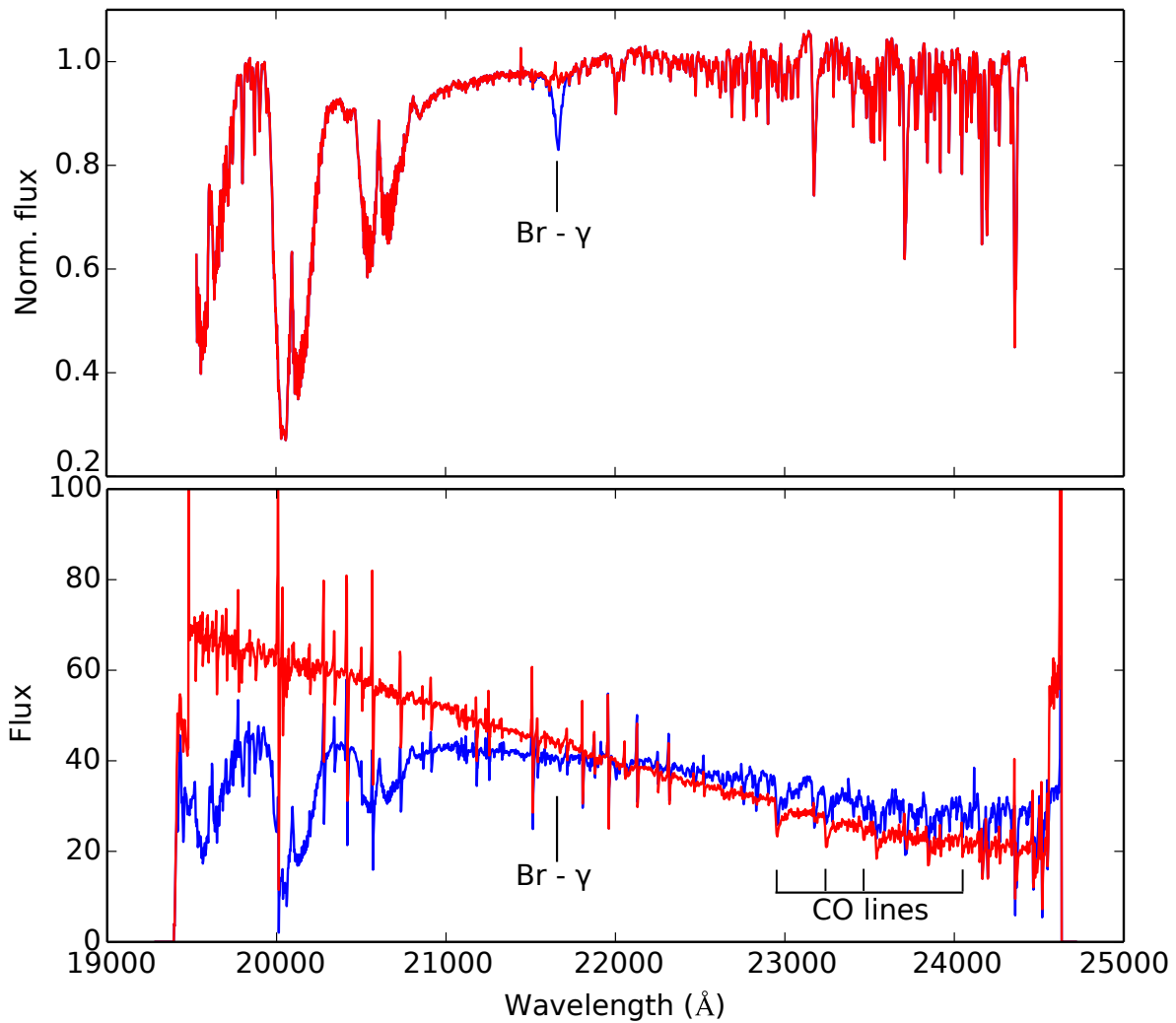


Figure 2.5: *Top*: Telluric spectrum before (blue) and after (red) the removal of the Brackett-gamma line. *Bottom*: Spectrum of NGC 300 before (blue) and after (red) the telluric correction.

Table 2.2: Characteristics of the telluric stars used for NGC 300

Night (kpc)	Stars	Star type	Effective temperature (K)
2013-08-16	Hip021576	B6V C	14100
2013-10-03	Hip003820	B8V C	11800
2013-10-02	Hip109849	B8II C	13596
2013-08-13 T07	Hip108908	B8V C	11800
2013-08-13 T08	Hip001115	B3/5V D	17200

2.3.2 Other corrections

Cosmic rays can contaminate the science data. One way to remove their contribution from the spectra is to use a 3D version of the Laplacian Cosmic Ray Identification adapted by Davies (2008) from L.A Cosmic written by van Dokkum (2001). The algorithm is based on the Laplacian edge detection which enhances and detects boundaries in digital images. The advantage of this technique for cosmic-rays is that the code determines the sharpness of their edges rather than the contrast with their surroundings as it was usually done at the time. It allows a better discrimination of cosmic-rays from other features.

The spectra also need to be corrected from the heliocentric and barycentric radial velocities. Indeed, the motion of the Earth around the Sun affects the observed wavelength line emitted from a celestial object via the Doppler effect. It is therefore necessary to correct for the difference in wavelengths between observations taken in different dates, so all data are in the same reference frame. This can be done using scripts available for the community such as barycorr (Wright and Eastman 2014).

2.4 Stellar kinematic extraction

The stellar kinematic extraction from spectra relies on the measurement of the stellar line-of-sight (LOS) velocities from the Doppler shifts. To obtain these LOS velocity distribution (LOSVD), we use the penalized pixel fitting method.

2.4.1 The penalized pixel fitting method

The penalized pixel fitting (*ppxf*) method was designed by Cappellari and Emsellem (2004) to fit observed spectra. First, we adopt a model for the galaxy spectrum which is the convolution between a library of K stellar templates (T_k) and a broadening function $B(x)$:

$$G_{model}(x) = \sum_{k=1}^K w_k [B * T_k](x) + \sum_{l=0}^L b_l \mathcal{P}_l(x) \quad (2.1)$$

The last terms $\mathcal{P}_l(x)$ are the Legendre polynomials of order l and correct for the low-frequency differences in spectral shape between the galaxy and the templates. Since we observe NGC 300 in the near-infrared, the library of template stars shall take into account

all possible contributing stars in the near-infrared along the line of sight. To that end, we use eight template stars from the library of high-resolution ($R > 45000$) infrared stellar spectra from Wallace and Hinkle (1996). Moreover, we convolve the templates with the line spread function (LSF) of the instrument. The LSF can be seen as the instrumental resolution analogous to the PSF but in the spectral direction. The broadening function is equal to $B(x) = \mathcal{L}(cx)$ where c is the speed of light and $\mathcal{L}(x)$ is the Gauss-Hermite series (van der Marel and Franx 1993; Gerhard 1993):

$$\mathcal{L}(v) = \frac{e^{-(1/2)y^2}}{\sigma\sqrt{2\pi}} \left[1 + \sum_{m=3}^M h_m H_m(y) \right] \quad (2.2)$$

where $y = (v - V)/\sigma$ and H_m are the Hermite polynomials.

The best fitting parameters for the LOSVD are then found via a χ^2 minimization which determines the disparity between the observed and the modeled galaxy spectrum (G and G_{model} respectively) over a set of N good pixels:

$$\chi^2 = \sum_{n=1}^N \frac{G_{model}(x_n) - G(x_n)}{\Delta G(x_n)} \quad (2.3)$$

where ΔG is the error on the measurement $G(x_n)$. The χ^2 minimization is a non-linear least-squares problem in which the searched parameters are (V , σ and the higher orders of the Gauss-Hermite moments) and the weights are ($w_1, \dots, w_K, b_0, \dots, b_L$). This pixel fitting is said *penalized* because the wanted parameters are fitted simultaneously but with an adjustable “penalty” term in the χ^2 . The purpose of this term is to force the solution to have a Gaussian-like shape⁸ when the signal-to-noise is too low and the higher moments cannot be constrained by the data. Overall, the χ^2 minimization is solved with the Levenberg-Marquardt method and the outputs are the mean velocity V , the velocity dispersion σ and the higher moments of the Gauss-Hermite series h_3 and h_4 . In terms of physics, these last two parameters can be seen as a quantification of the skewness and the kurtosis of the object respectively.

This extraction method of the LOSVD requires a high-enough S/N to be reliable (Kuijken and Merrifield 1993). To ensure this condition, we spatially bin the data using the Voronoi tessellation method (Cappellari and Copin 2003). This technique adapts the shape and the size of the bin according to the local S/N: for low S/N, a large number of pixels are binned together; when the S/N is high, the code keeps the original sampling. The threshold that sets the difference between “low” and “high” S/N is defined by the user. Figure 2.6 shows the Voronoi map of the central regions of NGC 300 with a target S/N of 20 which allows us to have a fractional scatter S/N^9 of 9.3%. At the end of this process, our final cube consists of 152 bins. Figure 2.7 displays the ratio S/N for each bin as a function of the distance from the central bin.

⁸Generally, LOSVD are well reproduced by Gaussians (Cappellari and Emsellem 2004).

⁹the fractional scatter $S/N \sigma_{frac}$ is defined as $\sigma_{frac}(\%) = \sqrt{S/N - (S/N)_{target}} / (S/N)_{target} * 100$ where $(S/N)_{target}$ is the target S/N.

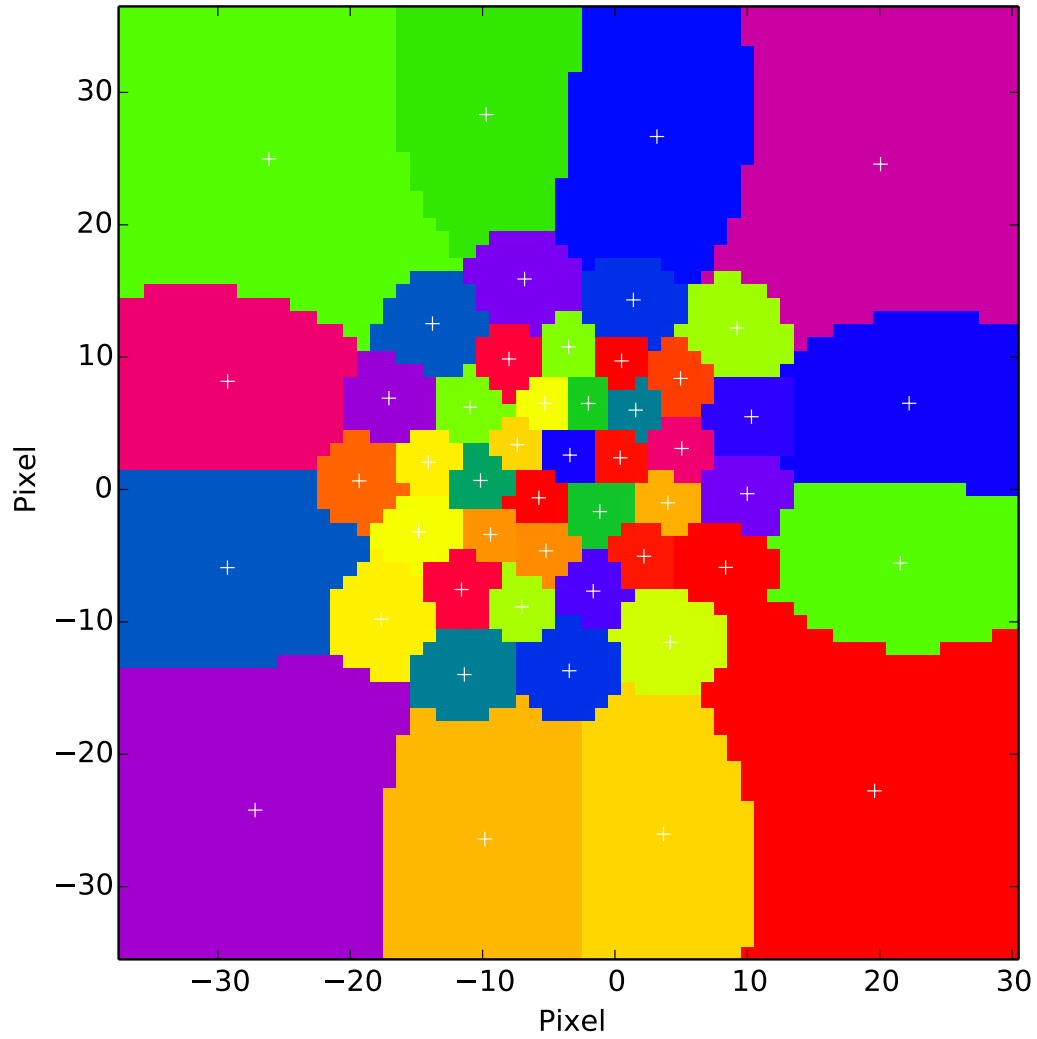


Figure 2.6: Voronoi binned map of the SINFONI datacube for the nuclear region of NGC 300.

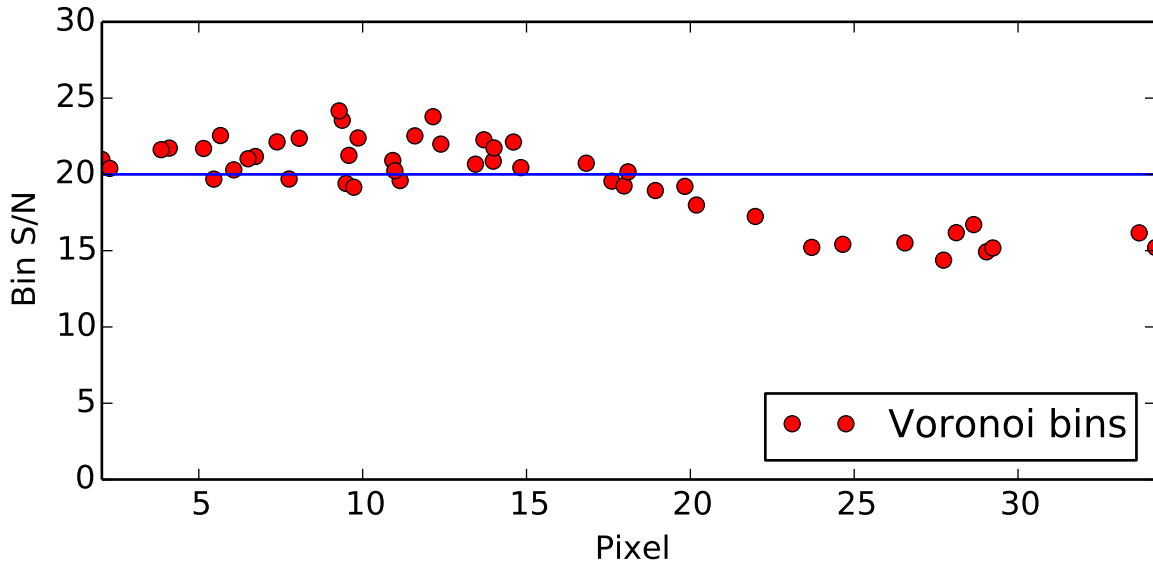


Figure 2.7: S/N as a function of the distance for binned data.

2.4.2 Stellar kinematics

Only the good bins (i.e. with a signal-to-noise higher than 20 and an error on the velocity dispersion lower than 20 km s^{-1}) were selected for the final calculation. Since we observe in the near-infrared, we focus the kinematics extraction on the CO-absorption lines (namely $^{12}\text{CO}(2-0)$, $^{12}\text{CO}(3-1)$, $^{13}\text{CO}(2-0)$ and $^{12}\text{CO}(4-2)$) which lie within a wavelength range from $22,800 \text{ \AA}$ to $23,950 \text{ \AA}$. The following figures, from the extraction of the CO lines and the preliminary kinematics maps were performed by Arianna Picotti. Figure 2.8 shows an example of a fit of the spectrum of a Voronoi bin in this wavelength range.

The velocity and velocity dispersion maps of the CO-lines in the nuclear region of NGC 300 are displayed in Figure 2.9. Interestingly, the nucleus does not seem to show a significant stellar rotation around the minor axis of the galaxy, with maximum velocities approaching 10 km s^{-1} . Since the system has very low inclination and is observed almost face-on, it comes to no surprise that we find a low velocity amplitude along the line of sight. Also, the nucleus of NGC 300 seems to be a system with low dispersion with a value around 20 km s^{-1} . This evaluation is higher than the one from Walcher et al. (2005) who measured a low-velocity dispersion of $13.3 \pm 2.0 \text{ km s}^{-1}$. This disagreement with other observations may come from some uncertainties on the line spread function. Also, the lack of error estimations in our kinematics prevents us from concluding on the velocity values we extracted.

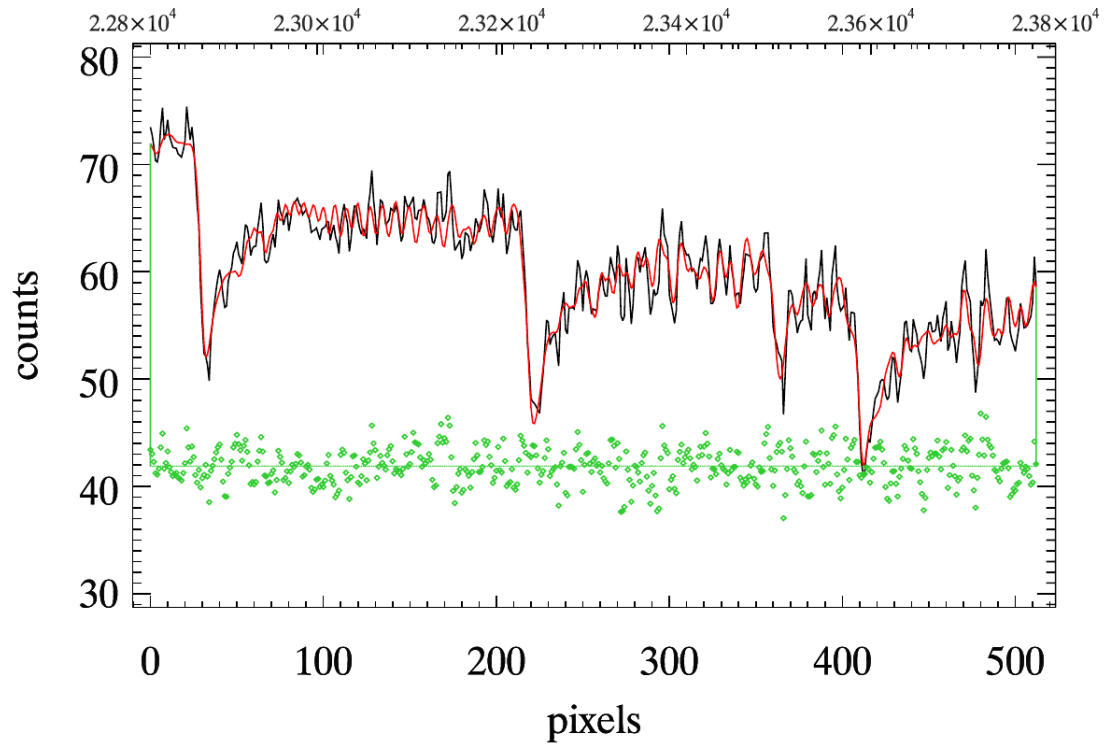


Figure 2.8: Example of a CO-absorption line spectrum (black) of a Voronoi bin. The fit using the ppxf method and the associated residuals are shown in red and green respectively. Credit: Arianna Picotti.

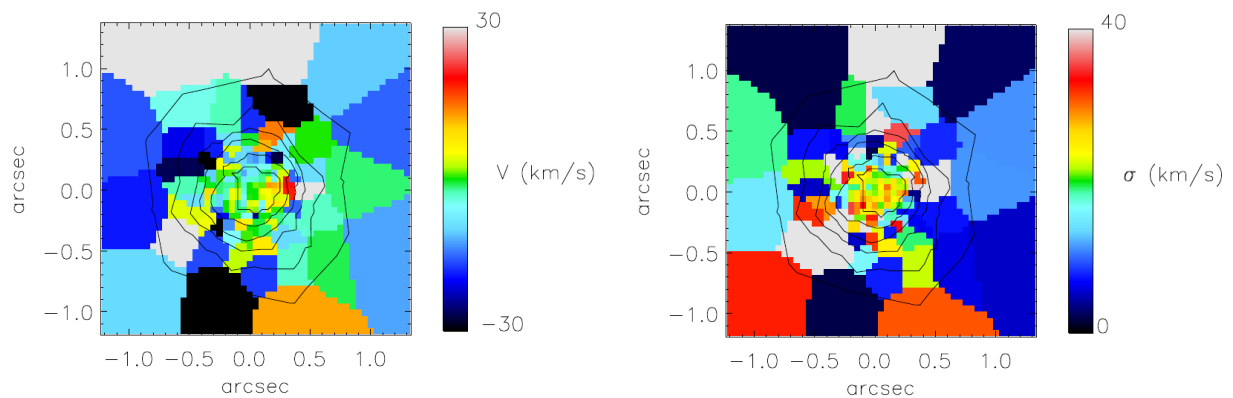


Figure 2.9: Maps of the CO absorption lines of the velocity (*left*) and velocity dispersion (*right*) of the nuclear region of NGC 300. We also display the iso-contours for the flux. Credit: Arianna Picotti.

2.5 Improvements and steps forward

2.5.1 Errors and h_3 and h_4 moments

The kinematic extraction we did in the previous was done without error calculation and with two moments only (the velocity and velocity dispersion). As next steps, it is mandatory to include the h_3 and h_4 moments and perform the Monte-Carlo simulations to estimate the errors on the various moments. Given the small rotation velocity and velocity dispersion of the nucleus we observe, the latter will be of crucial importance for the interpretation of such values.

2.5.2 The Line Spread Function

As we briefly mentioned in the last section, the stellar templates we used to fit the LOSVD need to be convolved with the instrument LSF. For an ideal instrument with infinite resolution, the shape of the LSF would be a δ -function. In reality, for a proper spectrograph, the LSF is well approximated by a normalized Gaussian function. However, for the **SINFONI** detectors, emission lines have broader wings than a Gaussian. Moreover, the LSF also varies across the field of view. Hence, we need to measure the LSF, e.g. from the sky lines in each spaxel of our data cube.

The procedure for extracting the LSF is the following: we follow the same reduction process on the science cube as described in Section 2.3 without subtracting the sky and without applying the offset frames correction. We then measure the spectral resolution across the detector using the strong isolated sky lines with close doublets (such as the OH-lines) which we know the central wavelength. We then locate the peak values of the chosen emission lines, subtract the continuum and normalize the line flux to the peak flux and we finally sum all lines.

For the sake of time, we did not use the LSF from the observation of NGC 300 and instead used the LSF from a different **SINFONI** observation of NGC 7793 (analysed by Arianna Picotti, see her Master Thesis). This galaxy shares some similarities with NGC 300: it is a spiral galaxy of the same Hubble type as NGC 300, it is observed in the Sculptor constellation like NGC 300 but with a higher inclination of 53.7° (Carignan 1985), and it contains a nuclear cluster. We thus expect the differences between the LSFs to be minimal and not to influence the resulting kinematic determination.

2.5.3 Stellar dynamics: Jeans Axisymmetric model

One goal of the observations of the nuclei of galaxies is to determine their properties such as their mass, and to compare these properties with other systems to better understand their history and stellar orbital make-up. In the case of IFS observations, the extraction of these information is done with the help of dynamical models. One that has been used for the study of galactic nuclei over the past years is the Jeans Axisymmetric Model (JAM),

introduced by Cappellari (2008). This technique relies on the Multi-Gaussian Expansion (MGE) parameterization (Emsellem et al. 1994; Cappellari 2008) which decomposes parametrized quantities such as the luminosity density and the mass density as a set of Gaussian functions. These two quantities are then injected in the Jeans equations to get the components of the velocity-dispersion tensor.

The method provides proper motions and radial velocities for axisymmetric and spherical systems and can be used for observations of galactic nuclei. In particular, we recover the mean second moment of the LOS velocity in the plane of the sky coordinates $v_{rms}^2 = v_r^2 + \sigma^2$ where v_r and σ are the radial velocity and the velocity dispersion of the system extracted from the kinematics in Section 2.4.2. We will be then able to fit our observations with the model given some parameters such as a mass-to-light ratio or black-hole mass. Combined with the surface brightness of the nuclear regions, it will thus be possible to constrain the enclosed dynamical mass of the nuclear cluster.

2.6 Conclusion

In this chapter, I have described a case study of the extraction of the kinematics of the central region of the spiral galaxy NGC 300. After a brief overview of the properties of the galaxy and its nuclear cluster, I have presented the near-infrared observations from the SINFONI instrument. I have then detailed the different steps for the extraction and the corrections of the data with the SINFONI pipeline. I also depicted the ppxf method and the intermediate steps that have been undertaken so far to extract the kinematic maps of the nucleus of NGC 300. Our preliminary results suggest that the nucleus of NGC 300 shows little stellar rotation and low dispersion which comes to little surprise considering NGC 300 is observed nearly face-on. These low velocities were also observed in previous studies by Walcher et al. (2005), although the values do not match and a proper computation of the uncertainties on the velocity and velocity dispersion will be necessary to confirm these trends.

We also described the other necessary steps that unfortunately were not completed because of time constraints. As mentioned above, the determination of the errors on the velocity measurement in particular is crucial since these would allow us to get a better interpretation on the velocity amplitude of the nucleus. Afterwards, using the JAM model, the mass of the NC will be estimated, although the low-inclination of the system will likely introduce some degeneracy in the measurement.

The galaxy we have examined in this chapter is one example of a larger sample of nucleated galaxies whose nuclei will be studied in the future by Neumayer et al. Comparisons of their properties like their kinematics and mass with respect to their close environment would help to have a better grasp on their evolution and formation.

Chapter 3

Importance of gas reservoirs in the formation of NCs

The content of this chapter has been published in:

“New insights on the formation of nuclear clusters”

Guillard, N., Emsellem, E. & Renaud, F., 2016, MNRAS, 461:3620-3629

The example of NGC 300 described in the previous chapter showed typical information we can extract from IFU observations, allowing us to further constrain the properties of galactic nuclei. The following step is to understand why nuclei possess such properties and how they acquired them. In other words, the goal is to determine the physics involved in the formation of NCs. As a reminder, the two main formation scenarios that have been proposed so far (see the first two rows of Figure 3.1) are:

- in-situ with gas infalling onto the galactic centre and triggering star formation.
- migration where a massive cluster forms, then migrates towards the centre by dynamical friction.

These formation scenarios imprint specific signatures on the properties of NCs. Probing the galaxy properties or examining the above-mentioned scaling relations should thus help us to disentangle between the various formation scenarios. The power-law relation between the mass of the NC and the velocity dispersion of the galaxy host observed by Ferrarese et al. (2006) is not reproduced by the in-situ scenario (see analytical model from Antonini 2013), while predictions from the migration model, including a dry-merger step, seem to be more successful (Antonini 2013; Arca-Sedda and Capuzzo-Dolcetta 2014). Dynamical simulations from Hartmann et al. (2011) also show that the mergers of star clusters in models tuned for NGC 4244 and M33 retrieve the properties expected from the scaling relations.

More recent studies emphasise the fact that these two scenarios are not exclusive and likely contribute together to build the properties of the NC (den Brok et al. 2014; Cole

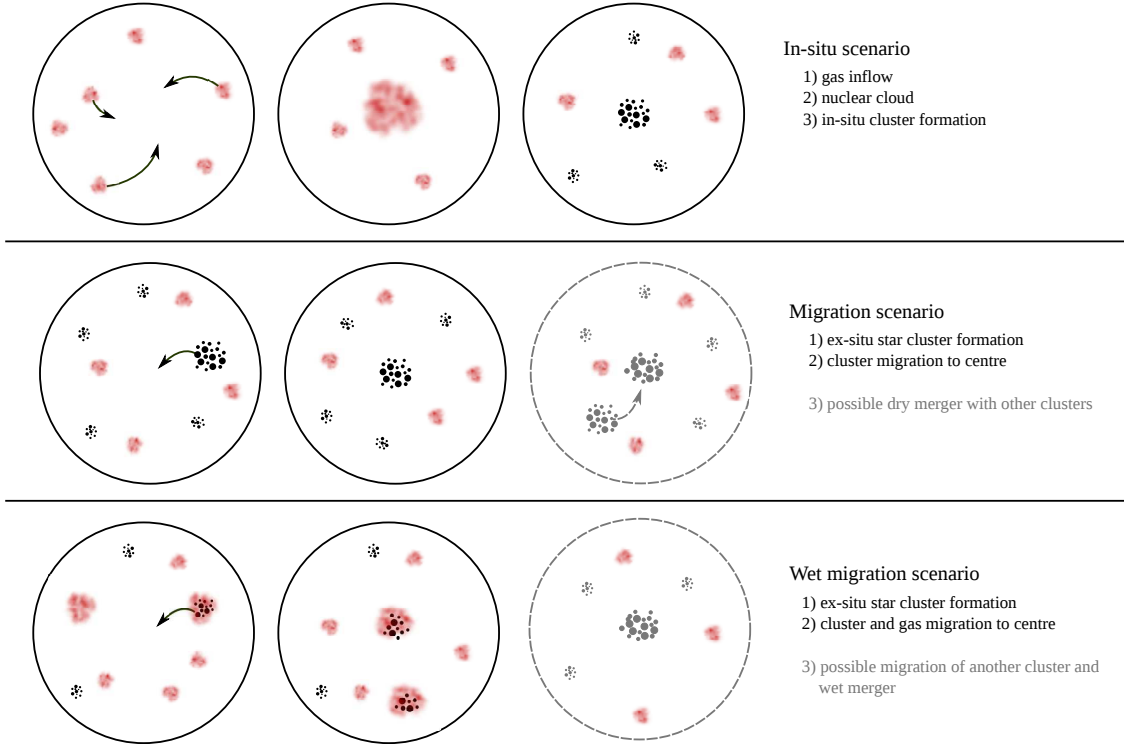


Figure 3.1: Schematics representation of NC scenarios from the literature and the one proposed in this work.

et al. 2016). Hartmann et al. (2011) points out that despite the fact that properties induced by cluster mergers are in agreement with observations, in-situ star formation could still contribute for $\sim 50\%$ of the mass of the NC. Semi-analytic models by Antonini et al. (2015) lead to similar conclusions showing that stars formed in-situ contribute to a large fraction (up to 80%) of the total NC mass.

To further investigate the diverse origins of stellar population in NCs, we present a self-consistent hydrodynamical model of NCs formation in its galactic context. Using a parsec-resolution hydrodynamical simulations of a gas-rich dwarf galaxy, we propose a new scenario for the formation of NC (see bottom panel of Fig. 3.1) based on ex-situ formation of massive clusters, their continuous growth, migration to the galactic centre, potentially followed by a *wet* merger with other clusters bringing their own gas reservoirs.

In Section 3.1, we describe the numerical methods. The formation scenario of the NC is described in Section 3.2. We show the interaction between the NC and the galactic cluster population in Section 3.3 and finally discuss the implications of this new scenario in Section 3.4.

3.1 Numerical tools and convergence

We already described in Section 1.3.1 of the Introduction the tools we use for this work and we just make a quick summary in the following paragraphs.

We run hydrodynamical simulations of an isolated dwarf galaxy using the Adaptive Mesh Refinement (AMR) code `RAMSES` (Teyssier 2002). We define 3 types of particles: the dark matter (DM), the stars included in the initial conditions (hereafter referred to as primitive stars), and stars we formed during the course of the simulations (hereafter referred to as new stars). The code solves the equations of motion with a particle-mesh scheme. The code uses a softening of the gravitational acceleration for the DM and primitive stars of 7 pc, while the softening for the new stars is the local resolution of the AMR grid, which is specific to each simulation (see Table 3.1 in Sect. 3.1.1). For the gas, the code solves the Euler equations on the AMR grid, allowing the densest regions to be refined while keeping a low resolution on more diffuse media. To avoid the artificial fragmentation of the densest regions, we add a pressure floor that ensures that a thermal Jeans length is always resolved by at least four cells. The physical ingredients we use in this simulation are similar to the ones used in Renaud et al. (2015).

The size of the simulated volume is of $30 \times 30 \times 30$ kpc³, with the least resolved cells spanning 120pc. We run a set of 3 simulations in which we vary the maximal resolution from 15 pc³ to 3.5 pc³ (see Table 3.1). The galaxy is modeled in isolation, thus neglecting the cosmological context. The simulations have been run on the C2PAP facilities (Excellence Cluster, Garching) for about 1 million CPU-hours on 512 cores.

The gas is heated by ultraviolet radiation and cooled down by atomic cooling tabulated at solar metallicity (Courty and Alimi 2004). The minimal temperature reached is of 200K.

Star formation follows the Schmidt law: $\rho_{\text{SFR}} = \epsilon \rho / t_{\text{ff}} \propto \epsilon \rho^{3/2}$ where ρ is the gas density, ϵ is the dimensionless efficiency of the star formation and $t_{\text{ff}} = \sqrt{3\pi/(32G\rho)}$ is the free-fall time. This only concerns densities higher than a given threshold. We set an efficiency of 2% and a density threshold of 100 cm⁻³, so that the star formation rate (SFR) of the dwarf is about 0.1 M_⊙. This corresponds to the rates observed for galaxies of $\sim 10^9$ M_⊙ at redshift z=2-3 which is the type of galaxies we model in this work (Behroozi et al. 2013). The stellar particles have a mass of 130 M_⊙.

The stellar feedback recipes we used are described in Renaud et al. (2013). Photoionization is modeled by creating a Strömgren sphere around massive stars (20% of the stars mass explode as SNe) younger than 10 Myr. The radius of the sphere depends on the ambient gas density and the time-varying stellar luminosity. The interstellar medium (ISM) in the sphere is heated up to 4×10^4 K. In the bubble, the code injects momentum-driven feedback in the form of radial velocity kicks to model radiative pressure. Type II supernova (SN) feedback is implemented as a Sedov blast wave (see Dubois and Teyssier 2008 for details). SN injects 10⁵¹ erg in a kinetic form. Feedback from a potential active galactic nucleus is not included in these simulations.

3.1.1 Initial conditions and final state

Galaxies with stellar mass of $\sim 10^9 - 10^{10} M_{\odot}$ have the highest fraction of nucleated galaxies (Pfeffer et al. 2014), and we therefore set the total baryonic mass of our galaxy model in this range, namely to $3.3 \cdot 10^9 M_{\odot}$. Taking conditions representative of redshift $z \sim 2 - 3$ low-luminosity galaxies, we set the gas mass fraction to 70% of the baryonic mass (Daddi et al. 2010), the stellar and gaseous masses being 10^9 and $2.3 \cdot 10^9 M_{\odot}$, respectively. The DM halo has a mass of $10^{11} M_{\odot}$, following the scaling relation between DM halo and stellar disc from Ferrero et al. (2012). We model the DM halo with a Navarro-Frenk-White (NFW) profile (Navarro et al. 1996) that has a concentration of 16 and a virial radius of 120 kpc. We truncate the halo at a radius of 15 kpc since we focus on the central regions of the galaxy.

At $t = 0$, our simulation volume is composed of both gaseous and stellar exponential discs embedded in a dark matter halo. We use the code `PyGME` (Python Multiple Gaussian Expansion) to generate the stellar component, the DM and gas. This code makes use of the Multi-Gaussian Expansion method (Monnet et al. 1992; Emsellem et al. 1994), and spatially decomposes the mass of the galaxy in a set of Gaussian functions. We used a total of 26 Gaussians to generate the galaxy components: 8 for the DM Halo, 9 for the stellar disc and 9 for the gas disc. The velocities of the particles are derived via the Jeans equations considering all components (gas, stars, dark matter) for the gravitational potential. The gas particles are then replaced by AMR cells. The initial properties of the galaxy are summarized in Table 3.1, and Fig. 3.2 displays the initial rotation profiles of the galaxy and of its components.

Star formation and feedback are not active at the beginning of the simulations. We progressively increase the refinement level of the grid. After a relaxation phase of 80 Myr we activate the SF and the feedback. After another 15 Myr of evolution, the simulation reaches the maximum spatial resolution with all physical processes activated. We then let the system evolve for ~ 2.4 Gyr.

At the end of the simulation, our galaxy has a stellar and gaseous mass of $1.5 \times 10^9 M_{\odot}$ and $3.1 \times 10^8 M_{\odot}$ respectively and a nuclear cluster has formed with a surface density of $2 \times 10^4 M_{\odot} \text{ pc}^{-2}$ (see right panel of Fig. 3.3).

We detect three smaller clusters orbiting around the nucleus with a period of a few hundreds Myr and orbital eccentricity between 0.3 and 0.6. The radial profile of the galactic surface density can be decomposed in three parts: the central region ($R < 200$ pc) which is dominated by new stars, a transition range for $0.2 < R[\text{kpc}] < 1$ and the outer part of the galaxy that exhibits an exponential profile with a scaling radius of 1.7 kpc.

3.1.2 Numerical convergence

When increasing the resolution, we have access to denser regimes of gas, which thus potentially increases the SFR. This increase is however regulated by feedback. We tested the efficiency in providing numerical convergence by running two additional otherwise identical simulations with maximum resolutions of 15 pc and 7.5 pc, respectively. Considering

Table 3.1: Initial conditions

Box length (kpc)	30
AMR coarse level	8
AMR finest level	11 12 13
Highest resolution (pc)	14.6 7.3 3.7
DM Halo	
Virial mass ($\times 10^9 M_\odot$)	100
Virial radius (kpc)	120
Cut radius (kpc)	15
Concentration	16
Profile	Navarro-Frenk-White
Number of particles ($\times 10^5$)	37.5
Primitive stars	
Mass ($\times 10^9 M_\odot$)	1
Profile	Exponential
Scale radius (kpc)	1
Cut radius (kpc)	7.5
Scale height (pc)	250
Cut height (pc)	750
Number of particles ($\times 10^5$)	15
Gas	
Mass ($\times 10^9 M_\odot$)	2.3
Profile	Exponential
Scale radius (kpc)	1.65
Cut radius (kpc)	7.5
Scale height (pc)	165
Cut height (pc)	750
Average number of cells ($\times 10^6$)	

the complex evolution in the early stages of these gas-rich simulations, it is not relevant to compare the local details (star formation distribution, high frequency features, etc) of each simulation. Still, it is important to figure out if the global properties do converge. Figure 3.4 thus shows that the SFR is quantitatively different between the 15 and 7.5 pc resolution simulations. The former has an almost constant SFR, while the latter shows a rapid increase within the first 500 Mr and a steady decrease hereafter. In that context, the 3.5 pc resolution simulation shows a very similar behaviour, even though the higher resolution allows to capture higher gas densities. This is confirmed by the fact that for the cumulative mass of new stars, convergence in the final stellar mass seems to occur between 7.5 pc and 3.5 pc. In short, the simulations at 7.5 pc and 3.5 pc form about the same amount of stellar mass ($4.8 \times 10^8 M_\odot$) by the end of the simulation. In the rest of the chapter, we thus focus on the simulation at the highest resolution, i.e. 3.5 pc.

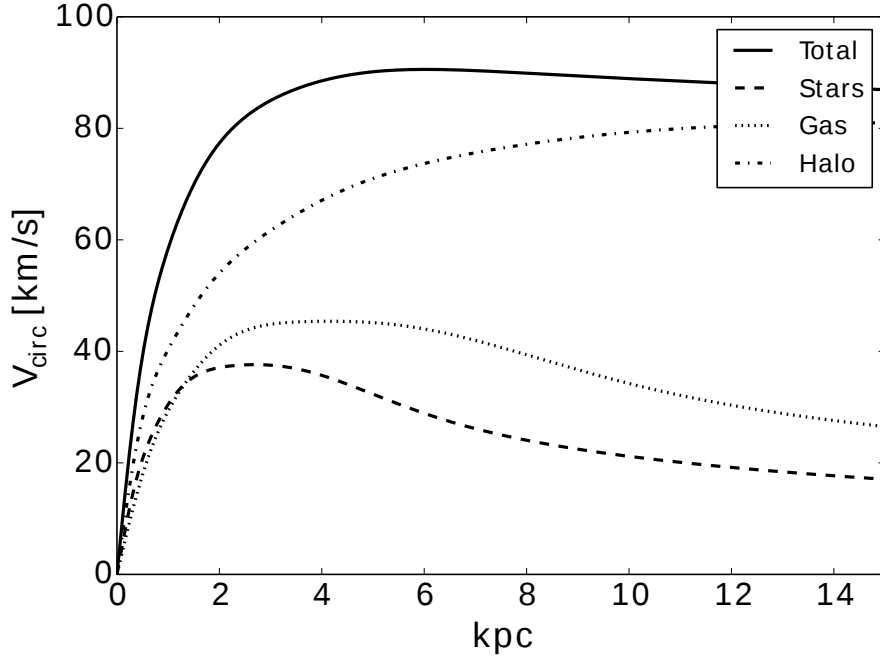


Figure 3.2: Rotation curves of the galactic components at $t = 0$ Myr.

3.1.3 Clusters detection

To detect star clusters, we use the friend-of-friend algorithm HOP (Eisenstein and Hut 1998). With this method, clusters are defined as over-densities regions above a given threshold. Namely, a cluster is detected when the peak of the local stellar density exceeds $1.5 M_{\odot} \text{pc}^{-3}$. Two clusters are then merged if the saddle density between them is higher than $1 M_{\odot} \text{pc}^{-3}$. The clusters properties can be significantly affected by the choice of parameters in this algorithm. Lowering the densities would obviously result into a contamination from the background stars, while increasing it would lead to more compact (detected) clusters. We test that changing the detection parameters by a factor of two slightly affects the derived properties of the clusters, but does not alter our conclusions.

3.2 Formation of NC

Based on the simulation, we propose a new scenario for the formation of nuclear clusters. This “wet migration” scenario consists of two main phases: the formation, growth and migration of a massive cluster toward the centre of the galaxy during which the cluster retains part of its gas, followed by a potential merger with another cluster.

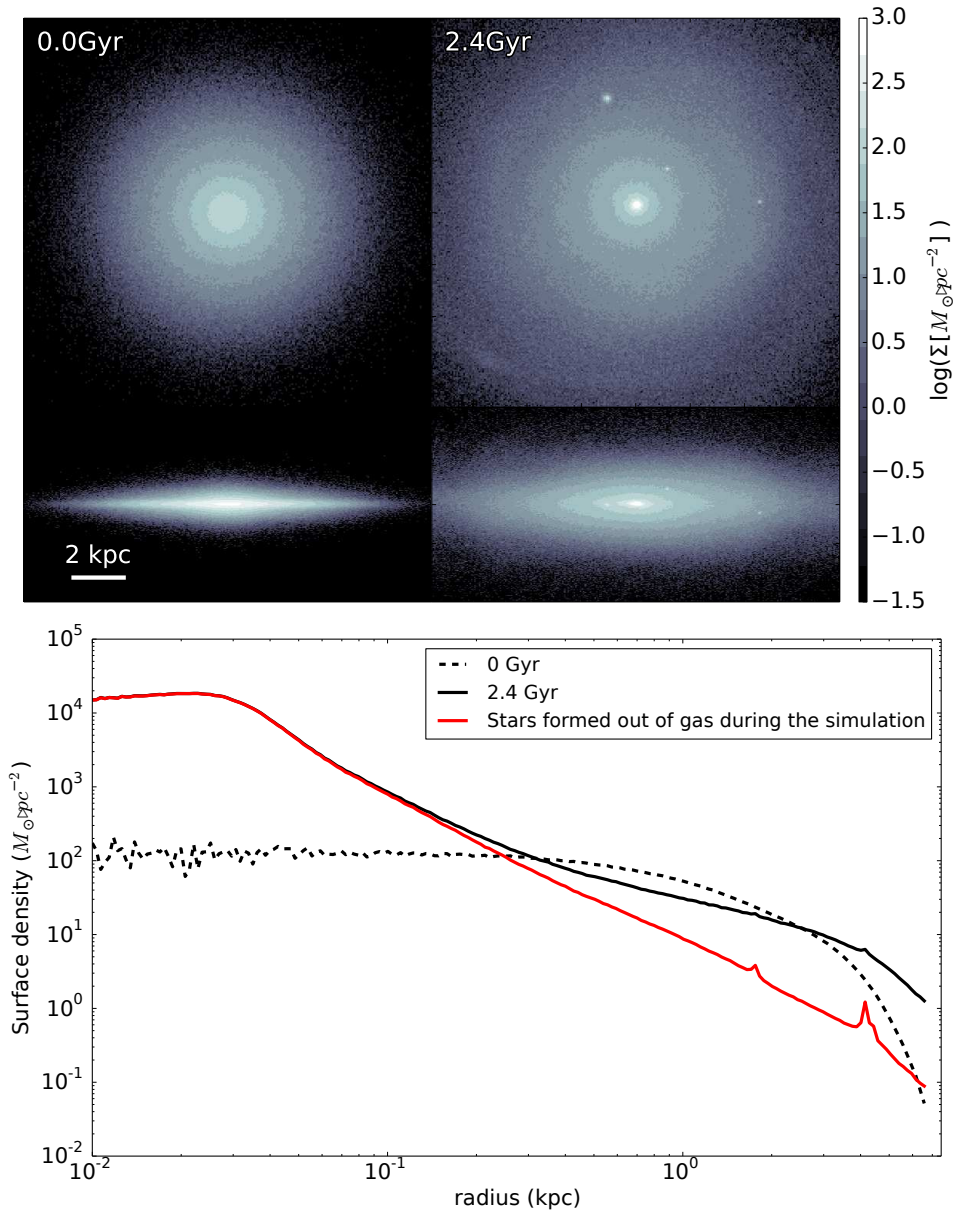


Figure 3.3: Top: Face-on and edge-on surface density maps of all stars at the beginning (left) and at the end (right) of the simulation. Bottom: Radial profile of the surface density of the galaxy at the beginning (**dashed**) and the end (**solid**) of the simulation. The new stars (red) dominate the central hundred parsecs.

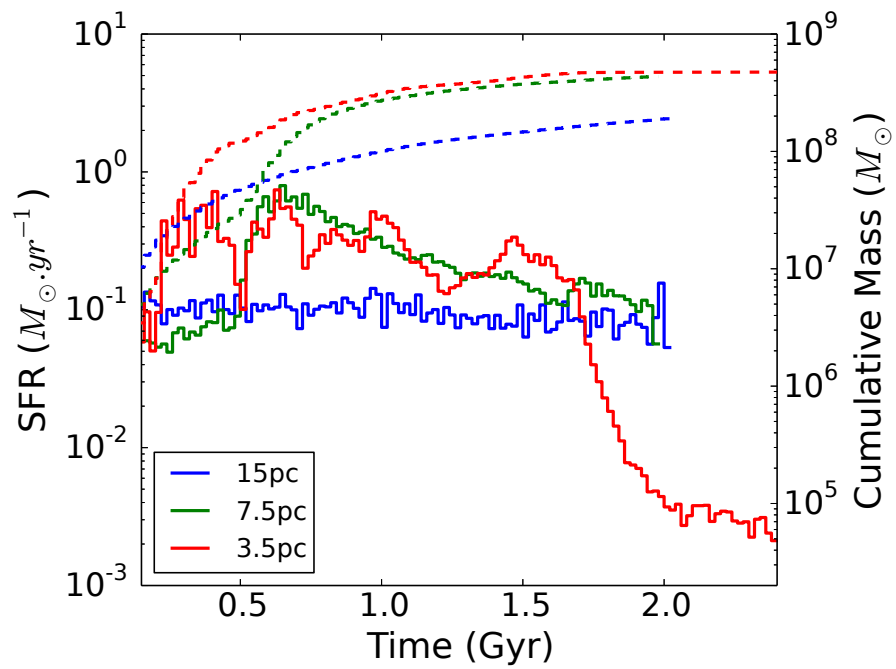


Figure 3.4: Cumulative Mass of new stars (dashed) and SFR (filled) for simulations at resolutions of 15 pc (blue), 7.5 pc (green) and 3.5 pc (red). At $t \sim 1.7$ Gyr, a merger between two massive clusters occurs, coinciding with a sharp drop of the SFR.

3.2.1 Formation by migration

The cluster seed of our NC (named Cluster1) forms 1.1 kpc away from the galactic centre, at $t = 562$ Myr. At this stage, gas is still the major baryonic component of the galaxy disc, which has a rather irregular structure (see Fig. 3.5). A variety of clusters also form at the same epoch, with masses ranging from $10^5 M_{\odot}$ to $10^7 M_{\odot}$. Cluster1 collapses out of a clump of $\sim 2 \times 10^7 M_{\odot}$ ($\sim 0.8\%$ of the galactic gas mass, see top panel of Fig. 3.6). The initial cluster has a stellar mass of $2 \times 10^4 M_{\odot}$, and converging flows supply the cluster with gas (see the gas velocity field in Fig. 3.6). The gravitational potential of Cluster1 is deep enough to retain this reservoir, keeping a relatively constant mass of gas ($2 - 3 \times 10^7 M_{\odot}$) in its vicinity despite its stellar feedback. Sustained star formation makes Cluster1 steadily grow in mass (see the solid lines in Fig. 3.7). Cluster1 also grows in size from ~ 12 pc to $30 - 40$ pc.

We can split the growth of Cluster1 into two phases:

- 1) a rapid growth during the first 100 Myr. The gas dominates the mass budget within 200 pc.
- 2) a slower growth in the following 800 Myr during which the mass of Cluster1 dominates the environment over the gas reservoir.

During the first phase, the amount of gas ($> 10^7 M_{\odot}$) remains higher or of the same order of magnitude than the mass of Cluster1 (see Fig. 3.7). Variations of the gas reservoir mass have a strong impact on the mass growth rate of Cluster1: a decrease of the reservoir mass stops the growth (e.g. at $t' = 60$ Myr where t' is the relative time after the cluster formation) and its refilling accelerates it (e.g. at $t' = 100$ Myr). The refilling occurs both by local infall and during interactions with another dense cluster bringing its own gas. The decrease is mostly due to star formation and to SN blasts from the cluster itself or its neighbours. Fig. 3.8 shows that, since its formation, Cluster1 is one of the main contributors to the global SFR.

Fig. 3.9 shows that Cluster1 migrates toward the centre relatively slowly. Indeed, it takes 350 Myr to Cluster1 to cover a radial distance of 1.2 kpc at $t < 900$ Myr. Multiple interactions between Cluster1 and the surrounding structures slightly affects its orbits, and disturbs its migration towards the galactic centre.

SNe also have an impact on the orbital evolution of the cluster. For example, at $t = 730$ Myr ($t' = 170$ Myr in relative time), Cluster1 experiences a burst of star formation (see Fig 3.8). The newly formed stars slowly drift away from the remaining gas clump (due to asymmetric drift e.g. Renaud et al. 2013). 10 Myr later, SNe feedback inject energy into the ISM, forming a bubble which is therefore off-centred with respect to the gas clump (see Fig. 3.10). Since the gas represents a significant fraction of the local mass budget (52% at that time for Cluster1, see Fig. 3.7), the local gravitational potential is significantly altered when the gas is expelled. As a result, Cluster1 gets a velocity kick which increases its orbital eccentricity, and sends it away from the galactic centre (see Fig. 3.9). About 50 Myr later, the cluster reaches its apocentre and moves back towards the centre, reaching

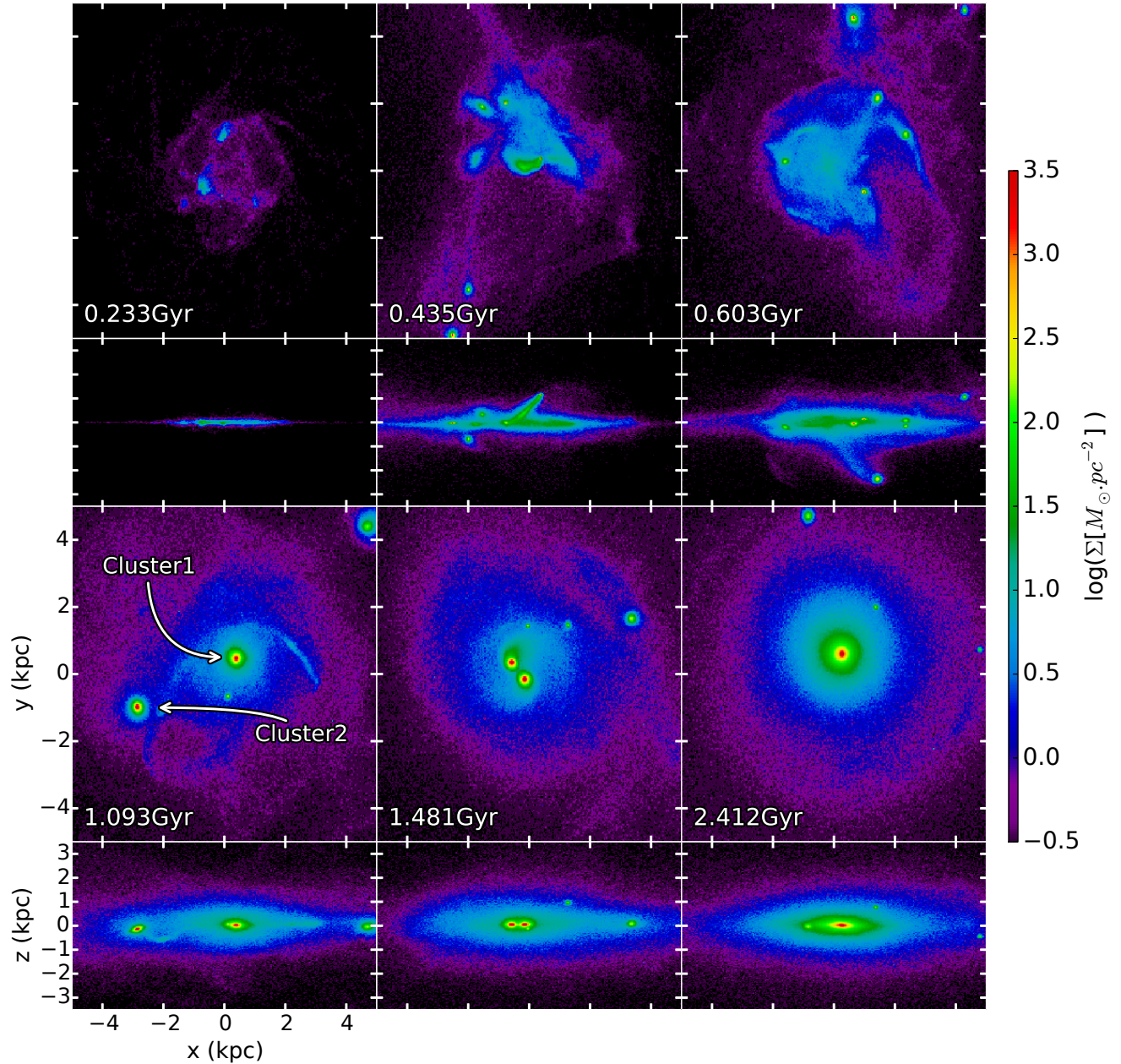


Figure 3.5: Surface density of stars that have been formed during the simulation. Cluster1 is the NC's seed. Cluster2 is the second most massive cluster in the simulation. It merges with Cluster1 at $t=1.7$ Gyr.

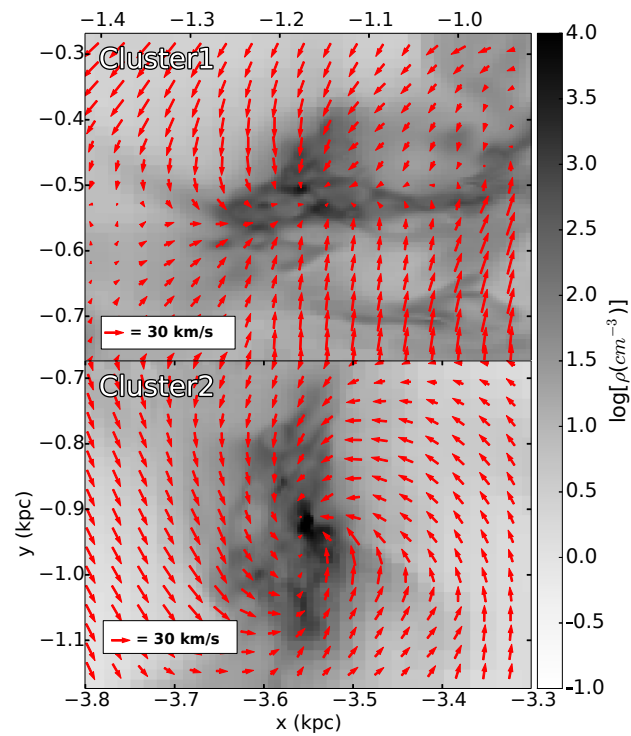


Figure 3.6: Maps of gas density at the earliest detection of the two most massive clusters in the galaxy. Cluster1 (top) forms the nuclear cluster by migration, while Cluster2 (bottom) merges later with the NC. The velocity field in the (x,y) disc plane is shown with red arrows.

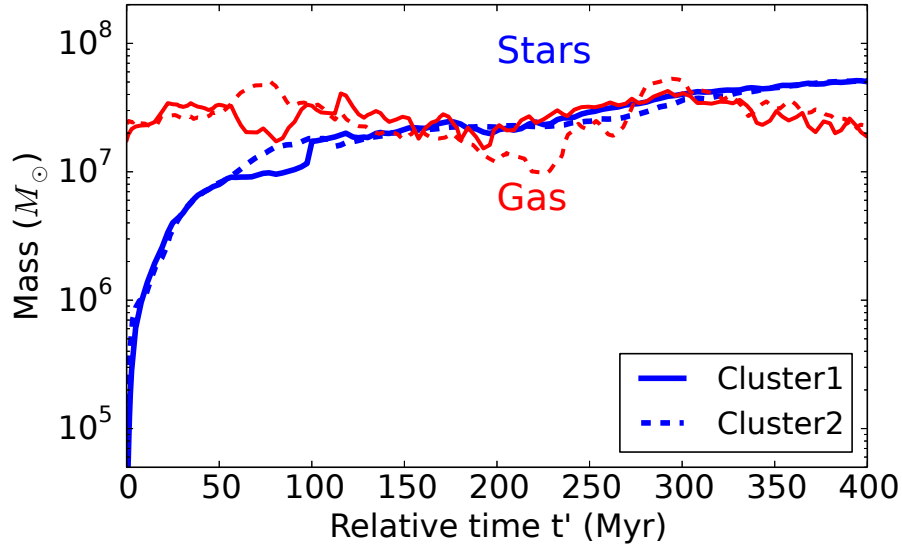


Figure 3.7: In blue: stellar mass of Cluster1 (solid) and of the second most massive cluster Cluster2 (dashed) starting at their respective first detection. In red: gas mass within 200 pc around the clusters. $t' = 0$ corresponds to the respective earliest detection epoch of the clusters. At $t' = 100$ Myr, Cluster1 merges with another cluster which rapidly increases its mass.

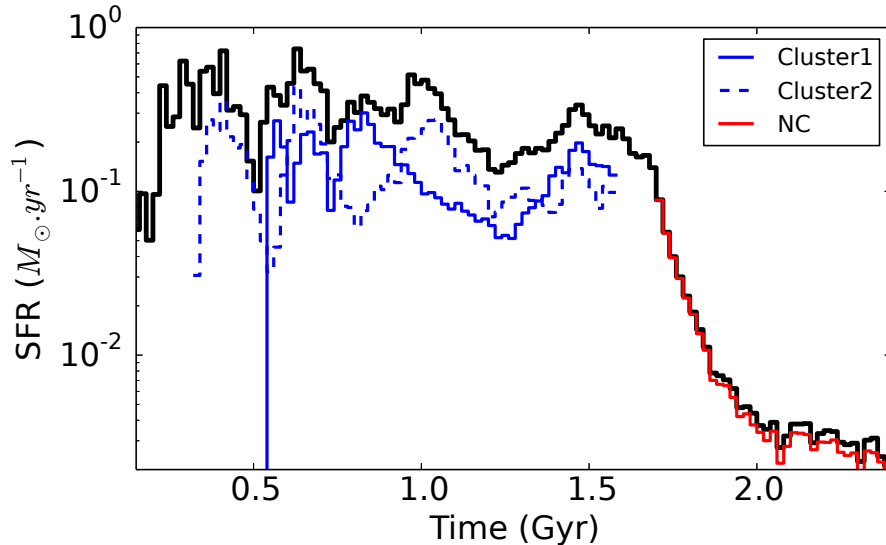


Figure 3.8: Contribution of Cluster1 (solid), Cluster2 (dashed) and their merger (NC, red) in the total SFR (black). The latter is dominated by Cluster1 and Cluster2 and by the NC in the end. Cluster1 and Cluster2 cannot be distinguished from each other after $t = 1.6$ Gyr.

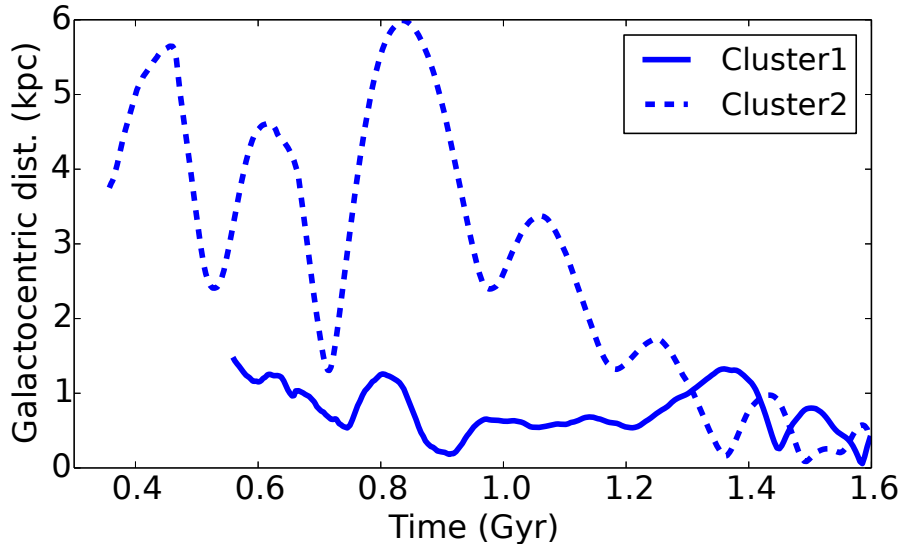


Figure 3.9: Galactocentric distance of Cluster1 (solid) and Cluster2 (dashed). The galactic centre is defined as the centre of mass of particles (stars + DM).

this time a smaller galactocentric distance ($d = 180$ pc at $t = 900$ Myr). At that stage, the cluster represents 67% of the galactic central (r_{1500pc}) mass. It interacts with the stellar and gaseous material in the central region of the galaxy, which makes the galactic centre ill-defined. Nevertheless, the orbit of Cluster1 remains close to the centre of the global potential so that we can then consider Cluster1 as a NC.

3.2.2 NC-cluster merger

Another massive ($4 \times 10^7 M_{\odot}$) cluster (Cluster2) evolves alongside Cluster1. It forms in a different environment (see bottom panel of Fig. 3.6) in the external region of the galaxy ($d = 3.8$ kpc, $t = 360$ Myr) where the stellar and gas densities are much lower. The ISM around Cluster2 is slightly less turbulent than around Cluster1 (Mach number of 0.33 and 0.66, respectively, on a scale of ~ 240 pc). The early mass evolution of Cluster2 is similar to that of Cluster1 (see Fig. 3.7). Figure 3.8 shows that Cluster2 is another important contributor to the overall SFR in the galaxy. We also note that the stellar mass dominates Cluster2 300 Myr after its formation, like Cluster1. Cluster1 and Cluster2 are thus initially in the same mass regime and share similar properties, while formed in rather different environments.

Figure 3.9 shows that after interactions with the sub-structures in the galactic disc ($t < 950$ Myr), Cluster2 loses angular momentum and progressively migrates towards the centre. We estimate that the dynamical friction time is ~ 1 Gyr (Chandrasekhar 1943; Mo et al. 2010), which is consistent with the time Cluster2 takes to reach the central region of the galaxy. At $t = 1.7$ Gyr, Cluster2 merges with the NC (initially Cluster1, which

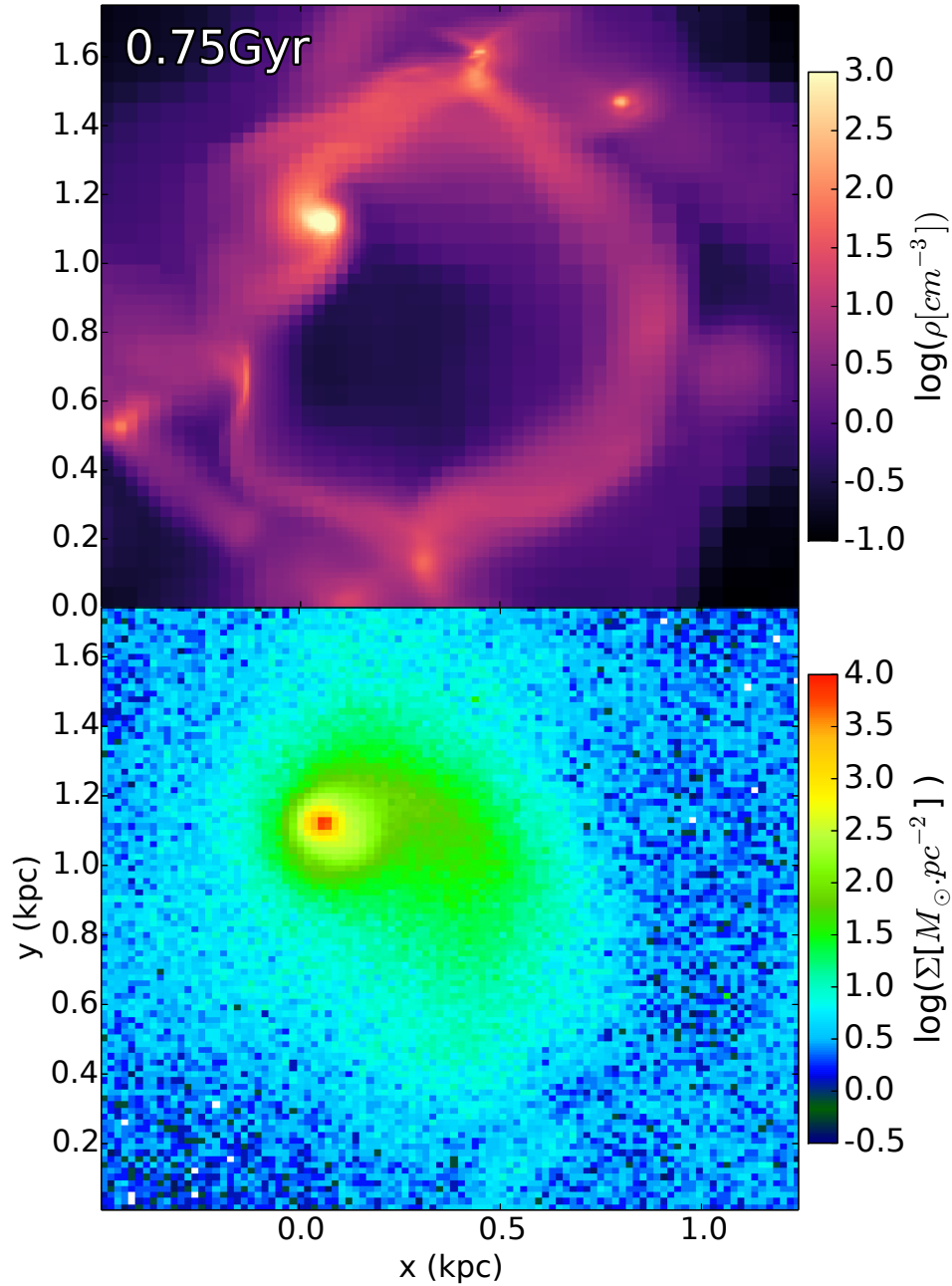


Figure 3.10: Maps of the gas (top) and new stars (bottom) densities. The shell from the supernova which explodes 5 Myr before is visible on the gas density map. The asymmetric extension of Cluster1 (on the right) is the combined result of its orbit and of the supernova blast.

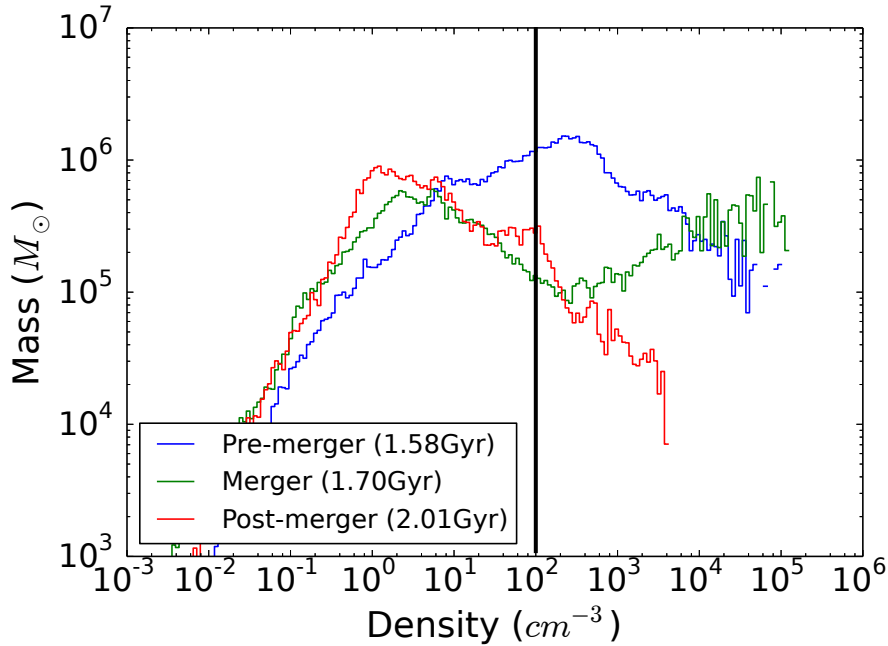


Figure 3.11: PDFs inside a $1 \text{ kpc} \times 1 \text{ kpc} \times 1 \text{ kpc}$ centred on the NC or centre of mass of the system (Cluster1-Cluster2) before they merge. The vertical line represents the density threshold for the SF.

migrated earlier). The resulting stellar system has a half-mass radius of $\sim 35 \text{ pc}$ and a mass of $1.8 \times 10^8 M_{\odot}$ (see bottom-right row of Fig. 3.5). Because of the transfer of orbital momentum from Cluster2 to the stars of the merger, the resulting NC is flattened in the orbital plane of the interaction (which coincides with the plane of the galactic disc), with an axis ratio of 0.4 ¹.

After the merger, the SFR drops by almost two orders of magnitude (see Fig. 3.8). Fig. 3.11 shows the evolution of the gas density Probability Distribution Function (PDF) within the central kpc, during the merger phase. Before the merger, the PDF yields a classical log-normal shape corresponding to supersonic ISM (Vazquez-Semadeni 1994), and a power-law tail for $\rho \gtrsim 2000 \text{ cm}^{-3}$ indicating self-gravitating gas (Elmegreen 2011; Renaud et al. 2013). The collision between the gas clouds around the NC and Cluster2 generates an excess of dense gas ($> 10^4 \text{ cm}^{-3}$), leading to a starburst localized in the central 25 pc. In the mean time, the tidal interaction strips gas from the outskirts of the clouds, thus depleting gas at intermediate density ($\sim 100 \text{ cm}^{-3}$). The dependence of star formation on $\rho^{3/2}$ implies that the depletion at intermediate densities approximately balances the central excess at high densities. Thus, despite the central mini starburst, the net SFR remains almost constant over 100 pc. After the merger, the central star formation has consumed a

¹We estimate the height and radius using iso-surface density contours of $10^3 M_{\odot} \text{ pc}^{-2}$ in its edge-on projection.

large fraction of the dense gas, and the associated feedback disperses most of the gas left in this volume. This lack of dense gas reduces significantly the SFR to a few $10^{-3} M_{\odot} \text{ yr}^{-1}$, thus almost quenching star formation in the NC.

3.2.3 Merger: a mandatory process?

To test the importance of the merging step in the formation scenario of the NC, we artificially remove the stars associated with Cluster2 from the simulation, before it interacts with cluster1 ($t = 500$ Myr, i.e. when Cluster2 has formed about half of its final mass). This procedure is sufficient to prevent the further formation of a massive cluster, and does not alter the large scale dynamics of the rest of the galaxy.

In this alternative simulation, a cluster similar to Cluster1 still forms at $t = 800$ Myr and reaches the centre in about the same amount of time, namely 300 Myr. The NC forms as described in Section 3.2.1. We then let the NC evolve for 700 Myr ($t = 1.7$ Gyr). However, the absence of another massive cluster being able to merge with the NC voids the second step of our scenario. All the effects associated with the merger phase (recall Section 3.2.2) are thus missing in the further growth of the NC. Namely,

- the depletion of the dense gas reservoir does not occur and the NC continuously forms stars. This affects the star formation history of the NC as shown in Fig. 3.12. In the merger scenario, both NC cluster progenitors form stars during their entire lifetimes, until star formation gets quenched at the time of the collision. This leads to the mixing of stellar populations with different ages, and the lack of a young population.
- the angular momentum re-distribution noted during the merger does not happen and the NC maintains an almost spherical morphology (axis ratio of 0.8), as opposed to the flattened shape visible in Fig. 3.5.
- Without merger, there is no increase of the angular momentum and the resulting NC exhibits a lower amplitude rotation than in the case of a merged system: the difference in angular momentum is approximately of a factor of 10.
- the resulting NC is less massive but has a similar size ($5 \times 10^7 M_{\odot}$ and 40 pc in our cases) without the merger step.

Note that the first three points could be used as observational diagnostics to establish the formation scenario of real NCs.

This demonstrates that the merger step is not mandatory for the formation of the NC, but can significantly alter the properties of the NC when it takes place.

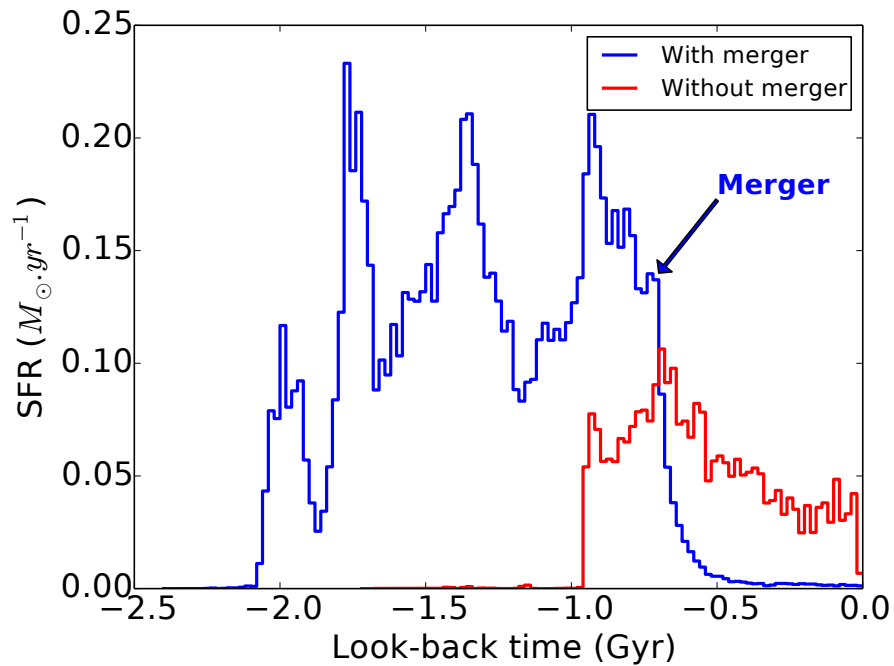


Figure 3.12: Star formation history 700 Myr after the formation of the final NC ($t=0$). Only the stars within a radius of 100pc centered on the NC are considered. When the NC experiences a merger (arrow at $t = -0.7$ Gyr), the stellar population of the NC is a mix of that of Cluster1 (formed at $t = -1.9$ Gyr) and that of Cluster2 (formed at $t = -2.1$ Gyr). Star formation is quenched after the event. When there is no merger, the stellar populations is only that of the NC progenitor (formed at $t = -0.9$ Gyr).

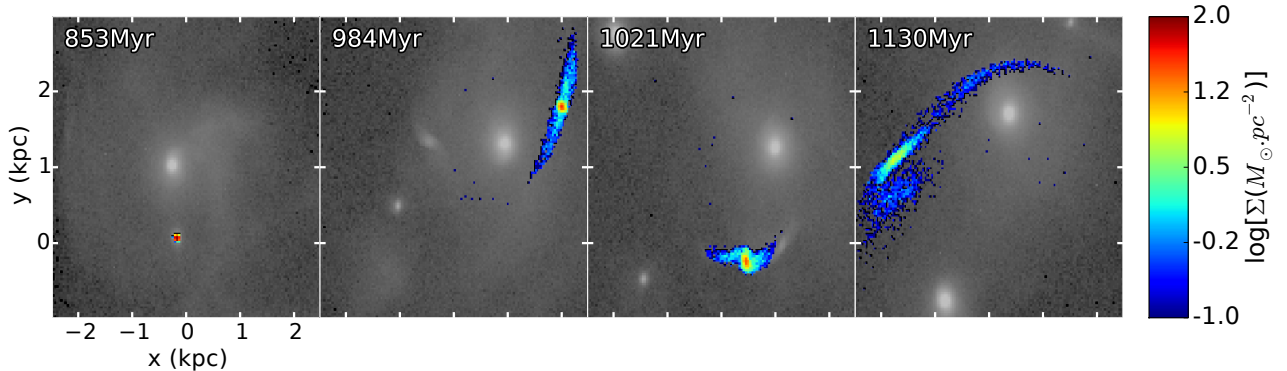


Figure 3.13: Disruption of a cluster through time. The galactic stellar background is shown in grey scale (Cluster1 is the closest to centre of the maps). The colour scale represents the surface density of the stars initially detected in the cluster (first panel). Interactions between clusters in the galaxy (mainly Cluster1 and Cluster2) generate tidal tails and eventually lead to the dissolution of the low density cluster.

3.3 Cluster populations

3.3.1 Cluster disruption

In our fiducial simulation, Cluster1 and cluster2 represents 15% of the new stars of the disc, and set the dynamics of their surroundings. The rest of the star cluster population thus experiences several interactions with Cluster1, Cluster2 and the NC, and some get disrupted by tidal forces. Signatures of tidal disruptions are visible throughout the simulation (see e.g., bottom-left panel of Fig. 3.5).

One example of this disruption process is shown in Fig. 3.13, where we monitor the stars of one cluster during about 300 Myr, until its complete destruction by tidal forces. At $t = 853$ Myr (first panel of Fig. 3.13), a bound cluster is detected 1 kpc away from Cluster1. The tidal interaction between Cluster1 and this $\sim 10^5 M_{\odot}$ cluster induces tidal tails (second panel of Fig. 3.13). Subsequent interactions, including one with the approaching Cluster2, accelerate the disruption, finally leading to complete dissolution. The tidal features can still be detected as elongated over-densities for another 250 Myr after the dissolution, until the surface density contrast with the background becomes too low. This situation is similar for other less dense clusters. This shows the key role of massive clusters such as Cluster1 and Cluster2 in the evolution of the cluster population as a whole, accelerating the disruption of the most fragile objects.

3.3.2 Surviving clusters

As illustrated in Fig. 3.5, some clusters survive the disruptive presence of the NC. We detect three of these clusters (named A, B and C) keeping a constant mass for most of the simulation ($\sim 10^6 M_{\odot}$, see Fig. 3.14 and Fig. 3.15). However, their mass evolutions

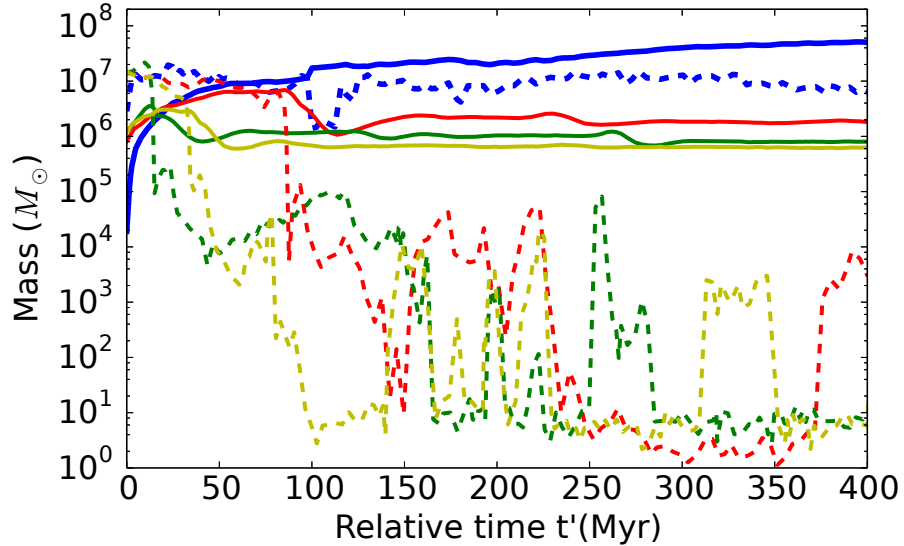


Figure 3.14: Evolution of the stellar (solid) and gas (dashed) mass of the clusters surviving the presence of the NC, compared to that of Cluster1 (blue). We measure the gas mass in a cube of 50 pc centred on the cluster. Each color corresponds to one cluster (A in red, B in green and C in yellow). As in Fig. 3.7, the time is relative, with $t' = 0$ marking the earliest detection of each cluster.

strongly differ from that of Cluster1 and Cluster2.

Their growth phase only lasts about 10-40 Myr. This star formation activity leads to a rapid injection of supernova energy into the ISM, but their lower density is not enough to retain the feedback winds, which thus depleting the gas reservoir mass by one to three orders of magnitude (in mass). Figure 3.16 illustrates this by showing the evolution of the gas density PDFs in the regions of the clusters.

For clusters A, B and C, stellar feedback happens to truncate the PDFs close to the density threshold associated with star formation, thus preventing further star formation. The rapid gas removal by stellar feedback in clusters A, B and C has a significant impact on the local gravitational potential. The least bound stars are then ejected from the clusters (Hills 1980; Boily and Kroupa 2003). This lowers the clusters masses by a factor 2 to 7 and their surface densities by one order of magnitude (see Fig. 3.15), which then remain roughly constant until the end of the simulation. The mass of the gas reservoirs shows fluctuations over time. A sharp increase of the gas mass can lead to an increase of the clusters mass for a short period. This is for example the case for cluster **B** at $t' = 250$ Myr in Fig. 3.14. The stellar mass of the cluster then decreases as the least bound stars are ejected from the cluster.

The main difference between NC progenitors and the rest of the cluster population is then their ability to retain a significant fraction of their stellar mass. In Cluster1 and Cluster2, the injected feedback energy is not high enough to significantly alter the existing

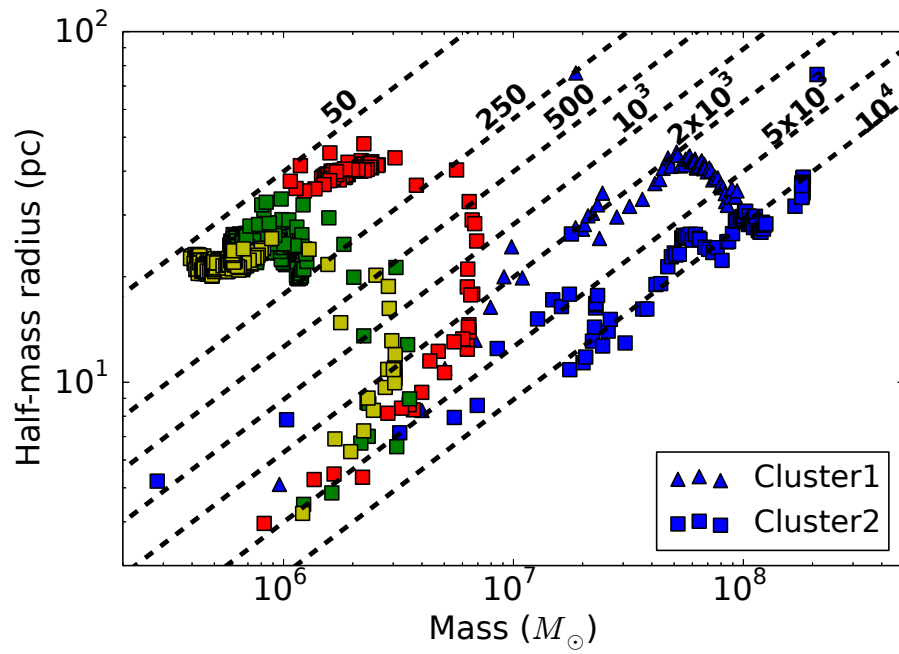


Figure 3.15: Evolution of size and mass of all clusters detected at the end of the simulation. Colours are as in Fig. 3.14. The dashed lines follow constant surface density values in $M_{\odot} \text{pc}^{-2}$.

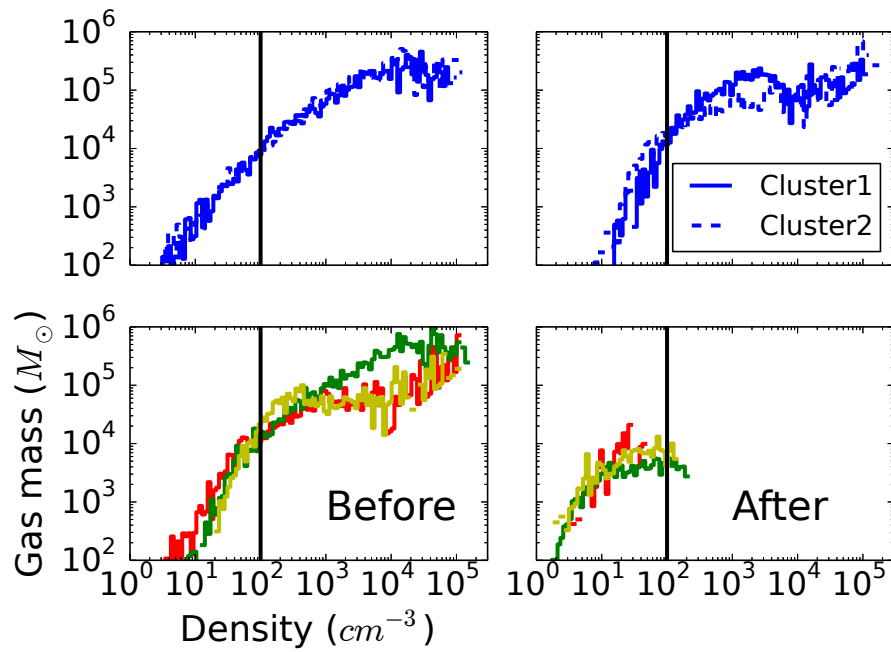


Figure 3.16: Gas density PDFs in regions of 50 pc centred on the clusters 5 Myr before (left column) and after (right column) the removal of gas by SN-blasts. The blue curve shows the evolution for Cluster1 and Cluster2 for reference. The vertical lines show the density threshold above which gas can be converted into stars.

gas reservoir. By keeping a dense gas reservoir, they can further form stars and become even more massive and resistant to subsequent tidal disruptions induced along their orbits. Altogether, these points indicate that the low density clusters have a much lower probability to survive and become seeds for a NC, in contrast with e.g., Cluster1 (see Section 3.2.1).

The dynamical friction time of clusters A, B and C is much longer, of the order of tenths of Gyr, since the dynamical friction time is inversely proportional to the cluster mass. Therefore they cannot contribute to the building of the NC through mergers within several Gyr, unlike Cluster2 (see Section 3.2.2).

3.4 Discussion & Conclusion

Using hydrodynamical simulations of an isolated gas-rich dwarf galaxy, we propose a “wet migration” scenario for the formation of nuclear clusters. The main steps are (see also Fig. 3.1):

- A population of star clusters forms across the galactic disc.
- Clusters dense enough to retain a gas reservoir around them maintain a star formation activity for a few 100 Myr, which steadily increases their masses.
- These clusters loose orbital energy through dynamical friction and interactions with the rest of the disc and migrates to the centre to form a nuclear cluster.
- The NC eventually experiences (wet) mergers with other dense clusters, increasing its mass and quenching its star formation activity.

The last step is not mandatory for the formation of the NC but strongly affect its properties (mass, shape, star formation history), as discussed in Section 3.2.3.

The other star clusters in the galaxy have lower initial densities, which affects their early evolution and tells them apart from the NC progenitors. They are either tidally disrupted by the central structures (including the NC itself) or have high orbital angular momentum which prevents them to interact with the NC and participate to its build-up.

By comparing the properties of the NC modeled with that of the observed population, Fig. 3.17 shows that our simulation is in line with the observed scaling relations (Georgiev et al. 2016). Our NC lies in the high mass and size regime (40 pc and $5 \times 10^7 M_{\odot}$ without merger, and 35 pc and $1.8 \times 10^8 M_{\odot}$ with merger). Although well within the dispersion of observational data, NCs in this mass range would be preferentially detected in slightly more massive galaxies. However, galaxies with different masses are likely to play different roles on the formation process of their NCs, as underlined by previous works. Observations by den Brok et al. (2014) favour the migration scenario in the low-mass regime ($\lesssim 10^9-10 M_{\odot}$, see also the theoretical confirmation by Arca-Sedda and Capuzzo-Dolcetta (2014)). The relative important of in-situ star formation increases with galactic mass, as showed by Antonini et al. (2015), suggesting that massive galaxies are more prone to drive gas flows toward the NC and fuel in-situ star formation than their low-mass counterparts.

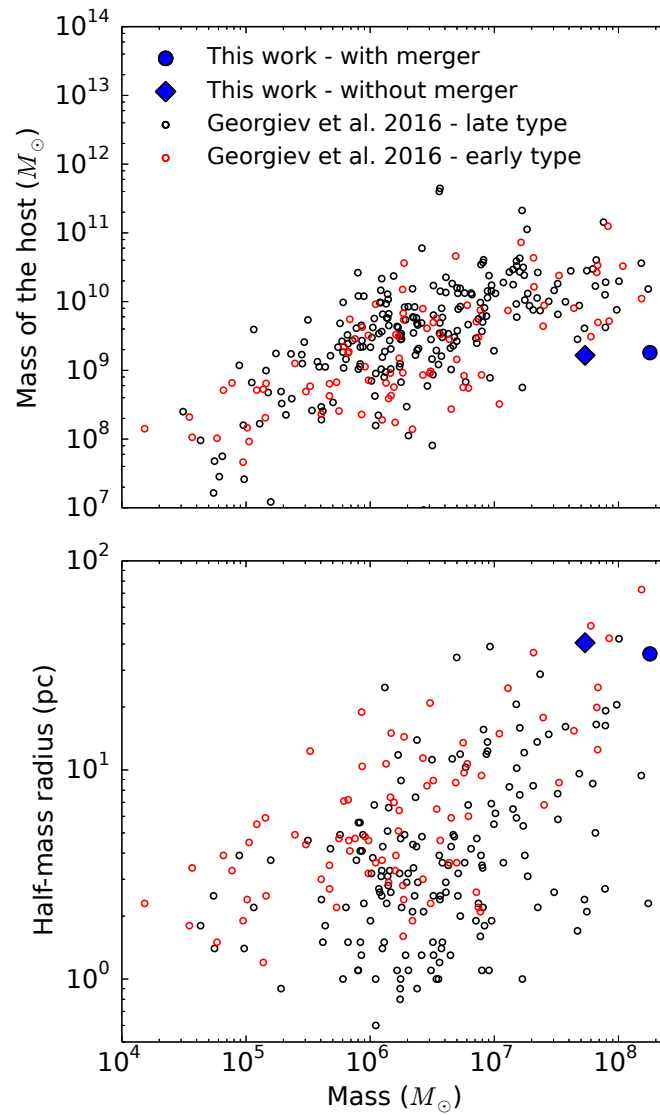


Figure 3.17: Position of the nuclear clusters formed in our simulation on the galaxy mass - observed cluster mass scaling relation (top) and in a size-mass diagram (bottom).

Such gas flows are related to kpc-scale dynamics of the galactic disc, in particular the presence of substructures. For instance, torques from bars are well-known to drive gas infall towards the galactic centre (Roberts et al. 1979; Athanassoula 1992; García-Burillo et al. 2014; Emsellem et al. 2015). This process would then supply the nuclear cluster with gas and maintain its star formation activity over long timescales. Ongoing star formation would then occur preferentially in the plane of the galactic disc (Seth et al. 2006; Böker 2010; Feldmeier-Krause et al. 2015), thus leading to a flattened NC. A similar morphology is predicted by our model in the case of a cluster merger. However in our case, the merger quenches star formation. Therefore, the absence of young stars in a flattened NC favours our merger scenario, while a young population denotes in-situ formation.

We also note that spiral arms would lead to star cluster formation providing more candidates for dry or wet mergers with the NC. It is however not clear whether these potential NC progenitors would survive the radial migration through spirals and bars (Fujii and Baba 2012). Probing these processes would require to model galaxies of different masses and disc stabilities over several rotation periods to allow for the formation and evolution of substructures.

Accounting for the cosmological context would also be key for replenishing the gas reservoir with low metallicity gas (through cold gas accretion), and/or triggering the formation and destruction of spirals and bars (Kraljic et al. 2012). Over such long timescales, and particularly in the redshift range considered here ($z \sim 2 - 3$), it is likely that a dwarf galaxy like that modeled here would experience interactions with its environment, either with other galactic systems or with the inter-galactic medium. Depending on the state of the cluster (growing seed or fully formed NC), we expect the outcome of these interactions to vary. On one hand, the perturbations will likely disturb the orbit of the seed. On the other hand, the dwarf may suffer from tidal stripping and its NC, if already formed, may become an Ultra Compact Dwarf galaxy (see e.g. Pfeffer and Baumgardt 2013 or Norris et al. 2015). The nature of the perturbation is also to be considered. A dwarf within a cluster-like environment will likely experience processes such as gas stripping or ram pressure. The resulting impact on the gas content can thus be significant, with either boosting or slowing down the growth of the NC progenitors. Along the same lines, mergers would possibly induce dramatic changes both in the morphology and star formation history of the galaxies. The migration and growth of an NC seed should be examined further in such contexts.

Such timelapses become comparable to the relaxation timescales of typical NCs ($\sim 10^9$ yr, although the massive ends of the population, including our case yield much longer timescales $\sim 10^{11}$ yr, see also Seth et al. 2006). Following the co-evolution of the NC and its host over such long periods would then require to consider collisional processes to properly treat the internal physics. Among other internal mechanisms, a full treatment of stellar evolution would provide insights on the formation of stellar mass black holes in the NC and its progenitor clusters.

Overall, this chapter emphasizes the decisive role of gas reservoirs onto the build-up of NCs, especially at high-redshift when gas dominates the local (i.e. at parsec scale) baryonic mass. As we have seen in this chapter, not all clusters are capable of retaining

their gas reservoirs that would allow them to potentially grow into NCs and instead, expel such reservoirs through feedback mechanisms. The next chapter focuses in more depth on the impact that feedback has on star clusters and their growth.

Chapter 4

Gas-stars cycle: impact of stellar feedback and application to NCs

The content of this chapter has been accepted in:

“Impact of radiation feedback on the assembly of star clusters in galactic context”
Guillard, N., Emsellem, E. & Renaud, F., 2018, MNRAS in press

As we have seen in previous chapter, gas plays a paramount role in the formation and evolution of nuclear clusters, especially at higher redshift when its fraction was much higher than it is today. The huge amount of gas collapses to form stars which in turn will inject energy back to the ISM, affecting its properties and future star formation. In this chapter, I investigate how such stellar feedback affects the properties of star clusters, with a particular emphasis on their growth, a vital step towards the formation of nuclear clusters.

4.1 Introduction

As we have seen in previous chapters, the formation of NCs is a complex question which relies on the coupling of several physical processes (e.g., star formation, stellar feedback) occurring in environments with extreme physical properties. At the time of their formation (up to 10 Gyr ago, see Cole and Debattista 2016 and references therein), gas is presumed to be abundant within the galactic disc, thus favoring the formation of star clusters (e.g. Arca-Sedda et al. 2015). Guillard et al. (2016) for example showed the importance of gas reservoirs of young clusters in the formation and growth of NCs. Such reservoirs are expected to be significantly perturbed by e.g., star-driven feedback.

Stellar feedback and its effect within galaxies have been extensively studied over the years (Hopkins et al. 2014, 2017; El-Badry et al. 2016; Nelson et al. 2015; Bournaud et al. 2010; MacLachlan et al. 2015; Krumholz et al. 2014; Raskutti et al. 2016; Howard et al. 2016; Grisdale et al. 2017). Such studies focused on various spatial scales and physical

processes. For example, at parsec (pc) and sub-parsec scale, numerical works have investigated the role of photo-ionization (Dale et al. 2012; Walch et al. 2012; Tremblin et al. 2014; Geen et al. 2016) or stellar winds (Wareing et al. 2017; Rey-Raposo et al. 2017) in the life of molecular clouds and the star formation within them. The model of feedback implemented by Núñez et al. (2017) in simulations of isolated Milky Way using various physical principles (stellar winds from young massive stars, heating by massive stars within Strömgren spheres, and limiting-cooling mechanism based on the recombination time of dense H_{II} regions) showed that star formation is more extended (in time and space) when all these physical mechanisms are used simultaneously than when pure thermal supernovae (SNe) feedback is used. Agertz et al. (2013) also showed that pre-SNe feedback (i.e. radiative pressure and stellar winds) is efficient at clearing the gas away from star-forming regions, thus making the subsequent heating from SNe even higher. At kpc-scales, other studies showed that stellar feedback is associated with violent events such molecular outflows (Geach et al. 2014; Hayward and Hopkins 2017) and helps shaping the gaseous content of galaxies (Ageritz and Kravtsov 2015, 2016). Since feedback is acting directly or indirectly from sub-parsec to kilo-parsec scales, dedicated hydrodynamical simulations had a hard time both covering the full spatial range and extending over long time-scales (Gyr). Moreover, most of these studies are based on conditions that are observed in the Local Universe, and it is thus still unclear how stellar feedback affects the ISM and the forming regions of star clusters in gas-rich discs. With present-day supercomputers, we can actually start to address these issues and the impact of stellar feedback from pc to kpc scales.

Individual feedback mechanisms are expected to play different roles in regulating the assembly of star clusters, and their non-linear interplay makes the matter even more complex to study. The aim of the present paper is to examine their relative contributions and determine how they influence the properties of young star clusters. Addressing these topics would allow us to better understand the direct impact that stellar feedback has on the gas properties, and consequently on that of star clusters when they first form (seeds) and evolve (e.g., growth, merging). The context of this study will be that of an isolated gas-rich galaxy. We choose to focus on a galactic stellar mass of about $10^9 M_{\odot}$, as this corresponds to the peak of the fraction of nucleated discs (Pfeffer et al. 2014). With such a setup we extend the study of Guillard et al. (2016), which will serve as a reference. To further understand the role of feedback, we use the same set of feedback recipes as in Chapter 3 (see Guillard et al. 2016), switching off all or part of the feedback components in turn, and comparing the properties of the forming and evolving star clusters. The physics recipes and initial conditions we employ in the present paper are similar to those of the reference simulation. In Section 4.2, we briefly describe the numerical methods. In Section 4.3, we compare the properties of the star cluster population when feedback is active or not. We finally provide a discussion and conclude in Section 4.4.

4.2 Numerical methods

In this section, we present numerical simulations following initial conditions and prescriptions similar to the ones in Chapter 3 (see also Guillard et al. 2016). Hence we only present here a summary, details being given in Guillard et al. (2016). We conducted hydrodynamical simulations of isolated gas-rich dwarf galaxies as in Chapter 3 with the Adaptive Mesh Refinement (AMR) code `RAMSES` (Teyssier 2002). The maximum and minimum resolutions for our AMR grid are respectively 3.7 pc and 120 pc. The softening of the particles coming from the initial conditions (namely the dark matter and the stars included in the initial conditions) is 7 pc while that of the stellar particles formed during the simulations (hereafter stars for simplicity) is 3.7 pc. The simulations have been run on the C2PAP facilities (Excellence Cluster, Garching) for about 1 million CPU-hours on 512 cores.

The isolated gas-rich dwarf galaxy we simulate has a stellar mass of $10^9 M_\odot$, a gas disc whose gas mass fraction is 70% of the baryonic mass and a Navarro-Frenk-White (NFW) (Navarro et al. 1996) dark matter halo component. The latter has a mass of $10^{11} M_\odot$ which follows the scaling relation between DM haloes and stellar discs as in Ferrero et al. (2012), a concentration of 16 and a virial radius of 120 kpc. We truncate the halo at a radius of 15 kpc thus focusing on the central regions of the galaxy. Both our stellar and gaseous discs have a radial and vertical exponential profile with a scaling radius of 1 kpc and 1.65 kpc (respectively) and a scale height of 250 pc and 165 pc (respectively).

Our simulations use the same recipes for star formation and stellar feedback which we used in Guillard et al. (2016) and which were described in the Introduction and Chapter 3. The star formation occurs when the gas reaches a density higher than 100cm^{-3} . The gas is then converted into stars with an efficiency of 2% per free-fall time. These stars have a mass of $130 M_\odot$. We then model stellar feedback coming from these new-formed stars with 3 processes: photo-ionization which creates H_{II} regions, radiative pressure (Renaud et al. 2013) and type II supernova (SN) (Dubois and Teyssier 2008). In more details, the radius of the H_{II} region is

$$r_{\text{HII}} = \left(\frac{3}{4\pi} \frac{L_*}{n_e^2 \alpha_r} \right)^{1/3} \quad (4.1)$$

where L_* is the luminosity of the central stellar source, n_e and α_r the density of electrons and the recombination rate respectively. Within each of these bubbles, we uniformly set the gas at a temperature of $4 \times 10^4 \text{K}$, i.e. significantly higher than the surrounding warm ISM. Although this temperature is a few times higher than the typical observed value (e.g. Lopez et al. 2011), we have checked that this difference does not affect our conclusions. The ionization of the ISM is done as followed: to speed-up the computation, one out of every ten stars radiates and ionizes the surrounding ISM with an energy ten times higher than a single source. Considering that star formation occurs in dense gas regions in a clustered way, this assures that all of these regions contain at least one bubble. Namely,

the luminosity follows:

$$L_* = L_0 M_* \eta_{\text{OB}} \begin{cases} 1 & \text{for } t_{\text{ff}} < a_* \leq 4 \text{ Myr.} \\ (4\text{Myr})/a_* & \text{for } 4 \text{ Myr} < a_* < 10 \text{ Myr.} \\ 0 & \text{else.} \end{cases} \quad (4.2)$$

where $L_0 = 6.3 \times 10^{46} \text{ s}^{-1} M_{\odot}^{-1}$, M_* is the mass of the star that spawned, a_* is the age of the source, $\eta_{\text{OB}} = 0.2$ the stellar mass fraction which explodes into SN and t_{ff} is the local free-fall time. If two H_{II} regions overlap each other, the code ensures that the ionized volume is conserved and merges the two bubbles if the separation between the two is smaller than their radii. Finally, the momentum feedback which here is carried by H_{II} regions, is injected under the form of velocity kicks and is proportional to L_* (see Renaud et al. 2013 for details):

$$\Delta v = s \frac{L_* h \nu}{M_{\text{HII}} c} \Delta t \quad (4.3)$$

where h is the Planck constant, M_{HII} the gas mass of the bubble, c the speed of light and ν the frequency of the flux representative of the most energetic part of the spectrum of the source. We consider here the luminosity of the Lyman- α and set $\nu = 2.45 \times 10^{15} \text{ s}^{-1}$. s is a dimensionless parameter accounting for the multiple electron scattering through the bubble and the decay of energy between each collisions. We set $s = 2.5$ as in Renaud et al. (2013).

Our stars explode as SNe after 10 Myr. The SNe are modelled as Sedov blasts (see Dubois and Teyssier 2008). The initial radius of the ejecta is 10 pc. The total mass removed from each cells affected by the blast wave when the SN explodes is $M_*(1 + \eta_{\text{OB}} + \eta)$ where η is the mass-loading factor for the winds. The mass loading factor η sets the allocation of the momentum between its mass and velocity terms. SNe inject 10^{51} erg of energy in kinetic form and the energy released to the gas by the debris is $E_d = \eta_{\text{OB}} \frac{M_*}{M_{\text{SN}}} E_{\text{SN}}$ where M_{SN} and E_{SN} are respectively the typical progenitor mass and the energy of an exploding type II supernova (i.e. 10^{51} erg). The initial Sedov blast wave propagates at a velocity given by $u_{\text{Sedov}} = \frac{\sqrt{2}}{5} \left[f_{\text{ek}} \eta_{\text{OB}} \left(\frac{\delta x}{\Delta x} \right)^3 \frac{1}{1 + \eta_{\text{OB}} + \eta} \right]^{1/2} u_{\text{SN}}$ where $f_{\text{ek}} = 0.05$, δx^3 is the volume of the cell where the explosion occurs, Δx is the radius of the shock from the centre of the explosion and u_{SN} is the velocity corresponding to the kinetic energy of one SN explosion. The momentum of the blast wave is then added to that of the gas.

Finally, we use the friend-of-friend algorithm HOP (Eisenstein and Hut 1998) to detect star clusters. The density thresholds for detection are the same for all simulations and as in Guillard et al. (2016). Namely, a cluster is detected when the peak of the local stellar density exceeds $1.5 M_{\odot} \text{ pc}^{-3}$ with an outer boundary limit of $0.5 M_{\odot} \text{ pc}^{-3}$ to prevent the detection of stars in the field. Two clusters are then merged if the saddle density between them is higher than $1 M_{\odot} \text{ pc}^{-3}$.

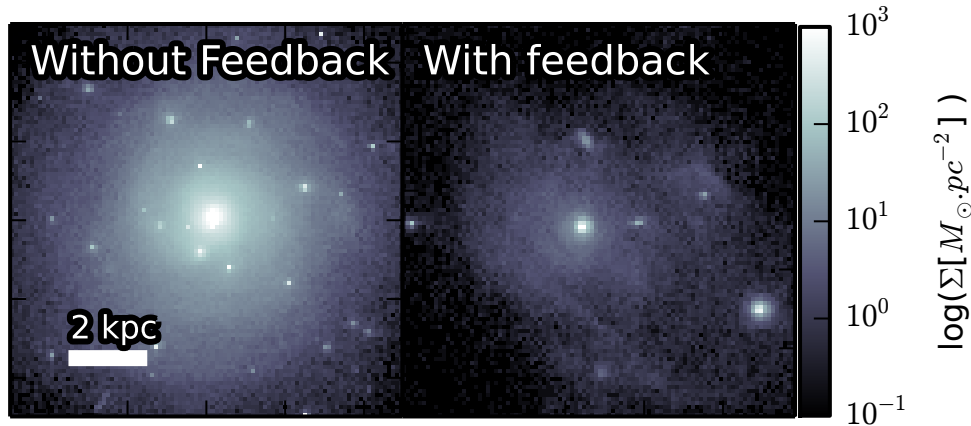


Figure 4.1: Face-on surface density of the stars formed during the simulations without (left) and with feedback (right). The displayed galaxies have evolved for 940 Myr. The star cluster population is different between the two cases: without feedback, a massive nucleus forms, surrounded by several tens of smaller and less dense clusters, while with feedback, only 5 clusters orbit around a nuclear cluster.

4.3 Stellar feedback and the star clusters population

In this Section, we examine how the star cluster populations are affected by feedback in our simulations. We thus present the results of test simulations for which part or all of the feedback modules are turned on or off.

4.3.1 The star clusters populations

We first choose to compare two sets of simulations: one from Guillard et al. (2016), which includes all mentioned feedback recipes (see Sect. 4.2), and another one with the same initial conditions but for which feedback is not active from the start.

Fig 4.1 illustrates the difference in the star cluster populations after 940 Myr of evolution in these two simulations. After nearly 1 Gyr of evolution, the star clusters population is already well established in both cases. At these times, the galaxies does not host dense gas clouds anymore, preventing the formation of additional star clusters.

The simulation without feedback exhibits 78 clusters at $t = 940$ Myr with a massive central cluster of $\sim 6 \times 10^8 M_{\odot}$, and has formed hundreds of them over that period. Most of these clusters ($\sim 90\%$) formed during the first 50 Myr after the trigger of star formation (at $t = 80$ Myr). This strongly contrasts with the outcome of the simulation when feedback is active: only 6 clusters including the nuclear cluster are observed at $t = 940$ Myr. The subsequent evolution during the next Gyr is also mild, with no drastic change in the cluster population: 2 clusters are destroyed by cluster-cluster interactions and the nuclear cluster experiences a merger at $t = 1.7$ Gyr (see Guillard et al. 2016 for details).

When feedback is active, we notice a lack of star clusters with mass lower than $10^5 M_{\odot}$

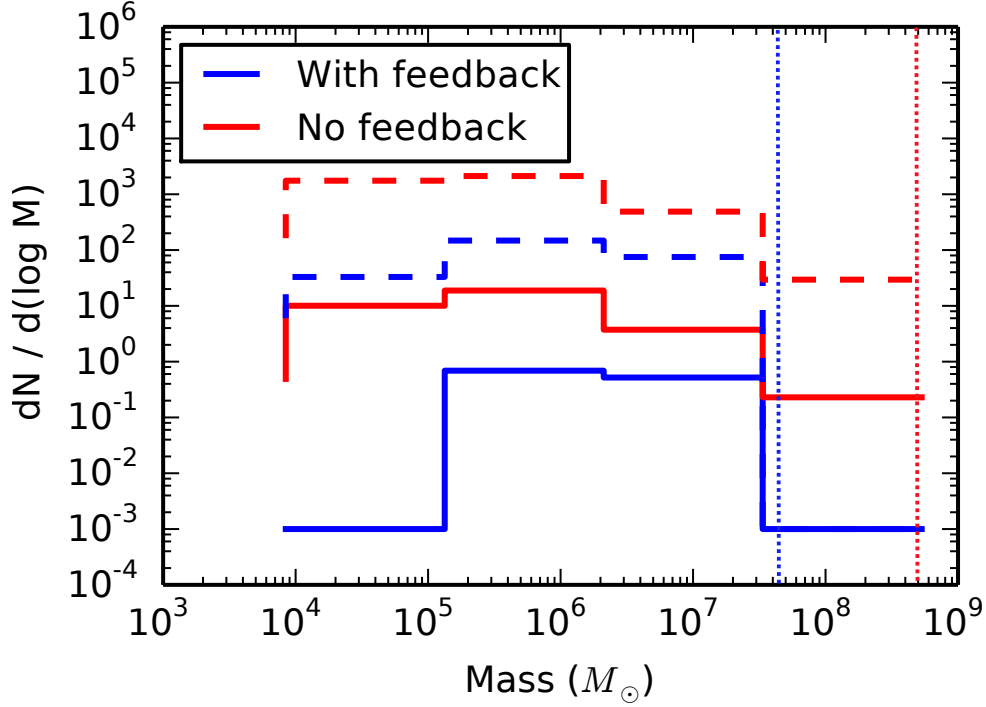


Figure 4.2: **Solid:** Cluster Mass Function (CMF) for the simulations with (blue) and without (red) feedback at $t = 940$ Myr. The dotted lines mark the mass of the nuclei in both simulations. We note that these distributions suffer from low-number statistics. **Dashed:** CMF stacked over 940 Myr i.e. for each output between $t = 0$ and $t = 940$ Myr (with an average frequency of 1 output every 5 Myr), we calculated the CMF and summed them over that period. They break at $10^4 M_{\odot}$ due to the lower limits of the density detection thresholds. We see that at $t = 940$ Myr, clusters with mass below $10^5 M_{\odot}$ are not observed when feedback is active. Stacked CMF shows that such clusters population existed during the evolution but was either destroyed or grew into more massive clusters.

at $t = 940$ Myr (see Fig 4.2): such lower mass clusters are detected at some point (see the stacked distribution of Fig 4.2) but either get systematically destroyed by cluster-cluster interactions or merged into more massive clusters, leaving that lower mass bin empty at $t = 940$ Myr. It is also worth noting the existence of a population of young stars accumulated in various regions of the disc, but these associations (with stellar densities below our detection threshold) are dispersed by stellar feedback and local variations in the local gravitational potential. This contrasts with the simulation without feedback which contains a few tens of such lower mass star clusters. Those clusters are located in the outer regions of the disc and do not interact with one another. This allows the lower mass-end clusters to survive for more than 2.5 Gyr.

The nucleus in the no-feedback run is also 10 times more massive ($5 \times 10^8 M_{\odot}$) than that of the reference simulation ($\sim 5 \times 10^7 M_{\odot}$). This is a direct consequence of both a higher merger rate in the former case (11 mergers for the no-feedback case) and a higher in situ star formation rate due to the absence of feedback. These mergers supply the nucleus with stars but also in gas which is brought together with the incoming clusters. Such events occur only twice in the reference simulation because of the limited number of clusters formed. Other surviving clusters of that simulation are gas-free within 10-20 Myr and do not evolve in mass afterwards.

4.3.2 The effect on dense gas

The different formation rate of the clusters between the two cases (15 clusters in 940 Myr with feedback and 320 without feedback) can be interpreted as a direct consequence of the effect of feedback on the availability of dense gas throughout the disc. Fig. 4.3 displays the evolution of the Probability Distribution Function (PDF) of the gas density at different times of the life of the two simulated low mass galaxies.

When feedback is on, the PDF has a log-normal shape for gas densities below 100 cm^{-3} with a peak at $\rho = 1 \text{ cm}^{-3}$. For higher densities, the shape of the PDF is a power law with a possible mass excess above $3 \times 10^3 \text{ cm}^{-3}$ (e.g., at $t = 300$ Myr) corresponding to the central regions of the gas reservoir of the most massive clusters. Such a power-law tail has been interpreted as the convolution of the classical log-normal shape from the turbulent gas with that of the self-gravitating gas clouds (Audit and Hennebelle 2010; Renaud et al. 2013). As time goes, dense gas is consumed to form stars while part of the lower dense gas cools down and evolves towards higher density, lowering the relative weight of the log-normal part of the PDF. At $t = 940$ Myr, the nuclear cluster has formed and the power-law seen in Fig. 4.3 is associated with its self-gravitating gas reservoir. The excess of mass in the highest density disappears due to the central star formation which consumes dense gas and the following gas dispersion induced by stellar feedback.

The major difference between the simulations with and without feedback occurs around the SF threshold at 100 cm^{-3} . When there is no feedback, a sharp transition is observed at this density, with a lack of gas at low density and an accumulation of gas with density between 100 cm^{-3} and 300 cm^{-3} . When compared with the simulation with feedback which displays a smoother transition at 100 cm^{-3} , this confirms that feedback redistributes dense

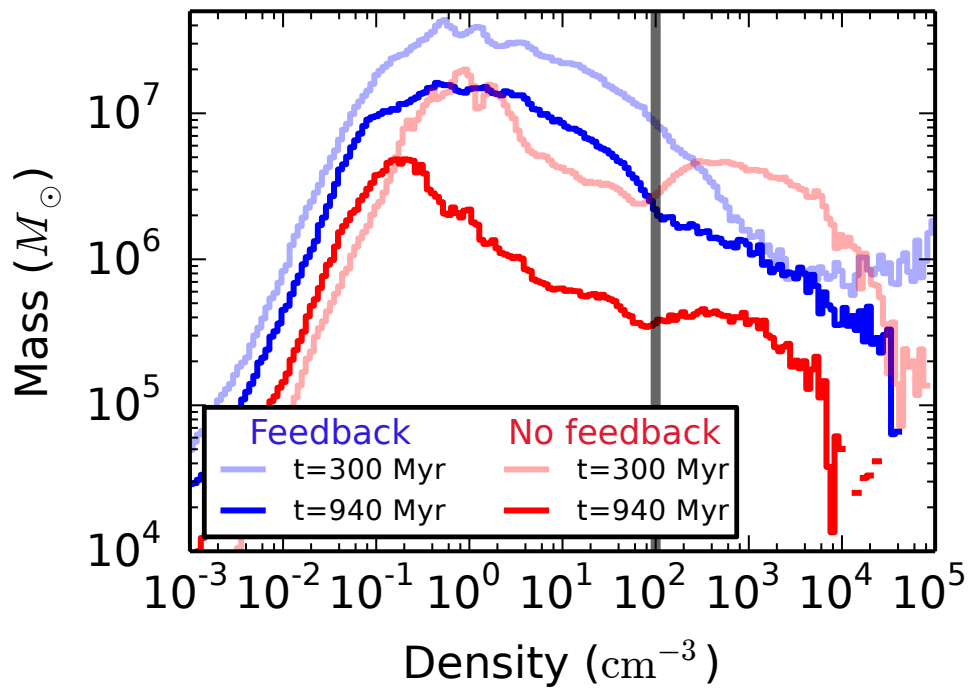


Figure 4.3: PDF of the gas density for simulations with (blue) and without feedback (red) within the galaxy at various times (showed in the legend). The vertical line marks the star formation threshold. At $t = 940 \text{ Myr}$, less gas is detected in the simulation without feedback than when it is on. This is due to a higher star formation rate (above $1 M_{\odot} \text{ yr}^{-1}$)

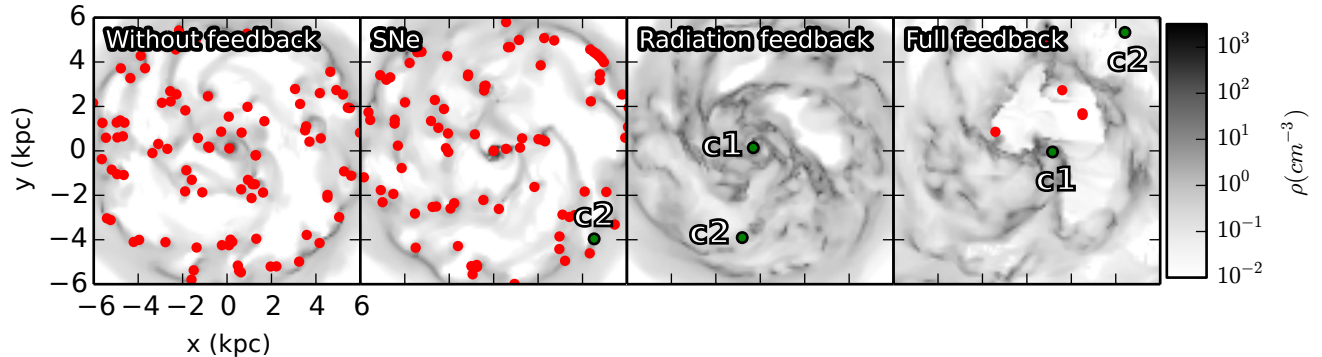


Figure 4.4: Face-on density maps of the gas at $t = 600$ Myr for simulations using different setups for stellar feedback: without feedback (left), SNe only (middle-left), H_{II} regions + radiative pressure (middle-right) and SNe + H_{II} regions + radiative pressure (right). The cases with full feedback and without feedback are the same as the ones discussed in the previous sections. The densities are averaged on 1 kpc along the line of sight. The initial conditions are the same for all simulations. Red circles show the position of star clusters. Green circles are the clusters which early evolution will be studied in Fig. 4.5 and Section 4.3.4. Clusters labeled as C1 keep their gas reservoir whereas clusters labeled as C2 expel their gas during the first 10 Myr after its formation. Star cluster populations in the no-feedback and SNe-only cases are similar in terms of number and individual mass. When radiative feedback is on, the ISM becomes less clumpy and the formation of clusters is reduced. The heating from H_{II} regions and radiative pressure redistribute the gas towards lower densities and slow down the formation of massive clumps from which star clusters could emerge.

gas towards lower densities (see e.g. Grisdale et al. (2017) and references therein). This redistribution thus leads to a relative lack of dense gas which can be used to form stars in general, and star clusters in particular. Overall, the gas redistribution induced by the stellar-driven feedback towards low densities is responsible for the smaller number of clusters. This redistribution of dense gas is also responsible for the non-growth mass of our clusters in our simulation with feedback, with the exception of 2 clusters which manage to keep their reservoir (see next Sections). It is also important to note that the absence of stellar feedback does not inhibit the accumulation of dense gas in the disc, since only thermal pressure can oppose the collapse of the clouds. In the next Section, we focus on the processes involved in this redistribution and how they affect the growth of star clusters.

4.3.3 Radiative versus Supernova feedback

In the previous Sections, we saw that adding stellar-driven feedback changes, as expected, the properties of the ISM and, consequently, that of the star clusters population. In this

section, we further investigate how individual feedback processes impact the growth of star clusters.

We address this question by running two additional simulations for which we single out SNe feedback, on one hand, and radiative feedback (H_{II} regions + radiative pressure), on the other hand. We start with an actual population of star clusters, hence following the mass distribution properties illustrated in Fig 4.2, and then focus on the subsequent evolution depending on the implemented feedback schemes. Fig. 4.4 illustrates the long-term impact of these recipes by showing the face-on density maps of the gas with the position of all star clusters detected at $t = 600$ Myr (about 500 Myr after the trigger of star formation).

Adding only feedback from SNe does not seem to significantly alter the morphology of the ISM on large scales, or the cluster population, compared with the no-feedback simulation. The energy coming from SNe locally increases the temperature of the surrounding gas. Here, SNe are located in dense gaseous regions. Without any mechanisms (e.g. ionization) to disperse such dense gas before the SNe explosions, one could expect the impact of SNe to be less effective on the local environment (e.g. Agertz et al. 2013). Hence, this gas (located in dense regions) manages to cool down on very short time-scales (~ 1 Myr) leaving most of the dense gas clouds intact. As a result, the seeds for star clusters are not heavily affected by SNe and their populations are similar in both cases (with or without SNe feedback) in terms of mass and numbers. This result was also observed at sub-parsec scales by Rey-Raposo et al. (2017), who showed that SNe locally heats the gas, which cools down very rapidly, causing less impact to clouds than stellar winds. We check that the properties of the ISM are not affected by the mass loading factor of the winds (i.e. the amount of gas carried in SNe debris). Using a mass loading of unity, thus affecting a higher gas mass but with smaller velocities, we observe no major differences for the PDF of the gas density or the cluster population in terms of number, size and mass. This suggests that the SNe are not the main actors altering the gas content of cluster-forming regions. We will discuss in Section 3.4 the impact of the numerical resolution and implementation on this result (see also e.g. Smith et al. 2017).

Major differences arise when radiative feedback is activated: the ISM is less clumpy and more turbulent than in the no-feedback or SNe-feedback cases, with more gas at densities between 1 cm^{-3} and 100 cm^{-3} (of the order of $5 \times 10^8 M_{\odot}$ at $t = 600$ Myr over the entire galaxy). This suggests that the redistribution of the gas towards lower densities (see Section 4.3.2) is mainly driven by the radiation from H_{II} regions. Hence, this leaves less dense gas over which massive star clusters can form which in turn leads to a lower massive star cluster formation rate: we form only tens of clusters over 500 Myr (a few clusters are observed at $t = 600$ Myr), as compared again to the hundreds in the simulations without feedback or with SNe only within the same time range. Similar observations can be made with the simulation using all feedback recipes.

4.3.4 The ability of clusters to grow

Radiative feedback also affects the growth in mass of star clusters. There are two ways a cluster can gain mass: using a local gas reservoir to convert dense gas into stars or through mergers with other clusters. Since the number of mergers is rather low in simulations using radiative feedback, we focus now on the growth by gas supply. Such process of gas re-accretion occurs in two clusters in our simulations using radiative feedback with the remaining clusters losing this reservoir a few Myr after their formation. Their ability to retain and accrete more of their gas depends on the balance between the gravitational potential of the cluster (i.e. its stellar and gaseous components) and the energy of the gas (internal and injected by feedback). Assuming systems in isolation, this balance can be estimated by comparing the total gravitational potential energy of the cluster with the internal energy (which we define here as the sum of the kinetic and thermal energy) of the gas, at a given time (thus ignoring the contribution from e.g., tidal fields).

We selected a few clusters from the simulations with full, radiative (H_{II} +radiative pressure), and SNe feedback, respectively. In the former two, we have chosen one cluster which manages to retain its gas for more than 20 Myr (respectively labeled as cluster Full-C1 and Rad-C1, also marked in Fig. 4.4), and one which expels its gas (resp. labeled as Full-C2 and Rad-C2). The C1-clusters are the NC progenitors. The C2 clusters have an initial (i.e. at the time of their first detection) stellar mass density of the order of $4 M_{\odot} \cdot \text{pc}^{-3}$ within the inner 25 pc radius, with a slightly higher density for the cluster Full-C2 of $10 M_{\odot} \cdot \text{pc}^{-3}$, due to an initially more massive dense gas component in this region. In the simulation with SNe only, we do not observe clusters which expel their gas after their formation. We thus only chose a cluster (SNe-C2) with similar initial stellar density than the other C1 and C2 clusters. All these clusters are shown in green in Fig. 4.4.

We follow all these clusters over their first 50 Myr. We also limit our estimations of the energies to the inner 25 pc around the cluster and systematically check that only one stellar dense structure is included. We then measure and plot the ratio of the internal energy of the gas to the total gravitational potential energy of the clusters, alongside their stellar and gaseous mass, which we present in Fig. 4.5. The energies are computed using the mass, velocities associated with the gaseous cells and stellar particles. The kinetic and thermal energies we calculate are defined respectively as $E_{\text{kin}} = 0.5 \sum_i m_i v_i^2$ and $E_{\text{therm}} = \frac{1}{M_{\text{tot}}} \sum_i 3/2 k_B m_i T_i$ where m_i is the mass of the gas cell i -th, v_i its velocity minus the average velocity of the field, k_B is the Boltzmann constant, T_i its temperature and M_{tot} the sum of all m_i . The gravitational energy is computed from the gravitational acceleration of the stars and the gas.

In the SNe-feedback simulation, the energy from SNe is immediately dissipated and the gravitational energy dominates (the energy ratio is always lower than unity). Thus, the gas is being retained within the close environment of the cluster, which can then slowly grow its stellar mass. Finally, we note that the gas mass within 25 pc is almost a constant, showing that the consumption of gas by star formation is balanced by the accretion of gas.

When including the radiation feedback, the C1 clusters retain their gas in both Radiative-only and full feedback cases, despite a bumpier evolution of its total (i.e. stars + gas)

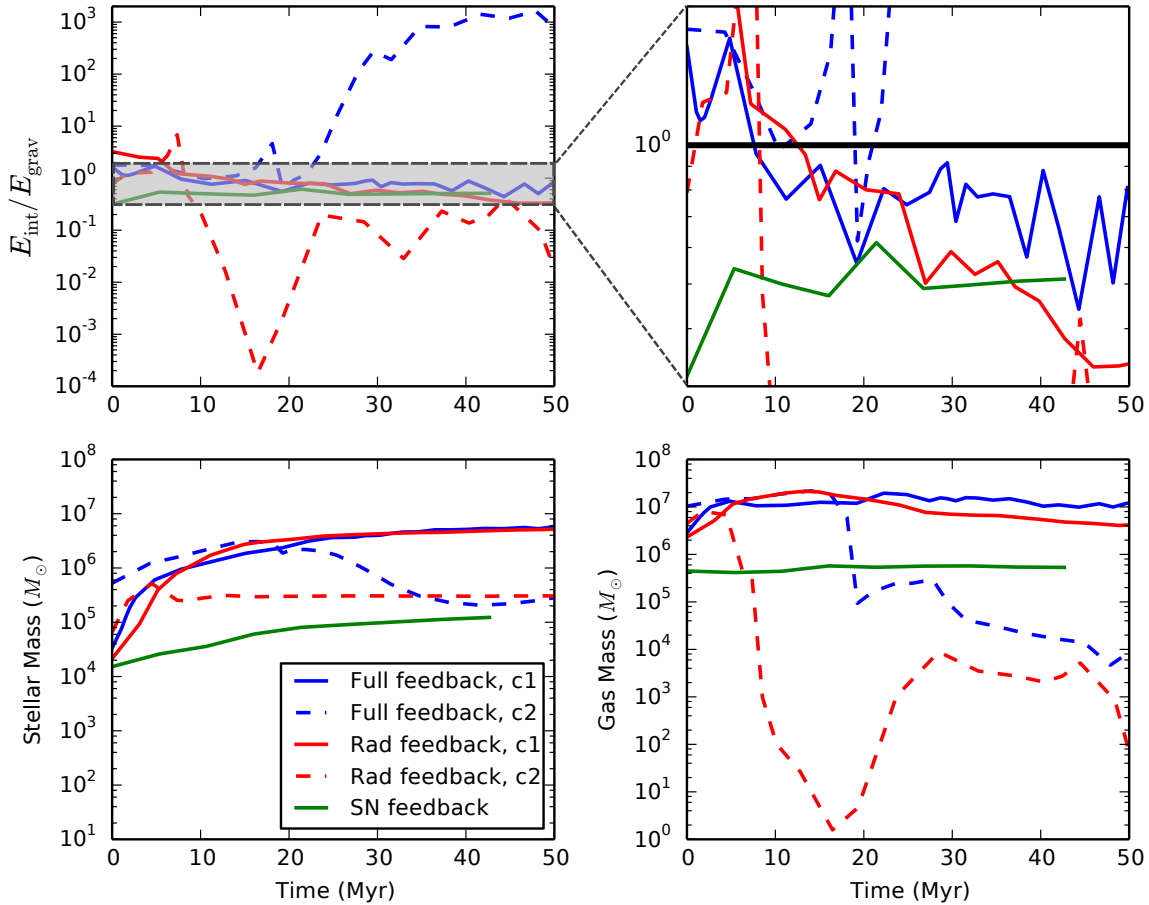


Figure 4.5: **Top**: Evolution of the ratio of the internal energy of the gas with the gravitational energy of the cluster taken in the 25 pc vicinity of the cluster (the grey area is zoomed in the top-right panel around the unity value for clarity). The time is relative, with $t = 0$ being the time of first detection. The different colours represent different simulations. The simulation using only radiative feedback is labeled here as Rad feedback. For the simulations with full and radiative feedback, solid lines display clusters (labeled as C1) which keep their gas reservoir, while dashed lines show clusters (labeled as C2) which expel it. **Bottom left**: Evolution of the stellar mass of the clusters during their first 50 Myr. **Bottom right**: Evolution of the mass of the gas reservoir.

energy. During their first 15 Myr, thermal energy associated with H_{II} regions is deposited into the ISM. Coupled with the mass of the cluster which is lower than that of the gas by at least one order of magnitude, internal energy dominates the potential with an energy ratio higher than 1. This ratio then slowly decreases in time, reflecting both the steady growth in stellar mass, and the build-up of a massive gas reservoir (the variations of the internal energy are less important than those of the gravitational energy by a factor of 2). The next 35 Myr sees the gravitational energy dominating over the internal energy of the gas, reaching a balance similar to that observed in the SNe-only case.

The evolution of the total energy of the C2 clusters is clearly different and partly linked with their gas environments. After respectively ~ 5 and ~ 20 Myr, both the stellar and gas masses of C2 clusters suddenly drop, the latter by several orders of magnitude. This follows the formation of a bubble around the cluster which heats up the gas. During these few Myr, the cluster enters a depleted region of (dense) gas in the disc, reducing the chances for the cluster to accrete more material. This actually leads to a simultaneous decrease of the internal energy of the gas and of the gravitational energy. The relative decrease between these two components determines the outcome energy ratio. For Full-C2, the mass of the gas reservoir significantly decreases after about 18 Myr as the cluster bathes in a hot 5×10^4 K ISM. This hot gas is not dense enough to be gravitationally bound to the cluster and the thermal energy dominates, leading to a significant increase of the energy ratio. For HII-C2, as thermal energy from H_{II} bubbles is deposited into the ISM, the cluster enters a low density gaseous region of the disc. The gas escapes from the cluster gravitation and the energy ratio dramatically decreases. In both cases, the **C2** clusters are almost cleared of their gas reservoirs in a few tens of Myr, and these are not replenished via accretion from the local environment. Note that the decrease of the gravitational energy of these C2 clusters also allows the stars with the highest kinetic velocity to escape.

Similarly to the SNe-only case, we test if the mass loading factor from SNe, now coupled with radiative feedback, affects the early evolution of the mass of star clusters. We thus conduct another simulation with all feedback recipes active and set $\eta = 1$. In such conditions, at $t = 600$ Myr, two clusters of $\sim 4 \times 10^5 M_{\odot}$ without gas reservoirs are detected. We also note that no nucleus forms by that time, in contrast with the reference simulation. The early evolution of the gas reservoir of the two detected clusters is shown in Fig. 4.6 and compared with the clusters C1 and C2 of the reference simulation. When the mass loading factor is 1, the early evolution of both gas reservoirs of star clusters is similar to the cluster C2 but anticipated by 5 or 10 Myr. We note that the first gas-clearing episode (occurring 10 and 21 Myr after the cluster formation) seems to be more efficient than in the reference simulation by an order of magnitude in mass. An intuitive explanation for this is that a low mass loading factor brings a larger volume of gas towards lower densities, which then facilitates the dissipation of the gas reservoir by radiative feedback. This shows the impact of non-linear coupling of different feedback processes (e.g. the radiative feedback and the SNe with the mass loading of the winds) on gas reservoirs and their potential ability to prevent the growth of massive clusters and NC progenitors. We finally note that, past the first depletion of the reservoir, some amount of gas is brought into the clusters (e.g. small increases of the mass reservoir at $t=10$ and 29 Myr for the red-dashed cluster). Since

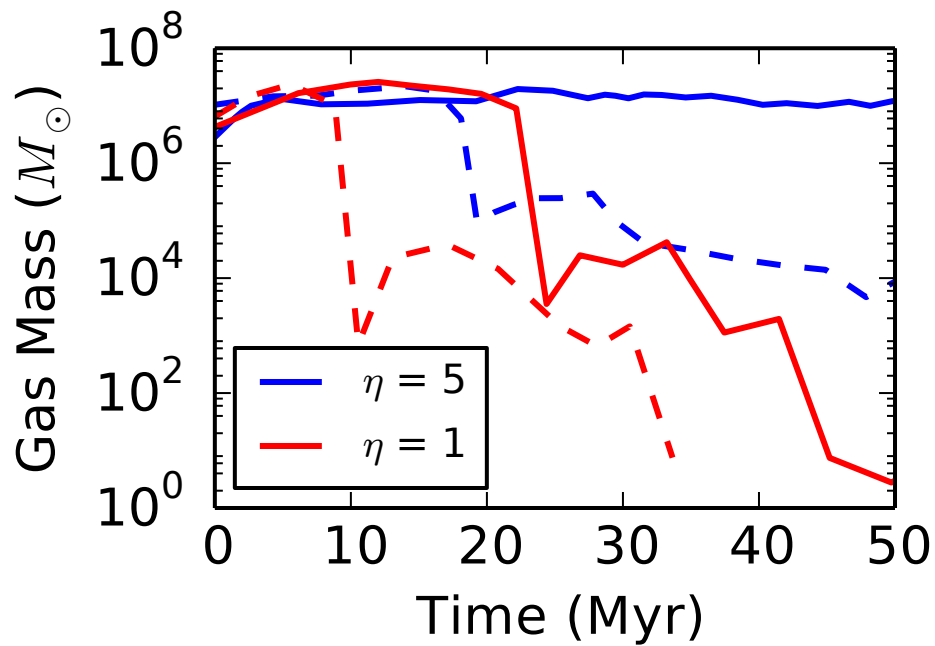


Figure 4.6: Early evolution of the mass of gas reservoirs in star clusters in simulations using a mass loading factor η of 5 and 1 (blue and red respectively). In the latter case, the chosen star clusters have survived up to $t=600$ Myr and lost their reservoir. Time is relative, with $t=0$ Myr being the time of formation. Each line style shows a different star cluster.

the mass loading factor also changes the velocity of the gas carried in the debris, some gas is able to come back onto the cluster. However, this gas is not dense enough to form new stars, and the stellar mass of the cluster does not change drastically after the first expulsion.

Overall, the evolution of star clusters is determined by a fragile balance between their own gravity and the physical properties of their gas. SNe seem to play a role only if they are coupled with radiative feedback. The gas density and temperature of the environment in which clusters evolve are major factors that can change the outcome of the gas reservoir. Massive star clusters are likely to grow if their density allows them to keep dense gas bound to them and if they continuously evolve in a dense gas environment during their first tens of Myr.

4.4 Discussion & Conclusion

Using hydrodynamical simulations of isolated gas-rich galaxies with different radiation feedback setups, we find that :

- SNe alone are (mostly) inefficient at affecting the gas reservoir, thus the early growth of star clusters. Feedback associated with H_{II} regions and radiative pressure seem to have a more significant impact, and are thus important components in the early life stages of star clusters.
- When radiation feedback is included, the growth of stellar clusters via gas accretion depends on the ability of the cluster to retain and/or replenish its gas reservoir. That ability is closely tied to the local environment of the cluster goes through during the first tens of Myr, and the corresponding availability of dense gas around the cluster as it orbits within the disc. This allows the simulation to develop two categories of star clusters in our simulations: those from which feedback expels the gas reservoir shortly after their formation, and those in a denser environment around which feedback fails at totally clearing the gas. We also note that low mass loading factors (i.e. 1 in our case) mass loadings for the SN blast coupled with radiative feedback can efficiently disperse dense gas, thus preventing the growth of star clusters.
- In HII or Full feedback simulations, we would expect only the massive end of the cluster distribution to survive (with the typical mass of a few 10⁵ to a few 10⁶ Myr in the present case) depending on the specific locations/trajectories of the clusters.

These conclusions are aligned with several studies. Based on timescale estimations, Krumholz and Matzner (2009) already argued that SNe should play a limited role as a source of feedback in star clusters since H_{II} regions inject their energy immediately after the star formation and do not have delays like SNe. In addition, results from Li et al. (2017) suggest that the impact of SNe is weaker in high-density environments which is where our clusters form (see their fig. 10). On galactic scales, Butler et al. (2017) showed that the combination of H₂ dissociation, photo-ionization from extreme ultraviolet photons

and SNe leads to different properties of the gas in terms of temperature and different spatial distribution of young stars compared to a case where only SNe are active. Our experiments point towards the same trends, emphasizing the paramount role of non-linear multi-component feedback, in particular in the formation of massive stellar objects.

The impact of feedback in numerical simulations obviously depends on the employed subgrid implementations of SNe and radiative feedback. Our work suggests that SNe alone are inefficient at disturbing the gas properties and the production of stars (see also Smith et al. 2017). Similar results have been observed when thermal feedback is used: it has been suggested that such inefficiency may be due to the fact that the SNe energy is distributed over too much mass, meaning that the temperature of the heated ISM around the SN is too low (Dalla Vecchia and Schaye 2008). A potential measure to stop the gas from over-cooling with only SNe would be to use a mechanical feedback like in Smith et al. (2017), as it injects momentum depending on the relevant scale of the SN remnant. In their work, Smith et al. (2017) showed this technique has the advantage to reach numerical convergence of the star formation rate even at resolution of 8.1 pc. Nonetheless, it is unclear how the non-linear coupling between this kind of feedback and radiation will affect the properties of the ISM and those of star clusters.

The implementation of the ingredients used for our radiative feedback also plays a role since the properties (size, mass, energy, etc) of H_{II} regions may vary, depending on the local conditions. In a gas-rich environment, such variations could directly impact the star cluster populations and its evolution. To illustrate this point, we can artificially increase the energy input for individual H_{II} regions while conserving the total injected energy (by lowering the number of H_{II} regions), the radial extent of the associated bubbles increasing accordingly (by a factor of about 10). Because the radius of the bubbles increases, we refer to this setting as clustered feedback.

Fig. 4.7 illustrates how such an imposed change in the energy injection scheme naturally perturbs the morphology of the galaxy by, ultimately, preventing the formation of a nucleus. Indeed, the local heating by larger H_{II} regions induces a decrease in the gas local density which alter its properties on a larger scale (i.e. kpc scales) and with it, the location and number of the forming star cluster sites. Larger gas-rich volumes are heated, and a larger fraction of dense gas is being shifted to lower densities, hence compromising the further growth of potential NC progenitors. Hence, calibrating the radiative feedback is of crucial importance if one wants to study the properties of gas in discs and the morphology of galaxies in general. Also, as the effect of radiative feedback depends on the gas density in the disc and thus on the spatial resolution, such calibration should be different between simulations of isolated discs and cosmological simulations.

Stellar feedback further encompasses several more coupled processes other than SNe or radiative feedback, some of which are not included in the present simulations (e.g., photoelectric heating, cosmic rays). Discussions on the relative effects of these feedback processes can be found (for dwarf galaxies) in e.g., Kim et al. (2013a,b); Hu et al. (2017); Forbes et al. (2016). Feedback from low and intermediate-mass stars could also impose a time delay of the star formation (Offner et al. 2009; Dale 2017), thus potentially lowering the number of clusters: such an effect has been ignored in our simulation as we do not

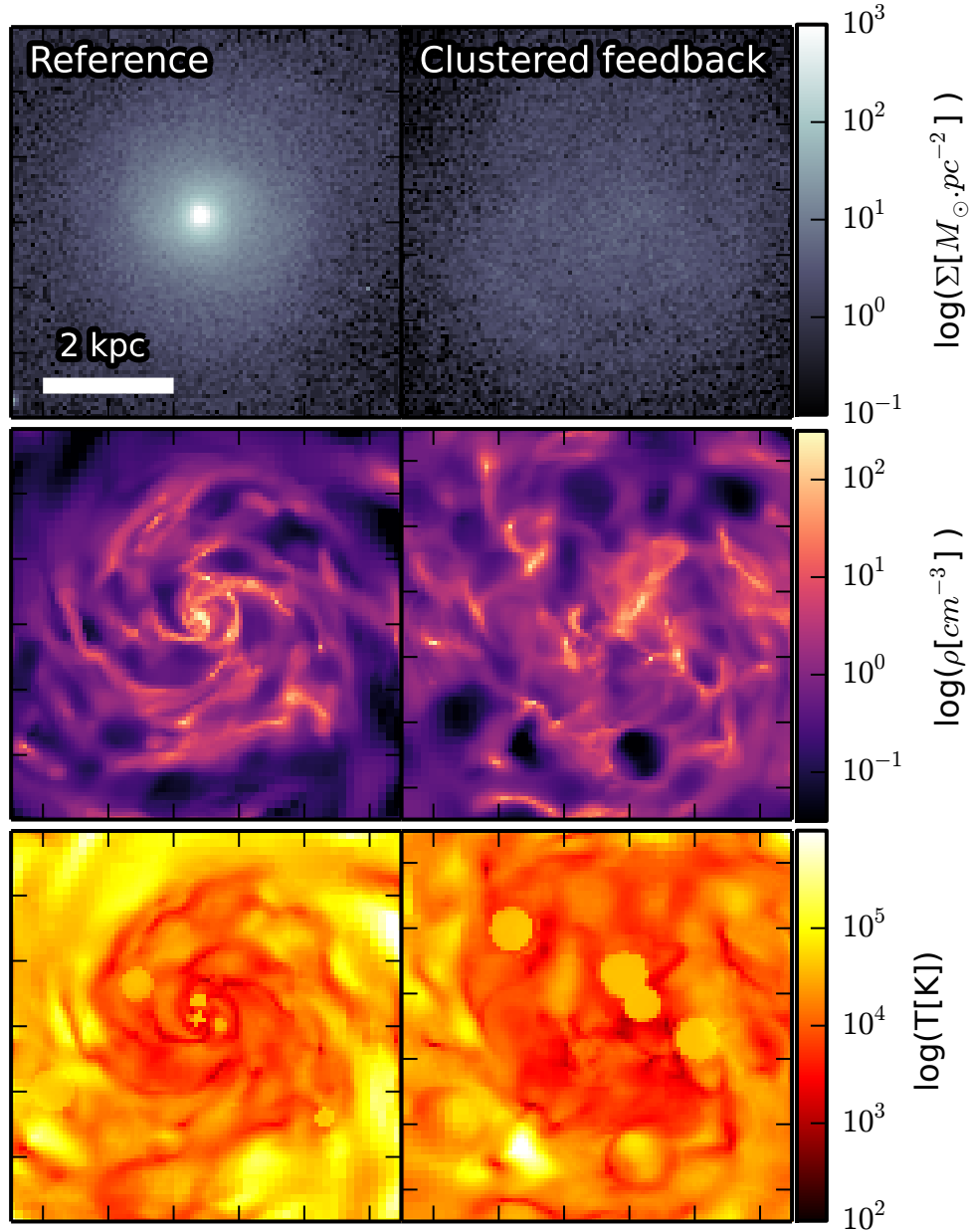


Figure 4.7: Stellar (**top**) and gas (**middle**) densities and gas temperature (**bottom**) maps using 2 different feedback setups at $t = 2.5$ Gyr. The left panels show our reference simulation. On the right panels, we generate 10 times fewer H_{II} regions but each of these are 10 times more energetic individually (to conserve the total energy injected into the ISM of the whole disc). This generates differences in the ISM and star clusters properties which modify in the end the morphology of our dwarf galaxy.

sample the initial mass function. Magnetic fields, which could suppress the expansion of H_{II} regions (Krumholz et al. 2007; Peters et al. 2011) are also not taken into account: their inclusion might enhance the ability for a cluster to grow since less volume would be heated by the bubbles. Finally, cosmic rays are currently thought to be generated by supernovae and massive stars winds which are conditions encountered in regions of massive star formation (VERITAS Collaboration et al. 2009; Bykov et al. 2017). The heating of the gas from cosmic rays might be an obstacle to a high-dense gas reservoir and thus to the growth of NC seeds.

In our simulations, these seeds all reach a mass of $\sim 10^6 M_{\odot}$ after a few Myr. High-resolution studies of individual Giant Molecular Clouds, such as Dale et al. (2012) showed that clusters above $\sim 10^6 M_{\odot}$ have a high enough escape velocity to prevent H_{II} regions to efficiently remove the gas from the clusters. This further illustrates the potential ability of the young massive clusters in general and NC progenitors in particular to retain their gas reservoirs in dense environments, like gas-rich galaxies and mergers. On the other hand, the lower mass clusters ($\lesssim 10^5 M_{\odot}$) are strongly impacted by ionizing feedback. We also note that the mass range and the parent GMC of our C2 clusters are in agreement with recent work from Howard et al. (2017) which studied the impact of the inclusion of radiation feedback on the efficiency of cluster formation, and established a relation between the maximum mass of a star cluster and the mass of the parent cloud ($M_{\text{cluster,max}} \propto M_{\text{cloud}}^{0.81}$).

Most of the clusters we have studied have densities of $\sim 10 M_{\odot} \text{pc}^{-3}$. Our spatial and mass resolution does not allow us to form low mass bound systems such as associations and open clusters. The typical stellar density for these objects goes from 0.01 to 1 Star.pc^{-3} for associations and open clusters, respectively. This would require sub-parsec resolution which is beyond the scope of this study. Lower mass clusters (e.g., $10^3 - 10^4 M_{\odot}$) are expected to be more vulnerable to feedback disturbances in a gas rich environment. Associations generally disperse over time-scales of 10 Myr and we would expect feedback to participate in the dissolution process.

Galactic and extragalactic environments are also likely to affect the properties of star clusters such as their mass or density. Open clusters are mostly observed in spiral arms (Dias et al. 2002) whereas more massive (forming) clusters are observed in e.g., starbursts and mergers (e.g., Portegies Zwart et al. 2010) or central regions (Böker et al. 2002)). For the specific cases of NCs, hosted at the centre of galactic discs, some studies (Emsellem et al. 2015; Torrey et al. 2016) suggest an interplay between star formation and feedback processes, leading to gas accretion-ejection cycles and possibly to complex integrated star formation histories (Feldmeier-Krause et al. 2015). In galaxy mergers such as the Antennae, young massive star clusters generate superbubbles of hundreds of parsecs (Camps-Fariña et al. 2017) in the nuclear regions which might take the least dense gas away and hence halt the star formation within these clusters.

Overall, this work emphasizes the importance of the calibration of feedback recipes, its impact on properties of the ISM and star clusters. We also underline the relevance of a more realistic galactic-scale environment (interactions, gas accretion) for the early formation and evolution of massive clusters. We will see in Chapter 5 that in the specific context of a cooling and collapsing gaseous halo, stellar feedback, and radiative feedback

in particular has similar if not more damaging effects on star clusters as the ones we have described in this chapter.

Chapter 5

Outlook: nuclear clusters and cosmological gas accretion

I have described in Chapter 3 how dwarf galaxies could be modeled with **RAMSES** using initial conditions of pre-existing stellar and gaseous discs. This setup is a useful trick that allows us to study a galactic system with predetermined properties and saves CPU time. Similarly, the dimensions of the box (< 100 kpc) compared with the maximal resolution we want to reach (\sim pc) make this experiment cheap in terms of computer time and allows us to focus only on secular processes. With this initial scheme (see Chapter 3 and 4), the initial shape and properties of the galaxy are fully controlled which makes comparisons or reproduction of other simulations easier. However, in such simulations, $\sim 84\%$ of the initial gas is consumed within the first 2.5 Gyr, most of the remaining gas being in the central region of the galaxy. Hence, on a timescale of a few Gyr, star formation rate reaches low values ($10^{-3} M_{\odot} \text{ yr}^{-1}$) with no further major secular events (e.g. star cluster formation or mergers). In reality, galaxies are not in isolation and thus experience processes such as interactions with other galaxies, ram pressure or gas accretion. As of now, a simulation encompassing cosmological and secular processes simultaneously at a parsec resolutions remains very challenging, especially at high redshift due to the large amount of dense gas available and the stellar driven feedback which both slow down the computation. In this chapter, I will describe how we can model the galaxy formation from the collapse of an initial rotating gas halo (Section 5.1). I will then study in Section 5.2 the formation and evolution of star clusters in this context and show that stellar feedback poses a serious challenge for their survivability. I will show in particular in Section 5.3 that radiative feedback is the main cause for clusters disruption and I will also examine in more depth the injection of energy from SNe and its consequence on star clusters.

5.1 Galaxy formation from halos

5.1.1 Modeling the halo collapse

One of the alternatives that would account for some cosmological mechanisms at a low cost is simulating a galaxy forming from the cooling of a hot gas halo, mimicking cosmological gas accretion. This prescription is based on the formation scenario of a thin-disc which was first described in Peebles (1969). In this model, a gas halo with a certain radial profile embedded in a dark matter halo (with a similar profile) gains a specific angular momentum similar to that of the dark matter (we show in Figure 5.1 the difference in the gas distribution between this approach and the one described in previous chapters). This gas radiates its energy through cooling processes and, following the standard picture of galaxy formation, forms a centrifugally supported disc in the center of the halo. This disc then gradually becomes larger from the inside-out as it accretes material from the outer region of the box. Due to the cooling and the increasing density of the gas, stars end up forming, creating a stellar disc.

This prescription requires 4 initial parameters for the halos from which we can compute the density profile and their rotational velocity: a virial velocity V_{vir} , a concentration parameter c (see below), the angular momentum and the gas mass fraction of the total system (gas;dark matter). The angular momentum given to the initial gaseous halo can be defined by a dimensionless spin parameter: $\lambda = j | E |^{1/2} G^{-1} M_v^{-5/2}$ (Bullock et al. 2001) where j is the specific angular momentum, E the energy of the halo, G the Newton gravitational constant and M_v the mass of the dark matter halo. Simulated cold dark matter halos showed that this spin has a typical value of $\lambda \sim 0.03$ with a range going from 0.01 and 0.1 (see e.g. Bullock et al. 2001; Macciò et al. 2007). For our simulations, we choose a spin parameter $\lambda = 0.04$ which is a typical value used for dwarf galaxies (e.g. Teyssier et al. 2013).

We choose a NFW profile (Navarro et al. 1996) for both the gas and dark matter initial halos. As a reminder, such profiles are given by:

$$\rho(r) = \frac{\rho_s}{r/r_s(1+r/r_s)^2} \quad (5.1)$$

where ρ_s is the characteristic density of the halo and r_s is its characteristic radius. Both of these quantities are determined from the concentration of the halo $c = r_{\text{vir}}/r_s$ and the virial velocity $V_{\text{vir}} = \sqrt{GM_{\text{vir}}/R_{\text{vir}}}$, given as fixed parameters at the beginning.

The rotational velocity of the gaseous halo is given by:

$$v_{\text{rot}} = \frac{j(r)}{r} \quad (5.2)$$

where $j(r)$ is the specific angular momentum given by:

$$j(r) = j_{\text{max}} \frac{M(< r)}{M_{\text{vir}}} \quad (5.3)$$

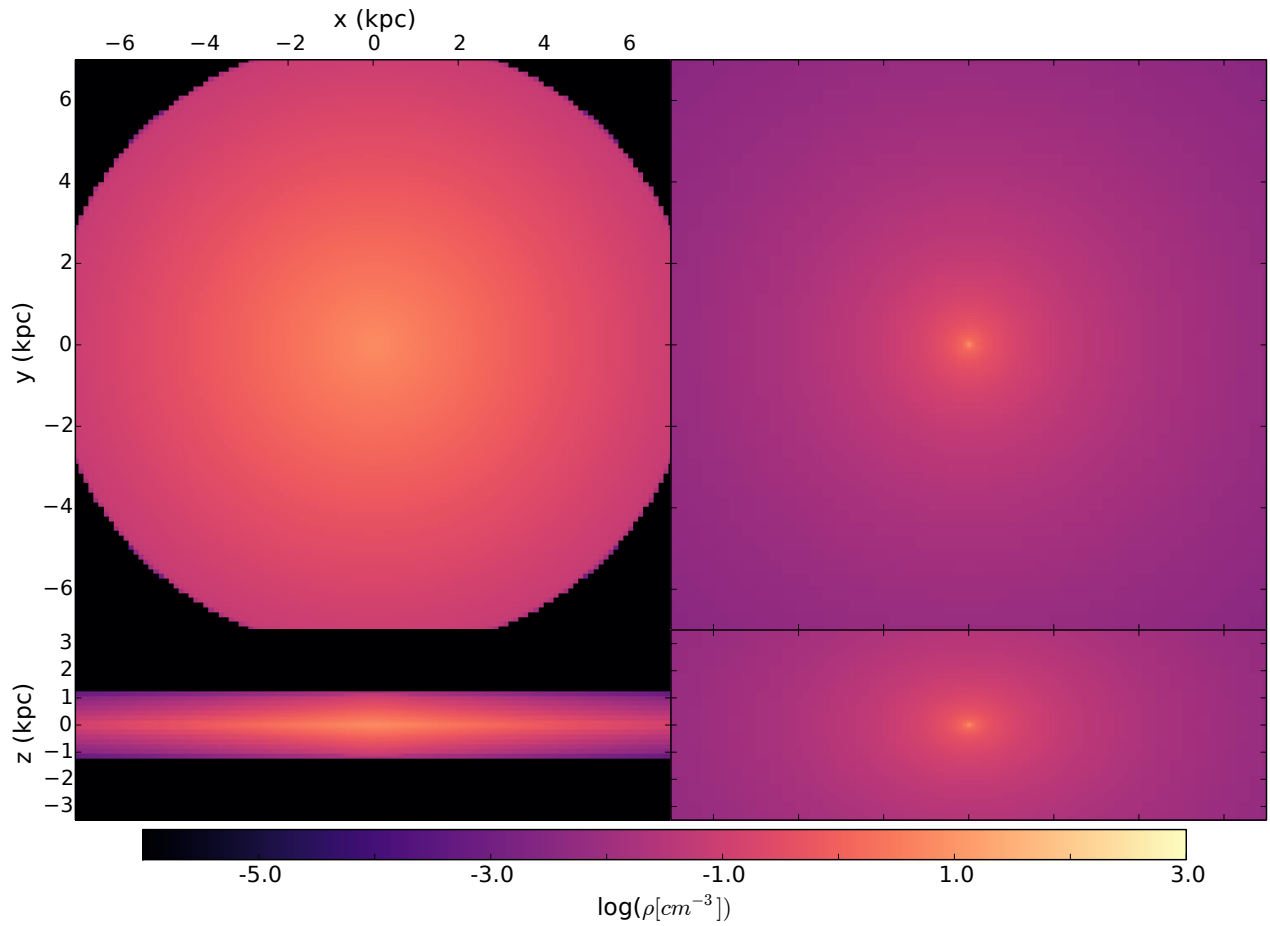


Figure 5.1: Initial conditions using pre-existing discs of gas and stars (left, only gas is shown) and a gaseous halo which cools down to form a disc later (right). Region in black on the left panels shows the hot ISM with densities lower than 10^{-6}cm^{-3} .

j_{max} can be calculated using the total angular momentum: $J = \int j(r)dM = 1/2j_{max}M_{vir}$ and the spin parameter λ . Using the virial theorem and using the relations between the virial mass and the virial velocity and the concentration c of the halo, the rotational velocity can be expressed as:

$$v_{rot} = 2\sqrt{\frac{2}{f_c}}\lambda V_{circ}c \frac{M(< r)}{M_{vir}} \frac{1}{r} f_c \quad (5.4)$$

where V_{circ} is the circular velocity at the virial radius and the variable f_c is given by:

$$f_c = c \frac{0.5 - \frac{0.5}{(1+c)^2} - \frac{\ln(1+c)}{1+c}}{(\ln(1+c) - \frac{c}{1+c})^2} \quad (5.5)$$

An additional exponential function f_{cut} is also included to prevent discontinuities issues at the borders of the simulated box.

The generation of the dark matter halo follows the same procedure as the one described in Chapter 3. Here, we give the dark matter a scaling radius of 59.5 kpc and a virial mass of $10^{10.5} M_\odot$. The total mass of dark matter is then used to compute the mass of the gaseous halo (using the gas mass fraction parameter). We use a gas fraction of 20% in the following example.

With this set of 4 initial parameters, it is possible to estimate a typical radius of the stellar disc that will form. Indeed, (Mo et al. 1998) showed that the scaling radius of the stellar disc roughly follows:

$$R_d = \lambda R_{halo} f(c, \lambda, m_d) \quad (5.6)$$

where R_{halo} is defined by the minimum between virial radius and cooling radius and $f(c, \lambda, m_d)$ is a function which depends on the initial halo concentration and the disc mass m_d (see Mo et al. 1998 for details). With the initial parameters we choose for the following simulations ($V_{vir} = 85 \text{ km.s}^{-1}$; $c = 16$; $\lambda = 0.04$; $f_{gas} = 0.20$) and our modeling of the dark matter halo, we aim at forming a stellar disc with a scaling radius of 1 kpc and a mass of $10^8 M_\odot$. The gas density threshold for star formation is 200 cm^{-3} .

In the next section, we describe the early evolution of the halo and the formation of the stellar disc and of the first star clusters, the latter being the focus of this work (see Chapter 3 and 4).

5.1.2 Early star formation

We take here the example of a halo with a virial mass of $10^{10.5} M_\odot$, a gas fraction of 20% and a spin of 0.04. The stellar disc does not form immediately after the beginning of the simulation, but is instead a step-by-step process. Indeed, the star formation rate in the simulated box does not monotonically increase but goes through several phases, as one can see in Figure 5.2. We see that the SFR increases after 20 Myr to reach a local maximum of $3.89 M_\odot \cdot \text{yr}^{-1}$ at $t=25$ Myr. Then, stars stop forming (at least to the same rate) for ~ 10 Myr. We notice during this short amount of time a local peak at $1 M_\odot \cdot \text{yr}^{-1}$. This corresponds to a small amount of stars forming at the center of the halo, where the gas

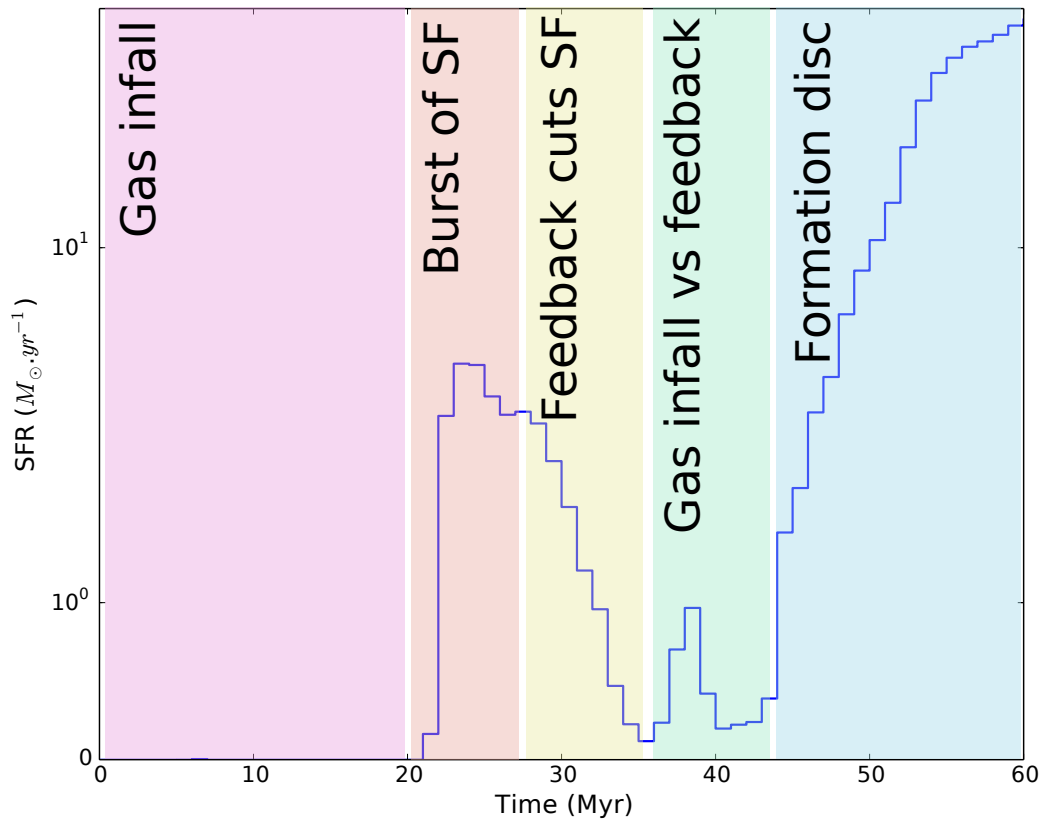


Figure 5.2: Early star formation rate. The early collapse of the gas leads to the formation of stars after 20 Myr. The resulting feedback disperses dense gas regions, interrupting star formation at $t = 35$ Myr. Due to the effects of gas infalling, stars manage to form again at $t = 43$ Myr and form the stellar disc.

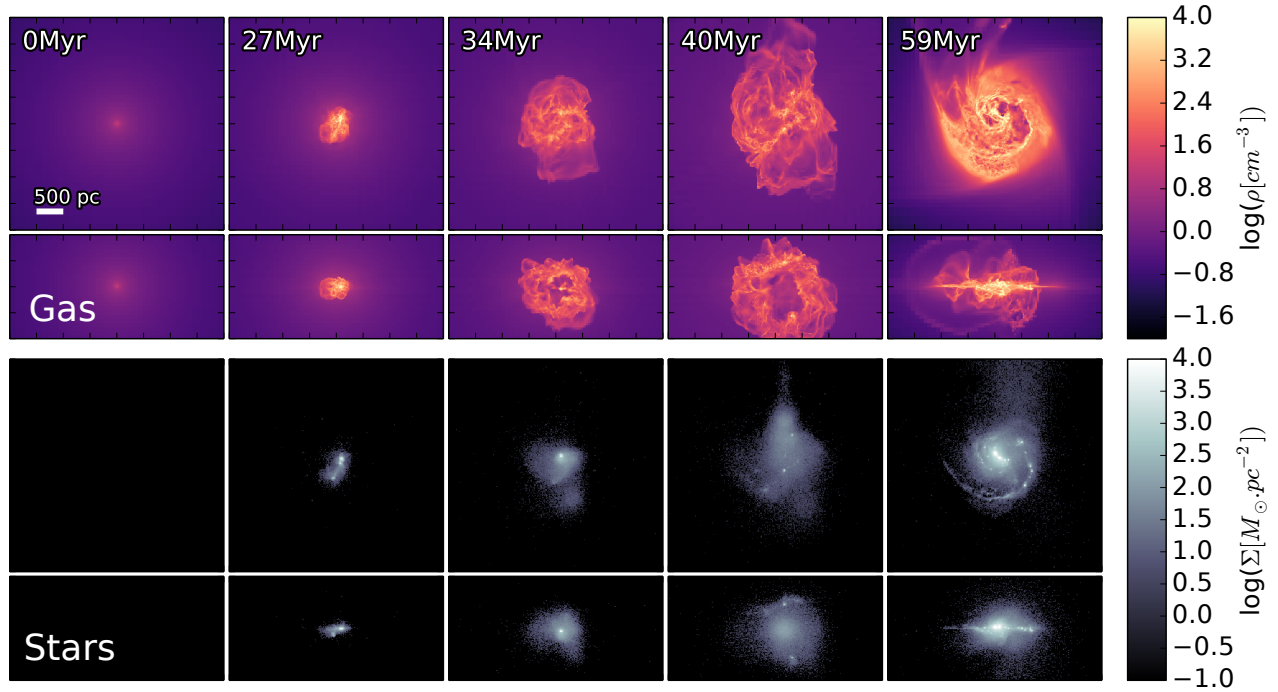


Figure 5.3: Face-on and edge-on density maps of the gas (*Top*) and stars (*Bottom*) during the first Myr of evolution, in a $4 \times 4 \times 2$ kpc region centered on the simulated box. The star formation history follows a four steps process: an accumulation of gas towards the potential well without star formation, bursting formation of the first generation of stars, cut of star formation from the resulting stellar feedback, re-activation of star formation.

had started to accumulate again. Finally, after $t = 44$ Myr, the SFR rises monotonically again to reach values of almost $20 M_{\odot} \text{ yr}^{-1}$. Overall, during the first tens of Myr, several processes are in action and can be decomposed in several steps, which are represented in the 5 panels of Figure 5.3:

- During the first 20 Myr, the gas moves towards the center of the gravitational potential. The progressive accumulation of gas near the potential well increases its density, although not at high enough levels to trigger star formation.
- After 20 Myr, the gas has reached high enough densities to collapse and form stars in an initial burst. This star formation episode is concentrated in the central region of the halo.
- This sudden star formation is followed by stellar feedback mechanisms which disperse the gas and almost completely shuts off the formation of new stars in this region.
- Gas from the outer regions of the halo keeps falling into the potential well as the feedback effects wear off due to the absence of significant star formation.

- Due to its infall, gas density starts to rise again in the central regions. The centrifugal force from the initial spin gives rise to a gaseous disc within which star formation takes place once the gaseous density is high enough.

Figure 5.3 also shows that star clusters form in the disc and, more interestingly near the center of the galaxy. These clusters have a mass of several $10^6 M_{\odot}$ and a typical size of tens of parsecs. This suggests that these clusters can be the progenitors of nuclear clusters. In the next section, I investigate if the above-described picture remains valid on longer timescales.

5.2 Radiation feedback: the challenge of forming star clusters populations

The example above showed us that star clusters may form in the early-stage of the galaxy formation. By using different sets of initial conditions, it should be possible to study and constrain the physical conditions of the formation of nuclear clusters in dwarf-like galaxies. As a starting point, we set up different virial masses for the dark matter halo of $10^{10.5}$ and $10^{11} M_{\odot}$ in order to get dwarf galaxies of approximately 10^8 and $10^9 M_{\odot}$ respectively. Obviously, the time needed for the galaxy to reach its aimed stellar mass will also depend on the gas fraction within the simulated box. We consider a gas fraction of 15% which is the typical value in the literature (e.g. Teyssier et al. 2013). We also use a gas fraction of 20% to more quickly reach the aimed galactic mass. In all simulations, the maximum resolution we can reach is set to 2.4 pc and the particle mass is around $220 M_{\odot}$. We run two simulations with a halo virial mass of $10^{10.5} M_{\odot}$ and a gas fraction of 15 and 20% (simulations *a* and *b*) and one simulation containing a halo with a virial mass of $10^{11} M_{\odot}$ and a gas fraction of 20% (simulation *c*)¹. Table 5.1 summarizes the parameters used for these simulations.

Figure 5.4 displays the face-on and edge-on stellar surface density of the galaxies after 600 Myr of evolution.

As one can see in Figure 5.4, after 600 Myr, our galaxies do not have a disc shape. Moreover, no star cluster populations can be observed in either galaxy. Yet, the example taken in Figure 5.3 shows the existence of such a cluster population. Hence, one or several processes destroyed or ejected those clusters out of the disc. In the following, we examine in more details the evolution of star clusters formed in simulation *c*. This simulation is the configuration closest to the isolated discs we have modeled in Chapter 3 and 4 in terms of aimed mass ($10^9 M_{\odot}$) and also is expected to be the most resilient to stellar feedback because of its higher mass.

Figure 5.5 shows the first 100 Myr of evolution of the stars in the simulation *c*. We can see that before $t = 60$ Myr, star clusters formed in the disc. These clusters have on average

¹The original intention was to explore a larger range of parameters in terms of halo mass and angular momentum. However, due to time constraints and supercomputer resources, we did not conduct these simulations.

Table 5.1: Initial conditions

Simulation name	a	b	c
Box length (kpc)		160	
AMR coarse level		8	
AMR finest level		16	
Highest resolution (pc)		2.4	
DM Halo			
Virial mass (M_{\odot})	$10^{10.5}$	$10^{10.5}$	10^{11}
Virial velocity (km/s)		85.	
Cut radius (kpc)		80	
Concentration		16	
Profile	Navarro-Frenk-White		
Number of particles (x 10^6)		5	
Softening (pc)		50	
Gas			
Spin		0.4	
Gas fraction (%)	15		20

a mass of a few $10^5 M_{\odot}$ (some clusters, less numerous, have a mass of $10^6 M_{\odot}$) while the disc has a mass of $1.3 \times 10^8 M_{\odot}$. The edge-on view indicates that ejecta of gas due to feedback are occurring in the disc. However, 10 Myr later, we clearly see that the stellar disc has expanded by 1 kpc in radius and from 100 to 600 pc along the axis perpendicular to the galactic plane. The gas follows the same expansion and exhibits gaps in the disc and massive ejecta in the vertical direction. After 80 Myr, the gaseous disc disappeared, leaving only residuals and gas streams coming from the external regions of the simulated box. The estimated inflow rate of these streams² is $\sim 3.5 M_{\odot} \cdot \text{yr}^{-1}$, which is relatively high for dwarf galaxies but of the same order as that observed in the dwarf spiral galaxy M33 ($2.9 M_{\odot} \cdot \text{yr}^{-1}$, see Zheng et al. 2017). The star clusters also vanished and the galaxy has further expanded by 500 pc.

The disruption of our star clusters is linked to the stellar feedback from both the clusters themselves and the diffuse stellar background. After 50 Myr, the formation of the disc and star clusters induces massive star formation (tens of $M_{\odot} \cdot \text{yr}^{-1}$). Consequently, stellar feedback from the diffuse new stars becomes effective during the next 10-20 Myr. SNe inject energy ($\sim 1.7 \times 10^{56}$ erg) into the gas and photo-ionization from the H_{II} heats up the temperature of the ISM to $4 \times 10^4 \text{K}$ all over the disc and at the same time. The combined actions of these processes dilate and push the gas away from the disc. Since the potential of the galaxy is still at that time dominated by gas, diffuse stars react to the changes in the galactic potential and follow the gas outwards, expanding the galaxy.

Due to their high-local density, the stellar core of the cluster is not at first heavily disturbed by the overall expansion of the gas. The latter still dominates the local potential

²We did not make any distinctions between cold and hot gas in this calculation.

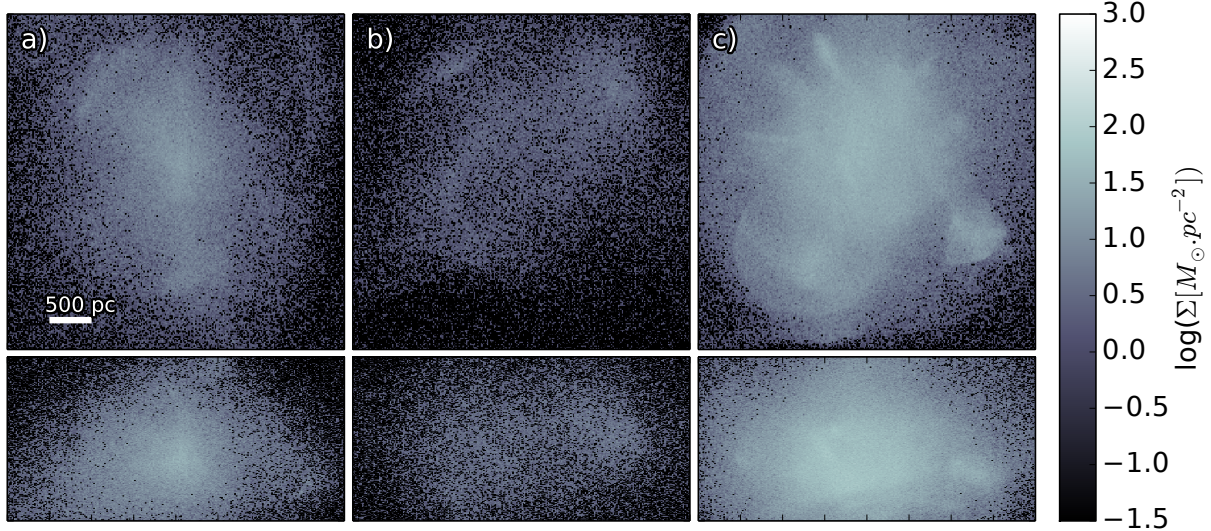


Figure 5.4: Stellar surface density maps for 3 simulations of forming dwarf galaxies centered on the global gravitational potential at $t = 600$ Myr. Face-on (**top**) and edge-on (**bottom**) views are displayed.

($\sim 10^7 M_{\odot}$ of gas against $2.1 \times 10^6 M_{\odot}$ of stars, so 83% of the local baryonic mass) and the clusters continue to form stars but the least bound stars leave the systems. During the next Myr, as the gas becomes hotter and more turbulent around the clusters and feedback from the newest stars tries to expel gas material away from the cluster, the density of gas within the clusters keeps decreasing and more and more stars become unbound. Once the gas density whose value depends on the location of the cluster and the gaseous density of its surroundings, is low enough, the cluster starts to expand until complete dissolution.

In summary, the destruction of the star clusters is due to the initial high star formation rate shaping the forming disc. The resulting stellar feedback expels the gas that composes the disc outwards, leading the expansion of the stellar disc. At the same time, stars are progressively unbound from the clusters by the expulsion of diffuse gas and the feedback within the cluster. In the next section, we investigate which component of our feedback model is responsible for the disruption of star clusters.

5.3 SNe feedback and star clusters

As we have seen in the previous section, stellar feedback destroys the star clusters within tens or hundreds of Myr. In order to better understand the relative contributions of the various feedback processes on star clusters in the context of halo cooling, we choose, like in Chapter 4 to activate only one process at a time. In this case, we choose to only use

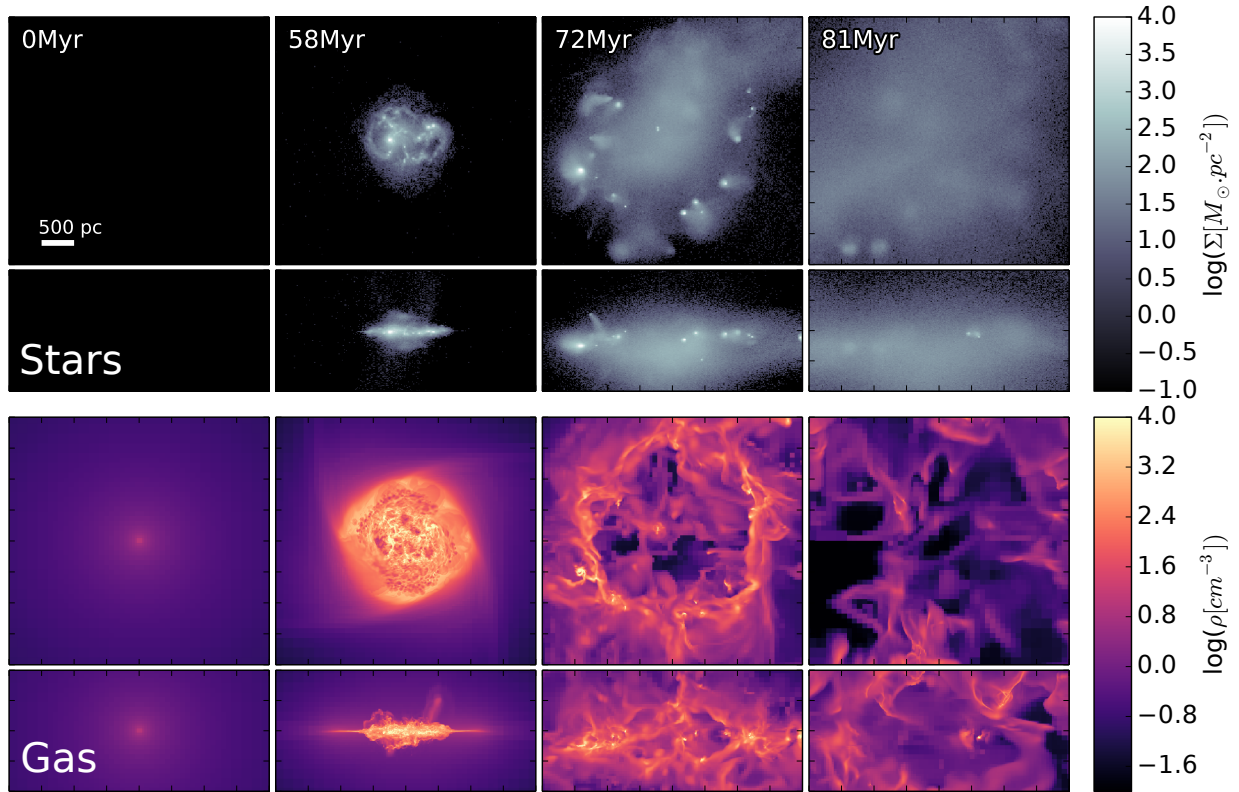


Figure 5.5: Stellar (**Top panels**) and gaseous (**Bottom panels**) density maps in simulation *c*. Face-on (respectively edge-on) are shown in each **Top** and **Bottom** panels.

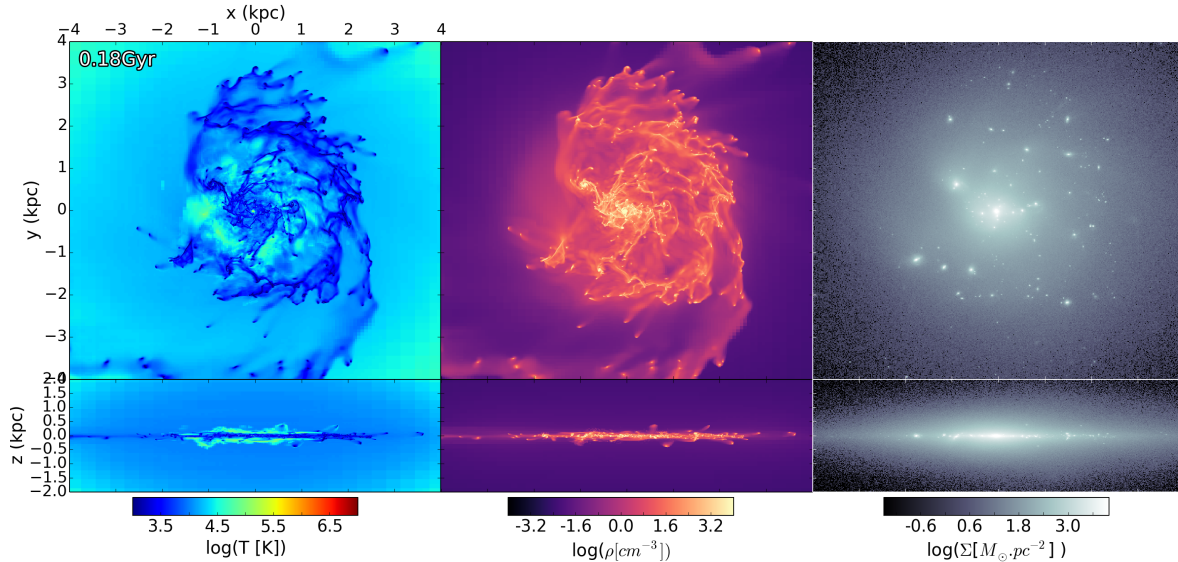


Figure 5.6: Temperature (*Left*) and density (*Middle*) maps for the gas and stellar surface density maps (*Right*) for simulations using kinetic feedback for supernovae, all with face-on (*Top*) and edge-on (*Bottom*) views. The snapshots were all taken at $t = 180$ Myr.

feedback coming from SNe and to investigate in more depth how star clusters are affected by the type (i.e. thermal or kinetic) of energy SNe inject.

5.3.1 Properties of the ISM

We simulate 2 halos forming galaxies using distinctively those two feedback injection models. For convenience, we will refer to these simulations as the kinetic and thermal simulation respectively. Maps of the temperature, gas density and stellar surface density at $t = 180$ Myr are shown in Figure 5.6 and Figure 5.7. We first notice that the gaseous and stellar discs are still in place after 180 Myr. The discs have formed during the first 50-60 Myr of evolution which corresponds to the monotonic increase of the star formation rate (see Figure 5.9 and text below). At $t = 180$ Myr, the galaxy discs have radii of 1 kpc and the stellar discs have a mass of $3.2 \times 10^9 M_{\odot}$ and $3.5 \times 10^9 M_{\odot}$ for the thermal and kinetic simulations respectively. This clearly indicates that radiative feedback plays a decisive role in star clusters dissolution. This result is in agreement with what we found in Chapter 4. If we compare the two simulations, a clear difference can be observed in the properties of the gaseous disc between the two cases. When we use a pure thermal feedback for SN, the gas is more turbulent than when pure kinetic feedback is used. The amount of hot gas (i.e. for temperature higher than 10^5 K) in the former case is of $7.2 \times 10^6 M_{\odot}$, compared to the $1.6 \times 10^6 M_{\odot}$ where kinetic feedback is used. This budget difference concerns gas with density lower than $\sim 3 \text{ cm}^{-3}$. The Probability Distribution Function (PDF) of the gas density also shows that at higher density, more gas is found in the case of an injection of kinetic feedback than a thermal one (see Figure 5.8). A divergence can be observed

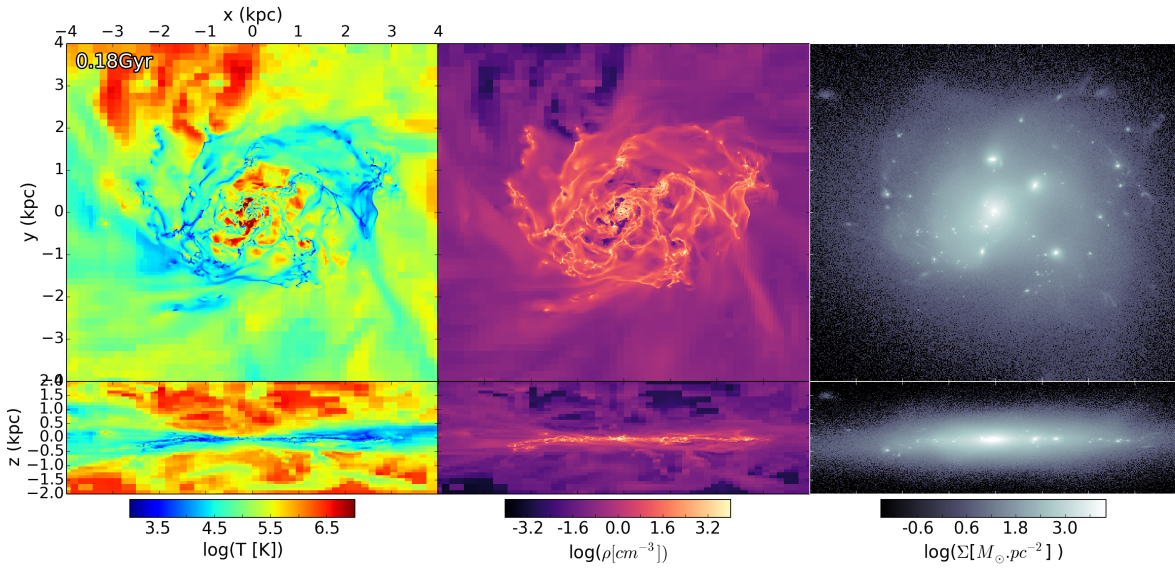


Figure 5.7: Same as Figure 5.6 but for simulations using thermal feedback

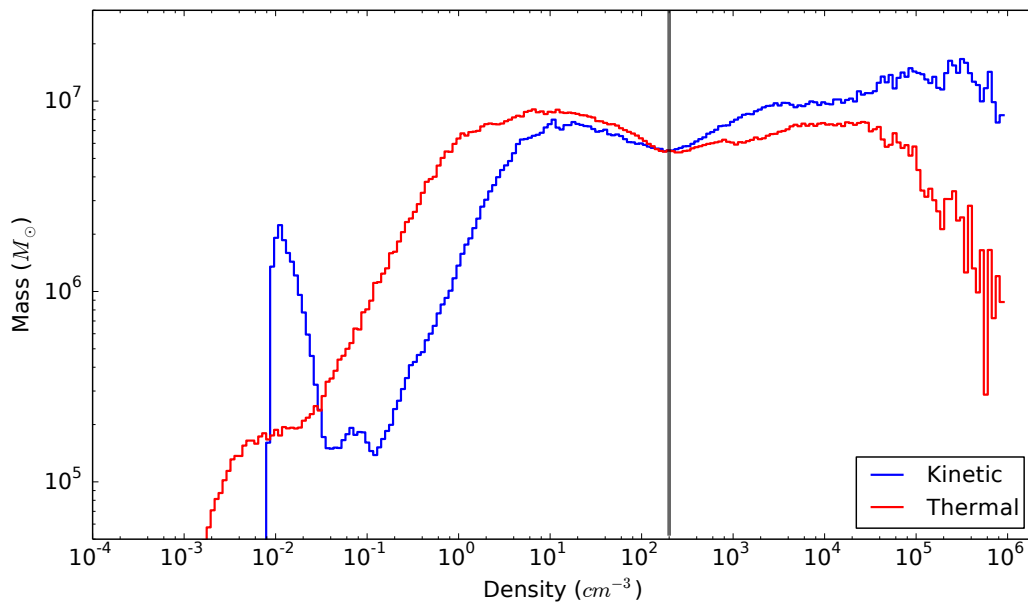


Figure 5.8: Probability distribution function of the gas density in a $(4 \times 4 \times 2)$ kpc box centered on the halo potential well in the simulations using only kinetic (blue) and thermal feedback. The vertical line displays the density threshold for star formation.

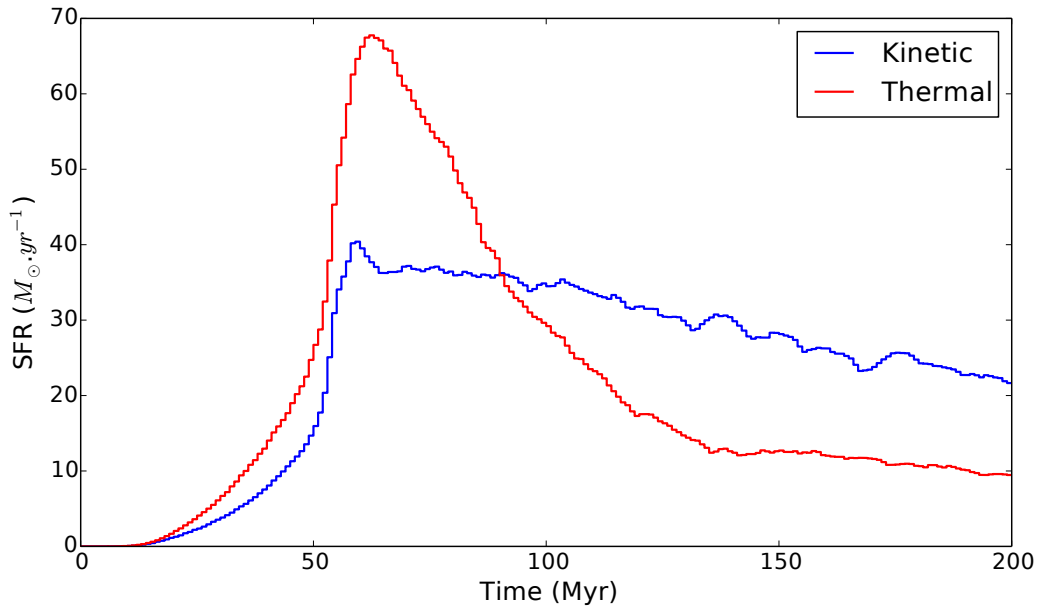


Figure 5.9: Star formation rate of the simulations using only kinetic (blue) and thermal feedback.

at $\rho = 2 \times 10^4 \text{ cm}^{-3}$ where we find $3.3 \times 10^8 M_{\odot}$ more gas in the kinetic feedback situation. This implies that the star formation in the latter case is higher than in the former. This is confirmed by the star formation rate which, after almost 200 Myr, for the kinetic simulation is two times higher than that in the thermal simulation (see Figure 5.9).

The evolution of the SFR shows interesting features. Firstly, we see that we do not recover the steps we described in the Section 5.1.2. Instead, the SFR rises in both thermal and kinetic simulations monotonically during the first 50-60 Myr. This period corresponds to the build-up of the disc. This early evolution of the star formation in those simulations indicates that radiative feedback is responsible for the ending of star formation we observed in Section 5.1.2. Secondly, there is a notable difference in the star formation evolution between the thermal and kinetic simulation, which is linked to the different properties of the ISM. The SFR in the thermal simulation increases a little more rapidly than its counterpart until they reach their maximum of almost $70 M_{\odot} \cdot \text{yr}^{-1}$ and $40 M_{\odot} \cdot \text{yr}^{-1}$ respectively. After reaching their respective maxima, the rate of forming stars decreases more rapidly in the thermal simulation until $t \sim 140 \text{ Myr}$. The evolution of the SFR suggests that during the setup of the discs, injecting thermal energy from SNe has less impact than injecting it in kinetic form and dissipates energy more efficiently. As the time of writing these lines, a physical explanation for this observation is still unclear and further investigations are required to address this question.

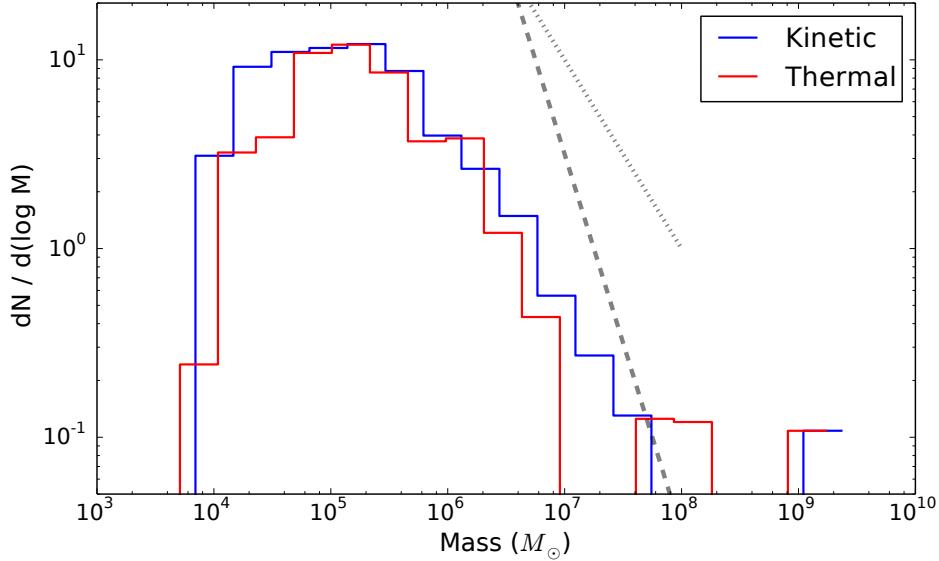


Figure 5.10: Cluster mass function in the simulations using only kinetic (blue) and thermal feedback at $t = 180$ Myr. Power-law functions of index -2 and -1 are displayed with the dashed and the dotted lines respectively.

5.3.2 Consequences on star clusters

As we have seen earlier, the galaxy in the kinetic simulation is slightly more massive than the one in the thermal simulation, although its growth is slower. Does this additional mass go into star clusters or into the disc? Does this slower growth have an impact on the star clusters populations?

In order to address these questions, we now study the basic properties of clusters. We detect these star clusters with the same friend-of-friend algorithm HOP we used in previous chapters although we change the thresholds values for the detection. A cluster is identified if the peak of the local stellar density exceeds $1.1 M_{\odot} \text{ pc}^{-3}$ with an outer boundary limit of $0.25 M_{\odot} \text{ pc}^{-3}$ to prevent the detection of stars in the field. Two clusters are then merged if the saddle density between them is higher than $0.8 M_{\odot} \text{ pc}^{-3}$. With this method, we detect 341 and 259 clusters at $t = 180$ Myr for the kinetic and thermal simulation respectively. We then extract a Cluster Mass Function (CMF) following the same procedure as in Chapter 4. Figure 5.10 shows the CMF in both simulations at $t = 180$ Myr. We can see that in the mass range between $10^4 M_{\odot}$ to $2 \times 10^6 M_{\odot}$, the CMFs of both simulations have similar profiles, although there are more clusters of $2 - 3 \times 10^6 M_{\odot}$ in the kinetic simulation. Above $10^6 M_{\odot}$, the CMFs in both simulations exhibit a power-law. The profiles start to diverge at these higher masses. The CMF power-law in the thermal simulation is cut at $10^7 M_{\odot}$ and three clusters of $\sim 10^8$, $\sim 2 \times 10^8 M_{\odot}$ and $\sim 1.7 \times 10^9 M_{\odot}$ are detected at the highest mass-end of the distribution. These clusters have grown in mass through few

major mergers with clusters of similar mass. The nucleus experiences additional mergers with smaller clusters (a dozen mergers) because of its proximity with these clusters. The power-law in the kinetic simulation has an index close to -1, whereas that of the thermal simulation is closer³ to -2. The slope observed for the thermal simulation seems to be in agreement with what is typically observed for example for star clusters in the Antennae where the power-law index is of -2 (Zhang and Fall 1999) or in M51 (Chandar et al. 2011). We note however that clusters observed in those studies have a mass range going from $10^3 M_{\odot}$ to $10^6 M_{\odot}$, slightly less massive than our star clusters.

This preliminary analysis of the CMFs tends to indicate that galaxies in the kinetic simulation will produce numerous star clusters spanning a large spectrum of masses from $10^4 M_{\odot}$ to $5 \times 10^7 M_{\odot}$. On the other hand, the galaxy in thermal simulation will tend to produce an intermediate-mass and very-massive population of star clusters. Interestingly, the most massive clusters, and our nuclear clusters in particular are not the oldest clusters for both simulations. They rather emerged at $t = 117$ Myr for one cluster and $t = 102$ Myr for the others in the thermal simulation. The nucleus progenitor in the kinetic simulation is even younger as it was detected at $t = 120$ Myr.

5.4 Summary and discussion

Using hydrodynamical simulations of forming dwarf galaxies, we have found that:

- When we use a full set of feedback recipes which includes SNe and radiative feedback, it is challenging to forming a sustainable star cluster populations in the disc from which a nucleus can emerge.
- Similarly to a situation where the galaxy properties are predetermined, radiative feedback plays a destructive role for star clusters.
- Injecting energy from SNe in a thermal form makes the ISM in the disc more turbulent and hotter than if injected in a kinetic form.
- The injection of energy from SNe in a kinetic or thermal form does not drastically affect the final properties of star clusters. However, we note that thermal feedback seems to prevent the existence of $10^7 M_{\odot}$ star clusters, even if an explanation for this observation is still lacking.

These preliminary results pave the way towards a more realistic description of star clusters and galactic nucleus in particular, in an extra-galactic context. They show that radiative feedback is the main destructive element for star clusters in the early forming stages of dwarf galaxies.

The destruction of star clusters we observe in our simulations is in clear contradiction with observations (e.g. Turner et al. 2012; Bastian et al. 2013; Genzel et al. 2014). It

³In the thermal simulation, the bins above $2 \times 10^7 M_{\odot}$ account for 3 clusters in total. We therefore consider that these clusters are not part of the main distribution of the CMF.

suggests that either our model is inaccurate or that, with our modeling, these clusters form much later in the evolution of low mass galaxies.

In the first case, one could modify directly our feedback scheme. In particular, the model we use is based on free parameters which need to be calibrated. Some of these parameters, such as the temperature of H_{II} regions can be constrained using observations (e.g. Lopez et al. 2011). Unfortunately, this can not be accomplished for all criteria which either are not observable quantities⁴ or are used for technical purposes (e.g. speed up the computation). Such calibration becomes even more difficult at higher redshift which pushes the capacities of the instruments to their limits. A potential workaround would be to use the properties of clumps either observed at high-redshift (e.g. Cava et al. 2018) or in simulations (Behrendt et al. 2016) and tune our parameters to reproduce as closely as possible the properties of those clumps. This task would be highly time-consuming given the high number of parameters our model incorporates and also would fail at understanding the physical origin of the clumps properties which is one of our goals.

In the second case, an extension of the simulation across several more Myr or Gyr would be required to check whether or not star and nuclear clusters form later on. Given the amount of gas falling onto the galaxy, we estimate that our galaxy would reach the aimed mass of $10^9 M_{\odot}$ in 300 Myr. This assumes that the accretion rate remains constant across that period and that all the infalling gas is immediately converted into stars which is unlikely due to the stellar feedback. We would thus need additional Gyr of evolution to get the galaxy we aimed at studying in the first place. Moreover, in this context, our model should account for cosmological structures and mechanisms such as galaxies interactions which can be relevant for the formation of massive clusters. As it was pointed out by Arata et al. (2018), during a merger between two dwarf galaxies, cold clouds could form through thermal instabilities via the metal radiative cooling of C_{II} but on the other hand, some orbital configurations of the interacting galaxies (prograde-retrograde merger) suppress the formation of such cold clouds. In any cases, considering this option would require a resolution high enough (i.e. parsec) to probe the forming sites of star clusters. While this is doable for dwarf-dwarf interactions, it becomes more challenging if one wants to encompass a full cosmological context with interactions with multiple galaxies, ram pressure etc.

On smaller spatial scales, going to higher densities for the gas by increasing the resolution could open doors to new effects and coupling processes relevant for star clusters. Our current resolution of 2.4 pc does not allow us to probe the internal structures of the clouds such as the filaments which have a subparsec size (Arzoumanian et al. 2011). Going down to this resolution would imply including additional physics such as magnetic fields which play an important but yet still not fully understood role for star formation (Wareing et al. 2016; Beuther et al. 2018). However, reaching these spatial scales in the context of galaxy formation for several hundreds or thousands of Myr, with non-linear couplings from the feedback (which slows down the computation) is still currently very challenging.

⁴For example, we use for SNe a constant f_{ek} which controls the amount of energy that is injected into a gas pressure or a gas velocity. Namely, we add a pressure term from SNe that scales as $(1 - f_{ek})$ while we add a velocity term scaling as $\sqrt{f_{ek}}$.

Another possible (and also more short-term) way to limit this effect would be to start the simulation with a resolution of [50 – 60]pc during the first 100 Myr, which is the time needed to form the disc. Because of the lower resolution, the gas maximum density would be lower, thus decreasing the star formation and consequently, the energy released by feedback mechanisms. In this (somewhat artificial) situation, we would not expect to form massive clusters yet because we would not reach the necessary high densities for the gas. Once the spatial resolution is increased to its maximum after 100 Myr, star formation and stellar feedback would reach their nominal efficiency in an already established disc. Hence, we would be in a situation similar to that described in Chapter 3 and Chapter 4 with the addition of gas accreting onto the disc. One could argue that everything happening to the stars and gas after we reach maximum resolution is biased by our adopted strategy. Although this approach would indeed be unrealistic in many ways, it could allow us to study the formation conditions of nuclear cluster progenitors when their host is subject to external gas infall.

Chapter 6

Summary and conclusions

This chapter summarizes the main findings of the Thesis and briefly suggests some outlooks for future studies.

The work presented in this Thesis is focused on the nuclear star clusters and the processes involved in their formation. Ubiquitous in many galaxies with various properties, their formation is yet a highly debated topic: the complex evolution of the galactic nuclei makes it difficult for observations to retrieve the original formation channel and numerical models have had arduous times including self-consistently the dynamics of the galaxy at a parsec resolution (the scale of nuclear clusters). The main question driving this Thesis is: What are the processes involved in their formation? This task was conducted from a theoretical perspective using state-of-the-art hydrodynamical simulations which consistently account for the dynamics of gas and stars. These simulations were handled with the Adaptive Mesh Refinement code **RAMSES**. Thanks to the AMR technique which allows us to increase spatial resolution where gas density is the highest, we can follow the dynamics of the gas and stars at a resolution of a few parsecs. We can use this formidable resolution to probe the formation sites of star clusters in a galactic context and thus have access to the forming conditions of nuclear clusters progenitors.

Firstly, as a first example, I have presented observations of the nucleus of the spiral galaxy NGC 300, using the integral-field spectrograph **SINFONI** which operates in the near-infrared. The goal of this observation is to analyze the rotating properties of the nucleus to then constrain the regulation of gas accretion on the nuclear cluster. I have explained how I reduced these observational data using the **SINFONI** data reduction pipeline. I have detailed the extraction of the kinematics and presented the first results which indicates that the nuclear region of NGC 300 shows low amplitude rotation with low stellar velocity dispersion values. I have then briefly described the next necessary steps like extracting the errors or the extraction of the higher moments like the skewness and the kurtosis. This project, although incomplete, contributes to a more ambitious study involving a larger sample of nucleated galaxies.

From a theoretical point of view, I have used the **RAMSES** code to perform parsec-resolution hydrodynamical simulations of dwarf-like galaxies, a choice motivated by the fact that the nucleated fraction of galaxies is at its peak in this mass range. Using a gas

fraction above 50% and basic recipes for star formation and stellar feedback, I have found that nuclear clusters can form through a wet merger scenario. When the gas density is high enough, a massive star cluster forms in the gas-rich disc. This nucleus seed keeps a gas reservoir, and grows further in stellar mass thanks to internal star formation while at the same time, migrating to the center through a combination of interactions with other substructures and dynamical friction. It is also possible (but not mandatory) that a merger with another dense cluster and its own gas reservoir occurs. If such an event takes place, the properties of the nuclear cluster are altered and we observe a quenching of the local star formation. This formation mechanism for nuclear cluster follows the trend of studies that claim that the formation of nuclear clusters follows a mix of the 2 scenarios described by the current paradigm (“*in-situ*” and “*dry-merger*”). More importantly, it emphasizes the critical role of gas during the process.

Following this project, I have investigated how stellar feedback affects the dynamics of the gas and consequently that of potential nuclear cluster progenitors. I have showed that radiation feedback (photo-ionization and radiative pressure) plays a more important role than type-II supernovae in destroying dense gas structures, and altering or quenching the subsequent cluster formation. The radiation emitted by feedback also disturbs the clusters mass growth, by increasing the internal energy of the gas component to the point when radiation pressure overcomes the cluster gravity. Ultimately, this can slow or even prevent the formation of nuclear clusters which is heavily linked to its gas reservoir. I have also emphasized how these results depend on the calibration we give to stellar feedback. Due to the non-linear effects of feedback, a change of calibration (such as the size of H_{II}) can modify the properties of the ISM and star clusters, prevent the formation of massive clusters and ultimately that of nuclear clusters.

Finally I have studied the formation of nuclear clusters in a broader context by mimicking cosmological gas accretion, forming galaxies from the collapse of a gaseous halo embedded in dark matter. This set of simulations was realized for various gas fractions and various dark matter halos with a mass range corresponding to dwarf galaxies. During the first 60 Myr, when the disc starts to form, we observe the creation of a large population of star clusters with typical masses of $[10^5 - 10^6 M_{\odot}]$. However, due to the high star formation involved in the formation of the disc, the resulting stellar feedback disrupts the gaseous disc. This leads to the expansion of the stellar disc and to the disruption of all star clusters. Simulating galaxies with only SNe active showed that hundreds of star clusters are able to form and survive for at least 100 Myr in the disc, showing that radiative feedback is the main cause for the star clusters destruction when all feedback recipes are included. I have then investigated in more depth the role of SNe with the following simple question: in a context of external gas accretion, does injecting energy from SNe in a kinetic or thermal form alter the properties of star clusters and nuclear clusters? In this situation, first results show a clear difference in the gas properties, with a ISM hotter and more turbulent when thermal energy is injected. They also suggest that injecting the energy in kinetic form can favor the formation of massive clusters and potentially nuclear clusters progenitors.

Overall, this Thesis has allowed me to assess the physical mechanisms involved in

the formation of nuclear clusters and to stress the primary role of gas. It also helps understanding the part stellar feedback, and especially radiation feedback, may play by disturbing the physical state of the gas and the properties of nuclear cluster progenitors to the point where the latter can not grow and are instead disrupted.

Several extensions of this work are possible. As I have stated earlier, radiative feedback mostly plays a destructive role for nuclear clusters progenitors unless the latter are dense enough. In a context where we have “cosmological” gas accretion, such surviving conditions are never met. Since we do observe nuclear and star clusters in the local Universe, this means that the feedback model we use is either too simplistic in terms of physics or badly calibrated, or that star clusters form at later stages of the galaxy evolution. Hence, future projects could focus on incorporating more recipes into the model such as photoelectric heating or investigate the space parameters to better constrain them with observations. Because of their deeper gravitational potential, exploring other more massive regimes for galaxies (e.g. Milky Way-like mass) could also help limiting the impact of stellar feedback on star clusters. Also, it would be an interesting check to simulate galaxies over longer periods of time (10 Gyr) to see if a new star cluster population is able to form beyond the first hundred Myr. It is also possible that other physical processes unrelated to feedback need to be added. For example, it has been shown that galaxy mergers can lead to the formation of massive clusters. Also, with the increasing power of supercomputers, we are now starting to perform cosmological simulations with parsec-like resolutions. These challenging simulations would allow us to study high-redshift dwarf galaxies in a full cosmological context and further understand the formation of nuclear clusters progenitors.

Appendix A

Example of namelist in RAMSES

```
&RUN_PARAMS
cosmo=.false.
pic=.true.      !particle in cell (DM and old_stars)
poisson=.true. !gravity
hydro=.true.   !gas
nrestart=0
nremap=5       !nb of coarse timesteps before a remap of the grid
               !over all cpus
nsubcycle=9*2  !After nsubcycle timesteps, synchro of dt : dt = nsubcycle*dt_min
ncontrol=1
/

&OUTPUT_PARAMS
foutput=20     !writing frequency of outputs (every foutput dt_coarse)
noutput=1      !
tout=500.0     !Can be an array. Otherwise end of simulation
/

&INIT_PARAMS
filetype='ascii' !Initial conditions (IC), ASCII format
initfile(1)='/gpfs/scratch/pr85ti/di29pol/Simu_large_Dwarf_nfw_July15/IC/' !location of IC
/

&AMR_PARAMS
levelmin=8     !l_min allowed
levelmax=17    !l_max allowed. Need to be accurate values here -->
               !monitor the refinement levels during the simulation
ngridmax=20000 !nb max of allowed grid per cpu (1 grid = 8 cells)
npartmax=20000 !nb max of allowed particles per cpu
boxlen=30.0    !length of the box in kpc; code units can be found in patch/units.f90
/

&POISSON_PARAMS
gravity_type=0
epsilon=1.0d-4 ! Stopping criterion for the iterative Poisson solver
cg_levelmin=999
```

```

cic_levelmax=12 !cloud in cell, level of refinement max for particles (star+DM)
/
                !must be around 10-20pc

&BOUNDARY_PARAMS
nboundary=6
bound_type= 2, 2, 2, 2, 2, 2
ibound_min=-1, 1, -1, -1, -1, -1
ibound_max=-1, 1, 1, 1, 1, 1
jbound_min= 0, 0, -1, 1, -1, -1
jbound_max= 0, 0, -1, 1, 1, 1
kbound_min= 0, 0, 0, 0, -1, 1
kbound_max= 0, 0, 0, 0, -1, 1
/

&PHYSICS_PARAMS
!!!!!!!!!!!!!!!!!!!!!!!!!!!!!!!!!!!!!!
!!! Star Formation
!!!!!!!!!!!!!!!!!!!!!!!!!!!!!!!!!!!!!!
isothermal=.false. !true:force temperature on the EOS/false : temperature >= T_eos
!!! isothermal=.true.
cooling=.true.      !activation or not of cooling /
                    !must be opposite of the value of isothermal

!!! cooling=.false.
g_star=1.66667D0
n_star=100.         ! Threshold for star formation in H/CC
!!! n_star=0.
eps_star=0.02      ! efficiency per free-fall time : rho_sfr=rho_gas/t_ff*eps_star
T2_star=235.0      !min temperature when eos_type='isothermal' /
                    !T=T2_star if isothermal=true, >= otherwise

!!!!!!!!!!!!!!!!!!!!!!!!!!!!!!!!!!!!!!
!!! Metals
!!!!!!!!!!!!!!!!!!!!!!!!!!!!!!!!!!!!!!
z_ave = 0.05 !!! metallicity in solar units
!!!!!!!!!!!!!!!!!!!!!!!!!!!!!!!!!!!!!!
!!! Feedback
!!!!!!!!!!!!!!!!!!!!!!!!!!!!!!!!!!!!!!
eta_sn=0.2         ! fraction of the stellar mass that explodes in SN (IMF)
yield=0.10         ! useless unless variable metallicity
f_w=5.0           ! Thermal SN : fw=0 / Kinetic SN= f_w=(1 to 10) loading factor
                    ! and f_ek>0.
f_ek=0.05         ! Kinetic SN : f_ek=0 to 1 and fw!=0.
rbubble=10.       ! radius of spheres for kinetic SN injection
                    ! (threshold at 3*cells in the code)
ndebris=1         ! used by thermal SN, leave 1 by default
nlev_sf=13.       ! defines the characteristic mass of new star particles.
                    ! Usually want ==effective levelmax
THII=2.D4         ! temperature of HII regions, typically 1E4-1E5 K
                    ! (>0: feedback HII + radative / =0: only SN feedback /
                    ! <0: feedback radative only)
rhominHII=0.1     ! threshold density, no feedback HII+radiative bellow

```

```

rhodelayHII=1.D9 ! density in H/CC used to delay feedback HII+radiative.
                    ! negligible except for very high resolution, leave it.
multiscat=5.0      ! "trapping factor" kappa: number of effective diffusions.
nHII_skip=10      ! one out of nHII_skip OB-star ionizes the gas.
Tmax_global=5.0D9 ! maximal temperature allowed
jeans_ncells=4.
max_sf_eff=0.3    ! For the saturation of SF at very high density
/

&HYDRO_PARAMS
gamma=1.666667
courant_factor=0.5  !=cell_size/(2*speed)
slope_type=1
riemann='acoustic'
/

&REFINE_PARAMS
! use F. Renaud's plot_eos (python) tool to optimize these for EOS cooling
m_refine= 5*50,4*20000 !7*50.
    !refine if nb of DM+old_stars > m_refine per cells
mass_sph = 5*2e-6,4*1. ! 4.5E-7
    !mass per particle : refine if M_gas > mass_sph*m_refine
interpol_type=0
interpol_var=1
jeans_refine=5*4,4*-1 ! 4 ! refine if cell size does not resolve Ljeans 4 times.
                    ! Use if cooling=true
/

&EOS_PARAMS
!!! TEST with ISOTHERMAL SET UP
!!!eos_type='pseudo_cooling' !shape of the eos.
                                !if pseudo_cooling, density threshold = nH_H_cc_threshold
eos_type='isothermal'          !shape of the eos.
                                !if isothermal, T_eos=T2_star
nH_H_cc_threshold=0.1
!!! Here we set it up to make sure that we have an effective levelmax
!!! which corresponds to the Jeans Length
level_jeans=13 ! usually levelmax effective
jeans_polytrope=3 ! 1=highest Tjeans(default), 2=middle, 3=lowest
/

&GROUP_PARAMS
gal_center_x= 0.          !galaxy position in kpc. multiple galaxies if multiple values
gal_center_y= 0.
gal_center_z= 0.
Vgal_x= 0.                !galaxy velocity in 65 km/s.
Vgal_y= 0.
Vgal_z= 0.
gal_axis_x= 0.           !galaxy spin axis

```

```
gal_axis_y= 0.
gal_axis_z= 1.
Mgas_disk= 2.3           !gas mass in 10^9 M_sun
typ_radius= 1.65        !galaxy radii in kpc
cut_radius= 7.5
typ_height= 0.165      !galaxy heights in kpc
cut_height= 0.750
rad_profile= 'exponential' !galaxy radial and z profiles
z_profile= 'exponential'
ic_part_file= 'ic_part_dwarfs.dat'
Vcirc_dat_file= 'Vcirc_dwarfs.dat'
IG_density_factor= 1.E-6 !density of the uniform halo at t=0, factor=rho_Halo/rho_lim
compatibility_vfactor= .true.
/
```

Appendix B

Clustered feedback

We present here in more details the physical changes occurring when we use the clustered feedback described in Chapter 4. In particular, we focus on the short-timescale alterations of the ISM properties.

In order to better understand which process directly prevents the formation of a nucleus when clustered feedback is used, we conduct an experiment with the following protocol:

- We extract a snapshot at $t = 550$ Myr from our reference simulation ($\beta = 10$). At that time, the star cluster progenitors which will later merge to build a NC are not formed yet.
- We let the galaxy evolve for the two feedback setups (reference and clustered feedback). We focus on the first 5 Myr, before the ISM gets more globally affected by the change of feedback prescription.
- We focus on a region with high star formation activity (*i.e.* $10^{-1} M_{\odot} \text{ yr}^{-1}$) where a cluster is about to form in the reference simulation, namely a $3 \times 3 \text{ kpc}^2$ box close to (but offset from) the centre.

The resulting gas density maps and location of formed stars are presented in Fig. B.1.

We note that the densest star forming sites are preserved in both cases: a high star formation site can be seen on the top right corner as well as in the middle-bottom area. We also notice a coherent H_{II} bubble exploding around the massive star cluster (top-right corner) which is not observed in the reference case. The dense filaments-like structures we witness in the reference simulation are quickly dissolved by localized feedback in just 5 Myr when we use clustered feedback. The injected energy in the clustered feedback simulation manages to affect very large spatial regions, thus leading to a significant drop in the availability of dense gas. This, in turn, induces a lower star formation rate as illustrated in Fig. B.1: three times more stars are produced within 5 Myr in the reference simulation than when clustered feedback is used ($1.3 \times 10^6 M_{\odot}$ and $4.1 \times 10^5 M_{\odot}$, respectively).

This difference in the gas morphology and the star formation rate is more due to a different spatial injection of thermal energy by the hot H_{II} regions than the momentum

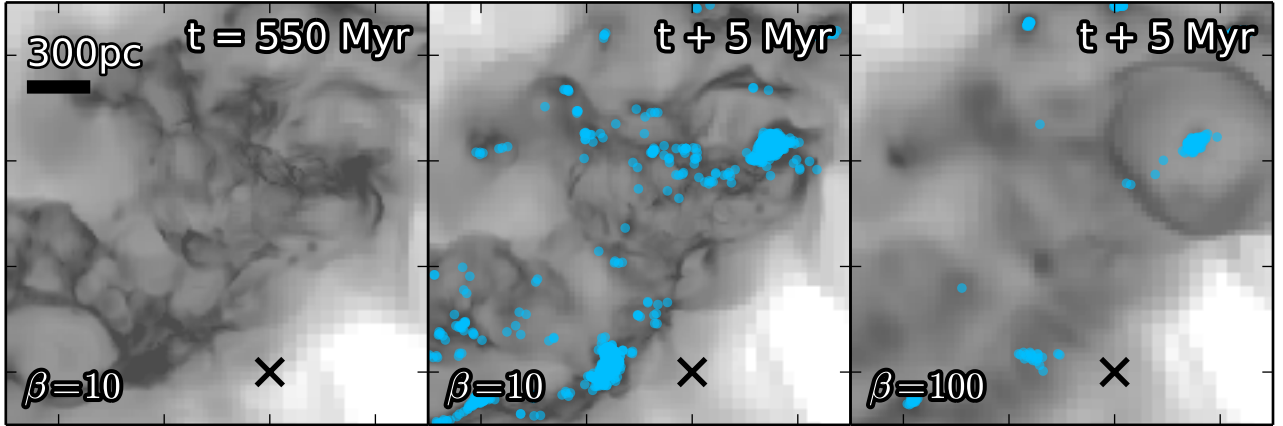


Figure B.1: Density maps of the gas at the starting time of the re-run (left), then 5 Myr after for $\beta = 10$ (middle) and $\beta = 100$ (right) over the region $[-2, 1, -1, 2]$ kpc in x and y coordinates. The density of the gas is averaged along a line of sight of 1 kpc in depth (z axis). Young stars that have formed during these 5 Myr are displayed in blue. The cross marks the gravitational potential centre of the galaxy. After 5 Myr, the altered properties of the ISM lead to a significantly different topology of the star formation sites.

produced individually by each bubbles. Indeed, during the first Myr, we form approximately the same amount of stars when the feedback is active: $2.0 \times 10^5 M_{\odot}$ (reference) and $2.2 \times 10^5 M_{\odot}$ (clustered feedback). The total momentum rate from H_{II} regions in this region is also similar: 1.5×10^{-3} for $\beta = 10$ and 1.3×10^{-3} for $\beta = 100$ (the units are in $L_{\odot} \cdot h \cdot \nu \cdot c^{-1}$). Only the spatial distribution of the gas local temperature changes (see Fig. B.2).

When using a clustered feedback, only a few bubbles form but they heat a large volume around the dense gas region and makes the gas less dense in that area. On the contrary, in the reference simulation, the gas is heated on more numerous but smaller volumes that are more homogeneously distributed in space, thus allowing the dense gaseous structures to prevail or to reconstruct. As a consequence, only the densest regions can form star clusters when clustered feedback is used. However, these young clusters see their potential gas reservoir dissipating from the gas heating from H_{II} regions.

From all of this, two results stand out:

- On short timescale (*i.e.* < 1 Myr), the properties of the star population do not seem to be significantly affected by the individual increase of the momentum deposited by H_{II} regions. However, the properties of the ISM are locally (*i.e.* at tens of parsec scales) changed: energy injection in the ISM via a few large bubbles seems to be more efficient in removing the dense and cold gas than more numerous but smaller ones.
- On longer timescales (*i.e.* > 5 Myr), the local variations in the ISM start to irre-

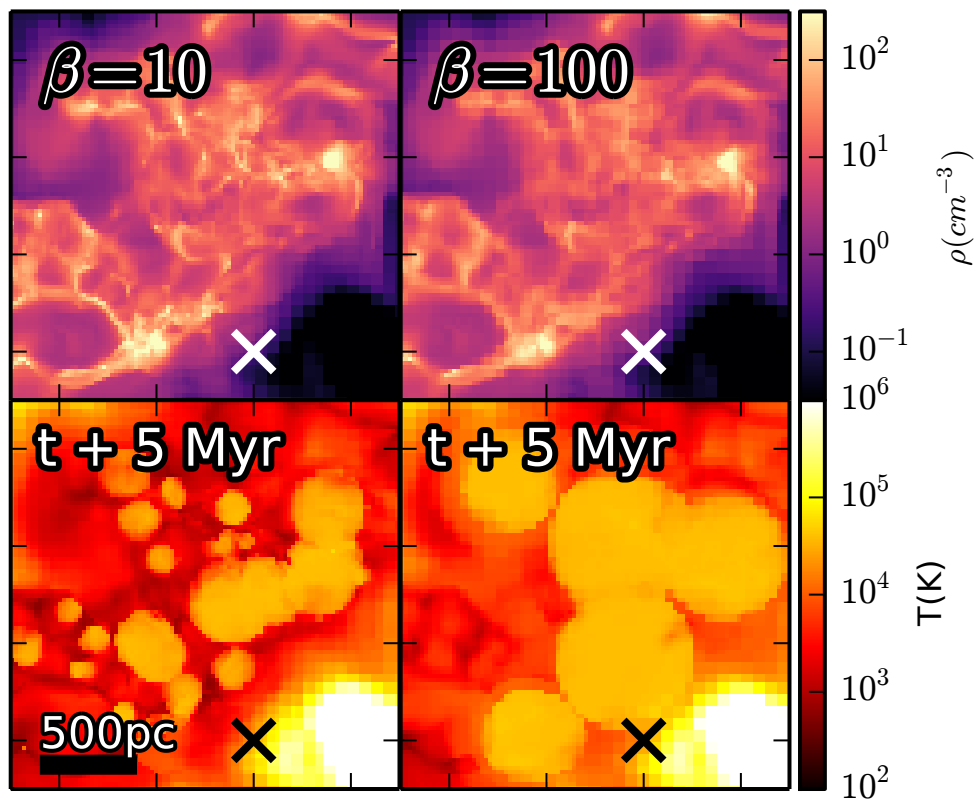


Figure B.2: Density (top) and temperature (bottom) maps for the reference (left) and ad-hoc simulation with $\beta = 100$ (right). The maps cover the same area as in Fig B.1. The cross marks the gravitational potential center of the galaxy. The maps shown are taken 5 Myr after the re-calculation: the global topologies of the ISM (*i.e.* locations of the over and under-densities) are mainly similar but local differences in the gas density within the bubbles arise, with more low-dense gas when $\beta = 100$. In that case, the heating from H_{II} regions covers a larger volume than in the reference simulation, making the gas less dense in these areas.

versibly alter its properties on more global scale (*i.e.* kpc scales) and with it, the location and number of the forming sites of star clusters.

Appendix C

Article from broader collaboration

This paper is the completion of a project I started during my first-year Master internship and that my former supervisor (Guillaume Dubus) finished in 2017. In this paper, we estimate the number of gamma-ray binaries in our Galaxy. Using observations-based and synthetic templates light curves, we assess the detection possibilities in the GeV and TeV energy range for surveys like *Fermi*-LAT (GeV) or CTA (TeV). We conclude that *Fermi*-LAT observations in the GeV range are more likely to detect gamma-ray binaries than TeV surveys.

This paper was published in 2017 in *Astronomy & Astrophysics*.

Sizing up the population of gamma-ray binaries

Guillaume Dubus¹, Nicolas Guillard², Pierre-Olivier Petrucci¹, and Pierrick Martin³

¹ Univ. Grenoble Alpes, CNRS, Institut de Planétologie et d'Astrophysique de Grenoble (IPAG), 38000 Grenoble, France
e-mail: Guillaume.Dubus@univ-grenoble-alpes.fr

² European Southern Observatory, Karl-schwarzschild-Str. 2, 85748 Garching, Germany

³ Univ. Paul Sabatier, CNRS, Institut de Recherche en Astrophysique et Planétologie (IRAP), 31028 Toulouse Cedex, France

Received 2 May 2017 / Accepted 10 August 2017

ABSTRACT

Context. Gamma-ray binaries are thought to be composed of a young pulsar in orbit around a massive O or Be star with their gamma-ray emission powered by pulsar spin-down. The number of such systems in our Galaxy is not known.

Aims. We aim to estimate the total number of gamma-ray binaries in our Galaxy and to evaluate the prospects for new detections in the GeV and TeV energy range, taking into account that their gamma-ray emission is modulated on the orbital period.

Methods. We modelled the population of gamma-ray binaries and evaluated the fraction of detected systems in surveys with the *Fermi*-LAT (GeV), H.E.S.S., HAWC and CTA (TeV) using observation-based and synthetic template light curves.

Results. The detected fraction depends more on the orbit-average flux than on the light-curve shape. Our best estimate for the number of gamma-ray binaries is 101_{-52}^{+89} systems. A handful of discoveries are expected by pursuing the *Fermi*-LAT survey. Discoveries in TeV surveys are less likely. However, this depends on the relative amounts of power emitted in GeV and TeV domains. There could be as many as ≈ 200 HESS J0632+057-like systems with a high ratio of TeV to GeV emission compared to other gamma-ray binaries. Statistics allow for as many as three discoveries in five years of HAWC observations and five discoveries in the first two years of the CTA Galactic Plane survey.

Conclusions. We favour continued *Fermi*-LAT observations over ground-based TeV surveys to find new gamma-ray binaries. Gamma-ray observations are most sensitive to short orbital period systems with a high spin-down pulsar power. Radio pulsar surveys (SKA) are likely to be more efficient in detecting long orbital period systems, providing a complementary probe into the gamma-ray binary population.

Key words. surveys – pulsars: general – Galaxy: stellar content – gamma rays: stars – X-rays: binaries

1. Introduction

Gamma-ray binaries are systems composed of a massive star in orbit with a compact object and are characterized by broad non-thermal emission peaking (in νF_ν) at energies above 1 MeV. The latter feature distinguishes gamma-ray binaries from high-mass X-ray binaries (HMXBs), whose spectral energy distribution peaks in X-rays, whereas the former feature distinguishes these binaries from recycled binary millisecond pulsars that have a low-mass companion. The compact object in gamma-ray binaries is likely to be a young, rotation-powered neutron star with non-thermal radiation due to the interaction of energetic pulsar wind particles with the stellar wind and radiation field of the O or Be companion. There is ample indirect evidence for this binary pulsar wind nebula scenario even though scattering in the stellar wind prevents detection of the expected radio pulsar in most gamma-ray binaries (see Dubus 2013, for a review). Accordingly, we explicitly assume in the following that the compact object in gamma-ray binaries is a pulsar. However, many of our results are equally applicable if the gamma-ray emission is powered by non-thermal jet emission from an accreting black hole (e.g. Massi et al. 2017). Clear evidence for gamma-ray jet emission exists for the accreting sources Cyg X-1 and Cyg X-3, but these objects are not gamma-ray binaries according to our definition because they are orders of magnitude more luminous in X-rays than in gamma rays.

There are six gamma-ray binaries detected in high energy (HE; 0.1–100 GeV) or very high energy (VHE; >100 GeV)

gamma rays. Of these, two were initially detected as HE gamma-ray sources in all-sky surveys (LSI +61°303, Gregory & Taylor 1978; and 1FGL J1018.6-5856; Ackermann et al. 2012), two were independently detected in HE gamma rays and X-rays before the association was made (LS 5039, Paredes et al. 2000; and LMC P3, Corbet et al. 2016), one was detected serendipitously in VHE observations of the Monoceros Loop (HESS J0632+057; Hinton et al. 2009), and one was detected in a radio pulsar survey (PSR B1259-63; Johnston et al. 1992). Follow-up observations established that these sources are binaries harbouring a massive star and that their non-thermal emission is modulated on the orbital period. In addition to those six gamma-ray binaries there are also four systems discovered in radio surveys with a young pulsar in orbit with a massive star, but where variable gamma-ray emission associated with the binary has yet to be detected because of low pulsar power, a long orbital timescale, and/or large distance. These four systems are PSR J0045-7319, PSR J1638-4725, PSR J1740-3052, and PSR J2032+4127 (see Stairs et al. 2001; Bassa et al. 2011; Madsen et al. 2012; Lyne et al. 2015, respectively).

Gamma-ray binaries are probably a short-lived phase in the evolution of massive star binaries, following the birth of the neutron star and preceding the HMXB phase, when the neutron star accretes material captured from the stellar wind instead of holding it back (see Tauris & van den Heuvel 2006, for a review on the formation of compact objects in binaries). Accretion occurs if the ram pressure from accreting matter is able to overcome the pulsar wind, turning off the pulsar mechanism

(Shvartsman 1971; Illarionov & Sunyaev 1975; Lipunov et al. 1994; Campana et al. 1995). A gamma-ray binary can thus transition to a HMXB on the typical spin-down timescale of young pulsars, i.e. a few 10^5 yr. The evolution of the companion eventually leads to a second supernova with the formation of another compact object. Therefore, besides the unique opportunities gamma-ray binaries provide to understand the physics of pulsar winds, these binaries also offer a window into the pulsar and orbital parameters of systems that remain bound after a supernova and constrain the formation paths to double neutron stars and coalescing compact objects.

Achieving these goals depends on our ability to explore the population of gamma-ray binaries. The number of gamma-ray binaries in our Galaxy has been estimated from a few dozen to a few thousand systems from population synthesis studies of HMXB evolution (Meurs & van den Heuvel 1989; Iben et al. 1995; Portegies Zwart & Verbunt 1996; Portegies Zwart & Yungelson 1998). Gamma-ray binaries are more likely to stand out in gamma rays rather than in radio, optical, or X-ray surveys where they are usually inconspicuous. The discovery of LMC P3 in the Large Magellanic Cloud suggests that we may have already accessed most of the observable gamma-ray binary population in our own Galaxy (Corbet et al. 2016).

Here, we aim to provide the first detailed estimate of the number of gamma-ray binaries based on HE and VHE observations and to evaluate the prospects for further discoveries. To do this, we simulated observations of gamma-ray binaries to assess the probability of detections in mock gamma-ray surveys that are designed to follow as closely as possible those performed or planned with the *Fermi* Large Area Telescope (*Fermi*-LAT), the High-Energy Stereoscopic System (H.E.S.S.), the High-Altitude Water Cherenkov observatory (HAWC), and the Cherenkov Telescope Array (CTA; Sect. 2). One difficulty in assessing the detectability is that the gamma-ray flux can vary strongly with orbital phase. We use input gamma-ray orbital light curves based on templates constructed from observations (Sect. 3) or based on a radiative model (Sect. 4). The estimated population size and expectations for future detections are discussed in Sect. 5.

2. Simulating surveys

We simulate a measurement as the flux average of the gamma-ray binary light curve integrated over a certain duration and energy range. The duration of the measurement, number of measurements (visits), and their distribution throughout time vary according to the type of instrumentation. The observability and detectability of the system depend on the assumptions made for each type of survey that was simulated. The observability only depends on the part of the sky surveyed and the location of the binary system. The detectability depends on the sensitivity of the survey, cadence of the visits, and emission properties of the system.

We simulate five types of surveys with properties as close as possible to existing or envisioned surveys, without carrying out a full end-to-end simulation of the observations and data analysis chain. In our opinion, current knowledge about the radiative mechanisms in gamma-ray binaries does not justify performing such complex and costly end-to-end simulations. The level of detail in our mock surveys is appropriate for the basic emission model that we develop in Sect. 4, which represents gamma-ray binary spectra at 1 GeV and 1 TeV with mono-energetic electrons. In the GeV domain, we simulate the *Fermi*-LAT third

catalogue (“3FGL-like”) and the *Fermi* All-sky Variability Analysis (“FAVA-like”). In the TeV domain, we simulate the H.E.S.S. Galactic Plane survey (“H.E.S.S.-like”), a “HAWC-like” survey, and the CTA Galactic Plane survey (“CTA-like”). A source is considered detected if its average flux in $\text{ph cm}^{-2} \text{s}^{-1}$ during the observation exceeds the threshold of the survey as defined below. We do not address the issue of how the detected gamma-ray source is identified as a gamma-ray binary, presumably through multi-wavelength follow-up observations. In particular, we make no attempt to investigate how binaries can be identified through a period analysis, such as that performed on the *Fermi*-LAT catalogue by Ackermann et al. (2012). Here, the orbital modulation only intervenes as the source of flux variability between observation windows.

2.1. The 3FGL-like survey

The 3FGL-like survey tests whether the binary would have been included in the third *Fermi*-LAT catalogue (Acero et al. 2015). The whole Galactic plane is covered so the gamma-ray binary observability is 100%. The measurement is assumed to last four years, ignoring any time variation in exposure. The threshold for detection is taken to be $10^{-9} \text{ ph cm}^{-2} \text{ s}^{-1}$ (1–100 GeV) based on the flux distribution of sources detected within 10° of the Galactic plane in Acero et al. (2015, see their Fig. 24). We set the energy threshold at 1 GeV because the HE component of binaries peak around this energy and because the Galactic diffuse emission, which we do not take into account, is weaker than at 100 MeV. The 3FGL catalogue includes LS 5039, LSI +61°303, and 1FGL J1018.6-5856. LMC P3 is also part of the catalogue but is confused with other sources in the Large Magellanic Cloud. We also consider, where indicated, the impact of continued *Fermi*-LAT observations in the future. This extended 3FGL survey assumes a detection threshold that is lowered by a factor 2 and an exposure that is increased by a factor 4 (16 yr of observations).

2.2. The FAVA-like survey

The FAVA-like survey is based on the search for 5.5σ deviations from a long-term average model of the GeV emission observed with the *Fermi*-LAT (Abdollahi et al. 2017). Following the FAVA procedure, we search for deviations on a weekly timescale, which sets the duration of the simulated measurement, over a time span of eight years. Again, any time variation of the exposure is ignored and the observability is 100%. We consider the system to be detected by this survey if its weekly average flux subtracted from its long-term average flux (over eight years) is greater than $10^{-6.5} \text{ ph cm}^{-2} \text{ s}^{-1}$ (>100 MeV). Although the exact threshold changes as a function of location in the Galactic plane and spectrum, this choice should be conservative based in Fig. 4 of Abdollahi et al. (2017). The FAVA survey is potentially more sensitive than the 3FGL survey to systems such as PSR B1259-63 with long orbital periods and short duty cycles for GeV emission. The second FAVA catalogue includes LSI +61°303 and PSR B1259-63.

2.3. The H.E.S.S.-like survey

The H.E.S.S.-like survey is based on the survey of the Galactic plane carried out by the H.E.S.S. collaboration since 2004 and is meant to be representative of what current imaging arrays of Cherenkov telescopes (IACTs) can achieve. The survey

covers only part of the Galactic plane, i.e. $-110^\circ \leq l \leq 65^\circ$. The observability of a system is decided by checking that it is observable for at least 2 h at some point in the year at a zenith angle smaller than 45° , assuming the geographical location of the H.E.S.S. array, and that its longitude is within the surveyed area. To produce a schedule of observations, we randomly distribute 25 visits of 2 h over a time span of eight years, i.e. we assume a uniform survey exposure of 50 h is achieved. We take into account that observations occur at night, ensuring each binary has a preferred observation season. However, we do not account for Moon-less operations, which influence the distribution of observable time on a monthly timescale. The latter effect averages out over a timescale of a few years, whereas the former (preferred season) does not. The measured fluxes from each visit are then averaged and compared to a detection threshold of $3.6 \times 10^{-13} \text{ ph cm}^{-2} \text{ s}^{-1}$ ($>1 \text{ TeV}$). This threshold corresponds to a flux of 20 mCrab¹. The exposure times and sensitivity are comparable to those of the H.E.S.S. survey². We also consider whether a detection could be claimed from a single visit, scaling the threshold by a factor $(50/2)^{1/2}$.

2.4. The CTA-like survey

The CTA-like survey is intended to test the potential performance of the CTA array in detecting new gamma-ray binaries. The guiding principles are identical to the H.E.S.S.-like survey. We assume that the survey is divided up into two blocks carried out in parallel during the first two years of operations, based on the plans for an initial Galactic Plane survey by the CTA Consortium (Vercellone 2017). The first block, carried out by the south array in Chile, covers longitudes $-60^\circ \leq l \leq 60^\circ$ down to a sensitivity of 2.7 mCrab using six visits of 2 h. The second block, carried out by the north array in the Canary Islands, covers $60^\circ \leq l \leq 150^\circ$ down to 4.2 mCrab in four visits of 2 h. We also consider the full survey covering the entire Galactic plane and carried out over a time span of 10 yr (see Fig. 6 in Vercellone 2017, for details). The observability of each system is decided as for the H.E.S.S.-like survey using the planned locations for the arrays.

2.5. The HAWC-like survey

Finally, we test for the detection of binaries using the extended air shower array HAWC. The high duty cycle and full-sky monitor capacity of HAWC can make it more sensitive to flaring gamma-ray binaries than IACTs such as H.E.S.S. and CTA. Here, the binary is observable if it transits with a zenith angle smaller than 45° at the location of the HAWC array in Mexico. We then simulate one measurement per day at the time of transit and with a duration equal to transit duration. The HAWC sensitivity after five years of operation is comparable to that achieved in the H.E.S.S. Galactic Plane survey, i.e. 20 mCrab above 1 TeV, assuming a source transit duration across the sky of 6 h (Carramiñana 2016). The threshold for daily detection is close to 1 Crab for a 6 h transit, corresponding to the transit time of a source that passes close to zenith, i.e. with a declination close to $+19^\circ$. The dependence of the threshold with source declination is taken into account using the curve showing

sensitivity as a function of declination for a $E^{-2.5}$ spectrum in Fig. 10 of Abeysekara et al. (2017). We test for detection in each daily measurement and in the accumulated exposure over five years of HAWC operations.

3. Extrapolating from observed gamma-ray binaries

We currently have five binaries with measured orbital modulations at both GeV and TeV energies and one with a GeV modulation (LMCP3). We aimed to find out the sensitivity of the surveys to the detection of these binaries. We estimated this sensitivity here by constructing a template light curve for each of the known gamma-ray binaries and, after proper scaling for distance, deriving the probability for detection once the binary was randomly located in the Galaxy.

3.1. Template light curves

Figure 1 shows template light curves for each of the known gamma-ray binaries based on the GeV and TeV observations available at the time of writing. In most cases, we simply took the phase-folded measurements and interpolated these measurements using splines. For PSR B1259-63, LSI +61°303, and HESS J0632+057, the error bars, phase coverage, or orbit-to-orbit variations make it difficult to assess the mean orbital light curves. In these cases, our templates are meant to be representative of the behaviour of the system in that they roughly capture the amplitude and phase variations that have been observed. The template GeV and TeV light curves are given in $\text{ph cm}^{-2} \text{ s}^{-1}$ integrated above 1 GeV and 1 TeV, respectively. We converted to these units assuming a simple power law when the data were not directly available in this format. The source of the data and the power-law photon index Γ (with $dN \propto E^{-\Gamma} dE$) that we used can be found in the caption to Fig. 1. Given the low statistics, the GeV light curve of HESS J0632+057 (not shown in Fig. 1) is described as a two bin light curve (orbital phases 0.0–0.5 and 0.5–1.0) using the spectral parameters in Table 1 of Li et al. (2017), who have reported the first detection of this system at GeV energies³.

Table 1 lists the detected systems for each mock survey presented in Sect. 2, given the template light curves and locations of the known binaries in the Galaxy. LSI+61°303 is not detected in the H.E.S.S.-like survey owing to its location. LS 5039 and LSI +61°303 are observable with HAWC but are undetected in the HAWC-like survey because of their unfavourable declinations; this non-detection is consistent with the 18 months of HAWC observations that have been reported to date (Abeysekara et al. 2017). PSR B1259-63 is always detected in the FAVA survey. The system is just below the threshold of the 3FGL survey when the four-year survey time span includes only one periastron passage of the 3.4 yr orbit, as observed. PSR B1259-63 has a very small probability ($<1\%$) of being detected in the H.E.S.S. survey because of its low duty cycle and flux, but this source a 50% chance of being detected in the CTA-like survey. HESS J0632+057 is outside the H.E.S.S. and initial CTA-like surveys; this source is detected in the full CTA survey. 1FGL J1018.6-5856 is only detected in the 3FGL-like survey and in the full CTA-like survey. LMCP3 is only detected in

¹ For the VHE surveys, we converted Crab units to integrated flux above 1 TeV using $1 \text{ Crab} \equiv 1.82 \times 10^{-11} \text{ ph cm}^{-2} \text{ s}^{-1}$, based on the Crab spectrum measured by Albert et al. (2008).

² <https://www.mpi-hd.mpg.de/hfm/HESS/pages/home/som/2016/01>

³ The *Fermi*-LAT detection reported by Malyshev & Chernyakova (2016) is compatible with the detection of the low energy end of the VHE spectrum rather than the detection of a distinct GeV spectral component as in the other gamma-ray binaries.

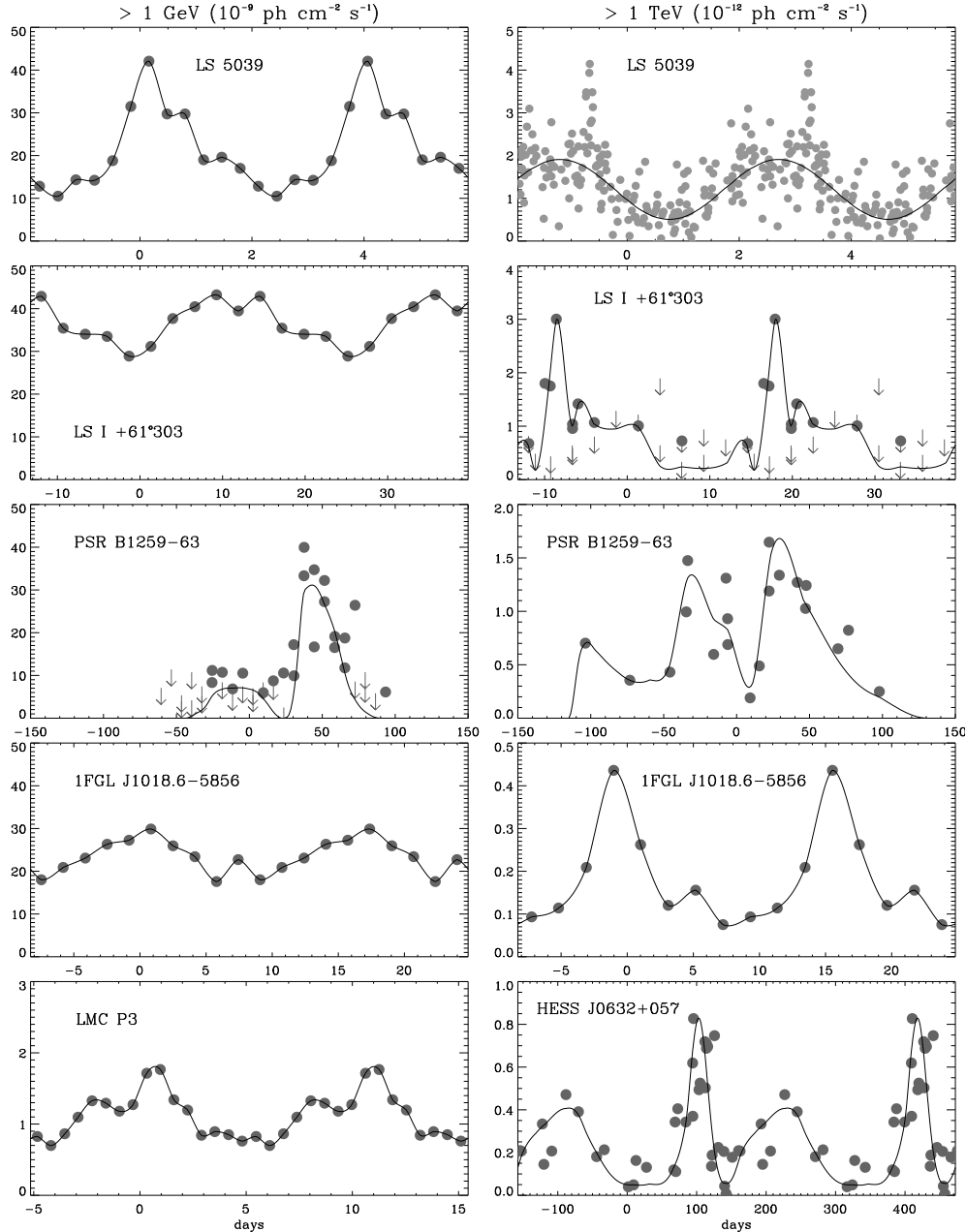


Fig. 1. Template light curves for known gamma-ray binaries. Two orbits are shown except for PSR B1259-63 where the plot focuses on periastron passage. The various measurements are shown in grey, with error bars omitted for clarity. Arrows indicate measurement upper limits. *Left:* photon flux integrated above 1 GeV in units of 10^{-9} ph cm $^{-2}$ s $^{-1}$ based on *Fermi*-LAT measurements. *Right:* photon flux integrated above 1 TeV in units of 10^{-12} ph cm $^{-2}$ s $^{-1}$ based on IACT measurements. The GeV and TeV data are taken from [Abdo et al. \(2009\)](#) and [Aharonian et al. \(2006\)](#) for LS 5039, where $\Gamma_{\text{GeV}} = 2.54$; [Hadasch et al. \(2012\)](#) and [Acciari et al. \(2011\)](#) for LS I +61°303, where $\Gamma_{\text{GeV}} = 2.42$ and $\Gamma_{\text{TeV}} = 2.6$; [Bordas et al. \(2016\)](#) for PSR B1259-63, where $\Gamma_{\text{GeV}} = \Gamma_{\text{TeV}} = 2.7$; [Ackermann et al. \(2012\)](#) and [Abramowski et al. \(2015\)](#) for 1FGL J1018.6-5856, where $\Gamma_{\text{GeV}} = 3.1$ and $\Gamma_{\text{TeV}} = 2.7$. The GeV data for LMC P3 are from [Corbet et al. \(2016\)](#), where $\Gamma_{\text{GeV}} = 2.8$. The TeV data for HESS J0632+057 are from [Aliu et al. \(2014\)](#).

the 3FGL-like survey. These results are fully consistent with the actual 3FGL, FAFA, and H.E.S.S. survey observations.

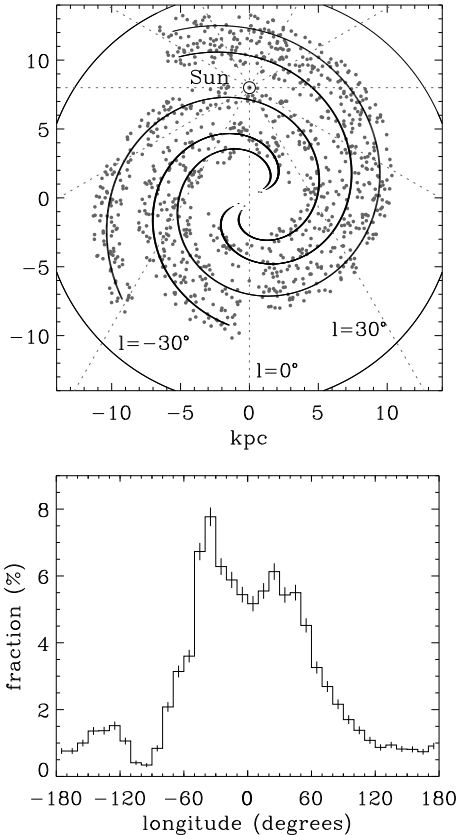
3.2. Galactic distribution

We assumed that gamma-ray binaries are located in or close to the spiral arms of our Galaxy, similar to the O and B stars and HMXBs to which they are directly related. The Galaxy is

modelled as four one-dimensional spiral arms. We used the arm formula of [Ringermacher & Mead \(2009\)](#) with parameters adjusted to reproduce the Galactic structure in Fig. 5 of [Russeil \(2003\)](#). Our Sun is 8 kpc away from the Galactic centre. Binaries are spread out uniformly across the Galaxy disk (15 kpc), keeping only those within 1 kpc of a spiral arm and more than 3 kpc away from the Galactic centre to account for the older stellar population in the bulge (see Fig. 2). The binaries are assumed

Table 1. Detected systems in the mock surveys based on the template light curves in Fig. 1.

Mock survey	Detected system
3FGL	LS 5039, LSI+61°303, 1FGL J1018.6-5856, LMC P3
FAVA	LSI+61°303, PSR B1259-63
H.E.S.S.	LS 5039
HAWC	none
CTA	LS 5039, LSI+61°303, PSR B1259-63
CTA (full)	LS 5039, LSI+61°303, PSR B1259-63, HESS J0632+057, 1FGL J1018.6-5856

**Fig. 2.** *Top:* map of randomly generated locations for gamma-ray binaries in the Galaxy. *Bottom:* longitude distribution of gamma-ray binaries under the assumptions described in Sect. 3.2.

to reside in the Galactic plane ($b = 0^\circ$). The model Galactic longitude distribution (Fig. 2) compares well to the HMXB longitude distribution plotted in Grimm et al. (2002) or Walter et al. (2015).

The ground-based surveys (H.E.S.S., HAWC, and initial CTA) access only part of the Galactic plane, hence only a fraction of the binaries are observable for them. These fractions are given in Table 2 for both a distribution along spiral arms, as described above, and a strictly uniform disk distribution. This makes little difference. In the following, we consider only the spiral arm distribution.

3.3. Detectable fraction based on observed light curves

Table 3 reports the detectable fraction of gamma-ray binaries in the various surveys based on a sample of 10^4 systems randomly

Table 2. Fraction (%) of observable binaries in each survey.

	H.E.S.S.	HAWC	CTA
Spiral	72.25 ± 0.28	55.85 ± 0.31	82.94 ± 0.23
Disk	75.26 ± 0.27	52.44 ± 0.31	80.94 ± 0.24

distributed in Galactic location and in starting orbital phase for each template light curve in Fig. 1 after scaling for distance. The light curves are then run through the simulated observations of each survey described in Sect. 2 to test for detection. For example, the 3FGL-like survey detects $77.9 \pm 0.8\%$ of the binaries that are assumed to have a GeV light curve identical to LS 5039. Here and in the remainder of the paper, the errors represent the 95% confidence interval derived from a likelihood analysis⁴.

1FGL J1018.6-5856 and LMC P3 have high enough luminosities that such systems are detectable anywhere in the Galaxy with the 3FGL survey. Unsurprisingly, the FAVA-like survey is best suited for low duty cycle light curves such as PSR B1259-63. Our analysis recovers that PSR B1259-63 is detected in FAVA, but would not include LSI+61°303. The latter is inconsistent with the FAVA catalogue and is the result of neglecting the orbit-to-orbit variations that are detected in this source (Ackermann et al. 2013). The FAVA-like analysis also fails to detect LS 5039 and 1FGL J1018.6-5856 since the amplitude of the flux variations on weekly timescales are insufficient to flag them. In this case, this is consistent with the actual FAVA results (Abdollahi et al. 2017).

The numbers remain small in the H.E.S.S. and HAWC-like surveys. The high sensitivity of the CTA array leads to detection fractions that are comparable to those achieved by the *Fermi-LAT*. Very few systems are detected as transients in the ground-based surveys (i.e. detected only in one visit); the flux increase compared to the average in a highly eccentric system rarely compensates the higher sensitivity threshold for observations on a shorter duration. Hence, the fraction of detected systems in VHE surveys decreases with longer orbital period even if the systems have comparable maximum TeV luminosities owing to a high eccentricity.

The fractions in Table 3 give an estimated detection probability from which we can constrain the maximum size of the

⁴ Here, we estimate the probability p to detect a binary in a survey. We find m detections after running a random sample of n systems through our mock survey procedure. The likelihood function is $L(p) = C_n^m p^m (1-p)^{n-m}$, where C_n^m is the binomial coefficient. The function has a maximum L_m for $p = m/n$. Defining the test statistic as $T = 2 \log(L_m/L)$ and applying Wilks' theorem, the 95% confidence interval on p is calculated from the interval, where $T \leq 3.84$ (the cut-off value in a χ^2 distribution with one degree of freedom beyond which the probability $\leq 5\%$). The chosen number of systems n to simulate is a compromise between computational time and statistical error.

Table 3. Fraction of detected systems in each survey using the light curves in Fig. 1 as templates (see Sect. 3.3).

	LS 5039	LS I+61°303	PSR B1259-63	HESS J0632+057	1FGL J1018.6-5856	LMC P3
P_{orb} (days)	3.9	26.5	1236.7	315	16.5	10.3
Eccentricity	0.35	0.54	0.87	0.83	–	–
Distance (kpc)	2.9	2.0	2.3	1.6	5.4	50
$F_{\text{max,GeV}}$ (ph s ⁻¹)	4.2×10^{37}	2.1×10^{37}	2.0×10^{37}	2.9×10^{35}	1.0×10^{38}	5.4×10^{38}
$F_{\text{max,TeV}}$ (ph s ⁻¹)	1.9×10^{33}	1.4×10^{33}	1.1×10^{33}	2.5×10^{32}	1.5×10^{33}	–
HE surveys (%)						
FAVA	0.6 ± 0.2	1.4 ± 0.2	12.6 ± 0.7	<0.1	8.0 ± 0.5	30.6 ± 0.9
3FGL	77.9 ± 0.8	67.1 ± 0.9	3.5 ± 0.4	0.8 ± 0.2	100	100
3FGL (extended)	100	97.3 ± 0.3	7.7 ± 0.5	1.9 ± 0.3	100	100
VHE surveys (%)						
H.E.S.S.	10.3 ± 0.6	3.2 ± 0.4	1.5 ± 0.3	0.8 ± 0.2	5.2 ± 0.5	–
HAWC	7.7 ± 0.5	2.1 ± 0.3	0.4 ± 0.1	0.3 ± 0.1	4.0 ± 0.4	–
CTA	65.8 ± 0.9	23.7 ± 0.8	7.0 ± 0.5	5.1 ± 0.4	35.2 ± 0.9	–
CTA (full)	98.0 ± 0.3	47.0 ± 1.0	21.2 ± 0.8	11.2 ± 0.6	70.0 ± 0.9	–

underlying population⁵. Any other existing system with identical properties to 1FGL J1018.6-5856 or LMC P3 would have been detected since the detection probability is 1. For LS 5039, knowing that the system is detected in the 3FGL survey, the 77.9% probability implies with >95% confidence that there are at most three systems with comparable light curves in our Galaxy and most likely only one. The same conclusion is reached for LS I+61°303. For PSR B1259-63, given the FAVA detection, the 12.6% detection probability implies 7^{+26}_{-6} such systems in our Galaxy. Therefore, on average, there may be one more LS 5039 or LS I+61°303 type system, and six other PSR B1259-63-like systems in the Galaxy that could have escaped detection in the *Fermi*-LAT data.

The VHE detection probabilities are not as constraining as those of HE except for HESS J0632+057. The detection probability is only 0.8% in both the 3FGL and H.E.S.S.-like surveys. The lack of detection in those surveys (HESS J0632+057 is outside the H.E.S.S. survey area; Sect. 3.1) places an upper limit of <231 on the number of HESS J0632+057-like systems in the Galaxy. The initial CTA-like survey should detect 11^{+8}_{-6} of those 231 systems or reduce their estimated number to 8^{+30}_{-7} should it only detect HESS J0632+057 after the full 10 year Galactic Plane survey. The Cherenkov Telescope Array Galactic Plane survey will thus be able to strongly constrain the number of such systems.

4. A synthetic population

In the preceding section we estimated the number of existing gamma-ray binaries from the properties of the known systems. However, these systems represent only the upper end of the luminosity function of gamma-ray binaries. In this section we estimate this number from a synthetic population model. Building this population requires a model for the gamma-ray emission of binaries, which is a bold enterprise given the current knowledge. While there is general agreement that anisotropic inverse Compton scattering of photons from the star and $\gamma\gamma$ pair production at TeV energies must play a role, since these processes naturally lead to orbital modulations the details vary significantly from

⁵ We take the detection probability p derived by the simulation and find the population n that maximizes the likelihood (see footnote 4) to detect m observed systems. Here, $m = 1$ for each type of gamma-ray binary.

model to model. Modulated Doppler boosting is also very likely to intervene if the emission occurs in a pulsar wind bow shock. Reproducing the orbital phases of gamma-ray detections in systems with Be companions, such as PSR B1259-63, has proven particularly difficult; this is possibly because of the complex interaction between the pulsar and the circumstellar material surrounding its companion. In the following, we adopted a simple model with the intention of minimizing the number of parameters while still being able to produce orbital light curves comparable to the observed light curves.

4.1. Orbital parameters

The binary eccentricities e were assumed to follow the thermal distribution (Ambartsumian 1937) $p(e)de = 2ede$ with the additional conditions that $e < e_{\text{max}} = 1 - (P_{\text{orb}}/2 \text{ days})^{-2/3}$ to ensure that the companion does not fill more than 70% of its Roche lobe at periastron and that the binaries are circularized ($e = 0$) for $P_{\text{orb}} \leq 2$ days (see Moe & Di Stefano 2017, and references therein). The inclination of the system is derived by randomly picking a vector on a sphere. The argument of periastron and the orbital phase at the time of the first simulated observation are picked from a uniform distribution between 0 and 2π . Finally, we uniformly sampled the logarithm of orbital periods between 1 and 10^4 days in order to assess the fraction of detected systems as a function of P_{orb} , except in Sect. 4.4 where this is slightly modified for a more realistic representation of the P_{orb} distribution of HMXBs.

4.2. Radiation model

We assumed that the radiation is due to Compton upscattering of stellar photons with an initial energy ≈ 10 eV. The GeV (resp. TeV) emission then requires electrons with a Lorentz factor $\gamma = 10^4$ (resp. $\gamma = 10^6$). For simplicity, we assumed monoenergetic distributions at these energies. This is supported by the observed GeV spectra of gamma-ray binaries, which generally consist of a hard power law with an exponential cut-off around 1 GeV. This is also admissible in the TeV range where soft power laws are observed such that most of the photons have an energy close the threshold energy of the VHE observations. The true particle distributions are likely to be more complex, but the GeV and TeV emissions are dominated by electrons of these

energies and assuming more complex distributions (power laws, see Sect. 5) does not have a significant impact on the results.

We computed the inverse Compton bolometric power radiated by these particles, assuming that they are located at the position of the compact object. If the electron distribution is isotropic, the light curve in the Thomson approximation for Compton scattering is given by

$$L_\gamma = N_e \sigma_T c U_\star (1 - \beta\mu) \left[(1 - \beta\mu)\gamma^2 - 1 \right], \quad (1)$$

where $U_\star = (1/c)\sigma_{\text{SB}}T_\star^4(R_\star/d_\star)^2$ and T_\star is the star temperature, R_\star its radius, d_\star its distance to the particles, and $\mu = \cos\theta$ represents the angle between the line of sight and the binary axis. The angle θ varies from $\pi/2 + i$ (superior conjunction) to $\pi/2 - i$ (inferior conjunction) with i the system inclination. The massive star was assumed to have a radius of $10R_\odot$ and temperature of 33 000 K. The analytic formula is valid for $\gamma = 10^4$, where the Thomson approximation is acceptable. However, stellar photons scatter in the Klein-Nishina regime when $\gamma = 10^6$. Hence, we numerically integrated the Compton kernel to derive the anisotropic emitted power instead of using Eq. (1) (see Dubus et al. 2010).

The total number of electrons N_e is related to the injected power in particles P_{inj} by

$$N_e = \frac{P_{\text{inj}}}{\gamma m_e c^2} \times \min\{\tau_{\text{esc}}, \tau_{\text{ic}}\}, \quad (2)$$

where τ_{esc} is the escape timescale of the particles from the gamma-ray emitting region (see below) and τ_{ic} is the inverse Compton loss timescale, which in the Thomson regime is

$$\tau_{\text{ic}} = \frac{\gamma m_e c^2}{\frac{4}{3}\sigma_T c U_\star \gamma^2}. \quad (3)$$

Hence, $\langle L_\gamma \rangle = P_{\text{inj}}$ (integrated over all angles) if the particles radiate efficiently before they leave the vicinity of the star ($\tau_{\text{ic}} \leq \tau_{\text{esc}}$), otherwise the radiated power is reduced to the fraction of particles that are in the emission zone $\langle L_\gamma \rangle = (\tau_{\text{esc}}/\tau_{\text{ic}})P_{\text{inj}}$. The latter can be rewritten using Kepler's third law as $L_\gamma \propto 1/d_\star \propto P_{\text{orb}}^{-2/3}$, hence there is a break in the distribution of $\langle L_\gamma \rangle/P_{\text{inj}}$ as a function of P_{orb} for the orbital period where $\tau_{\text{ic}} = \tau_{\text{esc}}$. This can be seen in Fig. 3, in which the mean of the average orbital luminosity is plotted for a sample of 10^4 binaries with orbital periods ranging from 1 to 10^4 days and randomly sampled eccentricities. The break is at $P_{\text{orb}} \approx 10$ days because we decided to set $\tau_{\text{esc}} = d_\star/c$. Such a fast escape timescale is reasonable in the context of gamma-ray binaries, where the accelerated particles flow away relativistically in a bow shock (Dubus et al. 2015). This assumption is also conservative in that it may underestimate the number of detections by minimizing the radiative efficiency. The influence of this choice on the results is further discussed in Sect. 5.2.

Since TeV photons are likely to create pairs by interacting with photons from the star, we calculated the expected $\gamma\gamma$ absorption at 1 TeV in the point source limit following Dubus (2006). Absorption reduces the average TeV luminosity for short orbital period systems, where the stellar radiation density is highest, resulting in a strong decrease of L_{TeV} with P_{orb} below 10 days (Fig. 3). The GeV emission is not affected by $\gamma\gamma$ absorption. However, we also took into account eclipses of the (point-like) gamma-ray emission zone by the star. This results in a slight decrease of the average GeV power at short P_{orb} , instead of the expected flat distribution $\langle L_\gamma \rangle = P_{\text{inj}}$. Hence, this

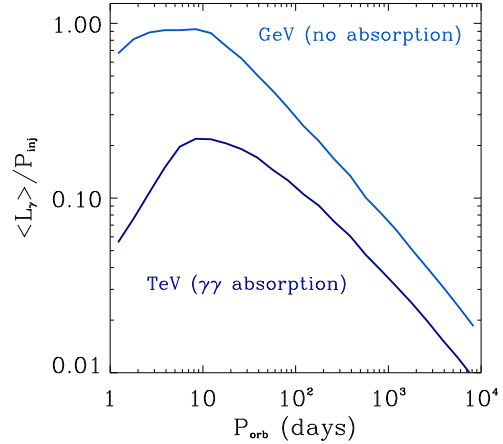


Fig. 3. Mean orbit-averaged gamma-ray flux, normalized to the injected power, as a function of P_{orb} (see Sect. 4.2).

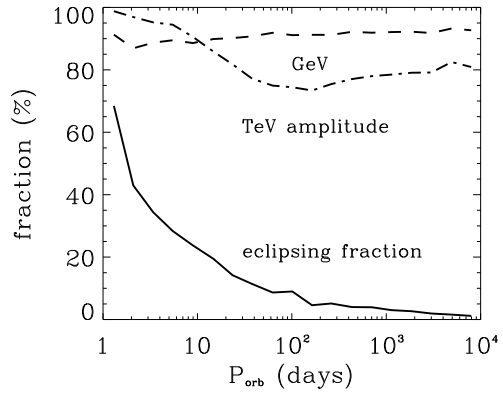


Fig. 4. Mean fractional amplitude of the simulated GeV (dashed line) and TeV (dash-dotted line) gamma-ray light curves (see Fig. 3) and fraction of the systems showing eclipses as a function of P_{orb} (thick line).

model predicts the radiative efficiency is maximum for systems with $P_{\text{orb}} \approx 10$ days.

Figure 4 shows the average fractional amplitude of the model TeV light curves, measured as $(f_{\text{max}} - f_{\text{min}})/(f_{\text{max}} + f_{\text{min}})$, where f is the flux. The mean amplitude increases slightly from short to long orbital periods owing to the larger eccentricities permitted (see Sect. 4.1) but eclipses and $\gamma\gamma$ absorption strongly increase the amplitude at short P_{orb} . The average TeV variability amplitude at long P_{orb} is about 80%, implying $f_{\text{min}} \approx 0.11f_{\text{max}}$. Figure A.1 shows examples of GeV and TeV light curves that are computed via the radiative model described in this section.

4.3. Detectable fraction based on synthetic light curves

To check for consistency with the results of Table 3, we produced 10^4 synthetic light curves using the orbital period and eccentricity (when known) for each observed system, i.e. leaving the system orientation free. We then normalized the synthetic light curves to the maximum observed luminosity. The systems are distributed throughout the Galaxy. The detection fractions in Table 4 are within a factor 2 or less of those in Table 3, showing comparable trends when looking at objects, orbital period, or surveys. The exception is PSR B1259-63 where the detected fraction in the 3FGL-like survey is a factor 5 higher because

Table 4. Fraction of detected systems in each survey using synthetic light curves as templates (see Sect. 4.3).

	LS 5039	LSI +61°303	PSR B1259-63	HESS J0632+057	1FGL J1018.6-5856	LMC P3
HE surveys (%)						
FAVA	0.9 ± 0.2	4.0 ± 0.4	10.7 ± 0.6	0.1 ± 0.1	16.7 ± 0.7	35.3 ± 1.0
3FGL	70.2 ± 0.9	39.9 ± 1.0	15.7 ± 0.7	0.3 ± 0.1	91.2 ± 0.6	99.7 ± 0.1
VHE surveys (%)						
H.E.S.S.	7.5 ± 0.5	5.7 ± 0.5	1.6 ± 0.3	0.7 ± 0.2	7.0 ± 0.5	–
HAWC	5.2 ± 0.4	4.4 ± 0.4	0.8 ± 0.2	0.3 ± 0.1	5.4 ± 0.4	–
CTA	50.4 ± 1.0	38.3 ± 1.0	10.8 ± 0.6	3.7 ± 0.4	47.8 ± 1.0	–

the model typically produces a lower amplitude light curve than observed, hence a higher average flux (see below). Despite this shortcoming, our simple radiative model should still be able to yield realistic estimates of the average detection rate for a population of systems.

We then produced synthetic light curves for a sample of binaries with random orbital parameters and a given injected power. Figure 5 shows the fraction of systems detected in the mock HE and VHE surveys discussed in Sect. 2, as a function of P_{orb} and P_{inj} . The FAVA-like survey is much less efficient at detecting systems than the 3FGL-like survey. At short orbital periods, the sensitivity is insufficient to detect systems on a time span of a week. At long orbital periods, the amplitude of the variations in the model light curves (Fig. 4) is insufficient to provide a significant advantage to this burst search strategy compared to the integration strategy employed in the 3FGL-like survey. The latter is extremely efficient when the injected power in HE-emitting particles exceeds 10^{35} erg s $^{-1}$, even for long P_{orb} compared to the integration time (four years).

The VHE surveys access only part of the Galactic plane so their maximum efficiency does not reach 100% even for high injected powers in VHE-emitting particles. The results show comparable efficiencies for the H.E.S.S.- and HAWC-like surveys. The design of these two surveys, notably the visit frequencies, does not appear to play a major role in the detectable fraction; the peak at $P_{\text{orb}} \approx 10$ to 100 days simply reflects the higher radiated luminosity expected for those orbital periods in the model (see Fig. 3). The CTA-like survey is much more sensitive, detecting nearly all accessible systems for $P_{\text{inj}} \geq 10^{35}$ erg s $^{-1}$ regardless of orbital period. Again, the sensitivity at long P_{orb} results from our model, which on average gives a minimum flux around 11% of the maximum flux (Fig. 4 and Sect. 4.2). This enables the detection of long orbital period systems even when the phases of maximum flux are not sampled by the visits.

4.4. Full population model

A full population model requires assumptions on the injected power P_{inj} and how it relates to the total available power \dot{E} measured by pulsar spin-down. The parameter P_{inj} is likely to be different for the GeV and TeV emitting particles, whether they arise from different populations or from the same power-law distribution. We used PSR B1259-63, which is the only system with a measured $\dot{E} = 8 \times 10^{35}$ erg s $^{-1}$, to estimate the power going to the GeV- and TeV-emitting particles. Simulating GeV and TeV light curves with the same orbital period and eccentricity as PSR B1259-63 (i.e. following the procedure described in Sect. 4.3), we found that injection fractions $P_{\text{GeV}} = 0.07\dot{E}$ and $P_{\text{TeV}} = 0.01\dot{E}$ are needed to reproduce, on average, the peak

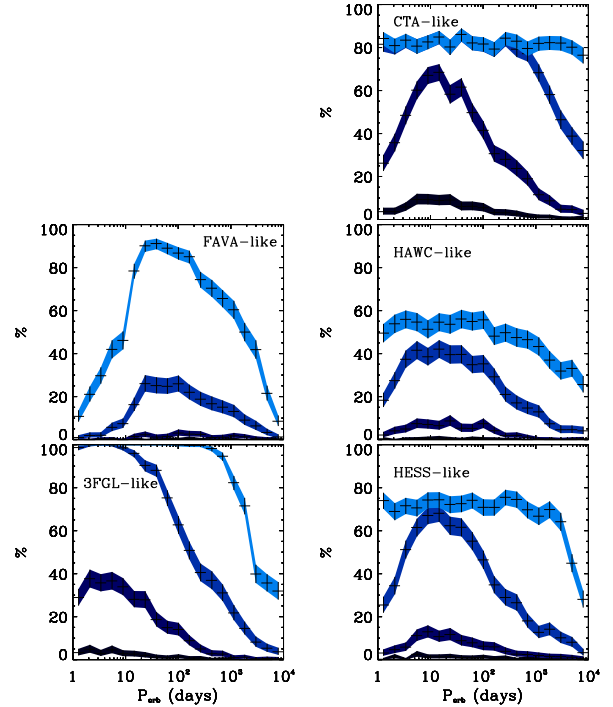


Fig. 5. Detected fractions in the HE (*left panels*) and VHE (*right panels*) surveys. Each panel contains four curves corresponding to $P_{\text{inj}} = 10^{33}, 10^{34}, 10^{35}, 10^{36}$ erg/s (dark to light blue sequence in each panel). The detection fraction increases when going from small P_{inj} (darker blue) to high P_{inj} (lighter blue) until the detected fraction saturates at the value given by the observable fraction (Table 2).

gamma-ray fluxes listed in Table 3, and we adopted these values in the following.

We built the mock population by randomly sampling probability distributions of \dot{E} and P_{orb} . Following Lutovinov et al. (2013), we took a flat distribution in $\log P_{\text{orb}}$ tapered by Gaussian edges at $\log P_{\text{orb}}$ (days) = 1.3 and 3.7. This probability distribution (Fig. 6, top left panel) results from the evolution of pre-HMXB binaries (Bhadkamkar & Ghosh 2012). For \dot{E} , we took as input the distribution of spin-down powers extracted from the ATNF pulsar catalogue (Manchester et al. 2005)⁶, selecting only those pulsars with a pulse period >10 ms and a spin-down timescale < 10^7 yr to exclude recycled millisecond pulsars. The resulting \dot{E} distribution is shown in the top right panel of Fig. 6.

We calculated the detection fraction in the various surveys from a random sample of 10^5 systems (Table 5). The

⁶ <http://www.atnf.csiro.au/people/pulsar/psrcat/>

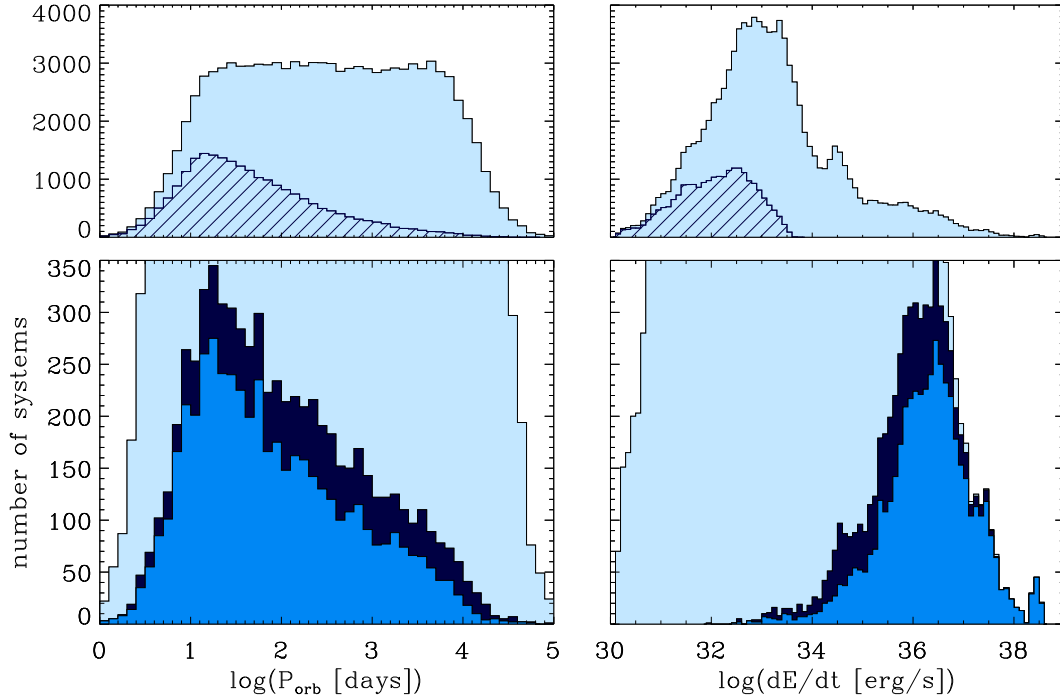


Fig. 6. Orbital period (*left panels*) and spin-down power distribution (*right panels*) of a random sample of 10^5 systems. *Top panels* show the full population as a light blue histogram with the line-filled fraction showing the distribution of the binaries that are accreting according to Eq. (4). The *bottom panels* zoom in to highlight the systems detected in any of the present-day surveys (combining the H.E.S.S., 3FGL, and FAVA-like surveys; medium blue histogram) or any of the future surveys (combining the full CTA, extended 3FGL, and HAWC-like surveys, dark blue histogram). The latter essentially shows the systems detected in any survey since a binary detected in one of the present-day surveys has a nearly >99% chance of being re-detected in one of the future surveys.

Table 5. Detection fractions for the population shown in Fig. 6.

Mock survey	Detection fraction (%)
3FGL or FAVA	4.83 ± 0.13
FAVA	1.96 ± 0.09
3FGL	4.73 ± 0.13
3FGL (extended)	6.21 ± 0.15
H.E.S.S.	1.17 ± 0.07
HAWC	0.88 ± 0.06
CTA	3.78 ± 0.12
CTA (full)	5.83 ± 0.15

distributions of detected systems in present-day or future surveys are shown in the zoomed-in bottom panels of Fig. 6. The detection fractions are biased towards short P_{orb} and high \dot{E} , as expected from the results of Sect. 4.3. The population model naturally accounts for the existence of radio pulsars in binaries that remain undetected in gamma rays because of their long orbital periods and low spin-down powers. PSR J0045-7319, PSR J1638-4725, PSR J1740-3052 with $P_{\text{orb}} = 51, 1941, 231$ days (resp.) and $\dot{E} = 0.2, 0.4,$ and 5×10^{33} erg s $^{-1}$ (resp.) are examples of such systems, which we do not expect to be readily detectable by the gamma-ray surveys (Stairs et al. 2001; Bassa et al. 2011; Madsen et al. 2012).

The pulsar wind pressure can be insufficient to hold off accretion from the stellar wind of the companion for low \dot{E} and short P_{orb} . In such a case, we considered that the system is an accreting HMXB. The accreted material can reach the neutron star surface or the neutron star magnetic field can propel material

out, depending on the respective locations of the co-rotation radius and magnetospheric radius, both of which are within the light cylinder. In both cases we considered that the system does not emit gamma rays. We used a simple criterion to test whether a system is accreting or not, assuming the massive star wind is isotropic, uniform with the same constant mass loss rate $\dot{M}_w = 10^{-6} M_{\odot} \text{yr}^{-1}$, and the velocity $v_w = 1000$ km s $^{-1}$ for all systems. The system is accreting if the pulsar spin-down power is less than

$$\dot{E} < 4 \times 10^{33} \left(\frac{\dot{M}_w}{10^{-6} M_{\odot} \text{yr}^{-1}} \right) \left(\frac{10^3 \text{ km s}^{-1}}{v_w} \right)^3 \left(\frac{0.1 \text{ AU}}{a_p} \right)^2 \text{ erg s}^{-1}, \quad (4)$$

where a_p is the binary separation at periastron (Illarionov & Sunyaev 1975). This criterion is simplistic in regards to the complex physics of wind launching, capture, Be circumstellar disks, etc. (Dubus 2013), but we chose values of \dot{M}_w and v_w that are likely to overestimate the fraction of accreting systems. We find about 23% of the sampled systems are accreting, mostly at short P_{orb} and low \dot{E} as shown by the line-filled histogram in the top panels of Fig. 6. Despite this, we find negligible overlap with the population of systems detected in the HE and VHE surveys because these select high \dot{E} systems; <0.4% of the detected systems are also flagged as accreting.

About 40% of the binaries that are detected in HE can be found in both the 3FGL and FAVA-like surveys, whereas less than 2% are detected only in the FAVA-like survey. The detection of PSR B1259-63 in FAVA without a concurrent detection in the 3FGL survey is therefore unlikely in our model, as the statistics in Sect. 4.3 already showed. However, PSR B1259-63

is close to our crude 3FGL detection threshold using the template light curve so details in the 3FGL detectability may come into play (orbit-to-orbit fluctuations, Galactic diffuse emission). The probability to detect a system in one of the VHE surveys (H.E.S.S., HAWC, and CTA-like) is $4.23 \pm 0.13\%$, with most of the detections arising from the CTA-like survey. Altogether, the probability to detect a gamma-ray binary in any of the surveys is $5.32 \pm 0.14\%$ (3FGL-, FAVA-, H.E.S.S.-, HAWC-, or CTA-like). Only a very small number are detected in VHE surveys without a detection in the HE surveys with this model. For instance, all of the systems detected by the H.E.S.S.-like survey are also detected by the 3FGL-like survey.

5. Discussion

5.1. Estimated population of gamma-ray binaries

We explored two ways to estimate the number of gamma-ray binaries. The first (Sect. 3.3) employed the light curves of the known systems as templates to evaluate the detection probability of identical systems distributed throughout the Galaxy. The results show that systems such as LS 5039, LSI+61°303, LMC P3, and 1FGL J1018.6-5856 are already detectable throughout most of the Galaxy, therefore it is highly unlikely that more than one or two have escaped notice (Table 3). Future HE detections are more likely to be of low duty cycle systems, such as PSR B1259-63, the total number of which is estimated at 7^{+26}_{-6} . One such anticipated detection is that of PSR J2032+4127, which is a 2×10^{35} erg s⁻¹ pulsar in an eccentric, >20 yr orbit around a Be star that will pass periastron in late 2017 (Lyne et al. 2015; Ho et al. 2017)⁷. The largest source of uncertainty is the number of HESS J0632+057-like systems with a ratio of TeV to GeV luminosity about two orders of magnitude higher than the other binaries (see Table 3 and Li et al. 2017). There may be as many as ≈ 230 such systems in our Galaxy; this is an upper limit that CTA will decrease to 8^{+30}_{-7} if none are discovered in the full Galactic Plane survey (Sect. 3.3).

The known systems represent only the upper end of the luminosity function of gamma-ray binaries. Thus, our second estimate for the number of gamma-ray binaries employed a full population model based on a series of assumptions on the radiative process, distributions of orbital parameters, and injected power (Sect. 4). In the HE domain, with four systems in the 3FGL and FAVA surveys (Table 1, excluding LMC P3 since it is not in the Galactic plane), the total parent population is estimated at 82^{+108}_{-56} systems based on the detection fraction in Table 5. In the VHE domain, with only LS 5039 detected in the H.E.S.S. survey, the parent population is constrained to 85^{+290}_{-81} systems. Combining all the information in Table 1 into the likelihood function, i.e. assuming four systems in the HE surveys, one system in H.E.S.S., none in HAWC, and at least five in the full CTA survey, the population is estimated at 101^{+89}_{-52} gamma-ray binaries in our Galaxy. These numbers are consistent with the predictions from population synthesis of HMXBs (Sect. 1).

Gamma-ray surveys are $\geq 50\%$ complete for $\dot{E} \geq 10^{36}$ erg s⁻¹ (Fig. 6), but they access only a handful of systems in a population of about a hundred binaries. A few additional systems, such as PSR J2032+4127, may be detected through their pulsed gamma-ray emission without showing binary-related

gamma-ray emission. We have not attempted to take this into account. The spin-down distribution of detected *Fermi*-LAT pulsars peaks at $\log \dot{E} = 35.5$ (see Sect. 5.2 below), suggesting this is unlikely to make a difference to the number of systems detected in gamma rays. A couple dozen binaries may be visible as accreting X-ray sources, indistinguishable from other HMXBs except perhaps through their neutron star spin periods or through propeller-induced behaviour. SAX J0635+0533 (Cusumano et al. 2000) and A0538-66 (Skinner et al. 1982) are possible examples. These two systems clearly have much faster spin periods (<70 ms) than all the other known X-ray pulsars in HMXBs (>1 to 1000 s), suggesting that the neutron star may not yet have spun down significantly from its birth period.

PSR J0045-7319, PSR J1638-4725, and PSR J1740-3052 are representative of the low \dot{E} systems that represent the majority of the pulsar plus massive star population: $\approx 55\%$ of the sampled systems have $\dot{E} \leq 10^{34}$ erg s⁻¹ and are not accreting. Adding in the 23% that are accreting, this implies that 78% of the population is inaccessible to gamma-ray surveys. Estimating their detection rate in radio (SKA) or X-ray surveys (eROSITA) is beyond the scope of this work, but we note that the long P_{orb} , high eccentricity systems are clearly more susceptible to be detected as radio pulsars (Lipunov et al. 1994), providing a complementary way to access the pulsar plus massive star population.

5.2. Systematic uncertainties in the population synthesis

How dependent are our results on the assumptions of the model? The Galactic distribution and binary parameters should not be a major source of concern since these have already been scrutinized in population studies of high-mass X-ray binaries (Walter et al. 2015). The distribution of \dot{E} for gamma-ray binaries is entirely unknown and taking as input the \dot{E} distribution of young pulsars in the ATNF catalogue probably suffers from a variety of selection biases; such biases are notably because it is not obvious that the birth spin period and evolution should be identical in isolated pulsars and binaries – if only because mass loss and kick during the supernova are necessarily weaker if the newly born neutron star is to remain bound to its companion. Yet, our assumption on \dot{E} is not likely to have a major impact on gamma-ray observations since these are mostly sensitive to the high end of this distribution. The \dot{E} distribution of detected binaries (Fig. 5) actually resembles the \dot{E} distribution of young pulsars detected in gamma rays with the *Fermi*-LAT⁸, which we find to be well approximated by a Gaussian centred at $\log \dot{E} = 35.5$ with a standard deviation $\sigma = 1$. Taking this distribution as input increases the detection fraction, decreasing the population size inferred from current observations without changing much the number of expected detections in future surveys. However, this distribution cannot account for the known radio pulsars in orbit around massive stars with low \dot{E} . The strongest impact of our assumption on the \dot{E} distribution is therefore on the relative numbers of pulsar plus massive star binaries that are found in radio and gamma-ray surveys.

The light curves of gamma-ray binaries have proven difficult to model, even in the cases in which we have the most information, questioning the validity of our radiative model. For instance, relativistic beaming of the emission is thought to be an important factor in shaping the light curves (e.g. An & Romani 2017). A refined light curve model is desirable but may not change our results much. First, despite its

⁷ PSR J2032+4127 is a pulsed *Fermi*-LAT source and coincident with an extended, persistent VHE source. This source does not yet show evidence for variable gamma-ray emission related to binary motion, as seen in PSR B1259-63 and the other gamma-ray binaries.

⁸ <https://confluence.slac.stanford.edu/display/GLAMCOG/Public+List+of+LAT+Detected+Gamma-Ray+Pulsars>

simplicity, the detection fractions inferred from the model are broadly consistent with those inferred from the observed light curves (Sect. 3.1). Its main shortcoming is that it predicts lower amplitudes than observed, overestimating detection rates for PSR B1259-63-like systems. However, these do not dominate the detected systems (Fig. 6). Second, we experimented with a more complex radiative model, using a power-law distribution of particles and including Doppler boosting (assuming a particle bulk velocity of $c/3$ directed away from the star as in Dubus et al. 2010). There was surprisingly little difference between the detection fractions shown in Fig. 5 and those obtained with the more complex model despite substantial changes to the light curves from relativistic Doppler boosting, indicating that the flux level is more important than the detailed shape of the light curve in setting the detection fractions.

Improvements to our radiative model should thus concentrate on the injected power P_{inj} and the radiative efficiency $\tau_{\text{esc}}/\tau_{\text{ic}}$, both of which set the flux level. A longer escape timescale increases the radiative efficiency but this needs to be compensated by a lower fraction P_{inj}/\dot{E} in order to match the maximum flux from PSR B1259-63 (Sect. 4.4). For example, taking $\tau_{\text{esc}} = 10d/c$ implies a decreased injection fraction ($P_{\text{GeV}} \approx 0.02\dot{E}$ and $P_{\text{TeV}} \approx 0.002\dot{E}$). The combination yields an estimated population of 105^{+92}_{-54} systems, i.e. very close to our previous estimate of 101^{+89}_{-52} . The peak of the gamma-ray flux distribution is pushed to longer periods than in Fig. 3, leading to a flatter distribution in the fraction of detected systems as a function of P_{orb} . In principle, the P_{orb} distribution of detected gamma-ray binaries could thus be used to constrain τ_{esc} , assuming excellent knowledge of their parent P_{orb} distribution. A distribution of L_{γ}/\dot{E} as a function of P_{orb} would narrow down possibilities for the radiative and injection efficiency, which are presently only constrained by observations of PSR B1259-63. Gamma-ray observations of PSR J2032+4127 at periastron passage provide a second constraint on these efficiencies. Inversely, future observations of gamma-ray binaries as a population also have the potential to constrain the relative efficiencies in the GeV and TeV range, as described below (Sect. 5.3).

Many of our results remain applicable even if gamma-ray binaries are not powered by pulsar spin-down. The results of Sect. 3, based on the template light curves, do not depend on this assumption. The results of Sects. 4.1–4.3 are also applicable as long as the emission arises from electrons located close to the compact object (e.g. at the base of a jet) upscattering stellar radiation. Even if the compact object is a black hole, the compact object mass remains much lower than the companion mass, so any difference in orbits is minor for the radiation model. However, differences can be expected in the full population model (Sect. 4.4) since we made use of the distribution of spin-down powers of pulsars. We would need some assumptions on the distribution of jet power to perform an equivalent calculation and deduce the parent population. However, as stated in the introduction, we consider it very unlikely that gamma-ray binary emission arises from accretion-powered jets (Dubus 2013).

5.3. Future gamma-ray observations

We have aimed to discover what future observations hold in store. With an estimated population size of 101 gamma-ray binaries, up to 8 new binaries might be detected in an extended 3FGL survey with a most likely value of 2 new detections beyond the known sample. New discoveries are less likely in the VHE surveys. Once the expected detections (Table 1) are taken

into account – up to 3 new detections are predicted in the HAWC survey, 5 in the initial CTA survey, and 6 in the full CTA survey, with 95% confidence limits – the most likely outcome statistically is no new detection. The reason is that the detection probabilities remain small for these surveys.

Serendipitous discoveries in deep VHE observations of Galactic sources (e.g. HESS J0632+057) can complement the surveys. We find that the probability for a chance detection of a gamma-ray binary is $0.17 \pm 0.03\%$ in a 100 h CTA exposure towards the Galactic centre, covering 6° in Galactic longitude, and reaching 1 mCrab at 1 TeV. This is ≈ 1.7 times the detection rate from the Galactic Plane survey over a comparable area, i.e. there are roughly 7 previously undetected systems for every 10 systems detected in the Galactic Plane survey of this deep field. Having 20 such deep pointings, spread around the Galactic plane towards areas of special interest such as the Galactic centre, the Cygnus and Westerlund regions, or the Sagittarius-Carina spiral arm (see Fig. 2), adds 1.4% to the detected fraction with CTA. Combining surveys and deep pointings can thus yield a detection rate that is comparable to or greater than that in the Fermi-LAT survey.

Any discovery in a VHE survey would have a major impact on the estimated population number, raising it to higher values. A discrepancy could appear between the actual number of sources detected in the VHE and HE surveys since the model predicts that essentially all TeV sources should be detected at GeV energies. Some tension is already present in the model. The maximum likelihood L_m obtained by treating the HE and VHE surveys independently is $\geq 20\%$ for both, with corresponding population numbers of 82^{+108}_{-56} (HE) and 132^{+268}_{-86} (VHE). Combining the HE and VHE numbers into a single likelihood gives the estimate of 101^{+89}_{-52} systems presented above, but L_m drops to 4%. This low probability indicates that the model has difficulty accounting for both the number of GeV and TeV detections when they are taken from the same underlying binary population. This can be resolved by increasing the injection fraction P_{inj} at 1 TeV, with the effect of raising the detection probability in VHE surveys and lowering the parent population size to a value that slackens the tension with the HE constraints, or by lowering it at 1 GeV with opposite effects on detection probability and population size. Hence, the relative numbers of HE and VHE detections can constrain the relative injection efficiencies. In any case, regardless of the value of P_{inj} , the population of VHE-emitting systems is unlikely to be greater than 230 systems, otherwise HESS J0632+057-like systems would be detected in the 3FGL survey or in the H.E.S.S. Galactic Plane survey (Sect. 3.3). This number is close to the upper limit on the population size estimated from synthetic light curves (190 systems). Both estimates thus converge to a maximum gamma-ray binary population of ≈ 200 systems. With 200 systems, up to 10 (resp. 14) new binaries could be detected in the initial (resp. full) CTA survey, where the most likely number is 4 (resp. 6) discoveries.

6. Conclusions

We have modelled the population of gamma-ray binaries and evaluated the fraction of systems that can be detected in various HE and VHE surveys, taking into account the variability of their gamma-ray emission. The number of gamma-ray binaries is constrained to 101^{+89}_{-52} systems in our Galaxy. This number matches expectations from HMXB population synthesis.

Gamma-ray binaries are rare systems and we do not expect a watershed of discoveries in the near future. Pursuing the

Fermi-LAT survey to ≈ 2024 should lead to a handful of discoveries of mostly PSR B1259-63-like systems. At very high energies, combining Galactic Plane surveys and deep observations of Galactic sources with CTA should provide a comparable number of discoveries. However, the number of HESS J0632+057-like systems with very weak GeV emission is a major source of uncertainty. Observations already indicate that the GeV and TeV emission originate from different particle populations. A VHE survey could therefore reveal a population of binaries that cannot be seen with the *Fermi*-LAT. Such a population is limited to $\lesssim 230$ systems based on the lack of HESS J0632+057-like systems in the *Fermi*-LAT 3FGL survey and the H.E.S.S. Galactic Plane survey. With 200 systems, four new gamma-ray binaries can be expected in the first two years of the CTA Galactic Plane survey. Of course, these numbers refer only to gamma-ray binaries and do not limit gamma-ray detections from other types of binaries such as novae, colliding wind binaries, binary millisecond pulsars, and microquasars.

Detecting a system depends more on its orbit-averaged flux than on the shape of the gamma-ray light curve. Thus, the scheduling of visits from ground-based instruments plays a minor role in setting the detected fraction. The average flux is set by the efficiency with which spin-down power is radiated in the HE and VHE bands. This is the most important source of uncertainty in our model. Ideally, this should be constrained by measuring the pulsar spin-down power and radiated luminosity for as many systems as possible. At present, this is limited to PSR B1259-63 with the possible addition of PSR J2032+4127 in the near future. Alternatively, this relative efficiency in the HE and VHE bands can be constrained statistically by the relative number of sources detected in HE and VHE surveys.

About 55% of pulsars in orbit around massive stars are hardly accessible to gamma-ray observations, which are most sensitive to the high \dot{E} , short P_{orb} systems. Low \dot{E} and long P_{orb} binaries are likely to be more efficiently accessed by radio pulsar surveys, which are thus fully complementary to the gamma-ray observations. Another significant fraction, $\approx 23\%$, may actually be visible as accreting X-ray pulsars or propellers instead of binary pulsar wind nebulae. Future work should strive to combine detection probabilities in gamma rays with detection probabilities in radio (SKA) and X-ray (eROSITA) surveys.

Acknowledgements. We are grateful to Masha Chernyakova, Markus Böttcher, and Jamie Holder for their careful CTA internal review that helped improve this work. G.D. and P.O.P. acknowledge support from Centre National d'Etudes Spatiales (CNES).

References

- Abdo, A. A., Ackermann, M., Ajello, M., et al. (Fermi-LAT Collaboration) 2009, *ApJ*, 706, L56
- Abdollahi, S., Ackermann, M., Ajello, M., et al. (Fermi-LAT Collaboration) 2017, *ApJ*, 846, 34
- Abeysekara, A. U., Albert, A., Alfaro, R., et al. (HAWC Collaboration) 2017, *ApJ*, 843, 40
- Abramowski, A., Aharonian, F., Ait Benkhali, F., et al. (H.E.S.S. Collaboration) 2015, *A&A*, 577, A131
- Acciari, V. A., Aliu, E., Arlen, T., et al. (VERITAS Collaboration) 2011, *ApJ*, 738, 3
- Acerro, F., Ackermann, M., Ajello, M., et al. (Fermi-LAT Collaboration) 2015, *ApJS*, 218, 23
- Ackermann, M., Ajello, M., Ballet, J., et al. (Fermi-LAT Collaboration) 2012, *Science*, 335, 189
- Ackermann, M., Ajello, M., Ballet, J., et al. (Fermi-LAT Collaboration) 2013, *ApJ*, 773, L35
- Aharonian, F., Akhperjanian, A. G., Bazer-Bachi, A. R., et al. (H.E.S.S. Collaboration) 2006, *A&A*, 460, 743
- Albert, J., Aliu, E., Anderhub, H., et al. (MAGIC Collaboration) 2008, *ApJ*, 674, 1037
- Aliu, E., Archambault, S., Aune, T., et al. (VERITAS and H.E.S.S. Collaborations) 2014, *ApJ*, 780, 168
- Ambartsumian, V. A. 1937, *Astron. Zhurn.*, 14, 207
- An, H., & Romani, R. W. 2017, *ApJ*, 838, 145
- Bassa, C. G., Brisken, W. F., Nelemans, G., et al. 2011, *MNRAS*, 412, L63
- Bhadkamkar, H., & Ghosh, P. 2012, *ApJ*, 746, 22
- Bordas, P., Dubus, G., Eger, P., et al., 2017, in 6th International Meeting on High-Energy Gamma-Ray Astronomy, AIP Conf. Proc., 1792, 040017
- Campana, S., Stella, L., Mereghetti, S., & Colpi, M. 1995, *A&A*, 297, 385
- Carramiñana, A. 2016, *J. Phys. Conf. Ser.*, 761, 012034
- Corbet, R. H. D., Chomiuk, L., Coe, M. J., et al. 2016, *ApJ*, 829, 105
- Cusumano, G., Maccarone, M. C., Nicastro, L., Sacco, B., & Kaaret, P. 2000, *ApJ*, 528, L25
- Dubus, G. 2006, *A&A*, 451, 9
- Dubus, G. 2013, *A&ARv*, 21, 64
- Dubus, G., Cerutti, B., & Henri, G. 2010, *A&A*, 516, A18
- Dubus, G., Lamberts, A., & Fromang, S. 2015, *A&A*, 581, A27
- Gregory, P. C., & Taylor, A. R. 1978, *Nature*, 272, 704
- Grimm, H.-J., Gilfanov, M., & Sunyaev, R. 2002, *A&A*, 391, 923
- Hadasch, D., Torres, D. F., Tanaka, T., et al. 2012, *ApJ*, 749, 54
- Hinton, J. A., Skilton, J. L., Funk, S., et al. 2009, *ApJ*, 690, L101
- Ho, W. C. G., Ng, C.-Y., Lyne, A. G., et al. 2017, *MNRAS*, 464, 1211
- Iben, I. J., Tutukov, A. V., & Yungelson, L. R. 1995, *ApJS*, 100, 217
- Illarionov, A. F., & Sunyaev, R. A. 1975, *A&A*, 39, 185
- Johnston, S., Manchester, R. N., Lyne, A. G., et al. 1992, *ApJ*, 387, L37
- Li, J., Torres, D. F., Cheng, K.-S., et al. 2017, *ApJ*, submitted [[arXiv:1707.04280](https://arxiv.org/abs/1707.04280)]
- Lipunov, V. M., Nazin, S. N., Osminkin, E. Y., & Prokhorov, M. E. 1994, *A&A*, 282, 61
- Lutovinov, A. A., Revnivtsev, M. G., Tsygankov, S. S., & Krivonos, R. A. 2013, *MNRAS*, 431, 327
- Lyne, A. G., Stappers, B. W., Keith, M. J., et al. 2015, *MNRAS*, 451, 581
- Madsen, E. C., Stairs, I. H., Kramer, M., et al. 2012, *MNRAS*, 425, 2378
- Malyshev, D., & Chernyakova, M. 2016, *MNRAS*, 463, 3074
- Manchester, R. N., Hobbs, G. B., Teoh, A., & Hobbs, M. 2005, *AJ*, 129, 1993
- Massi, M., Migliari, S., & Chernyakova, M. 2017, *MNRAS*, 468, 3689
- Meurs, E. J. A., & van den Heuvel, E. P. J. 1989, *A&A*, 226, 88
- Moe, M., & Di Stefano, R. 2017, *ApJS*, 230, 15
- Paredes, J. M., Martí, J., Ribó, M., & Massi, M. 2000, *Science*, 288, 2340
- Portegies Zwart, S. F., & Verbunt, F. 1996, *A&A*, 309, 179
- Portegies Zwart, S. F., & Yungelson, L. R. 1998, *A&A*, 332, 173
- Ringermacher, H. I., & Mead, L. R. 2009, *MNRAS*, 397, 164
- Russeil, D. 2003, *A&A*, 397, 133
- Shvartsman, V. F. 1971, *Soviet Astron.*, 15, 342
- Skinner, G. K., Bedford, D. K., Elsner, R. F., et al. 1982, *Nature*, 297, 568
- Stairs, I. H., Manchester, R. N., Lyne, A. G., et al. 2001, *MNRAS*, 325, 979
- Tauris, T. M., & van den Heuvel, E. P. J. 2006, in Compact Stellar X-ray Sources, eds. W. H. G. Lewin, & M. van der Klis (Cambridge, UK: Cambridge University Press), *Cambridge Astrophys. Ser.*, 39, 623
- Vercellone, S. 2017, in 6th International Meeting on High-Energy Gamma-Ray Astronomy, AIP Conf. Proc., 1792, 030001
- Walter, R., Lutovinov, A. A., Bozzo, E., & Tsygankov, S. S. 2015, *A&ARv*, 23, 2

Appendix A: Example synthetic light curves

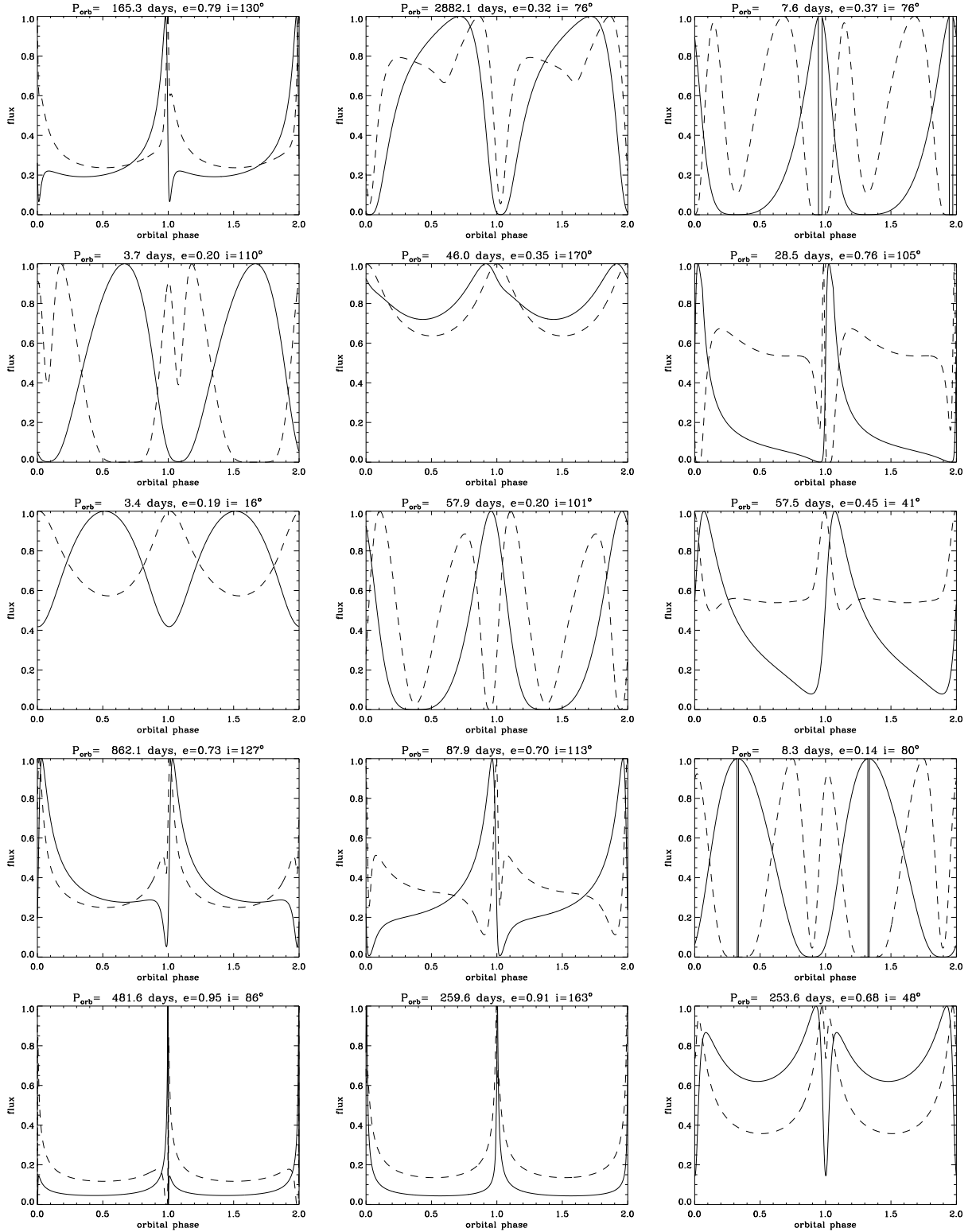


Fig. A.1. Example lightcurves computed from the model described in Sect. 4.2 (full line: GeV emission; dashed line: TeV emission, taking into account $\gamma\gamma$ absorption). The orbital period and eccentricity of the binary system is indicated in the title of each plot. The lightcurves are normalised to the maximum value. The systems shown here are a random selection of the systems flagged as detected in Fig. 6. Periastron passage is at phase 0.

Bibliography

- Agarwal M., Milosavljević M. 2011. “Nuclear Star Clusters from Clustered Star Formation”. *ApJ*, **729**:35. [ADS].
- Agertz O., Kravtsov A.V. 2015. “On the Interplay between Star Formation and Feedback in Galaxy Formation Simulations”. *ApJ*, **804**:18. [ADS].
- Agertz O., Kravtsov A.V. 2016. “The Impact of Stellar Feedback on the Structure, Size, and Morphology of Galaxies in Milky-Way-sized Dark Matter Halos”. *ApJ*, **824**:79. [ADS].
- Agertz O., Kravtsov A.V., Leitner S.N., Gnedin N.Y. 2013. “Toward a Complete Accounting of Energy and Momentum from Stellar Feedback in Galaxy Formation Simulations”. *ApJ*, **770**:25. [ADS].
- Andersen D.R., Walcher C.J., Böker T., Ho L.C., van der Marel R.P., Rix H.W., Shields J.C. 2008. “Caught in Formation: The Nuclear-Cluster-to-Be in NGC 2139”. *ApJ*, **688**:990–999. [ADS].
- Antonini F. 2013. “Origin and Growth of Nuclear Star Clusters around Massive Black Holes”. *ApJ*, **763**:62. [ADS].
- Antonini F., Barausse E., Silk J. 2015. “The Coevolution of Nuclear Star Clusters, Massive Black Holes, and Their Host Galaxies”. *ApJ*, **812**:72. [ADS].
- Arata S., Yajima H., Nagamine K. 2018. “Gas clump formation via thermal instability in high-redshift dwarf galaxy mergers”. *MNRAS*, **475**:4252–4262. [ADS].
- Arca-Sedda M., Capuzzo-Dolcetta R. 2014. “The globular cluster migratory origin of nuclear star clusters”. *MNRAS*, **444**:3738–3755. [ADS].
- Arca-Sedda M., Capuzzo-Dolcetta R., Antonini F., Seth A. 2015. “Henize 2-10: The Ongoing Formation of a Nuclear Star Cluster around a Massive Black Hole”. *ApJ*, **806**:220. [ADS].
- Arca-Sedda M., Capuzzo-Dolcetta R., Spera M. 2016. “The dearth of nuclear star clusters in bright galaxies”. *MNRAS*, **456**:2457–2466. [ADS].

- Arzoumanian D., André P., Didelon P., Könyves V., Schneider N., Men'shchikov A., Soubie T., Zavagno A., Bontemps S., di Francesco J., et al. 2011. “Characterizing interstellar filaments with Herschel in IC 5146”. *A&A*, **529**:L6. [ADS].
- Ashman K.M., Zepf S.E. 1992. “The formation of globular clusters in merging and interacting galaxies”. *ApJ*, **384**:50–61. [ADS].
- Athanassoula E. 1992. “The existence and shapes of dust lanes in galactic bars”. *MNRAS*, **259**:345–364. [ADS].
- Audit E., Hennebelle P. 2010. “On the structure of the turbulent interstellar clouds . Influence of the equation of state on the dynamics of 3D compressible flows”. *A&A*, **511**:A76. [ADS].
- Bacon R., Copin Y., Monnet G., Miller B.W., Allington-Smith J.R., Bureau M., Carollo C.M., Davies R.L., Emsellem E., Kuntschner H., et al. 2001. “The SAURON project - I. The panoramic integral-field spectrograph”. *MNRAS*, **326**:23–35. [ADS].
- Barnes J., Efstathiou G. 1987. “Angular momentum from tidal torques”. *ApJ*, **319**:575–600. [ADS].
- Bastian N. 2016. “Young Massive Clusters: Their Population Properties, Formation and Evolution, and Their Relation to the Ancient Globular Clusters”. In *EAS Publications Series*, edited by E. Moraux, Y. Lebreton, C. Charbonnel, volume 80 of *EAS Publications Series*, pages 5–37. [ADS].
- Bastian N., Schweizer F., Goudfrooij P., Larsen S.S., Kissler-Patig M. 2013. “Luminosity profiles and sizes of massive star clusters in NGC 7252”. *MNRAS*, **431**:1252–1263. [ADS].
- Behrendt M., Burkert A., Schartmann M. 2016. “Clusters of Small Clumps Can Explain the Peculiar Properties of Giant Clumps in High-redshift Galaxies”. *ApJ*, **819**:L2. [ADS].
- Behroozi P.S., Wechsler R.H., Conroy C. 2013. “The Average Star Formation Histories of Galaxies in Dark Matter Halos from $z = 0-8$ ”. *ApJ*, **770**:57. [ADS].
- Bennert V.N., Auger M.W., Treu T., Woo J.H., Malkan M.A. 2011. “The relation between black hole mass and host spheroid stellar mass out to $z \sim 2$ ”. *The Astrophysical Journal*, **742**(2):107.
- Beuther H., Soler J., Vlemmings W., Linz H., Henning T., Kuiper R., Rao R., Smith R., Sakai T., Johnston K., et al. 2018. “Magnetic fields at the onset of high-mass star formation”. *ArXiv e-prints*. [ADS].
- Blumenthal G.R., Faber S.M., Primack J.R., Rees M.J. 1984. “Formation of galaxies and large-scale structure with cold dark matter”. *Nature*, **311**:517–525. [ADS].

- Bode P., Ostriker J.P., Turok N. 2001. “Halo Formation in Warm Dark Matter Models”. *ApJ*, **556**:93–107. [ADS].
- Boily C.M., Kroupa P. 2003. “The impact of mass loss on star cluster formation - I. Analytical results”. *MNRAS*, **338**:665–672. [ADS].
- Böker T. 2010. “Nuclear star clusters”. In *Star Clusters: Basic Galactic Building Blocks Throughout Time and Space*, edited by R. de Grijs, J.R.D. Lépine, volume 266 of *IAU Symposium*, pages 58–63. [ADS].
- Böker T., Laine S., van der Marel R.P., Sarzi M., Rix H.W., Ho L.C., Shields J.C. 2002. “A Hubble Space Telescope Census of Nuclear Star Clusters in Late-Type Spiral Galaxies. I. Observations and Image Analysis”. *AJ*, **123**:1389–1410. [ADS].
- Böker T., Sarzi M., McLaughlin D.E., van der Marel R.P., Rix H.W., Ho L.C., Shields J.C. 2004. “A Hubble Space Telescope Census of Nuclear Star Clusters in Late-Type Spiral Galaxies. II. Cluster Sizes and Structural Parameter Correlations”. *AJ*, **127**:105–118. [ADS].
- Bournaud F., Duc P.A., Emsellem E. 2008. “High-resolution simulations of galaxy mergers: resolving globular cluster formation”. *MNRAS*, **389**:L8–L12. [ADS].
- Bournaud F., Elmegreen B.G., Teyssier R., Block D.L., Puerari I. 2010. “ISM properties in hydrodynamic galaxy simulations: turbulence cascades, cloud formation, role of gravity and feedback”. *MNRAS*, **409**:1088–1099. [ADS].
- Bourne M.A., Power C. 2016. “Simulating feedback from nuclear clusters: the impact of multiple sources”. *MNRAS*, **456**:L20–L24. [ADS].
- Bresolin F., Gieren W., Kudritzki R.P., Pietrzyński G., Urbaneja M.A., Carraro G. 2009. “Extragalactic Chemical Abundances: Do H II Regions and Young Stars Tell the Same Story? The Case of the Spiral Galaxy NGC 300”. *ApJ*, **700**:309–330. [ADS].
- Bullock J.S., Dekel A., Kolatt T.S., Kravtsov A.V., Klypin A.A., Porciani C., Primack J.R. 2001. “A Universal Angular Momentum Profile for Galactic Halos”. *ApJ*, **555**:240–257. [ADS].
- Busch G., Eckart A., Valencia-S. M., Fazeli N., Scharwächter J., Combes F., García-Burillo S. 2017. “Star formation and gas flows in the centre of the NUGA galaxy $\text{[AS-TROBJ}_{\text{NGC 1808}}\text{]}/\text{[ASTROBJ}_{\text{NGC 1808}}\text{]}$ observed with SINFONI”. *A&A*, **598**:A55. [ADS].
- Butler M.J., Tan J.C., Teyssier R., Rosdahl J., Van Loo S., Nickerson S. 2017. “Kiloparsec-scale Simulations of Star Formation in Disk Galaxies. IV. Regulation of Galactic Star Formation Rates by Stellar Feedback”. *ApJ*, **841**:82. [ADS].
- Bykov A.M., Ellison D.C., Gladilin P.E., Osipov S.M. 2017. “Supernovae in compact star clusters as sources of high-energy cosmic rays and neutrinos”. *ArXiv e-prints*. [ADS].

- Camps-Fariña A., Zaragoza-Cardiel J., Beckman J.E., Font J., Velázquez P.F., Rodríguez-González A., Rosado M. 2017. “Physical properties of superbubbles in the Antennae galaxies”. *MNRAS*, **468**:4134–4142. [ADS].
- Cappellari M. 2008. “Measuring the inclination and mass-to-light ratio of axisymmetric galaxies via anisotropic Jeans models of stellar kinematics”. *MNRAS*, **390**:71–86. [ADS].
- Cappellari M. 2016. “Structure and Kinematics of Early-Type Galaxies from Integral Field Spectroscopy”. *ARA&A*, **54**:597–665. [ADS].
- Cappellari M., Copin Y. 2003. “Adaptive spatial binning of integral-field spectroscopic data using Voronoi tessellations”. *MNRAS*, **342**:345–354. [ADS].
- Cappellari M., Emsellem E. 2004. “Parametric Recovery of Line-of-Sight Velocity Distributions from Absorption-Line Spectra of Galaxies via Penalized Likelihood”. *PASP*, **116**:138–147. [ADS].
- Cappellari M., Emsellem E., Krajnović D., McDermid R.M., Scott N., Verdoes Kleijn G.A., Young L.M., Alatalo K., Bacon R., Blitz L., et al. 2011a. “The ATLAS^{3D} project - I. A volume-limited sample of 260 nearby early-type galaxies: science goals and selection criteria”. *MNRAS*, **413**:813–836. [ADS].
- Cappellari M., Emsellem E., Krajnović D., McDermid R.M., Serra P., Alatalo K., Blitz L., Bois M., Bournaud F., Bureau M., et al. 2011b. “The ATLAS^{3D} project - VII. A new look at the morphology of nearby galaxies: the kinematic morphology-density relation”. *MNRAS*, **416**:1680–1696. [ADS].
- Capuzzo-Dolcetta R., Mocchi P. 2008. “Self-consistent simulations of nuclear cluster formation through globular cluster orbital decay and merging”. *MNRAS*, **388**:L69–L73. [ADS].
- Carignan C. 1985. “Surface photometry of the sculptor group galaxies - NGC 7793, NGC 247, and NGC 300”. *ApJS*, **58**:107–124. [ADS].
- Carollo C.M., Stiavelli M., Mack J. 1998. “Spiral Galaxies with WFPC2. II. The Nuclear Properties of 40 Objects”. *AJ*, **116**:68–84. [ADS].
- Carson D.J., Barth A.J., Seth A.C., den Brok M., Cappellari M., Greene J.E., Ho L.C., Neumayer N. 2015. “The Structure of Nuclear Star Clusters in Nearby Late-type Spiral Galaxies from Hubble Space Telescope Wide Field Camera 3 Imaging”. *AJ*, **149**:170. [ADS].
- Cava A., Schaerer D., Richard J., Pérez-González P.G., Dessauges-Zavadsky M., Mayer L., Tamburello V. 2018. “The nature of giant clumps in distant galaxies probed by the anatomy of the cosmic snake”. *Nature Astronomy*, **2**:76–82. [ADS].

- Chandar R., Whitmore B.C., Calzetti D., Di Nino D., Kennicutt R.C., Regan M., Schinnerer E. 2011. “New Constraints on Mass-dependent Disruption of Star Clusters in M51”. *ApJ*, **727**:88. [ADS].
- Chandrasekhar S. 1943. “Dynamical Friction. I. General Considerations: the Coefficient of Dynamical Friction.” *ApJ*, **97**:255. [ADS].
- Cole D.R., Debattista V.P. 2016. “Nuclear Star Clusters and Bulges”. *Galactic Bulges*, **418**:107. [ADS].
- Cole D.R., Debattista V.P., Varri A.L., Hartmann M., Seth A.C. 2016. “Spatial and kinematic segregation in star cluster merger remnants”. *ArXiv e-prints*. [ADS].
- Côté P., Piatek S., Ferrarese L., Jordán A., Merritt D., Peng E.W., Hasegan M., Blakeslee J.P., Mei S., West M.J., et al. 2006. “The ACS Virgo Cluster Survey. VIII. The Nuclei of Early-Type Galaxies”. *ApJS*, **165**:57–94. [ADS].
- Courty S., Alimi J.M. 2004. “Thermodynamic evolution of cosmological baryonic gas. I. Influence of non-equipartition processes”. *A&A*, **416**:875–888. [ADS].
- Cresci G., Mannucci F., Maiolino R., Marconi A., Gnerucci A., Magrini L. 2010. “Gas accretion as the origin of chemical abundance gradients in distant galaxies”. *Nature*, **467**:811–813. [ADS].
- Daddi E., Bournaud F., Walter F., Dannerbauer H., Carilli C.L., Dickinson M., Elbaz D., Morrison G.E., Riechers D., Onodera M., et al. 2010. “Very High Gas Fractions and Extended Gas Reservoirs in $z = 1.5$ Disk Galaxies”. *ApJ*, **713**:686–707. [ADS].
- Dale J.E. 2017. “The effect of the virial state of molecular clouds on the influence of feedback from massive stars”. *MNRAS*, **467**:1067–1082. [ADS].
- Dale J.E., Ercolano B., Bonnell I.A. 2012. “Ionizing feedback from massive stars in massive clusters - II. Disruption of bound clusters by photoionization”. *MNRAS*, **424**:377–392. [ADS].
- Dalla Vecchia C., Schaye J. 2008. “Simulating galactic outflows with kinetic supernova feedback”. *MNRAS*, **387**:1431–1444. [ADS].
- Deharveng L., Caplan J., Lequeux J., Azzopardi M., Breysacher J., Tarenghi M., Westerlund B. 1988. “H II regions in NGC 300”. *Astron. & Astrophys. Suppl. Ser.*, **73**:407–423. [ADS].
- den Brok M., Peletier R.F., Seth A., Balcells M., Dominguez L., Graham A.W., Carter D., Erwin P., Ferguson H.C., Goudfrooij P., et al. 2014. “The HST/ACS Coma Cluster Survey - X. Nuclear star clusters in low-mass early-type galaxies: scaling relations”. *MNRAS*, **445**:2385–2403. [ADS].

- Dias W.S., Alessi B.S., Moitinho A., Lépine J.R.D. 2002. “New catalogue of optically visible open clusters and candidates”. *A&A*, **389**:871–873. [ADS].
- Dubois Y., Teyssier R. 2008. “On the onset of galactic winds in quiescent star forming galaxies”. *A&A*, **477**:79–94. [ADS].
- Eisenhauer F., Abuter R., Bickert K., Biancat-Marchet F., Bonnet H., Brynnel J., Conzelmann R.D., Delabre B., Donaldson R., Farinato J., et al. 2003. “SINFONI - Integral field spectroscopy at 50 milli-arcsecond resolution with the ESO VLT”. In *Instrument Design and Performance for Optical/Infrared Ground-based Telescopes*, edited by M. Iye, A.F.M. Moorwood, volume 4841 of *Proc. SPIE*, pages 1548–1561. [ADS].
- Eisenstein D.J., Hut P. 1998. “HOP: A New Group-Finding Algorithm for N-Body Simulations”. *ApJ*, **498**:137–142. [ADS].
- El-Badry K., Wetzel A., Geha M., Hopkins P.F., Kereš D., Chan T.K., Faucher-Giguère C.A. 2016. “Breathing FIRE: How Stellar Feedback Drives Radial Migration, Rapid Size Fluctuations, and Population Gradients in Low-mass Galaxies”. *ApJ*, **820**:131. [ADS].
- Elmegreen B.G. 2011. “On the Initial Conditions for Star Formation and the Initial Mass Function”. *ApJ*, **731**:61. [ADS].
- Emsellem E., Cappellari M., Krajnović D., Alatalo K., Blitz L., Bois M., Bournaud F., Bureau M., Davies R.L., Davis T.A., et al. 2011. “The ATLAS^{3D} project - III. A census of the stellar angular momentum within the effective radius of early-type galaxies: unveiling the distribution of fast and slow rotators”. *MNRAS*, **414**:888–912. [ADS].
- Emsellem E., Cappellari M., Krajnović D., van de Ven G., Bacon R., Bureau M., Davies R.L., de Zeeuw P.T., Falcón-Barroso J., Kuntschner H., et al. 2007. “The SAURON project - IX. A kinematic classification for early-type galaxies”. *MNRAS*, **379**:401–417. [ADS].
- Emsellem E., Monnet G., Bacon R. 1994. “The multi-gaussian expansion method: a tool for building realistic photometric and kinematical models of stellar systems I. The formalism”. *A&A*, **285**:723–738. [ADS].
- Emsellem E., Renaud F., Bournaud F., Elmegreen B., Combes F., Gabor J.M. 2015. “The interplay between a galactic bar and a supermassive black hole: nuclear fuelling in a subparsec resolution galaxy simulation”. *MNRAS*, **446**:2468–2482. [ADS].
- Faesi C.M., Lada C.J., Forbrich J., Menten K.M., Bouy H. 2014. “Molecular Cloud-scale Star Formation in NGC 300”. *ApJ*, **789**:81. [ADS].
- Fall S.M., Efstathiou G. 1980. “Formation and rotation of disc galaxies with haloes”. *MNRAS*, **193**:189–206. [ADS].

- Feldmeier-Krause A., Neumayer N., Schödel R., Seth A., Hilker M., de Zeeuw P.T., Kuntschner H., Walcher C.J., Lützgendorf N., Kissler-Patig M. 2015. “KMOS view of the Galactic centre. I. Young stars are centrally concentrated”. *A&A*, **584**:A2. [ADS].
- Fellhauer M., Kroupa P. 2002. “Merging Massive Star Clusters as Building Blocks of Dwarf Galaxies?” *Ap&SS*, **281**:355–358. [ADS].
- Ferrarese L., Côté P., Dalla Bontà E., Peng E.W., Merritt D., Jordán A., Blakeslee J.P., Hasegan M., Mei S., Piatek S., et al. 2006. “A Fundamental Relation between Compact Stellar Nuclei, Supermassive Black Holes, and Their Host Galaxies”. *ApJ*, **644**:L21–L24. [ADS].
- Ferrero I., Abadi M.G., Navarro J.F., Sales L.V., Gurovich S. 2012. “The dark matter haloes of dwarf galaxies: a challenge for the Λ cold dark matter paradigm?” *MNRAS*, **425**:2817–2823. [ADS].
- Forbes D.A., Brodie J.P., Grillmair C.J. 1997. “On the Origin of Globular Clusters in Elliptical and cD Galaxies”. *AJ*, **113**:1652. [ADS].
- Forbes J.C., Krumholz M.R., Goldbaum N.J., Dekel A. 2016. “Suppression of star formation in dwarf galaxies by photoelectric grain heating feedback”. *Nature*, **535**:523–525. [ADS].
- Freudling W., Romaniello M., Bramich D.M., Ballester P., Forchi V., García-Dabó C.E., Moehler S., Neeser M.J. 2013. “Automated data reduction workflows for astronomy. The ESO Reflex environment”. *A&A*, **559**:A96. [ADS].
- Fujii M.S., Baba J. 2012. “Destruction of star clusters due to the radial migration in spiral galaxies”. *MNRAS*, **427**:L16–L20. [ADS].
- García-Burillo S., Combes F., Usero A., Aalto S., Krips M., Viti S., Alonso-Herrero A., Hunt L.K., Schinnerer E., Baker A.J., et al. 2014. “Molecular line emission in NGC 1068 imaged with ALMA. I. An AGN-driven outflow in the dense molecular gas”. *A&A*, **567**:A125. [ADS].
- Geach J.E., Hickox R.C., Diamond-Stanic A.M., Krips M., Rudnick G.H., Tremonti C.A., Sell P.H., Coil A.L., Moustakas J. 2014. “Stellar feedback as the origin of an extended molecular outflow in a starburst galaxy”. *Nature*, **516**:68–70. [ADS].
- Geen S., Hennebelle P., Tremblin P., Rosdahl J. 2016. “Feedback in Clouds II: UV photoionization and the first supernova in a massive cloud”. *MNRAS*, **463**:3129–3142. [ADS].
- Genzel R., Förster Schreiber N.M., Lang P., Tacchella S., Tacconi L.J., Wuyts S., Bandara K., Burkert A., Buschkamp P., Carollo C.M., et al. 2014. “The SINS/zC-SINF Survey of $z \sim 2$ Galaxy Kinematics: Evidence for Gravitational Quenching”. *ApJ*, **785**:75. [ADS].

- Georgiev I.Y., Böker T. 2014. “Nuclear star clusters in 228 spiral galaxies in the HST/WFPC2 archive: catalogue and comparison to other stellar systems”. *MNRAS*, **441**:3570–3590. [ADS].
- Georgiev I.Y., Böker T., Leigh N., Lützgendorf N., Neumayer N. 2016. “Masses and scaling relations for nuclear star clusters, and their co-existence with central black holes”. *MNRAS*, **457**:2122–2138. [ADS].
- Gerhard O.E. 1993. “Line-of-sight velocity profiles in spherical galaxies: breaking the degeneracy between anisotropy and mass.” *MNRAS*, **265**:213. [ADS].
- Gieren W., Pietrzyński G., Soszyński I., Bresolin F., Kudritzki R.P., Minniti D., Storm J. 2005. “The Araucaria Project: Near-Infrared Photometry of Cepheid Variables in the Sculptor Galaxy NGC 300”. *ApJ*, **628**:695–703. [ADS].
- Gillessen S., Genzel R., Fritz T.K., Eisenhauer F., Pfuhl O., Ott T., Schartmann M., Ballone A., Burkert A. 2013. “Pericenter Passage of the Gas Cloud G2 in the Galactic Center”. *ApJ*, **774**:44. [ADS].
- Gillessen S., Genzel R., Fritz T.K., Quataert E., Alig C., Burkert A., Cuadra J., Eisenhauer F., Pfuhl O., Dodds-Eden K., et al. 2012. “A gas cloud on its way towards the supermassive black hole at the Galactic Centre”. *Nature*, **481**:51–54. [ADS].
- Graham A.W., Spitler L.R. 2009. “Quantifying the coexistence of massive black holes and dense nuclear star clusters”. *MNRAS*, **397**:2148–2162. [ADS].
- Grisdale K., Agertz O., Romeo A.B., Renaud F., Read J.I. 2017. “The impact of stellar feedback on the density and velocity structure of the interstellar medium”. *MNRAS*, **466**:1093–1110. [ADS].
- Guillard N., Emsellem E., Renaud F. 2016. “New insights on the formation of nuclear star clusters”. *MNRAS*, **461**:3620–3629. [ADS].
- Gültekin K., Richstone D.O., Gebhardt K., Lauer T.R., Tremaine S., Aller M.C., Bender R., Dressler A., Faber S.M., Filippenko A.V., et al. 2009. “The M- σ and M-L Relations in Galactic Bulges, and Determinations of Their Intrinsic Scatter”. *ApJ*, **698**:198–221. [ADS].
- Harris W.E. 2010. “A New Catalog of Globular Clusters in the Milky Way”. *ArXiv e-prints*. [ADS].
- Hartmann M., Debattista V.P., Seth A., Cappellari M., Quinn T.R. 2011. “Constraining the role of star cluster mergers in nuclear cluster formation: simulations confront integral-field data”. *MNRAS*, **418**:2697–2714. [ADS].
- Hayward C.C., Hopkins P.F. 2017. “How stellar feedback simultaneously regulates star formation and drives outflows”. *MNRAS*, **465**:1682–1698. [ADS].

- Hills J.G. 1980. “The effect of mass loss on the dynamical evolution of a stellar system - Analytic approximations”. *ApJ*, **235**:986–991. [ADS].
- Hockney R.W., Eastwood J.W. 1981. *Computer Simulation Using Particles*. [ADS].
- Holtzman J.A., Faber S.M., Shaya E.J., Lauer T.R., Groth J., Hunter D.A., Baum W.A., Ewald S.P., Hester J.J., Light R.M., et al. 1992. “Planetary Camera observations of NGC 1275 - Discovery of a central population of compact massive blue star clusters”. *AJ*, **103**:691–702. [ADS].
- Hopkins P.F., Kereš D., Oñorbe J., Faucher-Giguère C.A., Quataert E., Murray N., Bullock J.S. 2014. “Galaxies on FIRE (Feedback In Realistic Environments): stellar feedback explains cosmologically inefficient star formation”. *MNRAS*, **445**:581–603. [ADS].
- Hopkins P.F., Wetzel A., Keres D., Faucher-Giguere C.A., Quataert E., Boylan-Kolchin M., Murray N., Hayward C.C., Garrison-Kimmel S., Hummels C., et al. 2017. “FIRE-2 Simulations: Physics versus Numerics in Galaxy Formation”. *ArXiv e-prints*. [ADS].
- Howard C., Pudritz R., Harris W. 2017. “Simulating radiative feedback and star cluster formation in GMCs: II. Mass dependence of cloud destruction and cluster properties”. *ArXiv e-prints*. [ADS].
- Howard C.S., Pudritz R.E., Harris W.E. 2016. “Simulating radiative feedback and star cluster formation in GMCs - I. Dependence on gravitational boundedness”. *MNRAS*, **461**:2953–2974. [ADS].
- Hu C.Y., Naab T., Glover S.C.O., Walch S., Clark P.C. 2017. “Variable interstellar radiation fields in simulated dwarf galaxies: supernovae versus photoelectric heating”. *ArXiv e-prints*. [ADS].
- Hubble E.P. 1936. *Realm of the Nebulae*. [ADS].
- J Kamkar S., Jameson A., Wissink A., Sankaran V. 2011. “Automated off-body cartesian mesh adaption for rotorcraft simulations”.
- Kang X., Zhang F., Chang R., Wang L., Cheng L. 2016. “The star formation history of low-mass disk galaxies: A case study of NGC 300”. *A&A*, **585**:A20. [ADS].
- Kim J.h., Krumholz M.R., Wise J.H., Turk M.J., Goldbaum N.J., Abel T. 2013a. “Dwarf Galaxies with Ionizing Radiation Feedback. I. Escape of Ionizing Photons”. *ApJ*, **775**:109. [ADS].
- Kim J.h., Krumholz M.R., Wise J.H., Turk M.J., Goldbaum N.J., Abel T. 2013b. “Dwarf Galaxies with Ionizing Radiation Feedback. II. Spatially Resolved Star Formation Relation”. *ApJ*, **779**:8. [ADS].

- Kim S.C., Sung H., Park H.S., Sung E.C. 2004. “UBVI Surface Photometry of the Spiral Galaxy NGC 300 in the Sculptor Group”. *Chin. J. Astron. Astrophys.*, **4**:299–310. [ADS].
- Koleva M., Prugniel P., De Rijcke S., Zeilinger W.W. 2011. “Age and metallicity gradients in early-type galaxies: a dwarf-to-giant sequence”. *MNRAS*, **417**:1643–1671. [ADS].
- Kraljic K., Bournaud F., Martig M. 2012. “The Two-phase Formation History of Spiral Galaxies Traced by the Cosmic Evolution of the Bar Fraction”. *ApJ*, **757**:60. [ADS].
- Kravtsov A.V., Klypin A.A., Khokhlov A.M. 1997. “Adaptive Refinement Tree: A New High-Resolution N-Body Code for Cosmological Simulations”. *ApJS*, **111**:73–94. [ADS].
- Kroupa P. 2005. “The Fundamental Building Blocks of Galaxies”. In *The Three-Dimensional Universe with Gaia*, edited by C. Turon, K.S. O’Flaherty, M.A.C. Perryman, volume 576 of *ESA Special Publication*, page 629. [ADS].
- Krumholz M.R., Bate M.R., Arce H.G., Dale J.E., Gutermuth R., Klein R.I., Li Z.Y., Nakamura F., Zhang Q. 2014. “Star Cluster Formation and Feedback”. *Protostars and Planets VI*, pages 243–266. [ADS].
- Krumholz M.R., Matzner C.D. 2009. “The Dynamics of Radiation-pressure-dominated H II Regions”. *ApJ*, **703**:1352–1362. [ADS].
- Krumholz M.R., Stone J.M., Gardiner T.A. 2007. “Magnetohydrodynamic Evolution of H II Regions in Molecular Clouds: Simulation Methodology, Tests, and Uniform Media”. *ApJ*, **671**:518–535. [ADS].
- Kuijken K., Merrifield M.R. 1993. “A New Method for Obtaining Stellar Velocity Distributions from Absorption-Line Spectra - Unresolved Gaussian Decomposition”. *MNRAS*, **264**:712. [ADS].
- Lada C.J., Lada E.A. 2003. “Embedded Clusters in Molecular Clouds”. *ARA&A*, **41**:57–115. [ADS].
- Leveque R.J. 1998. “Nonlinear Conservation Laws and Finite Volume Methods”. In *Saas-Fee Advanced Course 27: Computational Methods for Astrophysical Fluid Flow.*, edited by O. Steiner, A. Gautschy, page 1. [ADS].
- Li M., Bryan G.L., Ostriker J.P. 2017. “Quantifying Supernovae-driven Multiphase Galactic Outflows”. *ApJ*, **841**:101. [ADS].
- Linde A.D. 1982. “A new inflationary universe scenario: A possible solution of the horizon, flatness, homogeneity, isotropy and primordial monopole problems”. *Physics Letters B*, **108**:389–393. [ADS].
- Longmore S.N., Kruijssen J.M.D., Bastian N., Bally J., Rathborne J., Testi L., Stolte A., Dale J., Bressert E., Alves J. 2014. “The Formation and Early Evolution of Young Massive Clusters”. *Protostars and Planets VI*, pages 291–314. [ADS].

- Lopez L.A., Krumholz M.R., Bolatto A.D., Prochaska J.X., Ramirez-Ruiz E. 2011. “What Drives the Expansion of Giant H II Regions?: A Study of Stellar Feedback in 30 Doradus”. *ApJ*, **731**:91. [ADS].
- Lyubenova M., van den Bosch R.C.E., Côté P., Kuntschner H., van de Ven G., Ferrarese L., Jordán A., Infante L., Peng E.W. 2013. “The complex nature of the nuclear star cluster in FCC 277”. *MNRAS*, **431**:3364–3372. [ADS].
- Macciò A.V., Dutton A.A., van den Bosch F.C., Moore B., Potter D., Stadel J. 2007. “Concentration, spin and shape of dark matter haloes: scatter and the dependence on mass and environment”. *MNRAS*, **378**:55–71. [ADS].
- MacLachlan J.M., Bonnell I.A., Wood K., Dale J.E. 2015. “Photoionising feedback and the star formation rates in galaxies”. *A&A*, **573**:A112. [ADS].
- Melchior A.L., Combes F. 2013. “A cold-gas reservoir to fuel the M 31 nuclear black hole and stellar cluster”. *A&A*, **549**:A27. [ADS].
- Milgrom M. 2015. “MOND theory”. *Canadian Journal of Physics*, **93**:107–118. [ADS].
- Milosavljević M. 2004. “On the Origin of Nuclear Star Clusters in Late-Type Spiral Galaxies”. *ApJ*, **605**:L13–L16. [ADS].
- Mo H., van den Bosch F.C., White S. 2010. *Galaxy Formation and Evolution (Cambridge University Press)*. [ADS].
- Mo H.J., Mao S., White S.D.M. 1998. “The formation of galactic discs”. *MNRAS*, **295**:319–336. [ADS].
- Monnet G., Bacon R., Emsellem E. 1992. “Modelling the stellar intensity and radial velocity fields in triaxial galaxies by sums of Gaussian functions”. *A&A*, **253**:366–373. [ADS].
- Navarro J.F., Frenk C.S., White S.D.M. 1996. “The Structure of Cold Dark Matter Halos”. *ApJ*, **462**:563. [ADS].
- Nelson D., Genel S., Vogelsberger M., Springel V., Sijacki D., Torrey P., Hernquist L. 2015. “The impact of feedback on cosmological gas accretion”. *MNRAS*, **448**:59–74. [ADS].
- Neumayer N., Walcher C.J. 2012. “Are Nuclear Star Clusters the Precursors of Massive Black Holes?” *Advances in Astronomy*, **2012**:709038. [ADS].
- Neumayer N., Walcher C.J., Andersen D., Sánchez S.F., Böker T., Rix H.W. 2011. “Two-dimensional H α kinematics of bulgeless disc galaxies”. *MNRAS*, **413**:1875–1888. [ADS].
- Norris M.A., Escudero C.G., Faifer F.R., Kannappan S.J., Forte J.C., van den Bosch R.C.E. 2015. “An extended star formation history in an ultra-compact dwarf”. *MNRAS*, **451**:3615–3626. [ADS].

- Núñez A., Ostriker J.P., Naab T., Oser L., Hu C.Y., Choi E. 2017. “Modeling for Stellar Feedback in Galaxy Formation Simulations”. *ApJ*, **836**:204. [ADS].
- Offner S.S.R., Klein R.I., McKee C.F., Krumholz M.R. 2009. “The Effects of Radiative Transfer on Low-Mass Star Formation”. *ApJ*, **703**:131–149. [ADS].
- Payne J.L., Filipović M.D., Pannuti T.G., Jones P.A., Duric N., White G.L., Carpano S. 2004. “Multi-frequency study of extragalactic supernova remnants and H II regions. Sculptor group Sd galaxy NGC 300”. *A&A*, **425**:443–456. [ADS].
- Peebles P.J.E. 1969. “Origin of the Angular Momentum of Galaxies”. *ApJ*, **155**:393. [ADS].
- Peebles P.J.E., Dicke R.H. 1968. “Origin of the Globular Star Clusters”. *ApJ*, **154**:891. [ADS].
- Peng E.W., Jordán A., Côté P., Blakeslee J.P., Ferrarese L., Mei S., West M.J., Merritt D., Milosavljević M., Tonry J.L. 2006. “The ACS Virgo Cluster Survey. IX. The Color Distributions of Globular Cluster Systems in Early-Type Galaxies”. *ApJ*, **639**:95–119. [ADS].
- Peters T., Banerjee R., Klessen R.S., Mac Low M.M. 2011. “The Interplay of Magnetic Fields, Fragmentation, and Ionization Feedback in High-mass Star Formation”. *ApJ*, **729**:72. [ADS].
- Pfeffer J., Baumgardt H. 2013. “Ultra-compact dwarf galaxy formation by tidal stripping of nucleated dwarf galaxies”. *MNRAS*, **433**:1997–2005. [ADS].
- Pfeffer J., Griffen B.F., Baumgardt H., Hilker M. 2014. “Contribution of stripped nuclear clusters to globular cluster and ultracompact dwarf galaxy populations”. *MNRAS*, **444**:3670–3683. [ADS].
- Pflamm-Altenburg J., Kroupa P. 2009. “Recurrent gas accretion by massive star clusters, multiple stellar populations and mass thresholds for spheroidal stellar systems”. *MNRAS*, **397**:488–494. [ADS].
- Portegies Zwart S.F., McMillan S.L.W., Gieles M. 2010. “Young Massive Star Clusters”. *ARA&A*, **48**:431–493. [ADS].
- Price D.J., Bate M.R. 2008. “The effect of magnetic fields on star cluster formation”. *MNRAS*, **385**:1820–1834. [ADS].
- Raddick J., Lintott C.J., Schawinski K., Thomas D., Nichol R.C., Andreescu D., Bamford S., Land K.R., Murray P., Slosar A., et al. 2007. “Galaxy Zoo: An Experiment in Public Science Participation”. In *American Astronomical Society Meeting Abstracts*, volume 39 of *Bulletin of the American Astronomical Society*, page 892. [ADS].

- Raskutti S., Ostriker E.C., Skinner M.A. 2016. “Numerical Simulations of Turbulent Molecular Clouds Regulated by Radiation Feedback Forces. I. Star Formation Rate and Efficiency”. *ApJ*, **829**:130. [ADS].
- Renaud F. 2018. “Star Clusters in Evolving Galaxies”. *ArXiv e-prints*. [ADS].
- Renaud F., Agertz O., Gieles M. 2017. “The origin of the Milky Way globular clusters”. *MNRAS*, **465**:3622–3636. [ADS].
- Renaud F., Bournaud F., Duc P.A. 2015. “A parsec-resolution simulation of the Antennae galaxies: formation of star clusters during the merger”. *MNRAS*, **446**:2038–2054. [ADS].
- Renaud F., Bournaud F., Emsellem E., Elmegreen B., Teyssier R., Alves J., Chapon D., Combes F., Dekel A., Gabor J., et al. 2013. “A sub-parsec resolution simulation of the Milky Way: global structure of the interstellar medium and properties of molecular clouds”. *MNRAS*, **436**:1836–1851. [ADS].
- Rey-Raposo R., Dobbs C., Agertz O., Alig C. 2017. “The roles of stellar feedback and galactic environment in star-forming molecular clouds”. *MNRAS*, **464**:3536–3551. [ADS].
- Ricotti M., Parry O.H., Gnedin N.Y. 2016. “A Common Origin for Globular Clusters and Ultra-faint Dwarfs in Simulations of the First Galaxies”. *ApJ*, **831**:204. [ADS].
- Roberts Jr. W.W., Huntley J.M., van Albada G.D. 1979. “Gas dynamics in barred spirals - Gaseous density waves and galactic shocks”. *ApJ*, **233**:67–84. [ADS].
- Rosdahl J., Blaizot J., Aubert D., Stranex T., Teyssier R. 2013. “RAMSES-RT: radiation hydrodynamics in the cosmological context”. *MNRAS*, **436**:2188–2231. [ADS].
- Rossa J., van der Marel R.P., Böker T., Gerssen J., Ho L.C., Rix H.W., Shields J.C., Walcher C.J. 2006. “Hubble Space Telescope STIS Spectra of Nuclear Star Clusters in Spiral Galaxies: Dependence of Age and Mass on Hubble Type”. *AJ*, **132**:1074–1099. [ADS].
- Salaris M., Weiss A., Percival S.M. 2004. “The age of the oldest Open Clusters”. *A&A*, **414**:163–174. [ADS].
- Savorgnan G.A.D. 2016. “Supermassive Black Holes and their Host Spheroids III. The Mbh-nsph Correlation”. *ApJ*, **821**:88. [ADS].
- Schinnerer E., Böker T., Meier D.S. 2003. “Molecular Gas and the Nuclear Star Cluster in IC 342: Sufficient Inflow for Recurring Star Formation Events?” *ApJ*, **591**:L115–L118. [ADS].
- Schinnerer E., Böker T., Meier D.S., Calzetti D. 2008. “Self-Regulated Fueling of Galaxy Centers: Evidence for Star Formation Feedback in IC 342’s Nucleus”. *ApJ*, **684**:L21. [ADS].

- Schmidt M. 1959. “The Rate of Star Formation.” *ApJ*, **129**:243. [ADS].
- Schweizer F. 1987. “Star formation in colliding and merging galaxies”. In *Nearly Normal Galaxies. From the Planck Time to the Present*, edited by S.M. Faber, pages 18–25. [ADS].
- Scott N., Graham A.W. 2013. “Updated Mass Scaling Relations for Nuclear Star Clusters and a Comparison to Supermassive Black Holes”. *ApJ*, **763**:76. [ADS].
- Seth A., Agüeros M., Lee D., Basu-Zych A. 2008a. “The Coincidence of Nuclear Star Clusters and Active Galactic Nuclei”. *ApJ*, **678**:116–130. [ADS].
- Seth A.C., Blum R.D., Bastian N., Caldwell N., Debattista V.P. 2008b. “The Rotating Nuclear Star Cluster in NGC 4244”. *ApJ*, **687**:997–1003. [ADS].
- Seth A.C., Cappellari M., Neumayer N., Caldwell N., Bastian N., Olsen K., Blum R.D., Debattista V.P., McDermid R., Puzia T., et al. 2010. “The NGC 404 Nucleus: Star Cluster and Possible Intermediate-mass Black Hole”. *ApJ*, **714**:713–731. [ADS].
- Seth A.C., Dalcanton J.J., Hodge P.W., Debattista V.P. 2006. “Clues to Nuclear Star Cluster Formation from Edge-on Spirals”. *AJ*, **132**:2539–2555. [ADS].
- Smajić S., Moser L., Eckart A., Busch G., Combes F., García-Burillo S., Valencia-S. M., Horrobin M. 2015. “The nuclear gas disk of NGC 1566 dissected by SINFONI and ALMA”. *A&A*, **583**:A104. [ADS].
- Smith M.C., Sijacki D., Shen S. 2017. “Supernova feedback in numerical simulations of galaxy formation: separating physics from numerics”. *ArXiv e-prints*. [ADS].
- Teyssier R. 2002. “Cosmological hydrodynamics with adaptive mesh refinement. A new high resolution code called RAMSES”. *A&A*, **385**:337–364. [ADS].
- Teyssier R., Pontzen A., Dubois Y., Read J.I. 2013. “Cusp-core transformations in dwarf galaxies: observational predictions”. *MNRAS*, **429**:3068–3078. [ADS].
- Torrey P., Hopkins P.F., Faucher-Giguère C.A., Vogelsberger M., Quataert E., Kereš D., Murray N. 2016. “An instability of feedback regulated star formation in galactic nuclei”. *ArXiv e-prints*. [ADS].
- Tremaine S.D., Ostriker J.P., Spitzer Jr. L. 1975. “The formation of the nuclei of galaxies. I - M31”. *ApJ*, **196**:407–411. [ADS].
- Tremblin P., Anderson L.D., Didelon P., Raga A.C., Minier V., Ntormousi E., Pettitt A., Pinto C., Samal M.R., Schneider N., et al. 2014. “Age, size, and position of H ii regions in the Galaxy. Expansion of ionized gas in turbulent molecular clouds”. *A&A*, **568**:A4. [ADS].

- Turner M.L., Côté P., Ferrarese L., Jordán A., Blakeslee J.P., Mei S., Peng E.W., West M.J. 2012. “The ACS Fornax Cluster Survey. VI. The Nuclei of Early-type Galaxies in the Fornax Cluster”. *ApJS*, **203**:5. [ADS].
- van der Marel R.P., Franx M. 1993. “A new method for the identification of non-Gaussian line profiles in elliptical galaxies”. *ApJ*, **407**:525–539. [ADS].
- van Dokkum P.G. 2001. “Cosmic-Ray Rejection by Laplacian Edge Detection”. *PASP*, **113**:1420–1427. [ADS].
- Vazquez-Semadeni E. 1994. “Hierarchical Structure in Nearly Pressureless Flows as a Consequence of Self-similar Statistics”. *ApJ*, **423**:681. [ADS].
- VERITAS Collaboration, Acciari V.A., Aliu E., Arlen T., Aune T., Bautista M., Beilicke M., Benbow W., Boltuch D., Bradbury S.M., et al. 2009. “A connection between star formation activity and cosmic rays in the starburst galaxy M82”. *Nature*, **462**:770–772. [ADS].
- Walch S.K., Whitworth A.P., Bisbas T., Wunsch R., Hubber D. 2012. “Dispersal of molecular clouds by ionizing radiation”. *MNRAS*, **427**:625–636. [ADS].
- Walcher C.J., Böker T., Charlot S., Ho L.C., Rix H.W., Rossa J., Shields J.C., van der Marel R.P. 2006. “Stellar Populations in the Nuclei of Late-Type Spiral Galaxies”. *ApJ*, **649**:692–708. [ADS].
- Walcher C.J., van der Marel R.P., McLaughlin D., Rix H.W., Böker T., Häring N., Ho L.C., Sarzi M., Shields J.C. 2005. “Masses of Star Clusters in the Nuclei of Bulgeless Spiral Galaxies”. *ApJ*, **618**:237–246. [ADS].
- Wallace L., Hinkle K. 1996. “High-Resolution Spectra of Ordinary Cool Stars in the K Band”. *ApJS*, **107**:312. [ADS].
- Wareing C.J., Pittard J.M., Falle S.A.E.G. 2017. “Hydrodynamic simulations of mechanical stellar feedback in a molecular cloud formed by thermal instability”. *MNRAS*, **470**:2283–2313. [ADS].
- Wareing C.J., Pittard J.M., Falle S.A.E.G., Van Loo S. 2016. “Magnetohydrodynamical simulation of the formation of clumps and filaments in quiescent diffuse medium by thermal instability”. *MNRAS*, **459**:1803–1818. [ADS].
- White S.D.M., Rees M.J. 1978. “Core condensation in heavy halos - A two-stage theory for galaxy formation and clustering”. *MNRAS*, **183**:341–358. [ADS].
- Wright J.T., Eastman J.D. 2014. “Barycentric Corrections at 1 cm s⁻¹ for Precise Doppler Velocities”. *PASP*, **126**:838. [ADS].

- Zhang Q., Fall S.M. 1999. “The Mass Function of Young Star Clusters in the “Antennae” Galaxies”. *ApJ*, **527**:L81–L84. [ADS].
- Zheng Y., Peek J.E.G., Werk J.K., Putman M.E. 2017. “HST/COS Observations of Ionized Gas Accretion at the Disk-Halo Interface of M33”. *ApJ*, **834**:179. [ADS].
- Zinn R. 1985. “The globular cluster system of the galaxy. IV - The halo and disk subsystems”. *ApJ*, **293**:424–444. [ADS].

Nicolas Jean Xavier GUILLARD

PROFESSIONAL DATA

ADDRESS: ESO Headquarters
Karl-Schwarzschild-Str. 2
85748 Garching, Germany
PHONE: +49 89 3200 6293
EMAIL: nguillar@eso.org

RESEARCH INTERESTS

galaxy formation & evolution - dwarf galaxies - star clusters - nuclear/globular clusters - numerical simulation

RESEARCH EXPERIENCE

SEPTEMBER 2014 (ONGOING)	PhD, European Southern Observatory (ESO), Garching, GERMANY
Defense in MAY 2018	<i>Fueling and growth of galactic nuclei</i> Perform and analyse hydrodynamical simulations to understand how galactic nuclei form Reduce and analyse SINFONI data to study the nucleus of NGC300 Main supervisor: Emsellem. Associate supervisors: Neumayer, Renaud
MARCH-JUNE 2014	Master Internship, Observatoire astronomique de Strasbourg, Strasbourg, FRANCE <i>Evolution of star forming circumnuclear rings in barred and double-barred galaxies</i> Study of the formation of circumnuclear rings and star formation scenarios in double-barred galaxies. Supervisor: Prof. Hervé Wozniak
APRIL-JUNE 2013	Internship, IPAG, Grenoble, FRANCE <i>Simulation of gamma binaries population in the Galaxy</i> Development of an IDL code that estimates the number of potentially observable gamma binaries in the Galaxy. Supervisor: Dr. Guillaume Dubus
MAY-JUNE 2012	Internship, CENBG, Gradignan, FRANCE <i>Study of the SuperNEMO project calorimeter</i> Use of an electrons spectrometer Supervisor: Dr. Christine Marquet

EDUCATION

2012 – 2014 Master Degree (with honors) in Physics, UJF, Grenoble, FRANCE
Specialization : Astrophysics, Planetology and Plasmas
2009 – 2012 Bachelor diploma (with honors), Bordeaux 1, Bordeaux, FRANCE
2009 French Scientific Baccalaureat diploma (passed with distinctions), Lycée des Graves, Gradignan, FRANCE
Specialization : Physics and Chemistry

COMPUTER TIME

4 successful proposals at the Computational Center for Particle And Astrophysics (C2PAP, Germany) cluster in 2015, 2016, 2017 and 2018. Total of 11 million CPU hours, all as PI

CoI of an accepted proposal in 2017 for Grand Équipement National de Calcul Intensif (GENCI, France) program on Curie (France, PI: F. Bournaud, project of 16.4 million CPU hours)

ORGANIZATION OF SCIENTIFIC EVENTS

October 2016	LOC member of the ESO workshop DWARF GALAXIES
September 2016	SOC member of the Excellence cluster PhD event
July 2016	LOC member of the ESO conference DISCS IN GALAXIES
Since November 2015	Organizer of the Yellow Box Duty (technical preparation for lunch talks and Colloquium) at ESO

LIST OF PUBLICATIONS

Dubus, Guillard, Petrucci & Martin, 2017	Sizing up the population of gamma-ray binaries, A&A, 608, A59
Guillard, Emsellem & Renaud, 2016	New insights on the formation of nuclear clusters, MNRAS, 461, 3620-3629

WORK IN PROGRESS

Guillard, Emsellem & Renaud, MNRAS in press	Impact of radiation feedback on the assembly of star clusters in galactic context
---	---

CONFERENCE & WORKSHOP

2017	February	Ringberg, Germany	The exciting lives of galactic nuclei (invited talk) <i>Gas infall and cluster spiralling</i>
2016	October	Paris, France	Ramses User meeting (talk) <i>Formation of nuclear clusters: a bumpy road</i>
	September	Garching, Germany	Seminar <i>Formation of nuclear clusters</i>
	August	Heidelberg, Germany	Star Clusters: from Infancy to Teenagehood (talk) <i>Nuclear clusters in their infancy: a bumpy road</i>
	July	Sexten, Italy	The Role of Feedback in the Formation and Evolution of Star Clusters (talk) <i>Impact of feedback on nuclear clusters</i>
	July	ESO Garching, Germany	Discs in Galaxies (poster) <i>From galactic discs to nuclear clusters</i>
	July	Heidelberg MPIA, Germany	Seminar <i>Formation of nuclear clusters</i>
2015	November	Guildford, UK	Seminar
	October	Garching, Germany	Universe Colloquium (talk)
	September	Oxford, UK	Ramses User Meeting (talk) <i>Nuclear clusters in high-resolution simulations of dwarf galaxies</i>
	July	Garching, Germany	Seminar
	June	Prato, Italy	The Many Pathways to Galaxy Growth (talk) <i>Star clusters in high-resolution simulations of dwarf galaxies</i>
	April	Munich, Germany	Physics of the Interstellar Medium (talk) <i>Fuelling and growth of galactic nuclei</i>

Acknowledgements

First of all, I would like to thank my supervisor Eric for offering me this PhD position. Thank you for your trust, your guidance and your availability despite your other responsibilities at ESO (even after more than 3 years at ESO, I still don't know how your brain can manage a hundred tasks at the same time). Thank you for your patience especially during the papers-writing times. Thank you for your support and for giving me a freedom that, I am sure, a lot of PhD students would envy.

Thank you Florent for being my “second non-official” supervisor. You were my encyclopedia whenever I needed help on RAMSES or basic physics. Thank you for the energy (and also patience!) you invested in me. Without a doubt, my writing and presenting skills have improved thanks to your advice and honesty.

Thank you Nadine for guiding me into the realm of observations which was an unknown territory for me. Thank you Arianna and Mayte for the help you provided me with the extraction of the data. Thank you also Iskren, Torsten, Nikolay, Morgan and Anna for the insightful conversations we had at MPIA and the good time we spent in Heidelberg.

Thank you ESO students, fellows, postdocs, staff for many discussions, talks and conversations. Thank you Darshan, Tereza, Boris, Gael, Ivan, Marco, Dinko, Anne, Mathieu for making my time at ESO unforgettable. Thank you Stellar, Nelma for helping me in the administrative works. Many thanks to the librarians Uta and Dominic for their help and quick response to my requests. I am indebted to Ramona for her translation of the Thesis abstract.

Et puis évidemment, un immense merci à ma famille qui m'a soutenu pour cette première expérience à l'étranger et qui a dû supporter mon absence pendant que je buvais (modérément) des bières. Merci aussi aux amis proches. Merci Cyril, Thomas, Cathie, Antho et Dany pour ces moments de joie (et quelques fois de rage, on ne va pas se mentir) sur LoL qui m'ont aidés à décompresser et à penser à autre chose que la thèse. Merci à vous Julien et Kevin pour votre éternel soutien et pour les excellents moments que j'ai passé avec vous quand je rentrais en France.

“Do not look at stars as bright spots only. Try to take in the vastness of the universe.”

Maria Mitchell, Astronomer

